Internal Physical and Chemical Characteristics of Starless Cores on the Brink of Gravitational Collapse

by

Shadi Chitsazzadeh
B.Sc., Shahid Beheshti University, 2005
M.Sc., University of Western Ontario, 2009

A Dissertation Submitted in Partial Fulfillment of the
Requirements for the Degree of

DOCTOR OF PHILOSOPHY

in the Department of Physics and Astronomy

Internal Physical and Chemical Characteristics of Starless Cores on the Brink of Gravitational Collapse

by

Shadi Chitsazzadeh
B.Sc., Shahid Beheshti University, 2005
M.Sc., University of Western Ontario, 2009

Supervisory Committee

Dr. J. Di Francesco, Co-Supervisor
(Physics and Astronomy)

Dr. S. Ellison, Co-Supervisor
(Physics and Astronomy)

Dr. C. Pritchet, Departmental Member
(Physics and Astronomy)

Dr. R. Hamme, Outside Member
(Earth and Ocean Sciences)

Supervisory Committee

Dr. J. Di Francesco, Co-Supervisor
(Physics and Astronomy)

Dr. S. Ellison, Co-Supervisor
(Physics and Astronomy)

Dr. C. Pritchet, Departmental Member
(Physics and Astronomy)

Dr. R. Hamme, Outside Member
(Earth and Ocean Sciences)

ABSTRACT

Using various molecular line and continuum emission criteria, we have selected a sample of six isolated, dense concentrations of molecular gas, i.e., "cores", which are either starless (L694-2, L429, L1517B, and L1689-SMM16) or contain a protostellar Very Low Luminosity Object (VeLLO) and are currently experiencing gravitational collapse (L1014 and L1521F). Studying the molecular emission from dense gas tracers toward this sample of cores will help us gain a more detailed image of the internal physical conditions of dense cores and their evolution.

We observed the cores in our sample in NH_3 (1,1) and (2,2) emission using the Green Bank Telescope (GBT) and in N_2H^+ (1−0) emission using the Nobeyama Radio Observatory (NRO). L429 shows the most complicated structure among the cores in our sample. Also, the maxima of molecular line integrated intensities and dust continuum emission toward L429 show a significant offset. The rest of the cores in our sample are roughly round and the morphologies of line integrated intensities follow that of the corresponding continuum emission closely. Cores in our sample have gas kinetic temperatures $\sim 9 - 10$ K and therefore show comparable thermal velocity dispersions. L429 and L1517B are, respectively, the most turbulent and most quiescent cores in our sample. Finally, L1521F is the most centrally concentrated core of our sample.

L1689-SMM16 is the least previously studied core in our sample and had not yet been probed in molecular emission. Jeans and virial analyses made using updated measurements of core mass and size confirm that L1689-SMM16 is prestellar, i.e., gravitationally bound. It also has accumulated more mass compared to its corresponding Jeans mass in the absence of magnetic fields and therefore is a "super-Jeans" core. The high levels of $X(NH_3)/X(N_2H^+)$ and deuterium fractionation reinforce the idea that the core has not yet formed a protostar. Comparing the physical parameters of the core with those of a Bonnor-Ebert sphere reveals the advanced evolutionary stage of L1689-SMM16 and shows that it might be unstable to collapse. We do not detect any evidence of infall motions toward the core, however. Instead, red asymmetry in the line profiles of HCN (1−0) and HNC (1−0) indicates expansion of the outer layers of the core at a speed of $\sim 0.2 - 0.3$ km s^{-1}. For a gravitationally bound core, expansion in the outer layers might indicate that L1689-SMM16 is experiencing oscillations.

Radiative transfer modelling of NH_3 emission toward L694-2 and L1521F at low and high spatial resolutions show that the less evolved core, L694-2, is best described by relatively constant radial profiles of temperature and fractional NH_3 abundance. On the other hand, L1521F, which contains a protostellar VeLLO, is best described by a radial abundance profile that is enhanced toward the core centre and a radial temperature profile that decreases toward the core centre. Comparison of our results with previous studies on L1544, a well-studied starless core, imply that as dense cores evolve and progress toward the moment of collapse, they become more centrally concentrated. As a result, the gas temperatures at their centres decrease, leading to increase in levels of CO depletion factor and increase in NH_3 fractional abundance toward the centre.

Contents

List of Tables

List of Figures

ACKNOWLEDGEMENTS

To my advisor, James, thank you for giving me the opportunity to work on this project and learn from you. None of this would have been possible without your guidance, constant support, and patience. It was an absolute pleasure working with you. Thank you for everything!

To my advisory committee members, Sara, Roberta, and Chris, thank you for your support and guidance during my PhD studies!

To my dear friend, Sarah, thank you for being an unbelievably amazing friend and colleague. You were one of the reasons why my time in Victoria has been so enjoyable. I have learned a lot from you!

To my amazing friends, Azadeh H., Nima, Ghazal, and Azadeh F., thank you for being my family in Victoria!

To my fellow graduate students, thank you for all the fun times and being by my side every step of the way!

To Scott, Rachel, Yoshito, and Helen, thank you for being such amazing friends and collaborators. Thank you for everything that you taught me!

To Belaid Moa and Stephenson Yang, thank you for your incredible IT support for the modelling of my data!

To all of the support scientists at GBT, JVLA, NRAO, NRO, and Mopra, and IT support staff at HIA, thank you for sharing your knowledge with me, and helping me complete this project!

To Shima, thank you for being you! The best "best friend" one could ever hope for!

Lastly but certainly not the least, to my loving family, Maman, Baba, Maman-joon, Dayi-Hamid, Ali, and Ashkan. Only you could have supported me from miles and miles away! Everything that I am is because of you!

DEDICATION

For Maman and Baba.
Thank you for giving me wings to fly and roots to come back to.

To Georges Prosper Remi, for inspiring me to love adventures before I could read.

Chapter 1

Introduction

1.1 Star Formation

Stars are fundamental units of the Universe. They play a crucial role in the physical and chemical evolution of many astronomical environments, making understanding star formation one of the most important goals of astronomy. Molecular clouds, natural sites of star formation, are enormous complexes of dust and gas where temperature is approximately 15 K, number density is around 10^2 cm^{-3}, masses are on the order of 10^5 M$_\odot$, and typical sizes are approximately 50 pc[1] across (Figure 1.1; Stahler & Palla 2005). Thousands of molecular clouds exist in our Galaxy, mainly in the spiral arms.

The density structures of molecular clouds are observed to be non-uniform with local regions of significantly greater density in filamentary or clumpy shapes. The high column density (i.e., amount of material in the line-of-sight) of dust and gas in these regions leads to the obscuration of light as a result of scattering and absorption. This phenomenon is referred to as interstellar extinction and is represented by the opacity of the cloud (κ_λ). Opacity is a measure of the amount of emission removed from a beam of light propagating through a medium and is often expressed in terms of the "optical depth" (τ_λ). High optical depth (i.e., "optically thick") emission ($\tau_\lambda \gg 1$) comes mostly from a short distance into the (opaque) medium. Low optical depth (i.e., "optically thin") emission ($\tau_\lambda \ll 1$), however, comes from long distances into the medium or perhaps the entire (transparent) medium. The amount of optical depth depends on the characteristics of the material along the line-of-sight. In molecular

[1]Parsec (pc) is a unit of length commonly used in astronomy equal to 3.1×10^{16} metres.

Figure 1.1: Perseus molecular cloud (Credit: Gerhard Bachmayer).

clouds, the optical depth of molecular emission lines depends on abundances (i.e., higher column densities), therefore highly abundant molecules have optically thick lines. The optical depth of continuum emission depends on the abundance of dust and the wavelength of light. For example, Figure 1.2 shows optical and infrared (IR) continuum observations of the Trapezium cluster in the Orion Molecular Cloud (OMC). At optical wavelengths, the OMC is opaque to background starlight, but at longer wavelengths of IR, it becomes transparent and the embedded stars are visible. Thus, the OMC is optically thick at visual wavelengths but relatively optically thin at IR wavelengths.

Stars form out of centrally condensed **clumps** in molecular clouds. In general, clumps contain smaller substructures, commonly called **cores**, with densities on the order of 10^4 cm^{-3}, masses of 10 $M_\odot$, and characteristic size of 0.1 pc. Star formation mostly happens in the clustered environments of clumps. The complex observed geometry of these regions, however, makes studying the clustered star formation process a complicated task. There are also compact dense cores not embedded within clumps. Such **isolated dense cores** go through the star formation process in relative separation from the rest of the cloud. Due to their isolation, the evolution of these

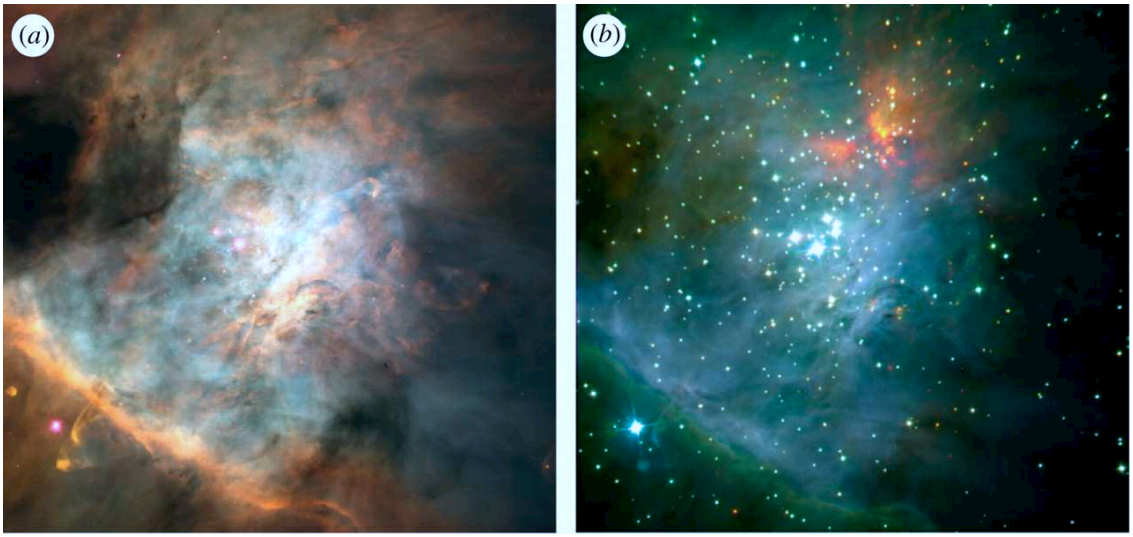

Figure 1.2: (a) Optical and (b) deep IR images of the embedded Trapezium cluster associated with the Orion Molecular Cloud using NASA Hubble Space Telescope (HST) and the ESO Very Large Telescope (VLT) (Lada & Lada 2003).

cores is minimally affected by environmental effects, making them ideal targets to study the star formation process.

Based on the IR emission from dense cores, many dense cores have been found to contain compact luminous sources, a.k.a. **Young Stellar Objects** (YSO). Dense cores which do not have any embedded YSOs are known as **starless cores**. As the link between the diffuse material in molecular clouds and protostars, starless cores are an important class of objects to study because they represent the physical conditions of dense gas prior to star formation.

1.2 Physical Characteristics of Cores

1.2.1 Initial Conditions of Star Formation

Star formation involves a sequence of different stages that starts with the fragmentation of a molecular cloud into dense, gravitationally bound starless cores. It continues with the collapse and evolution of these condensations due to the competing forces of gravity, thermal and turbulent pressure, and magnetic fields (e.g., Shu et al. 1987; Evans 1999; André et al. 2000). During a brief initial phase, the gravitational energy is released in the form of radiation, leading to the formation of a roughly isothermal fragment with strong central concentration of matter with a radial density gradient of

r^{-2} toward the innermost regions. At the end of this initial phase, an opaque **protostar** is formed in the centre. During the subsequent phase, the central object builds up its mass through accretion of the surrounding material. As the collapse continues onto the protostar, the temperature slowly increases. Powerful ejections of small fractions of the accreted material in the form of jets or outflows are usually a signature of this main accretion phase. These outflows are believed to carry away the excess angular momentum of the accreting material. When the central object has accumulated most (90%) of its final, main-sequence mass, it becomes a pre-main-sequence (PMS) star.

Though we have a rough idea of star formation, the details of its early stages of star formation are not very well understood. Measuring the physical characteristics of dense starless cores (i.e., their internal densities, temperatures, and dynamics) reveals the initial conditions of collapse close to the moment of protostellar formation.

1.2.2 Density Structure

Starless cores are observed in various forms and shapes from elongated filaments to compact, round structures. Observations of cores reveal their two-dimensional projection on the plane of the sky but it is difficult to determine their shape in three dimensions. It should also be noted that core morphologies and structures can depend on the observed frequency, angular resolution and sensitivity of the observations, as well as the intensity level chosen to define the boundary of the core and its surroundings. Dust emission is generally optically thin at (sub)millimetre wavelengths and hence is a good direct tracer of the column density within cores. To derive volume densities, however, information or assumptions about dust temperature, opacities, gas-to-dust ratio, geometry and telescope beam pattern are necessary.

Shu (1977) suggested a "singular isothermal sphere" with a radial distribution proportional to r^{-2} as the initial state of isolated dense cores prior to gravitational collapse. Observations of starless cores, however, have revealed an inner flattening in the density of these regions surrounded by sharp outer edges (e.g., see Ward-Thompson et al. 1994 or André et al. 1996). These observational evidences are better described by the "Bonnor-Ebert Spheres (BES)" (Ebert 1955; Bonnor 1956), the non-singular solutions to the hydrostatic equilibrium equation which are stable under external pressure. The density profiles of BES are characterized by two regimes: a central region with slowly decreasing density at smaller radii and a power-law decrease

in density ($\sim r^{-2}$) at larger radii. BES solutions have been widely used to reproduce the density profiles of starless cores (e.g., Evans et al. 2001; Kirk et al. 2005).

1.2.3 Temperature Structure

Cores are heated depending on how much they are exposed to local radiation fields present in the interstellar medium. Many theoretical studies of dust temperatures (T_d) in starless cores suggest a decrease in T_d from ∼12 K at the core surface to ∼7 K in the centre (e.g., Evans et al. 2001). Such gradients in T_d can be explained by cores being optically thin to their own radiation and therefore cooling down effectively by emitting IR photons. These results were confirmed on larger scales (0.05 pc) by ISO observations showing evidence for T_d values cooler at the centre than the edge ($T_d \sim$ 10-20 K) (e.g., Ward-Thompson et al. 2002), but the situation at smaller scales (0.01 pc) was unclear due to low spatial resolution. Some recent studies using data from Herschel Space Observatory (HSO) have presented T_d maps of starless and protostellar cores (e.g., Stutz et al. 2010), confirming positive temperature gradients outwards. The large beam size of the Spectral and Photometric Imaging Receiver (SPIRE), one of the three scientific instruments on HSO (∼37″ FWHM[2] at 500 μm), however, still prevented probes of T_d variations within the innermost regions. The coupling between gas kinetic temperature (T_K) and T_d at very high densities ($n > 10^5$ cm^{-3}) provides an indirect way to measure temperature at high resolution by studying molecular tracers of dense cores, such as NH_3. This coupling, however, does not apply to less dense cores and outer regions of even denser cores. The presence of cosmic rays[3] does not allow T_K to fall too far below T_d (Goldsmith 2001; Galli et al. 2002). If the core is not heavily shielded, ultraviolet photons from nearby young O and B stars can eject electrons from interstellar dust grains, leading the surrounding gas to warm up. In this case, T_K can increase to values even higher than T_d in the outer skirts of the core (Young et al. 2004b).

[2]Full Width at Half Maximum (FWHM) is an expression of the extent of a function, given by the difference between the two extreme values of the independent variable at which the dependent variable is equal to half of its maximum value. Here, FWHM of the Gaussian function representing the telescope beam profile is a measure of the telescope's angular resolution.

[3]An ubiquitous flux of particles, mostly consisting of relativistic protons with an admixture of heavy elements and electrons.

1.2.4 Velocity Structure

1.2.4.1 Bulk Motions

Kinematics of dense cores as well as their parent molecular cloud can be probed both across the plane of the sky and along the line of sight using the variations in the molecular line profiles. Comparing line profiles of effective core tracers (such as N_2H^+) with that of cloud tracers (such as CO isotopologues) has revealed that cores do not have ballistic motions[4] with respect to their ambient gas (Walsh et al. 2004). As we move toward the inner regions of the cores, however, observations of line profiles show evidence of differential rotation and angular momentum evolution in some cores. For instance, detection of velocity gradients (< 5 km/s) with projected rotational axes misaligned with the projected core axis is a tracer of rotation (see e.g., Lada et al. 2003). Infall motions have also been detected in cores using molecular line profiles. Detection of a self-absorption dip between a brighter blue peak and a fainter red peak in optically thick lines toward a core while optically thin lines are detected to be symmetric toward the same region is a signature of such inward motions (Figure 1.3). Such infall profiles have been detected toward many starless cores revealing inward velocities to be on the order of 0.1 km/s or less (see e.g., Lee et al. 1999).

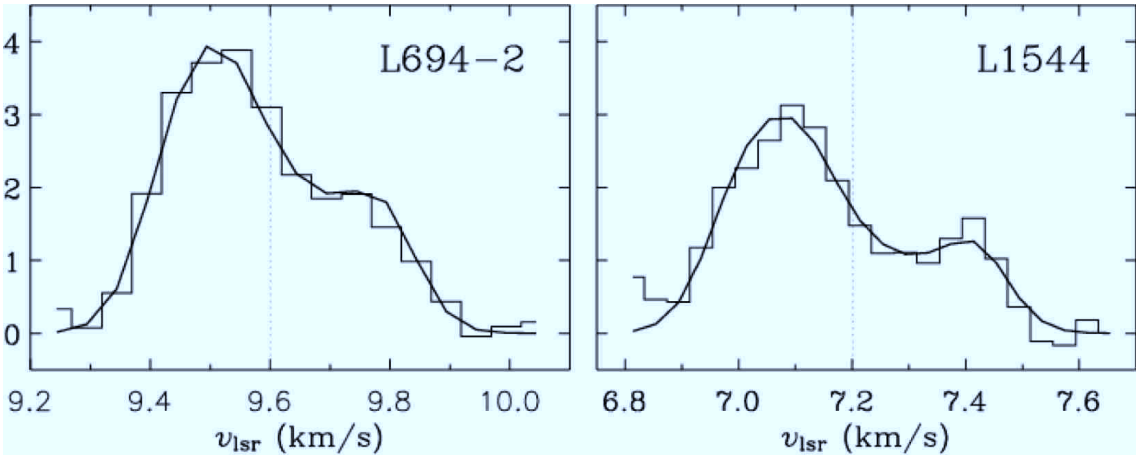

Figure 1.3: Histograms shows the spectra of one of the hyperfine components of N_2H^+ (1-0) transition form the starless cores L694-2 (left) and L1544 (right) (Williams et al. 2006). Brighter peaks are evidently blueshifted with respect to the source systemic velocity (dotted lines). The infall profile is successfully reproduced by a two layer radiative transfer model (solid curves) by Myers et al. (1996).

[4]Ballistic motion is movement of an object in a gravitational field.

1.2.4.2 Turbulent Motions

The observed velocity dispersion (the range of velocities about the mean gas velocity) (ΔV), is a measure of the total kinetic energy of gas within the cloud including thermal and turbulent (non-thermal) motions:

$$\Delta V^2 = \Delta V_{Tur}^2 + \Delta V_T^2, \tag{1.1}$$

where ΔV_{Tur} and ΔV_T are the contributions to the observed velocity dispersion due to turbulent and thermal motions, respectively.
Turbulent and thermal motions can be associated with macroscopic and microscopic motions of gas, respectively, providing pressure support against gravitational collapse in starless cores. Studying the velocity dispersion of molecular tracers yields information on the relative contributions from thermal and turbulent motions. The empirical Larson's law demonstrates the systemic variation of cloud size (L) with velocity dispersion (ΔV):

$$\Delta V \propto L^{0.5}. \tag{1.2}$$

On large scales (e.g., clouds), ΔV_T is an insignificant portion of the observed velocity dispersion. But what happens as we go to smaller size scales? At a certain length scale ($L_{Thermal} \sim 0.1$ pc), both thermal and turbulent velocity dispersions are equally important. But, as we move into even smaller scales ΔV_{Tur} becomes too low to make a significant contribution. At this point,

$$\Delta V \approx \Delta V_T. \tag{1.3}$$

The quiescent objects of size $L_{Thermal}$ present in molecular clouds and clumps are indeed "dense cores", natural birthplace of individual stars.

1.3 Observations of Isolated Cores

The dominant component of molecular clouds is molecular hydrogen (H_2) comprising approximately 70% of the mass of matter in these regions (Stahler & Palla 2005). Helium makes up most of the remaining mass. Even though dust grains and other molecules such as CO, H_2O, CH_3OH, etc. make up only a few percent of the mass of a molecular cloud, they are important constituents in determining its chemistry and

physics. Unfortunately, H_2 is very difficult to observe at low internal temperatures of molecular clouds. It is possible, however, to observe emission (typically rotational transitions) from other molecules to trace indirectly molecular hydrogen and probe physical parameters and evolution of the gas. In molecular cores, however, many prominent molecular tracers such as CO and its isotopologues are depleted through adsorption onto dust grains. N-bearing molecules, however, such as NH_3 and N_2H^+ appear to be resilient to depletion making these species ideal tracers of dense cores (Di Francesco et al. 2007 and references therein).

1.3.1 Ammonia

NH_3 is a symmetric top molecule. With some transitions excited at the low temperatures ($T < 10$ K) and high densities ($n \sim 10^{4-6}$ cm^{-3}) of dense cores, this species stands out as a reliable tracer of dense cores. The ability of the N atom to quantum tunnel through the hydrogen atom plane splits the $J = K$ rotational states into inversion doublets (The J and K quantum numbers are associated with the total angular momentum of the molecule and the angular momentum of the axis perpendicular to the hydrogen atom plane, respectively). The transition between these two levels gives rise to the main inversion lines, e.g., (1,1) or (2,2) (Stahler & Palla 2005). Other effects split the two inversion levels even further: The nitrogen nucleus has a non-spherical charge distribution and therefore a non-vanishing electric quadrupole moment, which can be torqued by the the variation of the electric field of the electrons. Therefore, the energy of this system depends on the orientation of the nuclear spin and the total angular momentum of the electrons, changing with the rotational state of the molecule. This effect will split each of the two inversion levels into three sublevels. Even further "hyperfine" splitting comes as a result of the magnetic interactions between the spins of the different nuclei in the molecule. In the end, the (1,1) and (2,2) rotational-inversion states show hyperfine structure with 18 and 21 lines, respectively. Some components are, however, blended together and some are too faint to be detected (Figures 1.4 and 1.5). The optical depth of the line can be effectively determined through relative intensities of the hyperfine components. Furthermore, the gas kinetic temperature (T_K) can be determined from the rotational temperature describing the relative populations of two rotational states such as the (1,1) and (2,2) transitions, assuming they both have similar line widths (e.g., see Ho & Townes 1983;

Rosolowsky et al. 2008; Friesen et al. 2009).

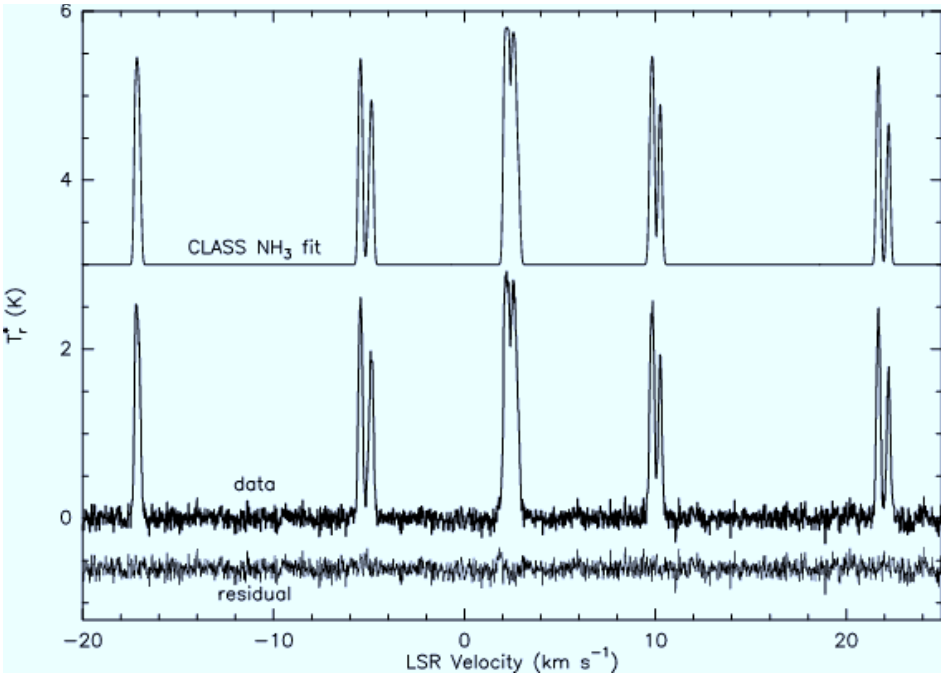

Figure 1.4: Hyperfine transitions of NH_3 (1,1) inversion line toward L183. The fit and fit residual are also shown and shifted for clarity (Pagani et al. 2007).

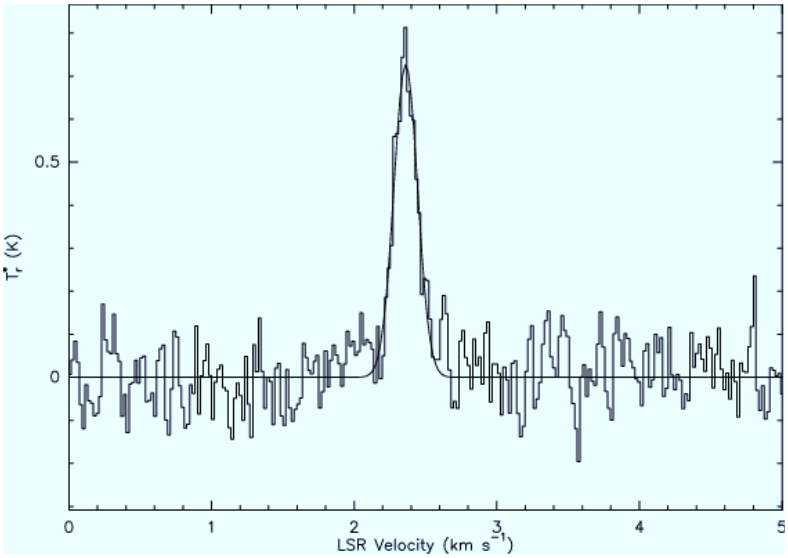

Figure 1.5: NH_3 (2,2) inversion line toward L183. Hyperfine components are too faint to be detected (Pagani et al. 2007).

Having the (line-of-sight averaged) kinetic temperature in hand, the line widths of NH_3 emission can be used to determine the internal velocity gradient in the core

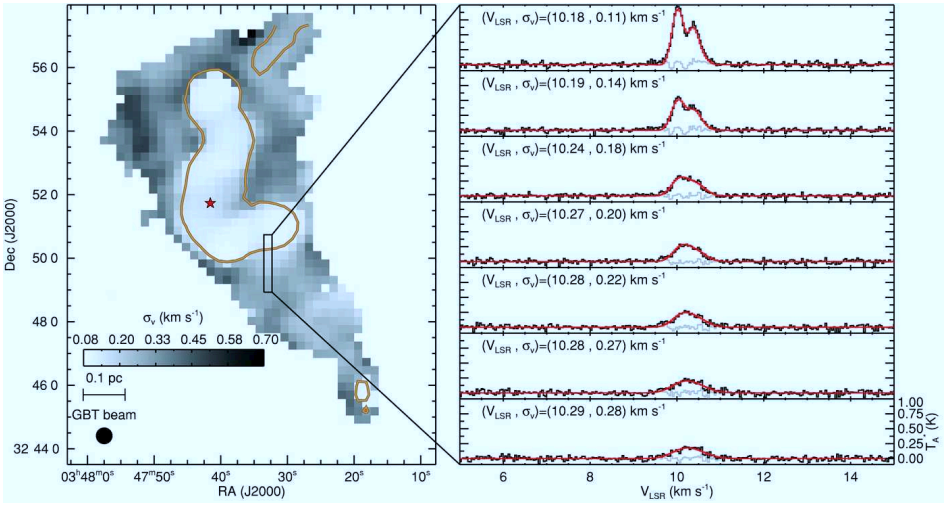

Figure 1.6: Velocity dispersion map of B5 derived from NH_3 observations at the Green Bank Telescope (GBT). The star shows the position of the embedded protostar. The systemic velocity and velocity dispersion obtained from the fit are displayed for each position. The coherent core is evident in the picture (Pineda et al. 2010).

and derive the relative importance of thermal and nonthermal (turbulent) motions in the dense cores (Barranco & Goodman 1998; Swift et al. 2005). Unlike the velocity dispersion in molecular clouds, known for years to be supersonic, velocity dispersions in dense cores tend to be subsonic, on the order of the thermal values, and also independent of scale. This phenomenon, commonly called a "transition to coherence", has been observed with other tracers of lower density gas (OH and $C^{18}O$ (1−0)) and higher density gas (NH_3) (Goodman et al. 1998). NH_3 emission, however, has been recently identified as the only tracer that can demonstrate the actual sharp transition between turbulent gas and more quiescent gas, so far (Pineda et al. 2010); (Figure 1.6).

1.3.2 Diazenylium

Another prominent tracer of the physical characteristics of dense cores is diazenylium (N_2H^+). Similar to NH_3, N_2H^+ is excited collisionally in these regions and remains abundant where other molecular tracers are either observed to deplete (e.g., CS and HCO^+), or are not easily excited and therefore are difficult to detect (e.g., pure hydrogen and deuterium species, such as H_2, see Di Francesco et al. 2007 and references therein). Furthermore, N_2H^+ is not found in shocked warm regions (Benson et al. 1998) and its abundance is reduced in outflows (Bergin et al. 1998), making it an

exclusive tracer of cold quiescent gas. The N_2H^+ (J = 1-0) rotational transition also shows hyperfine structure (Figure 1.7). Here, seven hyperfine components of this transition are characterized by the quantum numbers F_1, which results from the coupling of J with I_1 ($F_1 = J + I_1$, where $I_1 = 1$ corresponds to the nuclear spin of the outer nitrogen), and F ($F = F_1 + I_2$, where $I_2 = 1$ corresponds to the inner nitrogen). Fitting the hyperfine components simultaneously can be used to determine excitation temperature and line opacity (Caselli et al. 1995). Moreover, the radial distributions of column density, abundance, and line widths of nitrogen-based species in dense cores yield information on core collapse and its evolution. Notably, the line profiles of the N_2H^+ 1-0 transition can be used to derive the relative importance of thermal and turbulent motions (e.g., Di Francesco et al. 2004; Friesen et al. 2010b), and to search for evidence of core collapse (e.g., line wings, see Evans et al. 1999 and references therein). N_2H^+ emission is therefore an excellent probe of the physical structure and gas kinematics in dense cores. (Note that unlike NH_3 (1,1) and (2,2) emission lines, N_2H^+ (1−0) emission line cannot be used to estimate the internal kinetic temperature of the cores.)

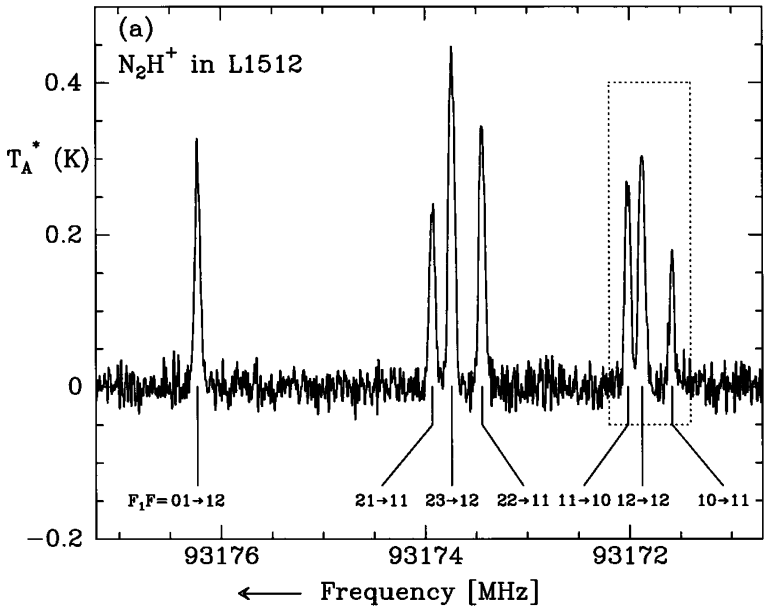

Figure 1.7: Hyperfine components of N_2H^+ (1−0) line toward L1512 (Caselli et al. 1995).

1.3.2.1 Previous Observations

Various authors have recognized the importance of a realistic model of radial variations in gas kinetic temperature in starless cores when interpreting observational data

(e.g., Di Francesco et al. 2007). For instance, radiative transfer models, widely used to interpret such data, depend critically on variations of kinetic temperature. Furthermore, Pavlyuchenkov et al. (2007) showed that the effect of chemical evolution in a starless core is degenerate with that of a nonuniform T_K profile. They argued that the assumption of isothermality, still used in many studies, is a critical factor in simulating molecular line formation. Even small temperature variations, likely to exist in starless cores, can affect considerably the interpretation of molecular line data and core properties. Quantifying the actual temperature structure for real cores is an important step toward understanding the initial stages of star formation.

Numerous authors have used NH_3 and N_2H^+ as tracers and probes of the physical and chemical structure of dense cores (e.g., Myers & Benson 1983; Benson et al. 1998; Caselli et al. 2002; Tafalla et al. 2002; Tatematsu et al. 2004; Crapsi et al. 2005a). Molecular surveys have shown that some molecules, such as CO and CS, are heavily depleted toward the core centres to the point where the abundance is decreased by at least 2 orders of magnitude compared to the abundances in the outer regions. Meanwhile, the abundance of N_2H^+ molecule remains constant, and the NH_3 abundance increases by factors of $\sim 1-10$ toward the innermost regions. These studies, however, used single dish data with low angular resolution and poor spatial sampling that limited probes of the gradients in the radial distribution of the emission. Recently, some studies have taken advantage of combining single dish and interferometric data to probe these species toward star forming regions. Their choice of targets, however, is focused on clustered environments that turned out to be difficult to interpret due to the complex geometry of these regions and the broad range of environmental effects involved in the process (e.g., Friesen et al. 2010a; Friesen et al. 2010b).

Crapsi et al. (2007) were the first to detect directly the gas temperature drop in a starless core. For L1544, they successfully combined limited interferometric (VLA) and single-dish data (Effelsberg, with angular resolution of $40''$) of NH_3 (1,1) and (2,2) emission. Including the interferometric data in the analysis revealed a drastic change in the T_K profile, showing through a two-dimensional Monte Carlo radiative transfer model (Hogerheijde & van der Tak 2000) that it is not uniform across the core but decreases toward the core centre from 12 K to 5.5 K. The temperature profile necessary to reproduce both datasets had a functional form of

$$T_K = (12 - \frac{6.5}{1 + (r/18'')^{1.5}}). \tag{1.4}$$

Including this new temperature profile into the analysis strongly affected our understanding of the chemistry of this one core. For example, its central density (estimated from dust continuum emission) increased by 50% over that derived by assuming a constant temperature of 8.75 K (Figure 1.8). Also, its NH_3 column density increased by a factor of ~ 2, indicating that NH_3 freeze-out is not significant in its core centre, unlike for CO.

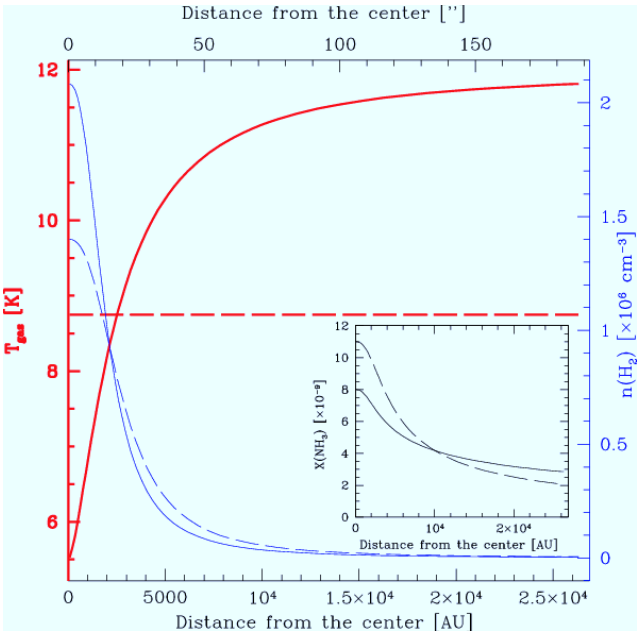

Figure 1.8: Temperature, density and NH_3 abundance profiles that best fit simultaneously the interferometric and the single dish observations toward the starless core L1544 are shown with solid lines. The best fit to the single dish data alone assuming a constant temperature at 8.75 K are reported in dashed lines for comparison (Crapsi et al. 2007).

1.4 Outline of the Dissertation

In this dissertation, we present a detailed study of molecular emission lines observed toward a sample of six isolated dense cores. Previous studies of molecular line and dust continuum emission toward this group of cores indicate that four of the cores in our sample are starless (L694-2, L429, L1517B, and L1689-SMM16; Crapsi et al. 2005a, Sadavoy et al. 2010a), and the remaining two contain protostellar Very Low Luminosity Objects (VeLLOs) and are currently experiencing gravitational collapse (L1521F and L1014; Crapsi et al. 2005a; Kauffmann et al. 2008). The isolation of these cores and their proximity makes them ideal targets for probing the internal physical conditions of dense cores prior to the moment of collapse.

Chapter 2 presents single-dish observations of L1689-SMM16, the least previously studied core in our sample, in NH_3 (1,1) and (2,2) emission using the GBT[5], in N_2H^+ (1−0) emission using the Nobeyama Radio Observatory (NRO)[6], and in NH_2D ($1^a_{1,1} - 1^s_{0,1}$), HCN (1−0), HNC (1−0), $H^{13}CO^+$ (1−0), and HCO^+ (1−0) emission using the Mopra telescope[7]. We will discuss the temperature distribution, kinematics, and abundance patterns observed toward L1689-SMM16, and present our findings regarding its dynamics and evolutionary stage.

Chapter 3 presents our single-dish observations of the remaining five cores in our sample in NH_3 (1,1) and (2,2) emission lines using the GBT, and in N_2H^+ (1−0) emission using the NRO. For each core, we will compare the morphologies of the integrated intensities of molecular emission lines with that of the dust continuum emission at 250 μm and present our results regarding their temperature distributions and kinematics.

Chapter 4 presents our observations of L1521F and L694-2 in NH_3 (1,1) and (2,2) at high spatial resolution using the Jansky Very Large Array (JVLA)[8]. We will

[5]The National Radio Astronomy Observatory is a facility of the National Science Foundation operated under cooperative agreement by Associated Universities, Inc.

[6]Nobeyama Radio Observatory is a branch of the National Astronomical Observatory of Japan, National Institutes of Natural Sciences.

[7]The Mopra radio telescope is part of the Australia Telescope National Facility, which is funded by the Commonwealth of Australia for operation as a National Facility managed by CSIRO. The University of New South Wales Digital Filter Bank used for the observations with the Mopra telescope was provided with support from the Australian Research Council.

[8]The National Radio Astronomy Observatory is a facility of the National Science Foundation

also discuss our results regarding radiative transfer modelling of NH_3 (1,1) and (2,2) spectra of L694-2 and L1521F at both low and high resolutions. We will compare our findings regarding the internal physical structure of these two cores with L1544, a well-studied starless core in Taurus molecular cloud, and draw conclusions regarding their evolutionary stages.

Finally, in **Chapter 5**, we will summarize the main results of this dissertation and discuss several possible expansions for future work.

operated under cooperative agreement by Associated Universities, Inc.

Chapter 2

Physical and Chemical Characteristics of L1689-SMM16, an Oscillating Prestellar Core in Ophiuchus

2.1 Introduction

Dense starless cores are the link between the diffuse material of molecular clouds and protostars. Measuring their densities, temperatures, and dynamics is the key to revealing the conditions close to the moment of protostar formation. Observations of molecular tracers have greatly improved our understanding of the gas dynamics in the different layers of dense cores. Since density decreases with radius, the gas excitation temperature (T_{ex}) for a moderately optically thick emission line also decreases with radius.[1] This decrease in T_{ex} leads to the absorption of the emission from the core centre by gas in the outer regions, resulting in a dip in the observed spectral profile. If the core is experiencing infall motions, the dip will be skewed toward higher (redder) velocities and a line profile is produced with the blue side brighter than the red side (blue asymmetry); see Myers et al. (1996) and De Vries & Myers (2005). Therefore, the presence of blue asymmetries in the line profile of molecular species such as CS (Lee et al. 2001) and N_2H^+ (Williams et al. 2006) observed toward some starless

[1]Note that due to the dependency of T_{ex} on the kinetic temperature (T_K), in starless cores with decreasing T_K toward the centre, T_{ex} can have a local minimum at an intermediate radius.

cores (e.g., L1544, L694-2, and L492) indicates the existence of inward motions inside the cores. On the other hand, if the core is experiencing outward motions, the self-absorption dip will be shifted toward lower (bluer) velocities, producing a spectral profile with the red side brighter than the blue side (red asymmetry). Asymmetrically red spectral lines have also been detected toward some starless cores such as B18-5, L1517B, and L1512 using molecular tracers that predominantly probe the outer layers of cores (e.g., HCN). These profiles indicated that the core foreground layers are expanding (e.g., Sohn et al. 2007).

Some cores show a mixture of blue *and* red asymmetries in the line profiles of a single tracer across the core, indicating that different parts of the core are moving in opposite directions, i.e., inward vs. outward (e.g., B68 from Lada et al. 2003, L1495A-N, L1507A, and L1512 from Lee et al. 2001). Such coexistence of inward and outward motions may indicate the presence of small amplitude oscillations inside or on the surface of the core (e.g., Lou & Shen 2004; Thompson & White 2004; Gao & Lou 2010; Lou & Gao 2011; Keto & Field 2005; Broderick et al. 2007; Stahler & Yen 2010). Lee & Myers (2011) suggest that this stage might be a transitionary state between a static core and a contracting one. It is therefore crucial to investigate the dynamics and chemistry of cores during this stage, one leading to core collapse and protostellar formation. (Note that core differential rotation can also lead to a mixture of blue and red asymmetries in spectral lines (see, e.g., Redman et al. 2004). In such cases, observing an optically thin tracer would be necessary to distinguish between pure rotation and other effects such as oscillation.) The starless cores B68 (Lada et al. 2003), FeSt 1-457 (Aguti et al. 2007), and L1517B (Fu et al. 2011) are some examples introduced as oscillating cores in the literature, in addition to the possible candidates, L1495A-N, L1507A, and L1512 (Lee & Myers 2011). In this chapter, we introduce another starless core, L1689-SMM16, that could be experiencing precollapse oscillations.

L1689 is an example of a region with ongoing star formation within the nearby Ophiuchus molecular cloud at a distance of 120 $\pm$ 5 pc (Loinard et al. 2008). L1689 appears to be less active compared to the adjacent, well-studied L1688 region of central Ophiuchus, and was first mapped in 850 μm continuum emission using the Submillimetre Common User Bolometer Array (SCUBA) on the James Clerk Maxwell Telescope (JCMT) by Nutter et al. (2006). They identified 21 sources using their submillimetre observations of L1689. We focus our attention on the 16th source, L1689-SMM16 (hereafter, just SMM16). A recent analysis by Sadavoy et al. (2010a)

revealed that SMM16 showed no evidence of an embedded young stellar object in Spitzer maps. SMM16 is unusually massive for a starless core, with a mass ($\sim$ 3.1 $M_\odot$) that exceeds its corresponding Jeans mass in the absence of magnetic fields (Sadavoy et al. 2010a; discussed further in §2.5.2). Furthermore, Herschel Gould Belt Survey (GBS) archival data of the Ophiuchus molecular cloud do not show any sources with continuum emission at 70 μm in the vicinity of SMM16 (André et al., in prep.). Starless cores with masses higher than their predicted Jeans mass represent an uncommon physical state and are therefore interesting targets for more in-depth investigations (Sadavoy et al. 2010b). Indeed, among the population of starless cores in all of Ophiuchus, SMM16 has one of the highest ratios of observed mass to Jeans mass, one more typical of the protostellar cores observed in the cloud. Therefore, SMM16 may be on the cusp of gravitational collapse. Its advanced evolutionary stage, close distance, and high concentration suggest that SMM16 represents an exciting opportunity to characterize the physical state of dense gas just prior to formation of a protostar.

In this chapter, we present single-dish observations of tracers of dense molecular gas toward SMM16 in the 3 mm and 12 mm bands. These data reveal the kinematics, temperature distribution, and abundance patterns toward SMM16. We also investigate the dynamics and evolutionary stage of SMM16 using these data. Below, §2.2 describes the details of our observations and data reduction methods and §2.3 offers a first glance at the morphologies of the observed molecular emission lines and a comparison with that of the continuum emission toward SMM16. We explain the spectral line analysis for each of the observed species in §2.4. We discuss our findings regarding the evolutionary stage of SMM16 and its dynamics in §2.5. Finally, §2.6 summarizes our results.

2.2 Observations and Data Reduction

We mapped SMM16 in molecular emission of NH_3, N_2H^+, $H^{13}CO^+$, HCO^+, HCN, HNC, and NH_2D. Our observations cover three closely adjacent sources, SMM14, SMM15, and SMM16, as mapped by Nutter et al. (2006). Figure 5 of Nutter et al. (2006) shows the location of the three sources. Of these three sources, SMM16 is clearly dominant. Assuming all three are optically thin in continuum emission and have a similar dust temperature, comparison of their total fluxes at 850 μm (1.5 Jy, 1.4 Jy, and 7.8 Jy for SMM14, SMM15, and SMM16, respectively; Nutter et al.

2006) shows that SMM16 has a much higher mass compared to the other two sources. Therefore, we treat the whole region as a single core. The observed transitions and the facilities used to acquire the data are listed in Table 2.1. For all observations presented in this chapter, the maps are centred at R.A. (J2000) = $16^h\ 31^m\ 39.2^s$, decl. (J2000) = $-24^\circ\ 49'\ 48''$ with the off-position for atmospheric subtraction centred at R.A. (J2000) = $16^h\ 33^m\ 33.6^s$, decl. (J2000) = $-24^\circ\ 59'\ 15.0''$. We describe our observation strategy and data reduction method for each dataset below.

Table 2.1: Observed transitions toward SMM16.

Molecule	Transition	Frequency (GHz)	Telescope
NH_3	J = 1, K = 1	23.694495 [1]	GBT
NH_3	J = 2, K = 2	23.722633 [1]	GBT
NH_2D	$J_{K_a,K_c} = 1^a_{1,1} - 1^s_{0,1}$	85.9262703 [2]	Mopra
$H^{13}CO^+$	J = 1 − 0	86.7542884 [3]	Mopra
HCO^+	J = 1 − 0	89.1885247 [4]	Mopra
HCN	J = 1 − 0	88.63185 [5]	Mopra
HNC	J = 1 − 0	90.66357 [6]	Mopra
N_2H^+	J = 1 − 0	93.1762527 [7]	NRO & Mopra

Note. — References: (1) Ho & Townes (1983), (2) Shah & Wootten (2001), (3) Schmid-Burgk et al. (2004), (4) CDMS (Müller et al. 2001; Müller et al. 2005), (5) CDMS entry of Splatalogue (Müller et al. 2001; Müller et al. 2005), (6) Lovas entry of Splatalogue (Lovas & Dragoset 2004), (7) Keto & Rybicki (2010)

2.2.1 Green Bank Telescope

Single-dish observations of the NH_3 (J, K) = (1,1) and (2,2) emission lines toward SMM16 were acquired using the 100-m diameter Robert C. Byrd Green Bank Telescope (GBT), located near Green Bank, WV, USA on March 1, 2011 starting at 08:15 UT for 3.75 hours. The observations were carried out using the On-the-Fly (OTF) mapping mode of the K-band Focal Plane Array (KFPA) with position switching (Masters et al. 2011). A circular map of $8'$ radius was made using daisy scans to ensure Nyquist sampling. The KFPA spectrometer was configured to have one spectral window with 7 beams, two polarizations, 50 MHz band-width, and 16,384 channels with 3-level sampling to observe the NH_3 (1,1) and (2,2) lines simultaneously. This setting provided velocity resolution of 0.04 km s^{-1} (i.e., frequency resolution of 3 kHz

at 23 GHz). The GBT beam is approximately 32″ FWHM at the observing frequency of 23 GHz. We checked the pointing accuracy of the GBT every 45 − 60 minutes. The average telescope aperture and main beam efficiencies were 0.64 and 0.82 respectively. The zenith opacity was determined using a local weather model. The average source elevation was 26°. Since the GBT map was made using daisy patterns, it has higher sensitivity toward the centre of the map. The final 1σ rms sensitivity of the central region (with radius R = 2′) of the original map where the target is located is 0.3 K on main beam temperature (T_{mb}) scale per 0.04 km s^{-1} velocity channel.

We used the GBT utility idlToSdfits to convert the data to AIPS SDFITS format. Subsequently, we used the AIPS DBCON, SDGRD, and FITTP procedures to combine and grid the data and produce the final data cubes in FITS format.

2.2.2 Nobeyama 45 m Radio Telescope

Single-dish observations of the N_2H^+ (J = 1−0) emission line toward SMM16 were carried out using the Nobeyama Radio Observatory (NRO) 45-m Telescope in Nobeyama, Japan on April 12−13, 2011. The observations were done using the OTF mapping mode, with the 25-BEam Array Receiver System (BEARS) as the front end (Sunada et al. 2000; Yamaguchi et al. 2000) to make a $4' \times 4'$ map of the region. For the receiver back end, we used a digital autocorrelator spectrometer (ACS) with 1024 channels and 8 MHz bandwidth and applied a Hamming window function (Sorai et al. 2000). This setting provided velocity resolution of 0.045 km s^{-1} (i.e., frequency resolution of 14.2 kHz at 93 GHz). The spectral channels of the final data were binned to 0.05 km s^{-1}. At 93 GHz, the telescope beam is $\sim 17''.8 \pm 0''.4$ FWHM and the main beam efficiency is estimated to be 44% (±3%), interpolated from observatory measurements at 86 GHz and 100 GHz. The on-sky angular separation of the BEARS receiver beams is 41″.

During the observations, the double sideband system noise temperature varied between 150 K and 250 K. The standard chopper wheel method (Kutner & Ulich 1981) was used to convert the output signal to the antenna temperature (T_A^*) scale corrected for atmospheric attenuation. The telescope pointing accuracy was checked every 90 minutes by observing an SiO maser source, T Oph, at 43 GHz with corrections less than 3″ during the total observing period. For pointing, we used the S40 receiver together with the facility acousto-optical spectrometer as the back end. To correct for the gain differences between the 25 beams of BEARS and the daily intensity

scale variation, we used calibration data obtained from observations toward Orion core 4 at R.A. (J2000) = $05^h\ 35^m\ 19.8^s$, decl. (J2000) = $-5^\circ\ 00'\ 53''$ (Tatematsu et al. 2008) using the SIS receiver S100 with the ACS. To reduce scanning artifacts in the map, we scanned along both R.A. and decl. directions and combined both datasets into a single map (Emerson & Graeve 1988). We convolved the data with a spheroidal function to calculate the intensity at each grid point of the final data cube with a spatial grid size of $7''.5$ (Sawada et al. 2008). The final effective resolution is $22''.9$. The final 1σ rms sensitivity of the observations is 0.2 K on the T_{mb} scale per 0.05 km s^{-1} velocity channels. The data were reduced using the Nobeyama OTF Software Tools for Analysis and Reduction (NOSTAR) and IDL of Research Systems Incorporated.

2.2.3 Mopra Telescope

We observed molecular line emission in the 3 mm band from multiple species (listed in Table 2.1) toward SMM16 using the Mopra 22-m single-dish radio telescope located 450 km north-west of Sydney, Australia on July $1 - 6$, 2011. We used the OTF mapping mode of Mopra telescope with position switching to make $5' \times 5'$ maps of each emission line. The scan rate was $3.85''$ per second. The map is made with $12''$ spacing between the rows, giving 25 rows per map. Since the Mopra beam at 90 GHz is $36''$ FWHM, the above row spacing ensured the Nyquist sampling of the emission. To reduce scanning artifacts in the maps, we scanned along both R.A. and decl. directions and combined both datasets into a single map. We observed the off-position once per scan row for a scan length of 1 minute. We used the Mopra Spectrometer (MOPS) in the zoom mode with 16 zoom-bands. Each MOPS zoom-band is 138 MHz wide with 4096 channels for each polarization. This configuration provided us with a bandwidth of 505 km s^{-1} and velocity resolution of 0.11 km s^{-1} in the 3 mm band.

We used the SiO maser source AH Sco to check the telescope pointing accuracy approximately every hour, maintaining pointing to better than about $10''$. The system temperature varied between 230 K and 300 K and was measured by paddle scans every 15 minutes. Data from the Mopra telescope are recorded in RPFITS format. We performed bandpass calibration with the LIVEDATA software package using scans on the off-position and fitting a 2nd order polynomial to the baseline. The output of LIVEDATA is recorded in single-dish fits format (sdfits). The GRIDZILLA software

package uses this output to build a uniformly gridded data cube. We averaged both polarizations. The spectra are weighted by the system temperature. The beam efficiency of Mopra is interpolated from the values measured at 86 GHz (0.49) and 115 GHz (0.42) (Ladd et al. 2005)[2]. The final 1σ rms sensitivity of the observations is 0.13 K on the T_{mb} scale per 0.11 km s^{-1} velocity channel.

2.2.4 Herschel Space Observatory

In this chapter, we also use 250 μm continuum emission data of Ophiuchus molecular cloud (containing SMM16) from Herschel-SPIRE that were taken as part of Herschel Gould Belt Survey (GBS; André et al. 2010; Ladjelate et al. 2014, in prep)[3]. These data products were provided by the Herschel GBS archive[4] and were produced by scanning the Ophiuchus field in two orthogonal directions at a rate of 60″ s^{-1} using both SPIRE and PACS bolometer cameras in parallel mode. For more information on the acquisition and reduction of these data, see Roy et al. (2014). The Herschel 250 μm beam is slightly elliptical (18″.7 × 17″.5) with a geometric mean FWHM of 18″.2. To focus on the flux density corresponding to the core, we removed the Planck offset that was added to Herschel GBS archive image (136.3 MJy sr^{-1} at 250 μm; Roy et al. 2014). Also, to completely remove the background continuum emission from SMM16's immediate environment, we calculated the average continuum emission in the pixels outside of the core (i.e., where NH_3 emission is not detected) and subtracted the scaled value appropriate to the respective resolution from the entire 250 μm continuum emission map of SMM16.

2.3 Results

Figures 2.1 and 2.2 show the integrated intensity maps of the observed emission lines toward SMM16, from the GBT, NRO, and Mopra. The integrated intensity maps

[2]Tsitali et al. (2013) found a lower beam efficiency for the Mopra telescope than that used here. For optically thin emission lines, molecular column densities are inversely proportional to the beam efficiency, and therefore lower beam efficiency would result in higher column densities. For optically thick lines, the effect is more complicated due to the additional impact on the excitation temperature.

[3]This research has made use of data from the Herschel Gould Belt Survey (HGBS) project (http://gouldbelt-herschel.cea.fr). The HGBS is a Herschel Key Programme jointly carried out by SPIRE Specialist Astronomy Group 3 (SAG 3), scientists of several institutes in the PACS Consortium(CEA Saclay, INAFIFSI Rome and INAF-Arcetri, KU Leuven, MPIA Heidelberg), and scientists of the Herschel Science Center (HSC).

[4]http://gouldbelt-herschel.cea.fr/archives

were made by summing over the entire emission spectrum including all hyperfine components (if present), excluding the channels with emission lower than twice the corresponding map rms noise level. The overlaid contours correspond to the continuum emission at 250 μm observed with Herschel-SPIRE (André et al. 2010; Ladjelate et al. 2014, in prep). The spectral line data shown in Figures 2.1(a, b), 2.1(c2), and 2.2 are overlaid with contours of dust continuum data smoothed to 32″ FWHM, 22″.9 FWHM, and 36″ FWHM, respectively, to match the spatial resolutions of the GBT, NRO, and Mopra data. In each map, the black dot shows the peak of the integrated intensity of the corresponding emission line and the empty triangles show the two local peaks of the continuum emission at 250 μm. Table 2.2 lists the J2000 positions of peak integrated intensity and rms noise levels of the integrated intensity maps of molecular emission lines. We used the task HISTO of MIRIAD to find the peak positions, which correspond to the pixel positions with highest integrated intensities. Figure 2.3 shows the spectrum at each of these respective positions. Note that due to the noisiness of the integrated intensity map of NH_3 (2,2), the location of the emission peak is very uncertain. Therefore, the NH_3 (2,2) spectrum in Figure 2.3 is toward the peak position of the NH_3 (1,1) emission. For comparison, Table 2.3 lists the peak positions and rms noise levels of the continuum emission map of SMM16 at 250 μm at its original resolution ($\sim$ 18″.2 FWHM) and at the resolution of the GBT data ($\sim$ 32″ FWHM).

Table 2.2: Peak positions and rms noise levels for integrated intensity molecular emission maps toward SMM16

Source of Emission	Spatial Resolution arcsec	R.A. J2000	Decl. J2000	rms ($\frac{\text{K.km}}{\text{s}}$)
NH_3 (1,1)	32	16 31 39.4	-24 49 42	1
NH_2D ($1^a_{1,1} - 1^s_{0,1}$)	36	16 31 41.9	-24 49 51	0.2
$H^{13}CO^+$ (1−0)	36	16 31 40.8	-24 50 36	0.3
HCN (1−0)	36	16 31 38.6	-24 49 51	0.3
HCO^+(1−0)	36	16 31 39.7	-24 52 6	0.3
HNC (1−0)	36	16 31 40.8	-24 50 22	0.2
N_2H^+ (1−0)	36 (Mopra)	16 31 39.7	-24 49 36	0.3
N_2H^+ (1−0)	22.9 (NRO)	16 31 39.2	-24 49 29	0.3

The morphology of the integrated intensity of the NH_3 (1,1) emission closely follows the morphology of the 250 μm continuum emission. The NH_3 (1,1) integrated

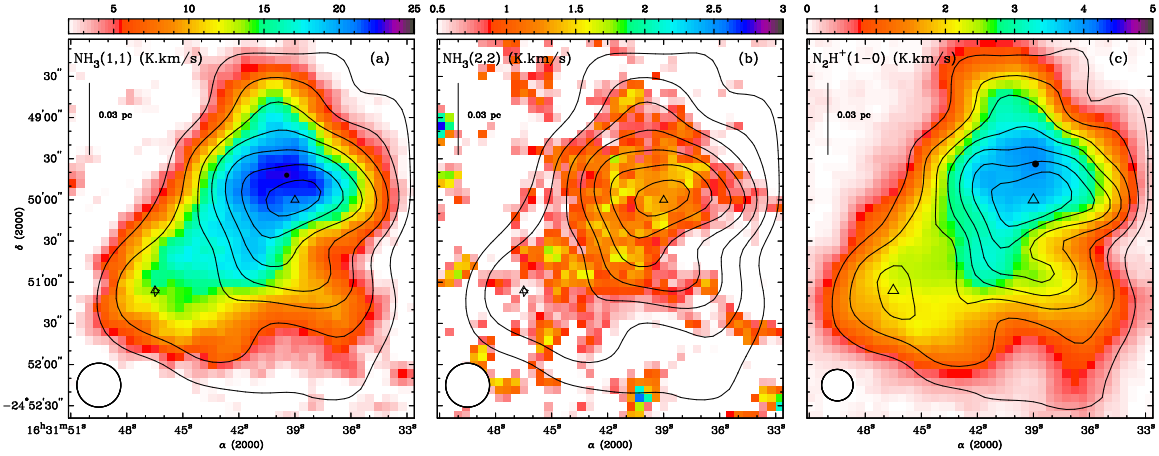

Figure 2.1: Integrated intensity maps of NH_3 (1,1) (a), NH_3 (2,2) (b), and N_2H^+ (1−0) (c) emission toward SMM16. The colour scale is in K km s^{-1}. The contours correspond to dust continuum emission at 250 μm. In panels (a) and (b), the resolution of the continuum data has been smoothed to that of the GBT data, $\sim 32''$ FWHM, and the contours start at 3.0 Jy beam^{-1} and increase in steps of 3.0 Jy beam^{-1}. In panel (c), the resolution of the continuum data has been smoothed to that of the NRO data, $\sim 22''.9$ FWHM, and the contours start at 1.5 Jy beam^{-1} and increase in steps of 1.5 Jy beam^{-1}. In panels (a) and (c), the black dot shows the peak of the integrated intensity of the corresponding molecular emission. Due to the noisiness of the integrated intensity map of NH_3 (2,2), a peak position is not indicated in panel (b). In all panels, the triangles show the peaks of the continuum emission. The circle delineates the size of the corresponding beam. The positions of the continuum and molecular emission peaks are determined separately for each resolution.

Table 2.3: Peak positions and rms noise levels for continuum emission at 250 μm observed using Herschel toward SMM16

Source of Emission	Spatial Resolution	R.A.	Decl.	rms
	arcsec	J2000	J2000	($\frac{\text{Jy}}{\text{beam}}$)
Continuum	18.2	16 31 38.9	-24 49 58	0.03
Continuum	32	16 31 39.0	-24 50 00	0.1

intensity has a single peak, which is located only $\sim 19''$ NNE from the peak of the continuum emission. The NH_3 (2,2) integrated intensity, however, is noisier, showing broad similarity to the dust emission but with a few small-scale peaks within the central region of the continuum emission. As with the NH_3 emission, there is broad consistency between the morphology of the N_2H^+ (1−0) emission and continuum emission. At $22''.9$ angular resolution, the peak of the N_2H^+ integrated intensity is $\sim 30''$ north of the continuum peak. Furthermore, NRO and Mopra observations of N_2H^+ (1−0) are consistent in both morphology and line intensity of the emission

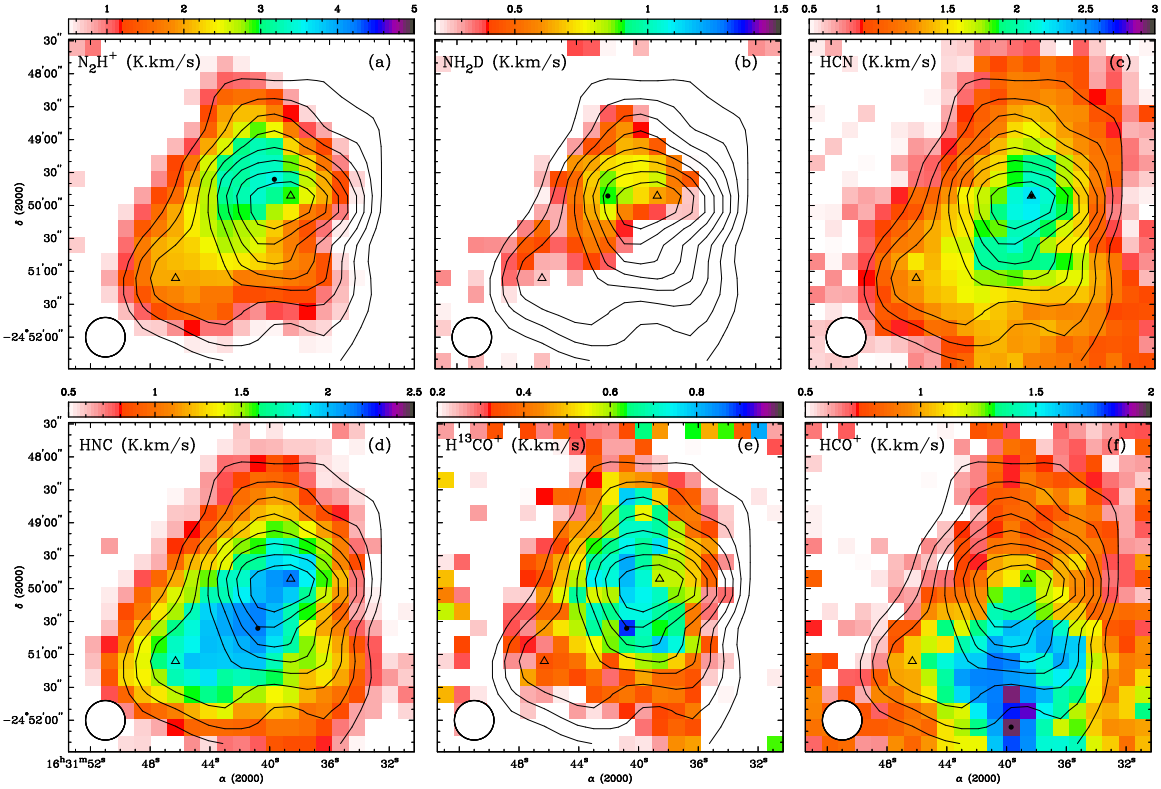

Figure 2.2: Integrated intensity maps of the emission from the six spectral lines in the 3 mm band observed using the Mopra telescope toward SMM16. The colour scale is in K km s^{-1}. The contours correspond to continuum emission at 250 μm, starting at 3.0 Jy $beam^{-1}$ and increasing in steps of 3.0 Jy $beam^{-1}$. The black dot shows the location of the integrated intensity peak of the corresponding species and the triangles show the peaks of the continuum emission. The resolution of the continuum data has been smoothed to the resolution of the Mopra data, $\sim 36''$ FWHM. The circle delineates the size of the Mopra beam.

(when smoothed to common resolution).

NH_2D emission is significantly less widespread and fainter compared to the NH_3 and N_2H^+ emission. Unlike the dense core L1544, where the peak of NH_2D emission coincides with the continuum emission peak (Crapsi et al. 2007), the location of the NH_2D emission peak toward SMM16 is $\sim 45''$ east of the continuum emission peak. Pillai et al. (2011) observed a similar offset toward the pre-protocluster region, G35.20w, and suggested that it could be due to the presence of protostars at the location of the continuum peak warming up the environment, leading to the return of CO to the gas phase and a corresponding decrease in the abundance of deuterated species, such as NH_2D. SMM16 does not appear to have yet formed a protostar, however, and temperature maps derived from NH_3 (1,1) and (2,2) emission show no

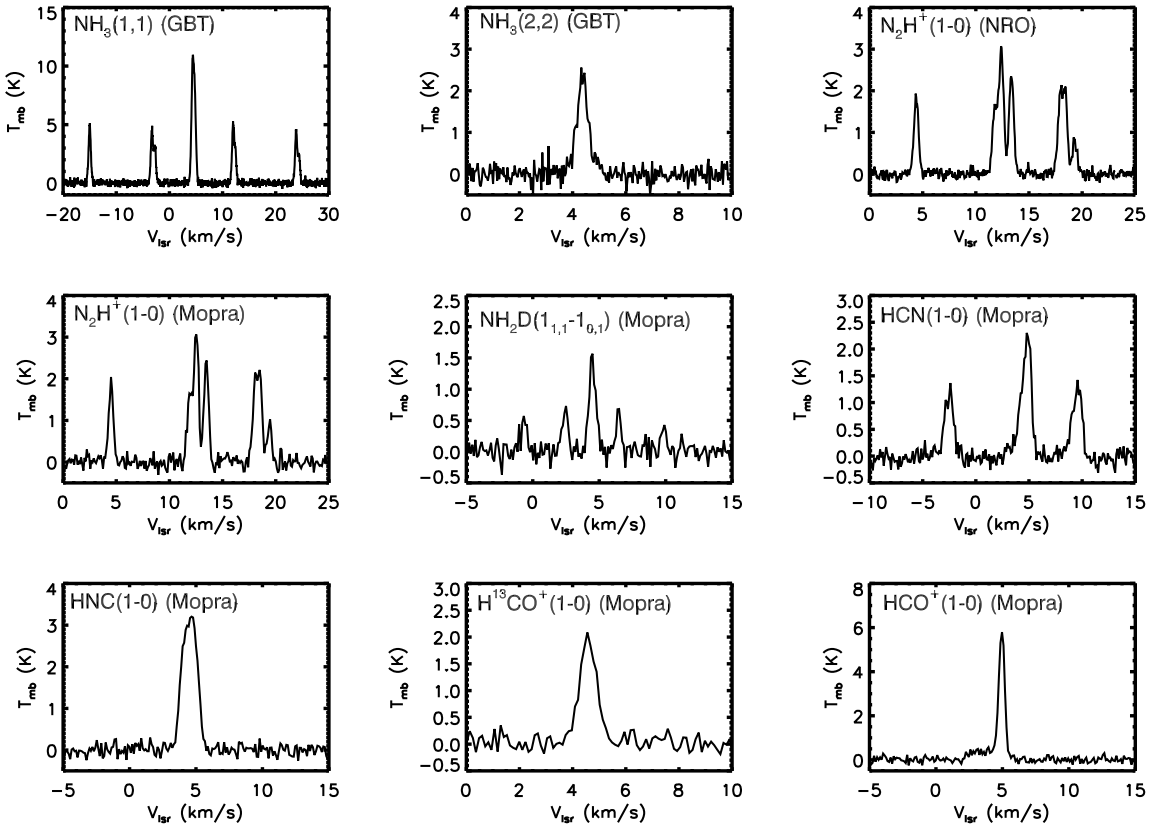

Figure 2.3: Spectra of the observed transitions toward their corresponding peak positions (listed in Table 2.2). Note that due to the noisiness of the integrated intensity map of NH_3 (2,2), the location of the emission peak is very uncertain. Therefore, the NH_3 (2,2) spectrum in this figure is toward the peak position of the NH_3 (1,1) emission.

signs of warming at the position of the continuum peak. Therefore, the reason behind the unexpected offset between the locations of NH_2D and continuum emission peaks is unknown. Although the location of NH_2D emission peak is uncertain due to the relatively low signal-to-noise ratio (SNR) of the Mopra data, there is an obvious offset between the locations of NH_2D emission and the continuum emission peaks.

The morphologies of the HCN and HNC emission somewhat follow the continuum emission morphology, less closely than the NH_3 and N_2H^+ emission. The HCN emission peak coincides exactly with the continuum emission peak but the HNC emission peak is located $\sim$42″ SE of the continuum peak. The HCO^+ and $H^{13}CO^+$ emission are both offset from the continuum emission. The spatial extent of the $H^{13}CO^+$ (1−0) emission is smaller than the spatial extent of the continuum emission. The peak position of $H^{13}CO^+$ (1−0) integrated intensity is particularly uncertain and offset $\sim$54″ toward the SE of the continuum peak, and at a position close to the HNC emission

peak. The spatial extent of the HCO^+ (1−0) emission is larger than that of $H^{13}CO^+$ (1−0) and does not match that of the dust continuum emission nearly as well as the previous lines.

Among all of the species observed toward SMM16, NH_3 and N_2H^+ emission follow best the morphology of the continuum emission. These results are in agreement with previous comparisons between the morphology of NH_3 and N_2H^+ emission with that of dust emission in other cores (e.g., Walsh et al. 2007; Friesen et al. 2009; Pineda et al. 2010). The morphologies of HCN (1−0), HNC (1−0), and $H^{13}CO^+$ (1−0) emission follow that of the continuum emission to some extent. The HCO^+ (1−0) emission, however, is located at a large offset ($\sim 2'.3$) from the continuum emission. Finally, the morphology of NH_2D ($1^a_{1,1} - 1^s_{0,1}$) emission does not show a significant similarity to that of continuum emission, although this could be due to the limited extent of the NH_2D emission region.

2.4 Line Analysis

For each of the observed molecular transitions, the local standard of rest line centroid velocity (v_{LSR}), observed velocity dispersion (σ_v), and line intensity were determined using Gaussian fits (except for the HCN (1−0) and HNC (1−0) spectra; see §2.4.2). The hyperfine structure of the emission lines NH_3 (1,1) and (2,2), N_2H^+ (1−0), NH_2D ($1^a_{1,1} - 1^s_{0,1}$), HCN (1−0), and HNC (1−0) are fitted using a multi-Gaussian function with fixed frequency separations between transitions. The Gaussian fitting procedure was performed in IDL using the MPFITFUN package (Markwardt 2009) presented by Friesen et al. (2010b) and Friesen et al. (2013). For the emission lines showing hyperfine structure (HFS), we calculated the excitation temperature (T_{ex}) and total opacity (τ) of the emission line using the relative frequencies and line intensities of the hyperfine components. The relative frequencies and line strengths of the hyperfine components of the NH_3 (1,1) and (2,2) transitions are taken from Kukolich (1967). Table 2.4 lists the relative frequencies and line ratios of the observed transitions in the 3 mm band and their corresponding hyperfine components.

In Local Thermodynamic Equilibrium (LTE), assuming equal and constant excitation conditions for all hyperfine components, the observed main beam temperature, T_{mb}, for a given transition with HFS can be written as a function of frequency ν by

$$T_{mb,\nu} = \Phi(J(T_{ex}) - J(T_{bg})) \times (1 - \exp(-\tau_\nu)), \tag{2.1}$$

Table 2.4: Observed transitions toward SMM16 in 3 mm.

Molecule	Transition	Hyperfine Transition	Frequency (GHz)	Intensity
NH_2D[1]	$J_{K_a,K_c}=1^a_{1,1}-1^s_{0,1}$	F′−F″= 0−1	85.9247829	0.111
		F′−F″ = 2−1	85.9257031	0.139
		F′−F″ = 2−2	85.9262703	0.417
		F′−F″ = 1−1	85.9263165	0.083
		F′−F″ = 1−2	85.9268837	0.139
		F′−F″ = 1−0	85.9277345	0.111
$H^{13}CO^+$ [2]	J = 1 − 0	$F'_1F'-F''_1F''$ = 0.5,1−0.5,0	86.754258	0.065
		$F'_1F'-F''_1F''$ = 0.5,1−0.5,1	86.754258	0.185
		$F'_1F'-F''_1F''$ = 1.5,2−0.5,1	86.754297	0.417
		$F'_1F'-F''_1F''$ = 1.5,1−0.5,0	86.754298	0.185
		$F'_1F'-F''_1F''$ = 1.5,1−1.5,1	86.754298	0.065
		$F'_1F'-F''_1F''$ = 0.5,0−0.5,1	86.754299	0.083
HCO^+ [3]	J = 1 − 0	none	89.1885247	1
HCN [4,5]	J = 1 − 0	F = 1 − 1	88.63042	0.33333
		F = 2 − 1	88.63185	0.55556
		F = 0 − 1	88.63394	0.11111
HNC [6,7]	J = 1 − 0	F = 0 − 1	90.66345	0.11111
		F = 2 − 1	90.66357	0.55556
		F = 1 − 1	90.66366	0.33333
N_2H^+ [8]	J = 1 − 0	$F_1F-F'F'_1$ = 10−11	93.1716086	0.03704
		$F_1F-F'F'_1$ = 12−12	93.1719054	0.18518
		$F_1F-F'F'_1$ = 11−10	93.1720403	0.11111
		$F_1F-F'F'_1$ = 22−11	93.1734675	0.18518
		$F_1F-F'F'_1$ = 23−12	93.1737643	0.25926
		$F_1F-F'F'_1$ = 21−11	93.1739546	0.11111
		$F_1F-F'F'_1$ = 01−12	93.1762527	0.11111

Note. — References: (1) Shah & Wootten (2001), (2) Schmid-Burgk et al. (2004), (3) CDMS (Müller et al. 2001; Müller et al. 2005), (4) CDMS entry of Splatalogue (Müller et al. 2001; Müller et al. 2005), (5) Sohn et al. (2007), (6) Snyder et al. (1977), (7) Lovas entry of Splatalogue (Lovas & Dragoset 2004), (8) Keto & Rybicki (2010)

where Φ is the beam filling factor of the source, T_{ex} is the line excitation temperature, T_{bg} is the temperature of the cosmic microwave background (2.73 K), and

$$J(T) = \frac{(h\nu/k)}{\exp(h\nu/kT)-1}. \tag{2.2}$$

The optical depth of the transition can also be written as a function of frequency in

the form of

$$\tau_\nu = \tau \sum_{j=1}^{N} a_j \exp\left[-\frac{(\nu - \nu_j - \nu_{LSR})^2}{2\sigma_\nu^2}\right], \tag{2.3}$$

where τ is the total optical depth of the line and N is the total number of hyperfine transitions. For any jth hyperfine component, a_j is the line strength and ν_j is the rest frequency. Characterizing the line with a single rest frequency, $\nu_{\rm rest}$, the frequency shift due to systemic motion of gas, ν_{LSR}, is given by

$$\nu_{\rm LSR} = \left(1 - \frac{v_{LSR}}{c}\right)\nu_{\rm rest}, \tag{2.4}$$

and the frequency dispersion of each hyperfine component is given by

$$\sigma_\nu = \frac{\nu_{\rm rest}}{c}\sigma_v, \tag{2.5}$$

which is similar for all hyperfine transitions (Johnstone et al. 2010). The FWHM of the line, Δv is then given by $\Delta v = 2\sqrt{2\ln 2}\sigma_v$. For all of the observations presented in this chapter, we assume $\Phi = 1$, i.e., the line emission fills the beam. If the observed line emission does not fill the beam, the calculated T_{ex} will be only a lower limit.

2.4.1 NH_3, N_2H^+, and NH_2D

We restricted our analysis of the NH_3 (1,1) and (2,2) data to pixels where the main NH_3 (1,1) component has a SNR higher than 10. For the N_2H^+ and NH_2D data, however, we used a SNR threshold of 5 for the N_2H^+ (1−0) isolated hyperfine component ($F_1F-F'F'_1 = 01-12$ at 93.1762527 GHz) and the NH_2D ($1^a_{1,1} - 1^s_{0,1}$) main hyperfine component ($F'-F''= 2-2$ at 85.9262703 GHz)[5].

Weighted means of the returned parameters (v_{LSR}, Δv, τ, and T_{ex}) from the HFS fits are shown in Table 2.5 for all three lines in their original spatial resolutions. We also calculated the error for each quantity per pixel. Due to the variations of the errors from pixel to pixel (for each quantity), we report in Table 2.5 the median value of the errors in all pixels included in the analysis as a representative value of the typical error. The median error is not equivalent to the error of the weighted mean, and should not be used to determine the signal-to-noise ratio of the corresponding

[5]Since the N_2H^+ (1−0) and NH_2D ($1^a_{1,1} - 1^s_{0,1}$) emission lines are weaker than the NH_3 (1,1) emission, we chose a lower SNR threshold to allow for the comparison of the emission from all three molecules over a similar area.

quantity. The error of the weighted mean is generally an order of magnitude lower than the corresponding median error. To make the comparison between the fitting parameters of the N_2H^+ data and the other two data sets easier, we smoothed the NRO map to the spatial resolution of the GBT data (32″ FWHM) and fit the spectrum at each pixel for the smoothed map as well. Table 2.5 lists the weighted mean and the median errors for the fitting parameters of the smoothed map as well. Note that the observed FWHM of the lines, Δv_{obs}, determined by the fitting routine are broadened by the instrumental velocity resolution, Δv_{res}. The reported observed line widths (Δv) in Table 2.5 are corrected for this artificial broadening, such that

$$\Delta v = \sqrt{\Delta v_{obs}^2 - \Delta v_{res}^2}. \tag{2.6}$$

Table 2.5: The weighted mean values of the fitting parameters of spectral line emission from the observed species toward SMM16. The values inside the brackets are the median errors.[a]

Spectral Line	v_{LSR} (km s^{-1})	Δv (km s^{-1})	τ	T_{ex} (K)	v_C[b] (km s^{-1})
NH_3 (1,1)	4.211 (0.004)	0.443 (0.009)	3.3 (0.2)	14.5 (0.6)	...
N_2H^+ (1−0) (22″.9)	4.361 (0.003)	0.44 (0.01)	3.8 (0.4)	5.5 (0.3)	...
N_2H^+ (1−0) (32″)	4.369 (0.002)	0.47 (0.01)	3.6 (0.2)	5.1 (0.2)	...
NH_2D ($1^a_{1,1} - 1^s_{0,1}$)	4.47 (0.01)	0.51 (0.03)	1.7 (0.6)	3.8 (0.3)	...
HNC (1−0)	4.602 (0.008)	0.66 (0.03)	1.5 (0.2)	8.3[c](0.2)	−0.34 (0.03)
HCN (1−0)	4.541 (0.008)	0.60 (0.02)	3.2 (0.2)	5.12[c](0.06)	−0.22 (0.01)

[a]The values inside the brackets are the median errors, not the errors of the weighted mean.

[b]The core internal velocity (v_C) is only available for HCN and HNC spectra that are fit using the HILL5 model (De Vries & Myers 2005). The negative value of velocity corresponds to outward motions.

[c]The reported values of T_{ex} for HCN and HNC correspond to peak excitation temperatures (see §2.4.2).

Figures 2.4a, 2.5a, and 2.6a show the v_{LSR} maps for the NH_3 (1,1), N_2H^+ (1−0), and NH_2D ($1^a_{1,1}-1^s_{0,1}$) emission lines, respectively. The v_{LSR} maps of all three emission lines look very similar, especially those of NH_3 (1,1) and N_2H^+ (1−0). The core shows a complex distribution of v_{LSR} between 4.0 km s^{-1} and 5.0 km s^{-1} with no obvious single gradient.

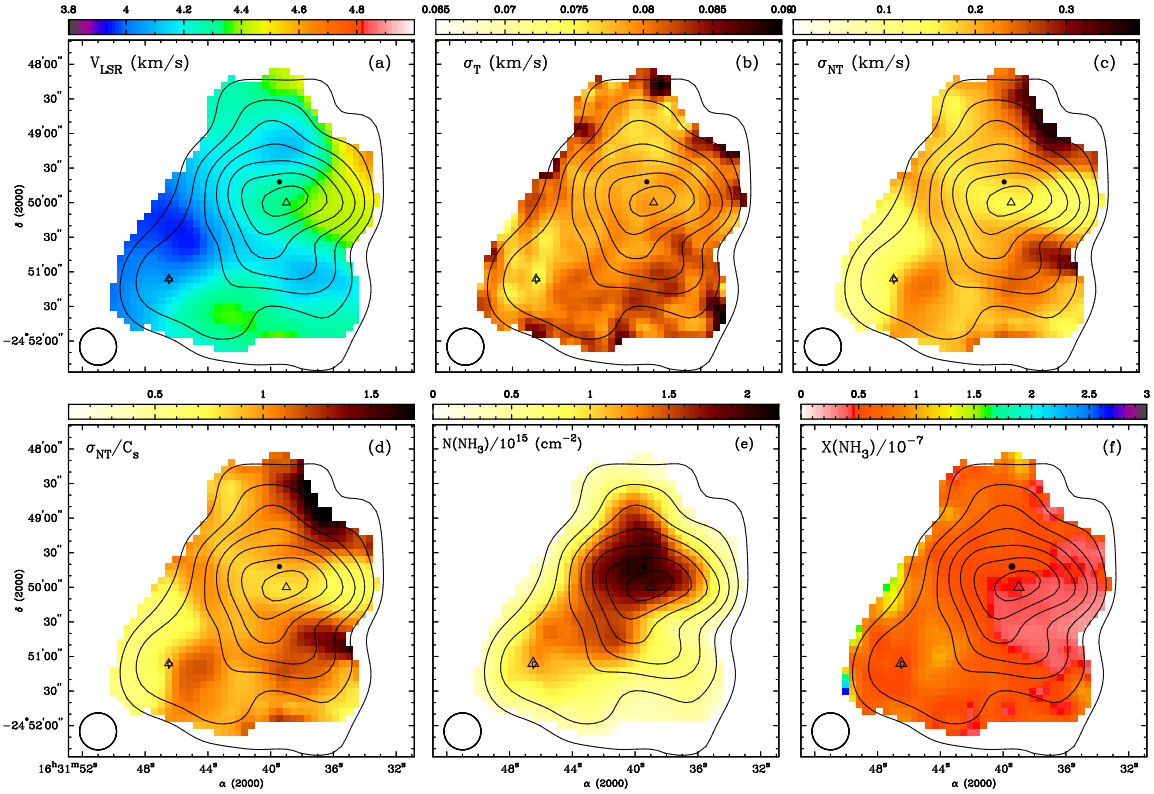

Figure 2.4: Maps of (a) v_{LSR}, (b) σ_T, (c) σ_{NT}, (d) σ_{NT}/c_s, (e) $N(\mathrm{NH_3})$, and (f) $X(\mathrm{NH_3})$ calculated using $\mathrm{NH_3}$ (1,1) emission toward SMM16 at 32″ FWHM. The contours correspond to continuum emission at 250 μm, starting at 3.0 Jy beam^{-1} and increasing by 3.0 Jy beam^{-1}. The black dot shows the peak of the $\mathrm{NH_3}$ (1,1) emission and the triangles show the dust continuum emission peaks. The resolution of the continuum data are smoothed to the resolution of the GBT data, $\sim$ 32″ FWHM. The 32″ FWHM beam of the GBT is delineated with the circle.

We used the fit parameters to determine some physical parameters. For $\mathrm{NH_3}$, the transitions between two rotational states with different K quantum numbers (e.g., (1,1) and (2,2)) are forbidden, therefore the rotational temperature corresponding to the relative population of the two states can be used to calculate the gas kinetic temperature (T_K; Ho & Townes 1983). We followed the method described by Friesen et al. (2013) to determine T_K for SMM16. Figure 2.7a shows the resulting kinetic temperature map of SMM16. The T_K values are generally low ($\simeq$ 11.5 K) in the eastern central region but increase towards the core edges ($\simeq$ 14 K).

Given the calculated values for T_K, we determined the thermal velocity dispersion

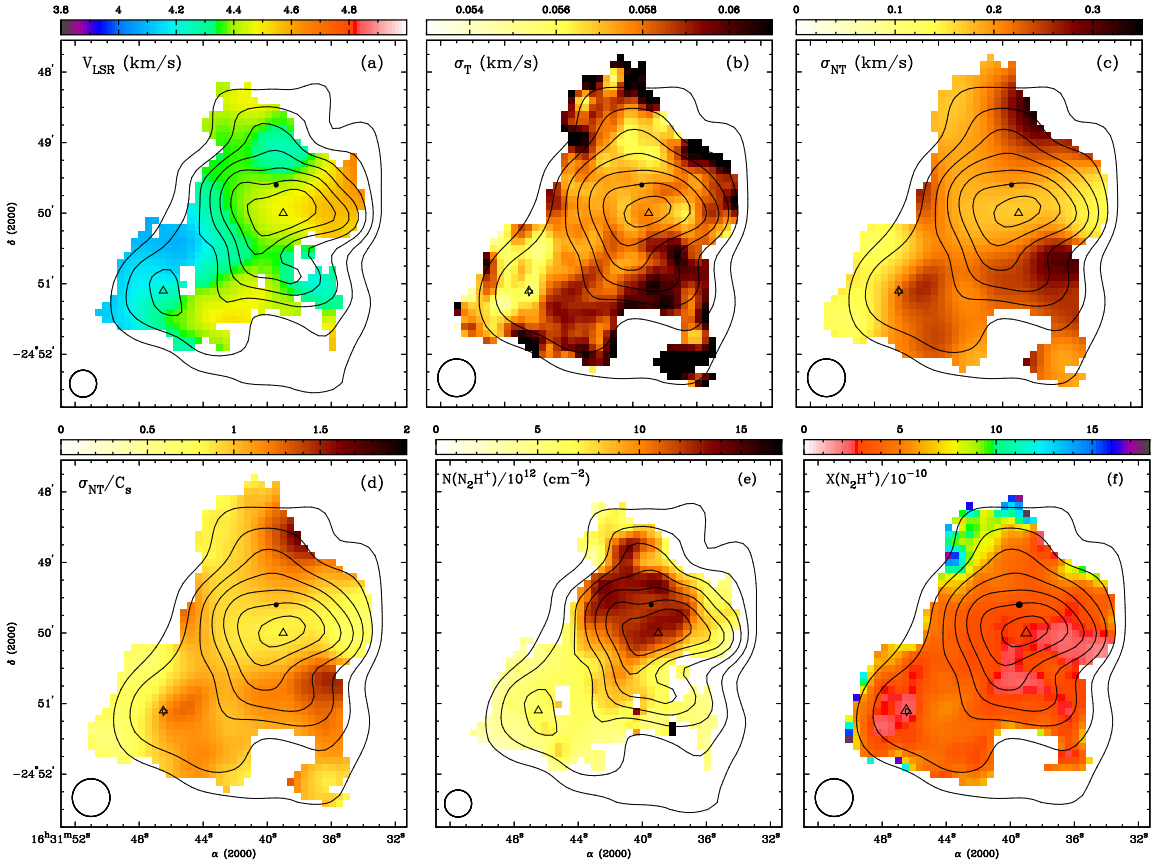

Figure 2.5: Maps of (a) v_{LSR}, (b) σ_T, (c) σ_{NT}, (d) σ_{NT}/c_s, (e) $N(\mathrm{N_2H^+})$, and (f) $X(\mathrm{N_2H^+})$ calculated using $\mathrm{N_2H^+}$ (1−0) emission toward SMM16. Maps of (a) v_{LSR} and (e) $N(\mathrm{N_2H^+})$ are at the NRO original spatial resolution ($\sim 22''.9$ FWHM). The contours correspond to continuum emission at 250 μm (smoothed to $\sim 22''.9$ FWHM), starting at 1.5 Jy beam^{-1} and increasing in steps of 1.5 Jy beam^{-1}. The rest of the plots are made using the $\mathrm{N_2H^+}$ (1−0) data smoothed to the resolution of the GBT, ($\sim 32''$ FWHM). The contours in these plots correspond to continuum emission at 250 μm (smoothed to $\sim 32''$ FWHM), starting at 3.0 Jy beam^{-1} and increasing in steps of 3.0 Jy beam^{-1}. The black dot shows the peak of the $\mathrm{N_2H^+}$ (1−0) integrated intensity and the triangles show the peaks of the continuum emission. The circle shows the corresponding spatial resolution of each plot.

(σ_T) of each of the molecular tracers using

$$\sigma_T = \sqrt{\frac{k_B T_K}{\mu\, m_H}}, \tag{2.7}$$

where k_B is the Boltzmann constant, μ is the respective molecular weight in atomic units, and m_H is the mass of the hydrogen atom. We also determined the thermal sound speed (c_s) of the gas by replacing μ with the mean molecular weight per free

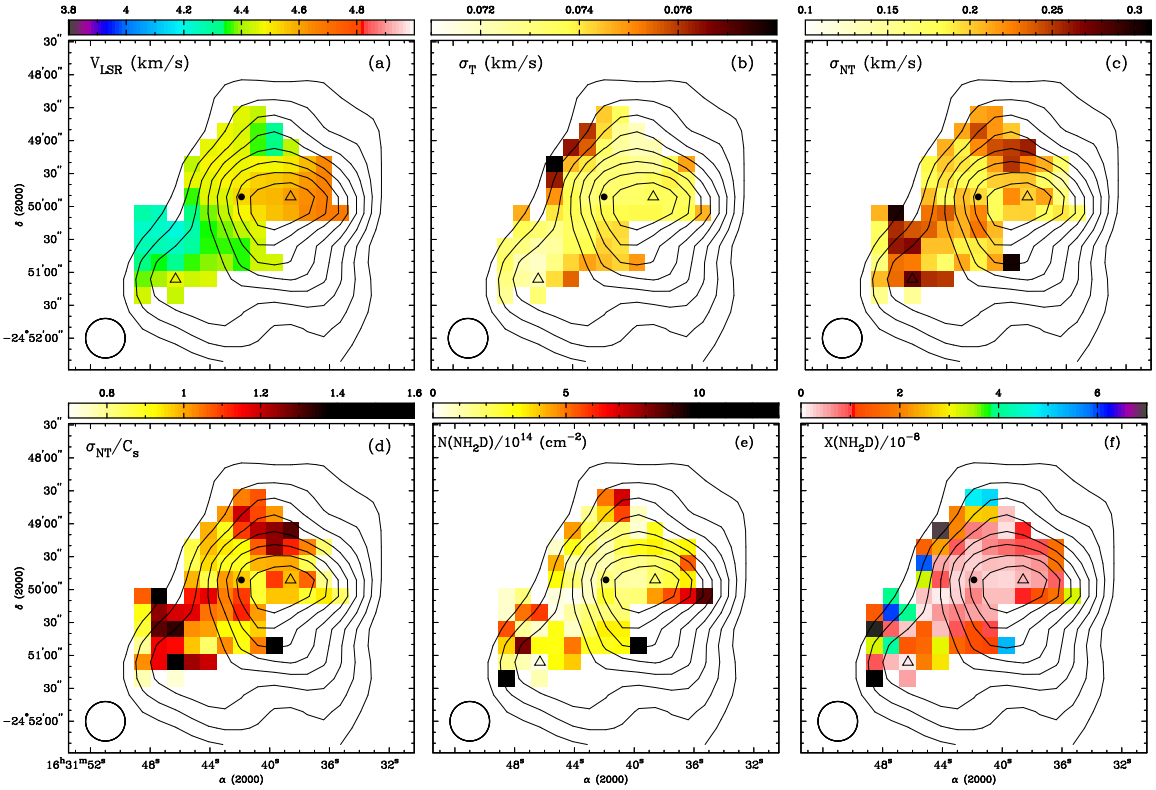

Figure 2.6: Maps of (*a*) v_{LSR}, (*b*) σ_T, (*c*) σ_{NT}, (*d*) σ_{NT}/c_s, (*e*) $N(\mathrm{NH_2D})$, and (*f*) $X(\mathrm{NH_2D})$ calculated using $\mathrm{NH_2D}$ ($1_{1,1}$ - $1_{0,1}$) emission toward SMM16 at 36″ FWHM. The contours correspond to continuum emission at 250 μm, starting at 3.0 Jy beam^{-1} and increasing in steps of 3.0 Jy beam^{-1}. The black dot shows the peak of the $\mathrm{NH_2D}$ ($1_{1,1}$ - $1_{0,1}$) integrated intensity and the triangles show the peaks of the continuum emission. The resolutions of the continuum data has been smoothed to that of the Mopra data, $\sim$ 36″ FWHM. The 36″ FWHM beam of the Mopra telescope is delineated with the circle.

particle $\mu_p = 2.37$ in the equation above . Given the determined σ_T, we calculated the nonthermal velocity dispersion (σ_{NT}) using

$$\sigma_{NT} = \sqrt{\sigma_v^2 - \sigma_T^2}. \tag{2.8}$$

Here, $\sigma_v = \Delta v/(2\sqrt{2\ln 2})$. Panels b, c, and d of Figures 2.4, 2.5, and 2.6 show maps of σ_T, σ_{NT}, and the nonthermal-to-thermal velocity dispersion ratio of the gas, given by σ_{NT}/c_s for $\mathrm{NH_3}$, $\mathrm{N_2H^+}$, and $\mathrm{NH_2D}$ emission lines, respectively, toward SMM16. For all three spectral lines, $\sigma_{NT}/c_s \simeq 1$ in most parts of the core, especially toward the centre. Although we see some localized increase in σ_{NT} toward the NW and SW, we do not detect a sharp "transition" to turbulent motions as observed by Pineda et al. (2010) toward the B5 region in the Perseus molecular cloud. Similar to some

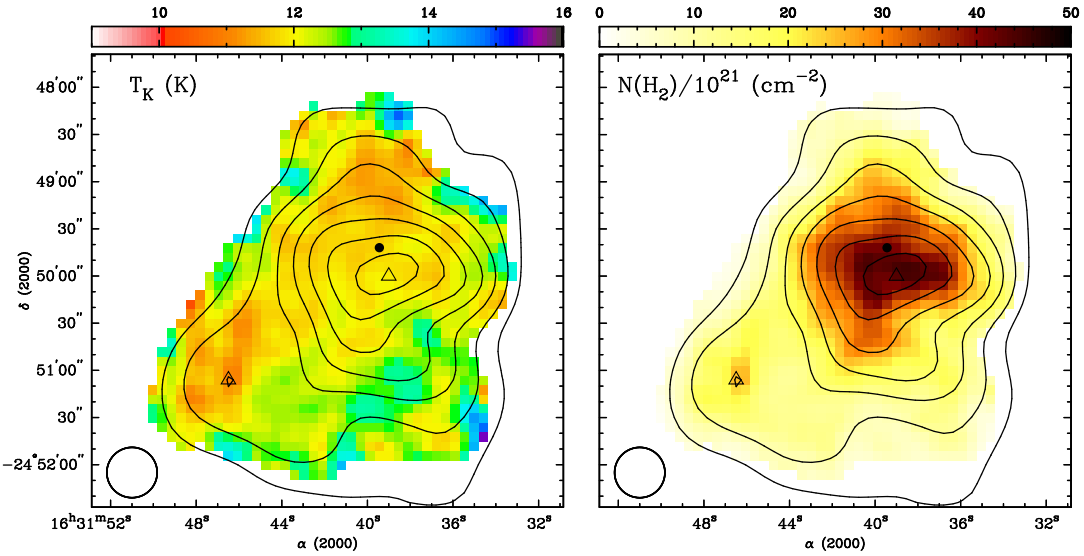

Figure 2.7: Maps of (a) T_K and (b) $N(\mathrm{H_2})$ toward SMM16. In both plots, the contours correspond to continuum emission at 250 μm, starting at 3.0 Jy beam^{-1} and increasing in steps of 3.0 Jy beam^{-1}. The black dot shows the peak of the NH_3 (1,1) integrated intensity and the triangles show the peaks of the continuum emission. The resolution of the continuum data has been smoothed to the resolution of the GBT data, $\sim 32''$ FWHM. The $32''$ FWHM beam of the GBT is delineated with the circle.

of the other starless cores in Ophiuchus, such as B68 (Lada et al. 2003), SMM16 is transonic and the core thermal and non-thermal motions are comparable.

Using the continuum data, we calculated the H_2 column density in each pixel with the expression

$$N(H_2) = \frac{S_\nu}{\Omega_m \mu_{H_2} m_H \kappa_\nu B_\nu(T_d)}. \tag{2.9}$$

Here, S_ν is the 250 μm flux density per pixel from the continuum emission toward SMM16, Ω_m is the beam solid angle, $\mu_{H_2} = 2.8$ is the mean molecular weight per hydrogen molecule (Cox 2000; Kauffmann et al. 2008), and m_H is the mass of the hydrogen atom. The dust opacity per unit mass $\kappa_\nu = 0.2$ cm^2 g^{-1} at 250 μm, which is consistent with the OH5 model by Ossenkopf & Henning (1994) for dust grains that have coagulated for 10^5 years and have developed thin ice mantles (Shirley et al. 2005). The OH5 model is also used by Shirley et al. (2005) to study the physical structure of the pre-protostellar core L1498. Note that the value of κ_ν at 250 μm may be half of an order of magnitude larger or smaller than the value used in this chapter (i.e., 0.2 cm^2 g^{-1}) depending on the adopted dust opacity model (Figure 3 of Shirley et al. 2005). The Planck function $B_\nu(T_d)$ is calculated at the dust temperature T_d.

In the central dense regions of cores (i.e., $> 10^5$ cm^{-3}; Di Francesco et al. 2007), the gas and dust temperatures should be largely coupled. In larger and more diffuse regions of molecular clouds, however, the gas and dust are decoupled and the gas can be warmer than the dust (Young et al. 2004a). Using the SMM16 mass and size estimation by Sadavoy et al. (2010a) (mass ~ 3.1 M$_\odot$ and effective radius ~ 0.049 pc), we estimated the average number density, $n \simeq 9.0\times10^4$ cm^{-3}, indicating that it is reasonable to assume that gas and dust temperatures are coupled across SMM16. Therefore, we used the calculated T_K map of the core to determine $N(H_2)$ per pixel. Figure 2.7b shows the H_2 column density map of SMM16. The H_2 column density peaks close to the continuum emission peak and drops off quickly toward the outer edges of the core.

Following the method described in Appendix A.1, we also calculated the NH_3, N_2H^+, and NH_2D column densities. Figures 2.4e, 2.5e, and 2.6e show the NH_3, N_2H^+, and NH_2D column density maps, respectively. The distributions of $N(NH_3)$ and $N(N_2H^+)$ across SMM16 follow that of $N(H_2)$ with the NH_3 and N_2H^+ column density peaks close to the peak of continuum emission and a relatively sharp decrease away from the core centre. The $N(NH_2D)$ distribution is very different, however, with *lower* values toward the continuum emission peak and higher values at the edge. Finally, given the calculated values of column densities, we determined the fractional abundances (X = molecular column density/$N(H_2)$) per pixel for each of the three molecules. Figures 2.4f, 2.5f, and 2.6f show the fractional abundances for NH_3, N_2H^+, and NH_2D, respectively. All three $X(NH_3)$, $X(N_2H^+)$, and $X(NH_2D)$ maps show a decreasing trend of molecular abundance with increasing $N(H_2)$ toward the core centre. A similar decrease in the abundance of N_2H^+ has been observed toward the centre of the starless core B68 by Bergin et al. (2002).

The weighted means and the median errors for T_K and $N(H_2)$ are listed in Table 2.6. The weighted means and the median errors for σ_{NT}, σ_T, σ_{NT}/c_s, molecular column densities, and fractional abundances for NH_3, N_2H^+, and NH_2D are listed in Table 2.7.

2.4.2 HNC and HCN

The HNC (1−0) and HCN (1−0) emission lines each have hyperfine structure with three components (Table 2.4). In our observations, the three hyperfine components of the HNC (1−0) are unresolved and effectively present a single line. All three hyperfine

Table 2.6: Statistics of T_K and $N(H_2)$ toward SMM16 determined using the fitting parameters for NH_3 emission and 250 μm dust emission.

Value	Weighted Mean	Median Error	Min	Max
T_K (K)	11.9	0.3	10.3	15.5
$N(H_2)$ ($/10^{22}$ cm^{-2})	1.35	0.05	0.13	4.5

Table 2.7: The weighted mean values of the physical properties of SMM16 determined using the fitting parameters of the observed emission spectra. The values inside the brackets are the median errors.[a]

Molecule	σ_T (km s^{-1})	σ_{NT} (km s^{-1})	σ_{NT}/c_s	N (cm^{-2})	X
NH_3	0.076 (0.001)	0.175 (0.005)	0.86 (0.03)	1.1 (0.1)$\times10^{15}$	5.0 (0.9)$\times10^{-8}$
N_2H^+[b]	0.0577 (0.0007)	0.192 (0.002)	0.95 (0.02)	8 (1)$\times10^{12}$	3.3 (0.9)$\times10^{-10}$
NH_2D	0.0735 (0.0005)	0.20 (0.01)	0.99 (0.06)	2 (1)$\times10^{14}$	5 (5)$\times10^{-9}$
HNC	...	...	...	1.1 (0.1)$\times10^{13}$	5 (1)$\times10^{-10}$
HCN	...	...	...	1.4 (0.1)$\times10^{13}$	8.1 (0.4)$\times10^{-10}$

[a]The values inside the brackets are the median errors, not the errors of the weighted mean.

[b]The results correspond to N_2H^+ (1−0) data smoothed to 32$''$ FWHM resolution.

components of the HCN (1−0), however, are clearly visible (e.g., see Figure 2.3). Under LTE conditions, the three hyperfine lines of HCN (1−0) have relative intensities of $F(0-1) : F(1-1) : F(2-1) = 1 : 3 : 5$, which are slightly different from the observed ratios toward SMM16. For instance, the observed ratio toward the peak of the HCN (1−0) emission for SMM16 is roughly $F(0{-}1) : F(1{-}1) : F(2{-}1) = 1 : 1 : 2$. Such anomalies have previously been detected toward other starless cores, such as TMC-1 (Gottlieb et al. 1975; Walmsley et al. 1982; Sohn et al. 2007; Loughnane et al. 2012). Note that due to the presence of such anomalies in the line ratios of HCN (1−0), the best fit parameters determined through spectral line fitting with an LTE model (as done in this chapter) are somewhat uncertain.

Unlike the line profiles of NH_3, N_2H^+, and NH_2D emission toward SMM16 that do not show any asymmetries, the HNC (1−0) and HCN (1−0) line profiles toward SMM16 both show red asymmetry. To fit these lines, we used the HILL5 model introduced by De Vries & Myers (2005) rather than Gaussian fits. This model consists

of a core with a systemic velocity v_{LSR} and a central peak excitation temperature T_{ex}. The far and near edges of the core have an excitation temperature of T_{bg}. $J_\nu(T)$ decreases linearly from $J_\nu(T_{ex})$ at the centre to $J_\nu(T_{bg})$ at the edges of the core forming a hill-shaped profile. The core has an optical depth of τ and the core material is moving at an inward or outward velocity v_C, where negative and positive values of v_C correspond to outward and inward motions, respectively. To fit the observed spectra using Equation (9) of De Vries & Myers (2005), we modified the fitting routine from Friesen et al. (2010b) using the function described in the provided HILL5 software[6] to determine the values for the five fitting parameters, v_{LSR}, Δv, τ, T_{ex}, and v_C at each pixel. Figure 2.8 shows the observed spectra of HNC (1−0) and HCN (1−0) (black) and the best-fit determined using the HILL5 model (red).

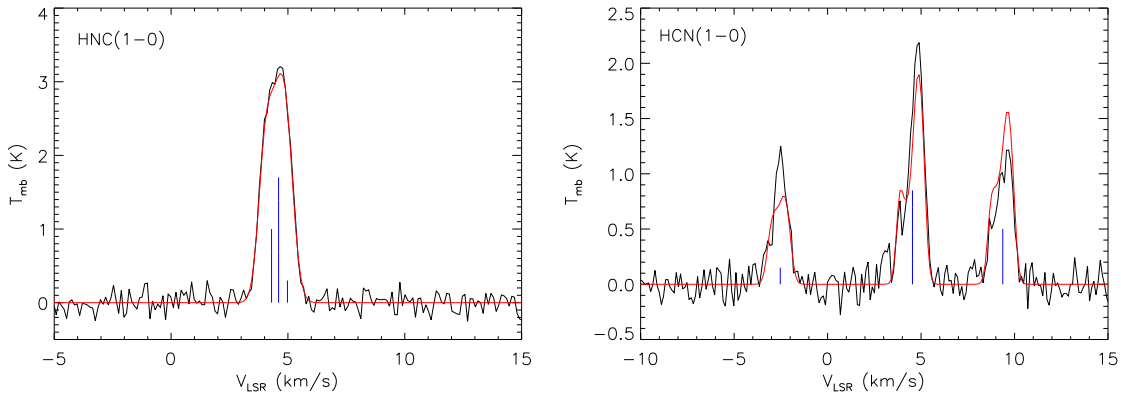

Figure 2.8: Spectra from the peak positions of HNC (1−0) emission (*left*) and HCN (1−0) emission (*right*) are shown in black. The fits determined using the HILL5 model (De Vries & Myers 2005) are shown in red. The blue vertical lines show the relative intensities and separations of the three hyperfine components of HCN (1−0) and HNC (1−0) transitions.

We also fit the observed HCN/HNC spectra with a multiple Gaussian fitting routine (explained in §2.4). The reduced χ^2 values for the HILL5 model and Gaussian fits are similar, e.g., 5.4 vs. 6.0 for HCN and 4.6 vs. 4.8 for HNC, respectively, but slightly favour the HILL5 model fit. The Gaussian fits do not reproduce the evident asymmetries of the same type seen in both the HNC line and the various components of HCN; the observed asymmetries are not due to the blending of hyperfine structure. Since the asymmetry is seen independently in these lines, we favour the interpretation of the HILL5 model, acknowledging that higher sensitivity observations of these lines or observations of other lines that trace similar conditions as HCN/HNC are needed to characterize the line profiles better. Note that the hyperfine components

[6]available at: *https://bitbucket.org/devries/analytic_infall/wiki/Home*

of HNC (1−0) are not resolved in our observations but we fit the spectra using three components. Thus, the T_{ex} and τ values of HNC (1−0) determined from such fitting are necessarily more uncertain than those determined for HCN (1−0) for which the hyperfine structure is perfectly resolved. In the following, we restricted our analysis of HCN/HNC data pixels where the SNR is higher than 10 in the main hyperfine component.

Figure 2.9 shows maps of v_C for HNC and HCN emission. The weighted mean values of v_C for HNC and HCN emission lines are -0.34 ± 0.03 km s^{-1} and -0.22 ± 0.01 km s^{-1}, respectively, with the negative values indicating outward motions. In a survey of 85 starless cores by Sohn et al. (2007), 20% of the sources showed a similar red asymmetry in HCN (1−0) emission.

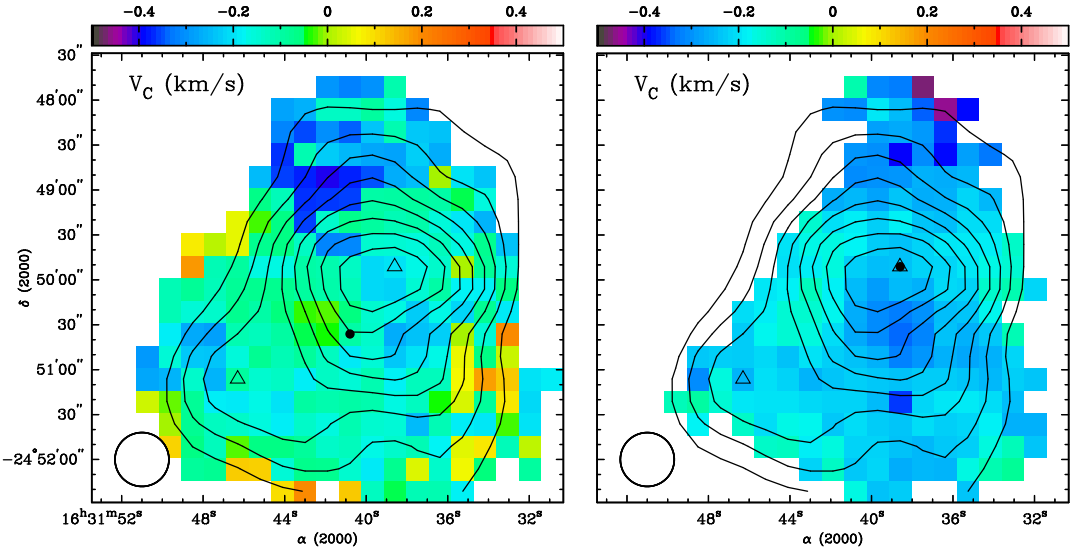

Figure 2.9: Maps of v_C determined using HNC (1−0) (*left*) and HCN (1−0) (*right*) emission spectra toward SMM16 at 36″ FWHM. The contours correspond to continuum emission at 250 μm, starting at 3.0 Jy beam^{-1} and increasing in steps of 3.0 Jy beam^{-1}. The black dot shows the corresponding molecular integrated intensity peak and the triangles show the peaks of the continuum emission. The resolution of the continuum emission data has been smoothed to that of the Mopra data, $\sim$ 36″ FWHM. In each panel, the 36″ FWHM beam of the Mopra telescope is delineated with the circle.

Table 2.5 lists the weighted mean and median error for each of the five fitting parameters for both HNC (1−0) and HCN (1−0) emission. Figures 2.10a and 2.10d show maps of v_{LSR} for HNC (1−0) and HCN (1−0), respectively. Compared to the complex distribution of v_{LSR} of NH_3 (1,1), N_2H^+ (1−0), and NH_2D ($1^a_{1,1} - 1^s_{0,1}$), both HNC (1−0) and HCN (1−0) show similar and more uniform distributions with a

single gradient across the core, suggesting a different velocity field is being traced by these molecules.

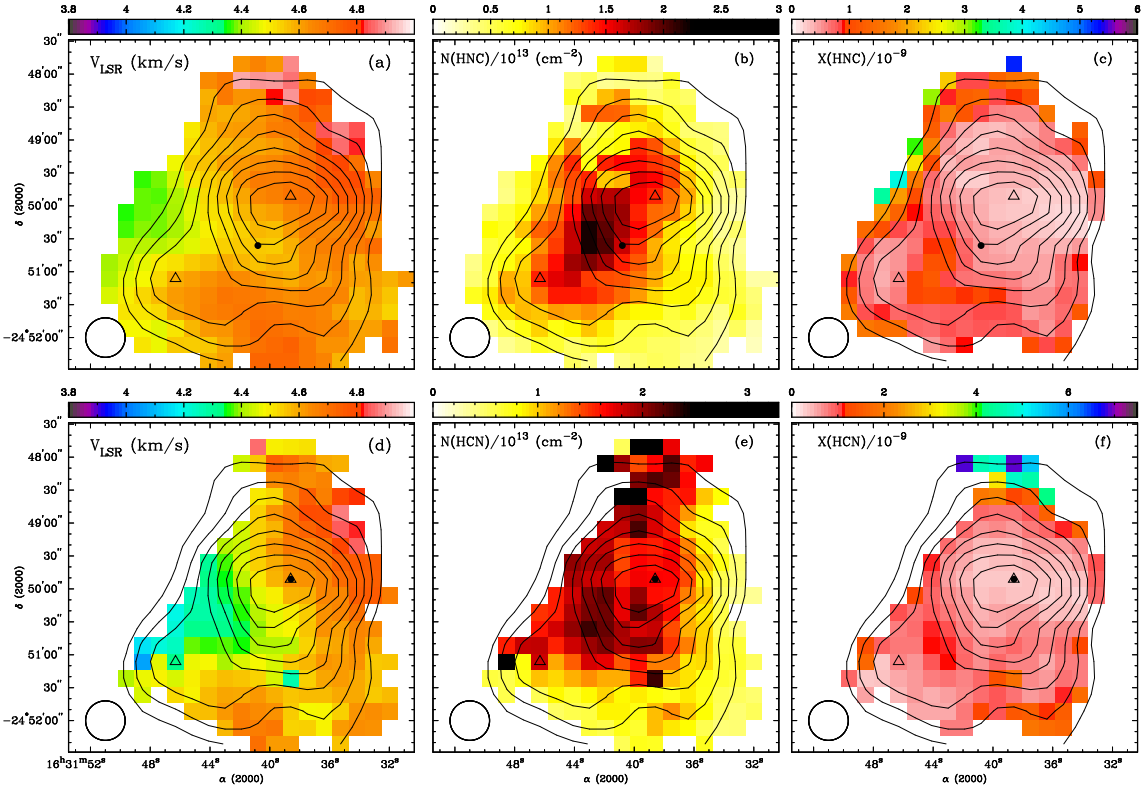

Figure 2.10: Maps of v_{LSR}, molecular column density, and fractional abundance calculated using HNC (1−0) (*top row*) and HCN (1−0) (*bottom row*) emission toward SMM16 at 36″ FWHM. The contours correspond to continuum emission at 250 μm, starting at 3.0 Jy beam^{-1} and increasing in steps of 3.0 Jy beam^{-1}. The black dot shows the peak of the corresponding integrated intensity and the triangles show the peaks of the continuum emission. The resolution of the continuum data has been smoothed to that of the Mopra data, $\sim$ 36″ FWHM. The 36″ FWHM beam of the Mopra telescope is delineated with the circle.

Following the method described in Appendix A.1, we calculated the HNC and HCN column densities (Figures 2.10b and 2.10e) and used the determined $N(H_2)$ from §2.4.1 to calculate the corresponding fractional abundances (Figures 2.10c and 2.10f). Table 2.7 lists the weighted mean and median error for these values. Equation (A.21) only applies to emission lines with Gaussian profiles. Though the HCN (1−0) and HNC (1−0) lines are not optically thin, their profiles appear Gaussian and their total optical depths are not extreme. For example, the weighted mean $\tau \sim$ 1-3 (see Table 5), and the τ values towards the location of maximum $N(H_2)$ are $\sim$ 1.2 and 3.5 for HNC (1−0) and HCN (1−0), respectively. (Indeed, these two lines are each

composed of hyperfine components whose optical depths are fractions of the total values.) Note that the HILL5 model returns the peak T_{ex}, not a mean T_{ex} value along the line of sight (De Vries & Myers 2005). In the HILL5 model, T_{ex} increases along the line of sight from the background value to a peak value. Equation (A.18), however, assumes that T_{ex} is constant along the line of sight. As a test, we also derived N(HNC) and N(HCN) using the results of the simple Gaussian fitting (explained in §2.4). The resulting HCN and HNC column densities were found to be within the errors to those values obtained from the parameters returned by the HILL5 model, e.g., weighted means (and median errors) of 1.4 (0.2) $\times$ 10^{13} cm^{-2} and 1.3 (0.2) $\times$ 10^{13} cm^{-2}, respectively. This similarity suggests our approximation of using the values obtained from the HILL5 model for Equation (A.21) for HCN and HNC is reasonable in the case of SMM16.

Figures 2.10b shows a N(HNC) peak $\sim$30″ East of the HNC integrated intensity peak and $\sim$75″ SE of the continuum peak, with N(HNC) also declining towards the edges of the core. Figure 2.10e shows no obvious peak location for N(HCN). Both Figures 2.10c and 2.10f show minima of X(HNC) and X(HCN), respectively, close to the continuum peak and increases toward the edges of the core. All maps are overlaid with contours of 250 μm continuum emission smoothed to the resolution of the Mopra data.

Models of gas-phase chemical networks, which take into account both ion-molecule and neutral-neutral reactions predict the ratio X(HNC)/X(HCN) to be close to unity in cold gas (e.g., Herbst et al. 2000 and references therein). This ratio has been observed to be mostly close to or above unity in molecular cloud cores (e.g., 0.54−4.5 from Hirota et al. 1998; 3−4 from Tennekes et al. 2006; $\sim$ 2 from Hily-Blant et al. 2010; $\sim$ 0.6 from Morales Ortiz et al. 2012); with no significant difference between starless and protostellar cores (Hirota et al. 1998 and Morales Ortiz et al. 2012). The mean value (weighted by the errors) of X(HNC)/X(HCN) is measured to be 0.7 across SMM16 with the median of the error $\sim$ 0.1. The measured abundance ratio toward SMM16, although being lower than unity, is indeed in the range observed previously in other cores by Hirota et al. (1998).

2.4.3 HCO^+ and $H^{13}CO^+$

The HCO^+ (1−0) line toward SMM16 shows extreme self-absorption (see Figure 2.3) with a red-skewed double peaked profile, which is an evidence of high optical depth

and possible expansion in the outer layer of the core (Lou & Gao 2011). Neither the multiple Gaussian fitting routine nor the HILL5 model provided an accurate fit to the strong self-absorption feature in the line profile of HCO^+ (1−0). Therefore, we do not present any further analysis on the HCO^+ (1−0) line emission in this chapter.

The $H^{13}CO^+$ (1−0) transition consists of a hyperfine structure over a frequency separation of $\sim$ 38.5 kHz (equivalent to a velocity separation of $\sim$ 0.14 km s^{-1} at 86.7 GHz; Schmid-Burgk et al. 2004). Our observed line profile with Mopra, however, resembles a single Gaussian (see Figure 2.3). The spectral resolution of our data is not sufficient to resolve the hyperfine structure of $H^{13}CO^+$ (1−0) and therefore it is uncertain which hyperfine transitions are contributing to the observed spectra. Thus, we do not provide any further analysis on the $H^{13}CO^+$ (1−0) line emission in this chapter.

2.4.4 The Origins of the Emission from Different Molecules in SMM16

The primary gas constituent of molecular clouds is the homonuclear molecule H_2 that is not easily excited at the cold temperatures of molecular cloud interiors ($T_K < 30$ K). Therefore, C-bearing molecules such as CO and its isotopologues are predominantly used to trace the interiors of molecular clouds. C-bearing species, however, suffer from molecular depletion toward the innermost regions of starless cores due to adsorption onto dust grains at high densities and low temperatures of the central regions of starless cores (Di Francesco et al. 2007 and references therein). Indeed, molecules such as HCN and HCO^+ among many other C-bearing molecules show significant decrease in abundance toward core centres (Tafalla et al. 2006). In comparison, N-bearing molecules such as NH_3 and N_2H^+ appear more resilient to depletion (or may deplete later) and provide better probes of the innermost regions of cores.

We detect decreasing trends of molecular abundances with increasing $N(H_2)$ toward the centre of SMM16 for both the observed C-bearing species (i.e., HCN and HNC) and the N-bearing species (i.e., NH_3 and N_2H^+). These decreases, however, are more significant and steeper for the C-bearing species. The fractional abundances of HCN and HNC at the core centre (i.e., the continuum peak) are both $\sim$ 4.2 times lower than the corresponding mean values at the outer edge of SMM16 ($\sim$ 0.065 pc from the core centre; for the definition of the outer edge see §2.5.2.1). In comparison, the central fractional abundances of NH_3 and N_2H^+ are only $\sim$ 1.7 times lower than

the corresponding mean values at the core edge, respectively. We interpret these abundance declines as being due to molecular depletions of various degree onto cold dust grains in the dense interior of SMM16. The steeper decreasing trends in the fractional abundances of the C-bearing molecules in SMM16 imply that their corresponding molecular lines are tracing predominantly the outer regions of the core. Although the fractional abundances of the N-bearing molecules also suffer from decreasing trends toward the core centre, their less steep decreases might suggest that they remain better probes of the inner region of SMM16. (Fractional abundance of NH_2D is not discussed here because the competing effects of enrichment by deuteration and depletion onto cold grains make interpreting its abundance structure difficult. For a discussion on the observed deuterium fractionation in SMM16 see §2.5.1.2.)

Note also that the integrated intensity and v_{LSR} distributions from HCN and HNC emission are similar to each other, e.g., more extended (see Figure 2.2) and simple NW-SE gradients (see Figures 2.10a and 2.10d, respectively). These differ significantly from the more compact integrated intensity (see Figure 2.1) and the more complex v_{LSR} distributions from NH_3 (1,1) and N_2H^+ (1−0) (see Figures 2.4a and 2.5a, respectively). Though radiative transfer models are needed to constrain better radial abundance gradients, these similarities and differences also suggest qualitatively that HCN/HNC and NH_3/N_2H^+ are tracing different layers of gas, i.e., outer and inner ones, respectively, in SMM16.

2.5 Discussion

2.5.1 Is SMM16 a Starless core?

Sadavoy et al. (2010a) distinguished between starless and protostellar cores in the Gould Belt molecular clouds (Ophiuchus, Taurus, Perseus, Serpens, and Orion) using 850 μm continuum data from SCUBA Legacy Catalogue (SLC) and 3.6−70 μm continuum data from the Spitzer Space Telescope. The dense core SMM16 was identified as starless in this catalogue. Furthermore, archival data of Ophiuchus obtained by the Herschel Gould Belt Survey (André et al., in prep.) do not show any sources with continuum emission at 70 μm in the vicinity of SMM16, also suggesting that SMM16 has not yet formed a protostar. In §2.5.1.1 and §2.5.1.2, we present further evidence supporting the starless nature of SMM16.

2.5.1.1 NH_3 and N_2H^+

In Figure 2.11, we show the distributions of azimuthal averages of T_K and σ_{NT}/c_s for both NH_3 and N_2H^+ spectra vs. the projected distance from the continuum peak (D) in SMM16. Note that T_K is calculated using hyperfine structure fitting of NH_3 (1,1) and (2,2) emission (see §2.4.1). We calculated the azimuthal averages with the dust peak emission at the centre and 6″ radial bins. In both panels, the dotted vertical lines show the radial bin beyond which some of the pixels in each bin are masked (and hence excluded from the average) due to low SNR. The error bars represent the azimuthal variation of T_K and σ_{NT}/c_s, respectively (i.e., the standard deviation).

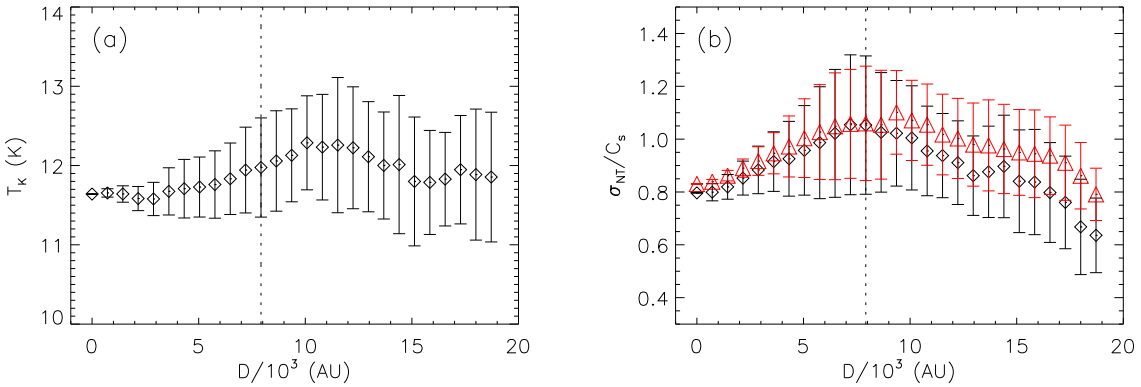

Figure 2.11: In both panels, data points show the distribution of azimuthal averages of the corresponding quantities vs. projected distance from the dust peak (D) for SMM16. The azimuthal averages are calculated with the dust emission peak at the centre and radial bins of 6″. The dotted vertical line shows the radial bin beyond which some of the pixels are masked due to low SNR. (a) Kinetic temperature, T_K, vs. D (note that T_K is calculated using hyperfine structure fitting of NH_3 (1,1) and (2,2) emission). (b) σ_{NT}/c_s vs. D for both NH_3 (black diamonds) and N_2H^+ (red triangles) line emission. The black and red error bars correspond to NH_3 and N_2H^+ data, respectively.

In Figure 2.11a, T_K values (although appearing constant within the errors) slightly decrease toward the centre of the core, i.e., with increasing H_2 column density, as might be expected from a starless core heated only externally by the interstellar radiation field. In Figure 2.11b, we show azimuthal averages of σ_{NT}/c_s for both NH_3 (black diamonds) and N_2H^+ (red triangles) line emission. The black and red error bars correspond to NH_3 and N_2H^+ data, respectively. For both species, the thermal and non-thermal motions appear to be on the same order, suggesting that SMM16 is transonic. There is a slight increase visible in σ_{NT}/c_s as we move away from the core centre. Toward the outer edges of the core, our estimations of azimuthal averages start to suffer from low SNR and decrease in the number of pixels included in the

average. Therefore, we are not confident that the decreasing trend of σ_{NT}/c_s on the outermost edge of the core is real. Again, no sharp transition to turbulent motions is seen in either tracer, unlike that observed by Pineda et al. (2010) toward the B5 region in the Perseus molecular cloud.

In a study of two dense cores both with Class I Young Stellar Objects (YSOs) offset from their centres, Hotzel et al. (2004) found an average $X(NH_3)/X(N_2H^+)$ of $\sim$ 140$-$190 toward the starless region of the cores, and 60$-$90 toward the regions close to the YSOs. In another study, Palau et al. (2007) found a tight connection between $X(NH_3)/X(N_2H^+)$ and the lack or presence of YSOs near (not necessarily inside) a core. The sources associated with YSOs showed lower values of $X(NH_3)/X(N_2H^+)$ $\sim$ 50, while starless cores showed higher values of $X(NH_3)/X(N_2H^+) \sim 300$. Furthermore, through observations of two cores in Ophiuchus, Friesen et al. (2010b) determined $X(NH_3)/X(N_2H^+) \sim 135$ for the starless core Oph B1 and ~ 65 for the protostellar core Oph B2. For SMM16, we measure the weighted mean of the abundance ratio ~ 140 and the median error ~ 20. This result indeed coincides with the range reported by previous authors for starless objects and further suggests that SMM16 has not yet formed a protostar.

2.5.1.2 Deuterium Fractionation

Observations and models have shown that C-bearing molecules deplete onto dust grains in the cold ($T < 20$ K) and dense ($n \geq 10^5$ cm^{-3}) environments of starless cores (Di Francesco et al. 2007 and references therein). This depletion leads to an increase in the abundance of H_2D^+, the progenitor of most deuterated molecules, such as NH_2D (e.g., Roberts & Millar 2000; Bacmann et al. 2003; Busquet et al. 2010). The deuterium fractionation, R_D (i.e., the abundance ratio of a deuterated species to its H-bearing counterpart), is a powerful tracer of the evolutionary stage of dense cores. A chemical model of prestellar cores by Aikawa et al. (2005) indicates that R_D increases as the core evolves to become more centrally concentrated. A survey of 31 starless cores by Crapsi et al. (2005b) indicated that in low-mass star forming regions R_D increases from $0.03 < R_D < 0.1$ for less evolved prestellar cores to $0.1 < R_D < 0.4$ toward more evolved starless cores. Busquet et al. (2010) carried out a survey of pre-protostellar and protostellar cores in a cluster forming region to investigate R_D as a tracer of the evolutionary stage of cores. The observations indicated higher values of R_D ($\simeq$ 0.1$-$0.8) toward the pre-protostellar cores compared to the lower

values ($\simeq 0.1$) toward the protostellar cores. It is also important to note that high deuteration fractionation levels (> 0.15) have been detected toward Class 0 protostars. For instance, a survey of N_2H^+ (1−0) and N_2D^+ (1−0) emission toward 20 Class 0 and Class 0/I protostars by Emprechtinger et al. (2009) showed that R_D remains high (> 0.15) even for a short while after the gravitational collapse has begun in the core. Subsequently, R_D decreases to levels as low as 0.03 for sources in transition between Class 0 and Class I.

We used the ratio $N(NH_2D)/N(NH_3)$ to determine the weighted mean R_D equal to 0.098 ± 0.006 toward SMM16 (here 0.006 is the error of the weighted mean) toward SMM16, which is in agreement with previous estimations of R_D toward other prestellar cores. The value of R_D and its error toward the peak position of NH_2D integrated intensity is equal to 0.10 ± 0.02. Hence, the starless nature of SMM16 is supported by the lack of a 70 μm continuum source in the vicinity of SMM16, slightly decreasing T_K toward higher $N(H_2)$, the observed transonic velocities of SMM16's gas, its high levels of NH_3/N_2H^+ abundance ratio, and its high deuterium fractionation level.

2.5.2 Stability Analysis

Sadavoy et al. (2010a) determined the mass (~ 3.1 $M_\odot$) and effective radius (~ 0.049 pc) of SMM16 using the 850 μm continuum data from the SLC (Di Francesco et al. 2008) assuming a dust opacity per unit mass, κ_ν, of 0.01 cm^2 g^{-1}, a distance of 125 pc to the Ophiuchus cloud, and $T_K = 15$ K. Using the measured values for mass and effective radius of SMM16 by Sadavoy et al. (2010a) and their assumed $T_K = 15$ K, we calculated the Jeans mass of SMM16 to be $\simeq 1.6$ $M_\odot$, indicating that SMM16 is slightly super-Jeans (Jeans mass is further described in §2.5.2.2). Given the very simple assumptions made, however, these results might not be very robust. To investigate further whether or not SMM16 is indeed a super-Jeans starless core, it is important to make more accurate estimations of its mass and size.

2.5.2.1 Density Profile

We assume SMM16 has the following volume density profile (King 1962; Tafalla et al. 2002; Dapp & Basu 2009):

$$\rho(r) = \begin{cases} \rho_c a^2/(r^2+a^2) & ; \quad r \leq R \\ 0 & ; \quad r > R \end{cases}, \tag{2.10}$$

where a and R are the radii of the inner flat region and the core, respectively, and ρ_c is the density of the central region, such that $a = \gamma \frac{c_s}{\sqrt{G\,\rho_c}}$, with γ a dimensionless proportionality constant. (Note that here the symbol γ is used instead of k as in the original paper by Dapp & Basu 2009). The central number density, n_c, depends on ρ_c such that, $n_c = \frac{\rho_c}{m_H \mu_p}$. The effect of temperature is taken into account in the thermal sound speed $c_s = \sqrt{k_B\,T_K/\mu_p}$. The above density profile is similar to but more generic than the density profile of a Bonnor-Ebert Sphere (BES; Ebert 1955; Bonnor 1956; Chandrasekhar 1957). Dapp & Basu (2009) analytically determined the column density profile of a sphere with the above volume density to be

$$\Sigma(x) = \frac{\Sigma_c}{\sqrt{1+(x/a)^2}} \times \left[\arctan\left(\sqrt{\frac{c^2-(x/a)^2}{1+(x/a)^2}} \right) / \arctan(c) \right], \tag{2.11}$$

where c $\equiv R/a$ and $\Sigma(x=0) \equiv \Sigma_c = 2a\rho_c \arctan(c)$. We converted H_2 column density of SMM16 to the total column density ($N_{total} = \frac{\mu_{H_2}}{\mu_p} N(H_2)$; Kauffmann et al. 2008) and azimuthally averaged N_{total} with the continuum emission peak at the centre and radial bins of 6″. To take completely into account the effect of beam convolution in fitting the observations, we made a 2-dimensional column density model using Equation (2.11) and convolved it with a 2-dimensional Gaussian with the same FWHM as that of the GBT beam (32″ FWHM). Similar to the observed N_{total}, we took azimuthal averages of the simulated convolved column density map and used the resulting profile to fit the azimuthally averaged total column density measured through observations. Note that in our calculation of $N(H_2)$ across SMM16 (Figure 2.7b), we assumed $T_d = T_K$ and used the T_K map of SMM16 (Figure 2.7a) determined through hyperfine fitting of the NH_3 data from the GBT (see §2.4.1 for details). Hence, the resulting $N(H_2)$ and N_{total} maps are similar to the GBT data in spatial resolution, i.e., $\sim 32''$ FWHM. In Figure 2.12, the diamonds show the azimuthal average of N_{total} versus the projected distance from the continuum emission peak and the curve shows the best

fit of Equation (2.11) to the observed N_{total}. The uncertainty in N_{total} is due to that of the continuum fluxes and T_K. Assuming a distance of 120 pc to the Ophiuchus molecular cloud (Loinard et al. 2008) and $T_K = 11.9$ K (weighted mean value of T_K for SMM16; see Table 2.6), the best values for fitting parameters are $a = 0.0227$ pc $\pm$ 0.0005 pc, $c = 2.8 \pm 0.2$, and $\Sigma_c = (5.9 \pm 0.1) \times 10^{22}$ cm^{-2}. These results yield an outer radius of $R = 0.065 \pm 0.004$ pc, $n_c \simeq (3.4 \pm 0.1) \times 10^5$ cm^{-3}, and $c_s \simeq 0.20$ km/s. Following Dapp & Basu (2009), core total mass $M = 4\pi\rho_c a^3 \left[\frac{R}{a} - arctan\left(\frac{R}{a}\right)\right]$, which yields $M = 4.7 \pm 0.6$ M$_\odot$. Our derived core radius (~ 0.065 pc) and total mass ($\sim$ 4.7 M$_\odot$) are both larger than the corresponding values determined by Sadavoy et al. (2010a) ($R \sim 0.049$ pc and $M = 3.1$ M$_\odot$). Given our determined values for the total core mass and R, we determined the mean number density, n, in SMM16 to be $\sim$ 7.1×10^4 cm^{-3}.

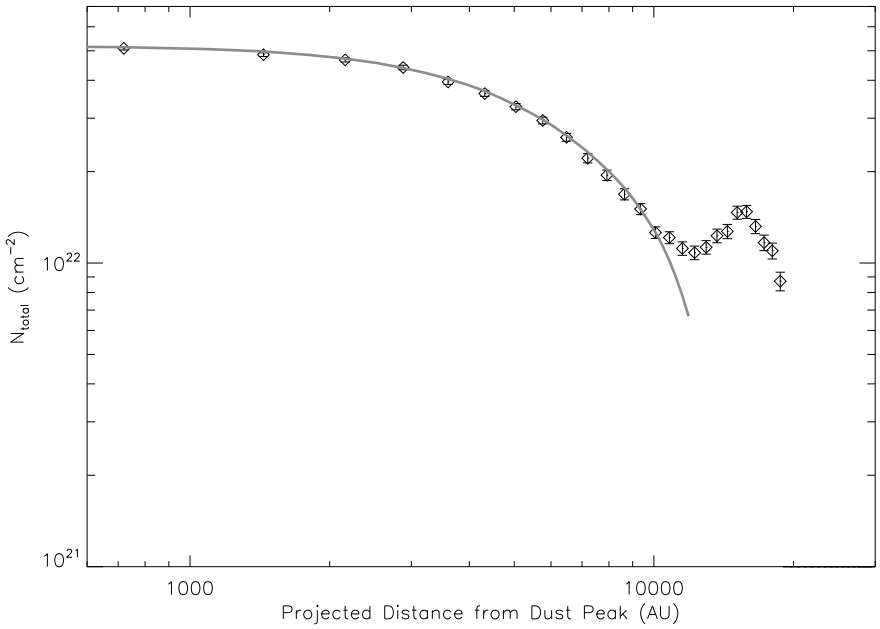

Figure 2.12: Azimuthal average of total column density N_{total} versus the projected distance from the continuum emission peak (diamonds). The curve is the best fit of Equation (2.11) to the data. Prior to fitting the observed N_{total}, we made a 2-dimensional column density model using Equation (2.11) and convolved it with a 2-dimensional Gaussian with the same FWHM as that of the GBT beam (32″ FWHM). We took azimuthal averages of the simulated convolved column density map and used the resulting profile (curve) to fit the azimuthally averaged N_{total} measured through observations.

Given the weighted mean value of T_K toward SMM16, we used the estimated values of the fitting parameters, a, c, and Σ_c, to determine the dimensionless parameter $\gamma \simeq 1.0$. In fact, estimation of the parameter γ can shed light on the dynamical stage

of the region of interest. Dapp & Basu (2009) argue that a critical BE sphere has $\gamma \approx 0.5$, and emphasize that a collapsing core shows a column density profile with γ higher than 0.5 and closer to 1. Our estimated value of γ suggests that SMM16 is unstable and consistent with a collapsing core. The effect of magnetic fields is not included in this analysis, however. As indicated by Dapp & Basu (2009), support from magnetic fields could be a contributing factor to the stability of prestellar cores like SMM16.

2.5.2.2 Comparison with Jeans Mass

The minimum mass for the gravitational fragmentation of a purely thermal clump is described by the Jeans limit. To explore the thermal stability of SMM16, we calculated the Jeans mass described by (Sadavoy et al. 2012)

$$M_J = 2.9 \left(\frac{T_K}{10\ \mathrm{K}}\right)^{1.5} \left(\frac{n}{10^4\ \mathrm{cm}^{-3}}\right)^{-0.5} \mathrm{M}_\odot. \tag{2.12}$$

Using the weighted mean value for $T_K = 11.9$ K and the determined value of the mean number density n, the Jeans mass of SMM16 is calculated to be $M_J \simeq 1.4\ \mathrm{M}_\odot$. The estimated total mass for SMM16 is $\simeq 4.7\ \mathrm{M}_\odot$, indicating that SMM16 is indeed a super-Jeans starless core. Our determined value of SMM16 Jeans mass is slightly lower than the value determined by Sadavoy et al. (2010a) ($\simeq 1.6\ \mathrm{M}_\odot$).

2.5.2.3 Comparison with Virial Equilibrium

To investigate the dynamical state of SMM16, we also calculated its virial mass (M_{virial}) and compared it to the total core mass. The virial mass is described by

$$M_{virial} = \frac{5\sigma^2\, R}{a\, G}, \tag{2.13}$$

where the velocity dispersion $\sigma = \sqrt{\sigma_{NT}^2 + c_s^2}$ and we used the weighted mean values of $\sigma_{NT} = 0.175$ km s^{-1} and $c_s = 0.206$ km s^{-1} inferred from the mean NH_3 line width. The parameter $a = a_1\, a_2$, where a_1 accounts for the nonuniformity in the core density distribution and a_2 accounts for the core ellipticity (Bertoldi & McKee 1992). For a core with a power-law density distribution, $\rho(r) \propto r^{-p}$, $a_1 = (1 - p/3)/(1 - 2p/5)$. Assuming the density profile of SMM16 is described by Equation (2.10), we used $p = 2$ to estimate $a_1 = 5/3$. Using Figure 2 of Bertoldi & McKee (1992) and assuming

SMM16 to be roughly spherical, we estimated a_2 to be ~ 1. The virial mass (M_{virial}) of SMM16 is therefore equal to 3.3 $M_\odot$. Comparing the total and virial masses to determine if SMM16 is gravitationally bound or transient (McKee 1999), a core is gravitationally bound if

$$\alpha = \frac{M_{virial}}{M} \leq 2. \tag{2.14}$$

For SMM16, we find $\alpha \simeq 0.7$, suggesting that SMM16 is indeed gravitationally bound with the potential for collapse, i.e., prestellar in nature.

2.5.2.4 Comparison with the Bonnor-Ebert Criteria

For a spherical and isothermal cloud of gas in hydrostatic equilibrium and confined by an external pressure, P_{ext}, the fluid density can be described by the Lane-Emden equation (Chandrasekhar 1967),

$$\frac{1}{\xi^2}\frac{d}{d\xi}\left(\xi^2\frac{d\psi}{d\xi}\right) = e^{-\psi}, \tag{2.15}$$

where $\xi = (r/c_s)\sqrt{4\pi G\rho_c}$ is a dimensionless radial parameter and $\psi(\xi) = -\ln(\rho/\rho_c)$. The Bonnor-Ebert model introduces a series of solutions characterized by the value of ξ at the core boundary R, $\xi_{max} = (R/c_s)\sqrt{4\pi G\rho_c}$. Clouds with $\xi_{max} > 6.5$ are unstable and prone to gravitational collapse and those with $\xi_{max} < 6.5$ are stable. For SMM16, we determined $\xi_{max} \simeq 10.4$, further suggesting that SMM16 is unstable to gravitational collapse. Such high values of ξ_{max} have also been observed by Kandori et al. (2005) toward starless Bok globules that are also believed to be unstable to gravitational collapse. The gravitationally unstable nature of SMM16 is also confirmed by the calculation of its critical BE mass (the largest stable mass supported by thermal pressure against gravitational collapse), $M_{BE} = 1.18c_s^4/\sqrt{G^3P_{ext}}$ (Basu & Jones 2004), where $P_{ext} = \rho_R c_s^2$ and ρ_R is the material density at the boundary of the core. For SMM16, using the outer radius of 0.065 pc (see §2.5.2.1) and Equation (2.10), we determined $P_{ext} = 6.2 \times 10^{-12}$ Pa and $M_{BE} = 0.75$ $M_\odot$.

2.5.2.5 Comparison with the Starless Core B68

B68 is the quintessential example of a critical BE sphere in the literature. Assuming distance of 125 pc, Alves et al. (2001) fit the column density profile of B68 using the BE model to determine $M_{BE} = 2.1$ $M_\odot$, outer radius of 0.06 pc, $T = 16$ K, and $\xi_{max} = 6.9 \pm 0.2$. They also calculate $P_{ext} = 2.5 \times 10^{-12}$ Pa for B68. Dapp &

Basu (2009) performed a similar analysis to find $M_{BE} = 1.17$ $M_\odot$, outer radius of 0.052 pc, $T = 11$ K, and $\xi_{max} = 7.0$. Furthermore, Dapp & Basu (2009) fit their model (Equation 2.10 in this chapter) to the observational data of B68. The best fit parameters yield a total mass $M = 1.2$ $M_\odot$, outer radius $R = 0.051$ pc, and radius of the flat inner region $a = 0.014$ pc. Assuming $T = 11$ K, Dapp & Basu (2009) determine $\gamma = 0.57$, concluding that B68 is quite similar to a critical BE sphere best fit by $\gamma = 0.54$. Comparing the above results for B68 with the determined values for SMM16, $\xi_{max} = 10.4$, $P_{ext} = 6.2 \times 10^{-12}$ Pa and $M_{BE} = 0.75$ $M_\odot$, $M = 4.7$ $M_\odot$, and $\gamma = 1.0$ (see §2.5.2.1), we conclude that the internal structure, mass, and size of SMM16 do resemble that of B68, however, SMM16 could be at a slightly more advanced, supercritical evolutionary stage.

Our stability analysis suggests that SMM16 is a super-Jeans and gravitationally bound core. It also appears to be supercritical from a BE perspective and more centrally condensed than the starless core B68. Without internal support beyond thermal motions, it is likely that SMM16 will experience gravitational collapse.

2.5.3 Internal Dynamics of SMM16

Though collapse (infall) motions may be expected from the analysis in §2.5.2, the red-skewed double-peaked line profile of HCO^+ (1−0) (suggestive of blue-shifted self-absorption) indicates expanding motions in the outer layers of SMM16. Furthermore, the analysis of the red asymmetry observed in the line profiles of HCN (1−0) and HNC (1−0) suggests that the expanding layer is moving at a speed of 0.2 km s^{-1} to 0.3 km s^{-1} (see §2.4.2). Although protostellar outflows can also produce similar red-skewed emission lines, we would expect such features to be highly localized and spatially compact. In case of SMM16, however, the red asymmetry in the line profiles of HCN (1−0) and HNC (1−0) and the red-skewed double-peaked line profile of HCO^+ (1−0) are observed everywhere across the core, indicating the presence of an expanding shell rather than a localized outflow. Similar spectral line features have been previously observed toward other starless cores such as B68 (Lada et al. 2003), FeSt 1-457 (Aguti et al. 2007), and L1517B (Fu et al. 2011; Sohn et al. 2007) and cores containing VeLLOs such as L1014 (Crapsi et al. 2005b) using dense molecular gas tracers such as emission from HCO^+, CS, and HCN. In the absence of a protostellar object, such expanding motions in the outer layers of a globule may indicate that the object is transient and not gravitationally bound. For a self-gravitating bound

object such as SMM16, however, an expanding envelope could be a sign of oscillating motions within the outer layers of the core (Lada et al. 2003; Aguti et al. 2007; Lou & Gao 2011).

Theoretical scenarios suggested by Keto & Field (2005), Broderick et al. (2007), Stahler & Yen (2010), and Anathpindika & Di Francesco (2013) as well as the theoretical picture of self-similar hydrodynamics for Envelope Expansion with Core Collapse (EECC; Lou & Shen 2004; Thompson & White 2004; Gao & Lou 2010; Lou & Gao 2011) all predict the possibility of oscillating motions in starless cores. Such oscillations could be due to an enhancement in the external pressure of a static core on large scales as a result of, e.g., a locally turbulent ISM or a nearby outflow or supernova that leads to an increase in the core density. These compression waves travel through the core and bounce back from the centre while the core adjusts its size and density profile to the increase in external pressure. These cores could be oscillating around an equilibrium configuration or might be evolving toward collapse in their central regions (Keto & Field 2005). According to the numerical model presented by Anathpindika & Di Francesco (2013), a core is more likely to experience oscillations as result of perturbation if it is surrounded by relatively warm gas ($\sim$ 35 K). Starless cores surrounded by cold gas ($\sim$ 15 K), however, are more likely to undergo gravitational collapse if perturbed. Numerical models estimate an oscillation period of a few 10^5 years (Anathpindika & Di Francesco 2013) and an oscillation lifetime of 10^6 years (Broderick et al. 2007). Indeed, such oscillations have been suggested for other starless cores such as, B68 (Lada et al. 2003), FeSt 1-457 (Aguti et al. 2007), and L1517B (Fu et al. 2011).

Our observations of dense molecular gas tracers that predominantly trace the central regions of SMM16 (i.e., NH_3 and N_2H^+) do not show evidence of any line profile asymmetries. There are, however, indications of mostly infall motions (e.g., L1517B; Lou & Gao 2011 and Fu et al. 2011) or a mix of inward and outward motions reported toward candidates of oscillating cores in the literature (L1495A-N, L1507A, and L1512; Lee & Myers 2011). According to the EECC model (Lou & Gao 2011), over time the central inward motions will increase due to self-gravity and the outer edge of the collapsed region moves outward and reaches the envelope. Eventually, the core will continue to collapse toward the centre and form a protostar.

To probe the internal motions within SMM16, we determined the degree of spectral asymmetry in the optically thick lines HNC (1$-$0) and HCN (1$-$0) using the normalized velocity difference, $\delta V = \frac{v_{LSR,\mathrm{thick}} - v_{LSR,\mathrm{thin}}}{\mathrm{FWHM_{thin}}}$, where $v_{LSR,\mathrm{thick}}$ and $v_{LSR,\mathrm{thin}}$

are the respective velocities of the peaks of the optically thick and thin lines, and $\mathrm{FWHM_{thin}}$ is the FWHM of the optically thin emission line profile (Mardones et al. 1997; Lee et al. 1999; Lee et al. 2001; Lee & Myers 2011). A negative δV indicates that the optically thick profile has a blue asymmetry and the corresponding material is in inward relative motion. On the other hand, a positive δV shows that the optically thick profile has a red asymmetry and suggests that the traced material is moving relatively outward. Figure 2.13 shows maps of δV for the optically thick lines HCN (1−0) and HNC (1−0) using N_2H^+ (1−0) and NH_3 (1,1) as the optically thin lines. It is evident that δV values for both HCN (1−0) and HNC (1−0) are predominantly positive across the maps, regardless of the choice of the optically thin line. These results indicate that both of the optically thick lines probe outward motions toward SMM16, which is also suggested by the HILL5 model (see §2.4.2).

Some oscillating cores (e.g., B68; Lada et al. 2003) show alternating inward and outward motions across their spherical surface. The velocity distribution of such movements can be described as a function of the real part of the spherical harmonic functions, $Y_l^m(\theta,\phi) = (-1)^m c_{lm} P_l^m(cos\theta)\exp(im\phi)$, where $P_l^m(cos\theta)$ is the Legendre function and c_{lm} is a normalization constant (Lada et al. 2003 and references therein). The number of alternating regions with inward and outward motions on the oscillating surface depends on the modal values, l and m. Figure 8 of Lada et al. (2003) shows the spherical harmonic oscillators for $0 \leq l \leq 3$. Lada et al. (2003) propose that B68 is experiencing $l = 2$ and $m = 2$ mode of oscillations. In their study of the oscillating core FeSt 1-457, Aguti et al. (2007) detect a similar asymmetry distribution to our observations toward SMM16, i.e., outward motions across the whole surface of the core. Aguti et al. (2007) suggest that FeSt 1-457 is either oscillating in the $l = 0$ mode, also called "breathing mode" (Keto et al. 2006), with outflow motions all over the core, or is experiencing a similar mode of oscillation to B68, but appears differently in the observations due to being edge-on to our line of sight.

Though the overall outward motion of SMM16 may indicate a breathing mode oscillation, some of the δV maps of SMM16 (Figure 2.13) show features which resemble higher oscillatory modes of spherical surfaces (e.g., see Lada et al. 2003). In particular, HCN vs. N_2H^+ or NH_3 (1,1) (Figures 2.13a and 2.13b) both show a similar triangular pattern with positive velocity offset extremes equally spaced about the continuum peak. (Similar features resembling these extrema are also seen at the same locations in the δV maps of HNC vs. N_2H^+ or NH_3 in Figures 2.13c and 2.13d). Moreover, in the highest SNR case of HCN vs. NH_3 seen in Figure 2.13b, three velocity offsets of

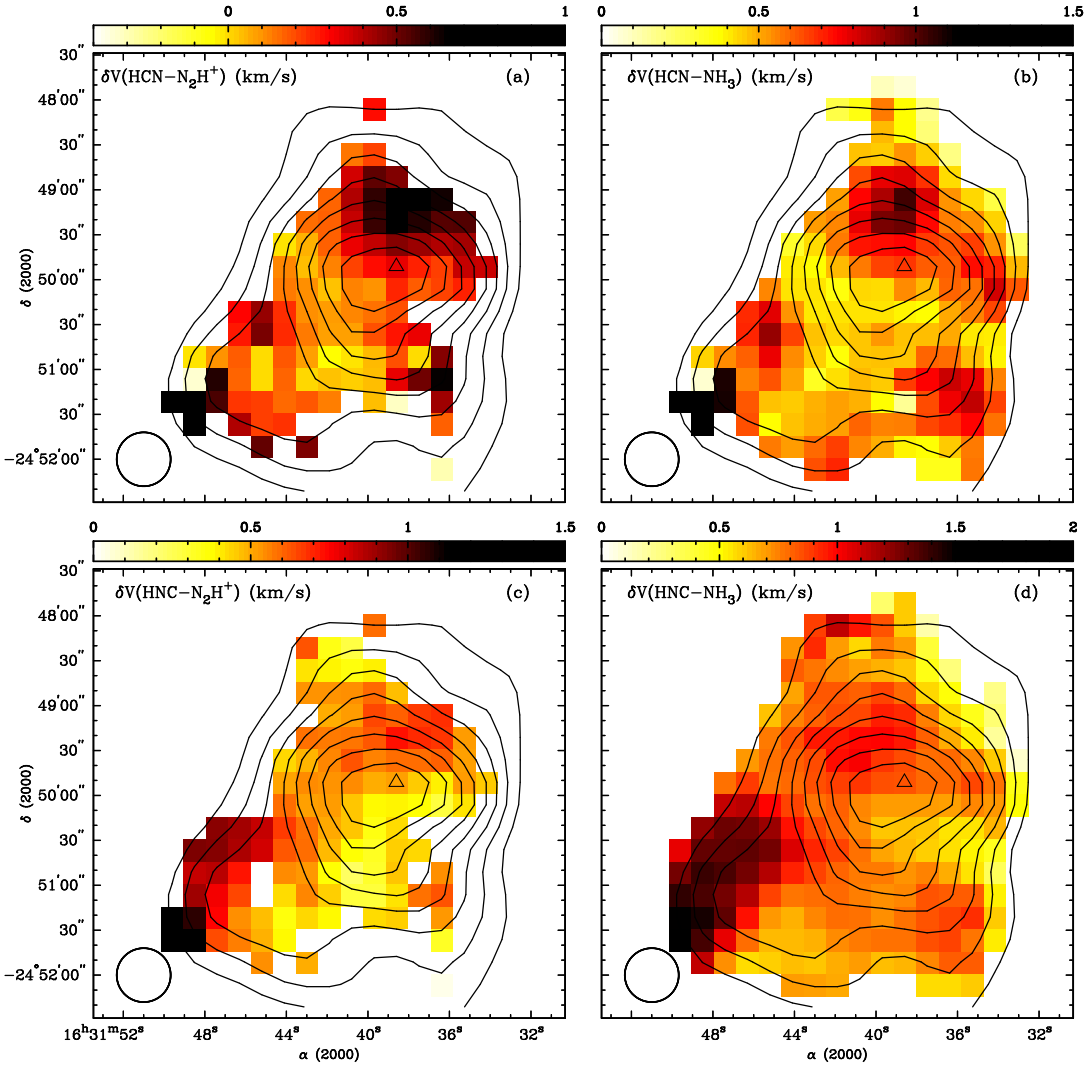

Figure 2.13: Maps of the degree of line asymmetries, δV, for the optically thick lines HCN (1−0) (*top row*) and HNC (1−0) (*bottom row*) toward SMM16. The line asymmetries are estimated by calculating the normalized velocity difference $\delta V = \frac{v_{LSR,\mathrm{thick}} - v_{LSR,\mathrm{thin}}}{\mathrm{FWHM}_{\mathrm{thin}}}$. To calculate the degree of spectral asymmetries for both HCN (1−0) and HNC (1−0), we used the following optically thin lines: isolated hyperfine component of N_2H^+ (1−0) (*left column*), and main hyperfine component of NH_3 (1,1) (*right column*). The contours correspond to continuum emission at 250 μm, starting at 3.0 Jy beam^{-1} and increasing in steps of 3.0 Jy beam^{-1}. The spatial resolutions of the NH_3 (1,1), N_2H^+ (1−0), and continuum emission data have all been smoothed to that of the Mopra data, $\sim 36''$ FWHM. In each panel, the triangle shows the location of the main continuum peak and the $36''$ FWHM beam of the Mopra telescope is delineated with the circle.

similar magnitude but less positive than the extrema above are found equally spaced between the velocity offset extrema. Overall, this pattern is reminiscent of that of the $l = 3$, $m = 2$ mode of oscillation of a spherical surface (see Lada et al. 2003).

Though it is necessary to use radiative transfer models to reproduce the spectra of SMM16, we speculate that at least the outer layers of SMM16, as traced by HCN and HNC, are oscillating, perhaps with a superposition of at least two modes (i.e., an $l = 0$ breathing mode and the $l = 3$, $m = 2$ mode). Further data are also needed to explore this intriguing possibility.

2.6 Summary

In this chapter, we presented single-dish observations of the starless core SMM16 in NH_3, N_2H^+, NH_2D, HCN, HNC, HCO^+, and $H^{13}CO^+$ emission. These observations lead us to believe that SMM16 is a gravitationally bound, supercritical (perhaps oscillating), chemically evolved starless core.

1. NH_3 (1,1) and N_2H^+ (1−0) emission follow the morphology of the continuum emission, suggesting that both lines trace the dense gas in the starless core. On the other hand, the morphologies of HCN (1−0), HNC (1−0), and $H^{13}CO^+$ (1−0) show less similarity to the continuum emission. The HCO^+ (1−0) emission is, however, very different, with a peak located at a large offset from the continuum emission. Due to the limited extent of NH_2D ($1^a_{1,1} - 1^s_{0,1}$) emission, it is difficult to conclude how well it is following the continuum emission and tracing dense gas.

2. We detect decreasing trends in the respective fractional abundances of NH_3, N_2H^+, NH_2D, HCN, and HNC toward the continuum emission peak. These decreases, however, are more significant and steeper for the C-bearing species (i.e., HCN and HNC) than that of the the N-bearing species (i.e., NH_3 and N_2H^+), suggesting qualitatively that the C-bearing and N-bearing species are tracing different layers of gas, i.e., outer and inner ones, respectively, in SMM16.

3. The line profiles of NH_3 and N_2H^+, which probe best the innermost regions of dense cores, do not show any evidence of asymmetries. If optically thin, these lines might be broadened by movement of gas in either direction (i.e., inward or outward). Meanwhile, the red-skewed double peaked profile of HCO^+ (1−0) and the red asymmetry in the line profiles of HCN (1−0) and HNC (1−0) reveal the expansion of the foreground layers of SMM16 at a speed of 0.2 km s^{-1} to 0.3 km s^{-1}.

4. The lack of a protostellar source in the vicinity of SMM16 in the archival Spitzer and Herschel data suggests that SMM16 is starless. This idea is further supported by the relatively high value of $X(NH_3)/X(N_2H^+)$ and large deuterium fractionation level toward SMM16.

5. Through fitting the H_2 column density profile of SMM16 with that of a general BE sphere, we determined the mass and radius of SMM16 to be $\sim$ 4.7 $M_\odot$ and R $\sim$ 0.065 pc, respectively. Comparing mass, radius, and material density of SMM16 with Jeans and BE criteria reveals that SMM16 is a super-Jeans core and unstable to gravitational collapse in the absence of other mechanisms of support. Furthermore, the virial analysis demonstrates that SMM16 is indeed a gravitationally bound core and not a transitionary object.

6. The presence of expanding outer layers has been observed toward other gravitationally bound starless cores and is considered evidence of oscillatory motions inside or on the surface of SMM16. Indeed, SMM16 might be oscillating about a mean configuration or is in transition from a static core to gravitational collapse and protostellar formation.

Chapter 3

Single-dish Observations of Highly Concentrated Dense Cores in NH_3 and N_2H^+ Line Emission

3.1 Introduction

Both line and continuum surveys have contributed to the important task of identification of starless cores. While dense gas tracers such as $C^{18}O$ and $H^{13}CO^+$ have been effective probes of dense cores and their kinematic behaviour, they also suffer from some shortcomings, such as line saturation due to high optical depth, excitation biases, and significant depletion due to molecular freeze-out toward core centres (see e.g., Caselli et al. 1999, Bacmann et al. 2002, and Chapter 2). Another key tracer of molecular clouds, submillimetre and millimetre dust emission in molecular clouds, has low opacities, no excitation biases, and is produced over a wide frequency range. The resulting sensitivity to low column densities has helped to reveal hundreds of compact continuum objects. Comparison with near- to far-infrared data, however, is necessary to find out if these objects are starless or protostellar. When it comes to the quality of the observational data, each tracer of molecular clouds has its own limitations. Molecular rotational line data suffer from coarser angular resolutions compared to that of infrared data due to the general longer wavelengths of the transitions excited in molecular clouds. On the other hand, submillimetre and millimetre continuum data may lack large-scale information due to the calibration methods used in these type of observations (chopping or sky background removal), while large-scale infor-

mation can be retained in molecular line data taken through position switching or frequency switching. The effectiveness of any method for the identification of starless cores ultimately depends on sensitivity and resolution of the data.

Evolved starless cores demonstrate certain chemical and dynamical characteristics, which can be used to probe their respective evolutionary stage. For example the relatively abundant CO molecule and its isotopologues are heavily depleted onto grain mantles toward the innermost regions of starless cores due to the high densities and low temperatures of these regions (e.g., see Bergin et al. 2001, Lai et al. 2003, and Young et al. 2004b). It is likely that the severity of depletion of a certain molecule depends on its respective binding energy onto dust grains. For example, nitrogen-bearing molecules are more resilient to depletion compared to carbon-bearing species. One of the main reasons suggested to explain their resilience to depletion is that in the initial stages of cloud formation, nitrogen is mainly found in the atomic form, which has a lower binding energy to the grain mantles and therefore does not adsorb to dust grains as effectively as CO. As the density increases, the N_2 molecule is formed as a result of neutral-neutral reactions between N atoms. Such a reaction happens significantly slower than the ion-neutral reaction that forms CO molecules. Therefore, while CO is heavily depleted, there are still N atoms available to maintain the formation of various nitrogen-bearing molecules. Also, CO is the main reactant of N_2H^+ and its depletion helps maintain the N_2H^+ abundance. Finally, the adsorption of N_2H^+ onto dust grains results in its recombination and return to the gas phase as N_2 and NH molecules, which are later transformed to NH_3 through other reactions. CO depletion in cold and dense starless cores leads to deuteration[1] enrichment as well. In molecular clouds, deuterium-bearing species such as H_2D^+ can be detected. At high densities and cold environments of cores, however, the abundance of such species increases as their main reactant, CO, is depleted. This effect leads to the propagation of deuteration to other species by chemical reactions and enhancement of deuterated isotopes such as N_2D^+ (see e.g., Bacmann et al. 2003; Crapsi et al. 2005a). These chemical evolutions provide us with a tool to gauge a core's respective evolutionary stage.

Dynamical characteristics of starless cores can also be used to reveal the evolutionary trend of these objects. As the core evolves and the accretion of material progresses, the innermost region of the core with flattened density profile becomes

[1]Deuterium is an isotope of hydrogen. The deuteron, nucleus of deuterium, contains one proton and one neutron, whereas the hydrogen nucleus contains no neutron.

smaller and more condensed, leading to the increasing H_2 density at smaller radii. The infall motion of material also alters the observed line profiles, causing them to broaden and depart from a Gaussian line profile. As explained previously (see Chapter 1 and Chapter 2), blue-asymmetry in the line profile, which is a signpost of inward motions, has also been detected toward many starless cores. These signatures are effective tracers of the relative evolutionary stage of starless cores.

Using the above criteria, we have selected five cores near or at the moment of collapse. This sample provides the exciting opportunity to use NH_3 data to improve our understanding of the initial conditions of collapse. The sample was selected from line and continuum surveys by Crapsi et al. (2005a) and Kauffmann et al. (2008) using several correlations between the chemical evolution indicators, such as:

- higher depletion factor of CO
- higher N_2H^+ column density
- higher N_2D^+ column density

and properties of dynamically evolved cores:

- higher H_2 column density
- broader N_2H^+ lines
- smaller flattened inner region
- stronger infall asymmetries

These cores are either starless and appear poised to collapse (L694-2, L429, and L1517B), or contain a VeLLO[2] where collapse may have just begun (L1521F and L1014).

In this chapter, we present single-dish observations of NH_3 (1,1) and (2,2) and N_2H^+ (1−0) emission lines as well as continuum emission at 250 μm toward five cores in our sample, L694-2, L429, L1517B, L1521F, and L1014. These data reveal the kinematic structure and (line-of-sight averaged) temperature distribution of these cores. In §3.2, we provide a short review of the results of previous studies on these cores. In §3.3, we explain the details of our observations and data reduction methods. We describe the morphologies of the observed molecular emission lines and compare them to that of the continuum emission in §3.4. §3.5 describes the analysis of the observed spectra toward each core. Finally, §3.6 summarizes our results.

[2]Objects with apparent protostellar nature but unusually low luminosity ($L < 0.1\ L_\odot$).

3.2 Previous Studies of Cores in Our Sample

3.2.1 L694-2

L694-2 is a roughly round-shaped core surrounded by filamentary structure and embedded in a small molecular cloud at a distance of 230 ± 30 pc (Kawamura et al. 2001). Figure 3.1 shows continuum emission at 250 μm toward L694-2 from Spectrometer and Imaging Receiver Array (SPIRE) photometer on Herschel. The core is isolated from molecular cloud complexes at the Galactic midplane and could be partially exposed to the warm and turbulent interstellar medium and not be completely shielded by cold quiescent environment of molecular clouds. L694-2 was first identified as starless by Lee & Myers (1999) using far infrared continuum data from Infrared Astronomical Satellite (IRAS).

There are various estimates for the central number density, mass, and radius of L694-2 reported in the literature, based on different datasets (molecular lines or continuum) or techniques. The central H_2 number density values reported are 1.1 × 10^5 cm^{-3} (using N_2H^+ spectra; Crapsi et al. 2005a), 2.2 × 10^5 cm^{-3} (using N_2D^+ spectra; Crapsi et al. 2005a), 9.0 × 10^5 cm^{-3} (using 1.2 mm continuum data; Crapsi et al. 2005a), and 3.1 × 10^5 cm^{-3} (using extinction data; Harvey et al. 2003a). Indeed, the estimation of a core mass depends on the number density and the choice of the core boundaries. For instance, the total mass estimations for L694-2 vary between 0.5 $M_\odot$ (using NH_3 data and assuming uniform gas density distribution inside a core radius of 0.08 pc; Levshakov et al. 2013), 1.0 $M_\odot$ (using N_2H^+ spectra and 850 μm continuum data and assuming a core radius of ∼ 0.05 pc; Williams et al. 2006), and 3.0 $M_\odot$ (using a BE sphere density profile with an outer radius of 0.15 ± 0.014 pc for the globule and using near-infrared extinction data; Harvey et al. 2003a). L694-2 has an ammonia core size of 0.08 pc (Levshakov et al. 2013).

L694-2 shows indications of infall asymmetry in emission spectra of DCO^+ (2−1) and CS (3−2) (Lee et al. 2004) and N_2H^+ (1−0) (Williams et al. 2006) and the infall velocities in the core have been estimated to be in the range of 0.05 km s^{-1} to 0.09 km s^{-1}. The v_{LSR} map of N_2H^+ (1−0) emission toward L694-2 shows C-shaped contours near the peak position (Williams et al. 2006), a possible signature of collapsing rotating cores (Walker et al. 1994; Narayanan et al. 1998; Narayanan et al. 2002). The rotation velocity of L694-2 is estimated to be slow and approximately 0.5 km s^{-1} pc^{-1} (Williams et al. 2006).

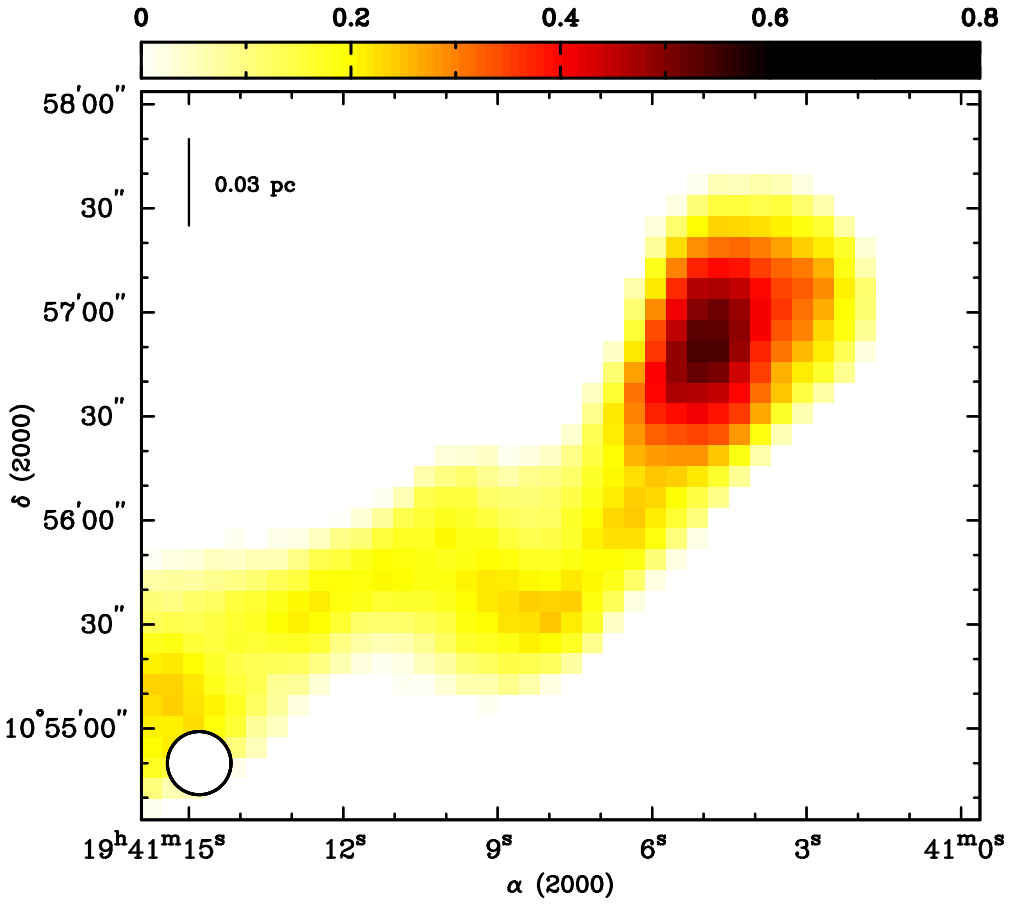

Figure 3.1: Continuum emission at 250 μm toward L694-2 obtained using Herschel-SPIRE. The data are in units of Jy beam^{-1}. The circle shows the size of the SPIRE beam with a geometric mean FWHM of $18\overset{''}{.}2$.

3.2.2 L1517B

L1517B is a starless core located in Taurus Molecular Cloud (TMC) at a distance of $\sim$ 140 pc (Elias 1978). Figure 3.2 shows continuum emission at 250 μm toward L1517B from Herschel-SPIRE. The kinetic temperature of L1517B is estimated to be approximately 9 K (e.g., Tafalla et al. 2002; Keto & Field 2005) and central number density values reported in the literature range between 2×10^5 cm^{-3} (e.g., Tafalla et al. 2002) and 5×10^5 cm^{-3} (Kirk et al. 2005). The estimated total mass values of L1517B vary from 0.5 $M_\odot$ (assuming a radius of 0.06 pc using NH_3 observations; Benson & Myers 1989) to 1.7 $M_\odot$ (by fitting 850 μm continuum data within a 150$''$ aperture using a BE profile; Kirk et al. 2005), and 3.89 $M_\odot$ (by adopting a general polytropic self-similar expanding envelope and collapsing core (EECC) hydrodynamic shock model to reproduce simultaneously continuum and several line profiles observed toward L1517B; Fu et al. 2011). Although, N_2H^+ emission spectra of L1517B appear to be Gaussian (Keto et al. 2004), red asymmetry has been detected in the HCN (1$-$0) spectra of the core (Sohn et al. 2007). L1517B may be experiencing the breathing mode of oscillation in cores (i.e., envelope expansion; Keto & Field 2005; Fu et al. 2011) while simultaneously collapsing at the centre (Fu et al. 2011).

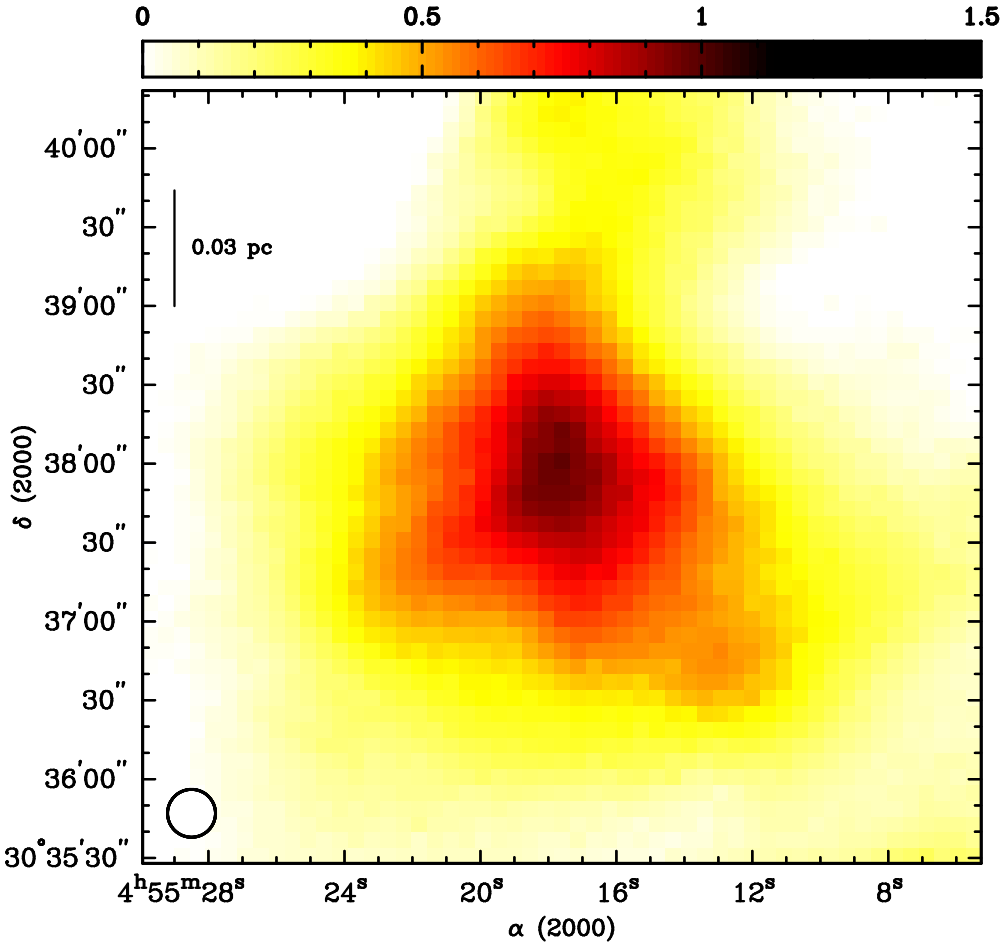

Figure 3.2: Continuum emission at 250 μm toward L694-2 obtained using Herschel-SPIRE. The data are in units of Jy beam^{-1}. The circle shows the size of the SPIRE beam with a geometric mean FWHM of $18\overset{''}{.}2$.

3.2.3 L429

L429 is a Bok globule in the Aquila Rift molecular cloud at a distance of 200 pc (Lee & Myers 1999). Figure 3.3 shows continuum emission at 250 μm toward L429 from Herschel-SPIRE. L429 shows red asymmetry (signature of expansion) in the N_2H^+ (1−0) spectra (Crapsi et al. 2005a) and in $F = 0-1$ and $F = 1-1$ hyperfine transitions of HCN (1−0) (Sohn et al. 2007). The $F = 2-1$ hyperfine transition of HCN (1−0), however, shows blue asymmetry indicating infall motions in the core. The hyperfine transitions of HCN (1−0) toward L429 are anomalous with $F = 0-1$ and $F = 2-1$ hyperfine lines having similar intensities. (Note that under LTE conditions, the three hyperfine lines of HCN (1−0) are expected to have relative intensities of $F(0-1) : F(1-1) : F(2-1) = 1 : 3 : 5$). This anomaly could be due to $F = 0-1$ having lower opacity compared to $F = 2-1$ and tracing deeper regions into the core (Cernicharo et al. 1984; Fuller et al. 1991). L429 is highly deuterated with $N(N_2D^+)/N(N_2H^+) = 0.28 \pm 0.05$ (Crapsi et al. 2005b). Deuteration is suggested to correlate with high central concentration and CO depletion (Crapsi et al. 2005b), implying that L429 is a highly evolved core.

Infrared images of the core obtained by Spitzer show an absorption feature at wavelengths shorter than 70 μm, which is likely a result of high concentration of material at the core centre (Stutz et al. 2009). L429 is suggested to have a very compact structure and concentrated density profile. The narrow observed line widths toward the core suggest that thermal pressure or turbulence do not provide adequate support against gravitational collapse and the magnetic field required to provide sufficient support needs to be surprisingly large. Stutz et al. (2009), therefore, suggest that L429 is currently either experiencing or on the verge of collapse.

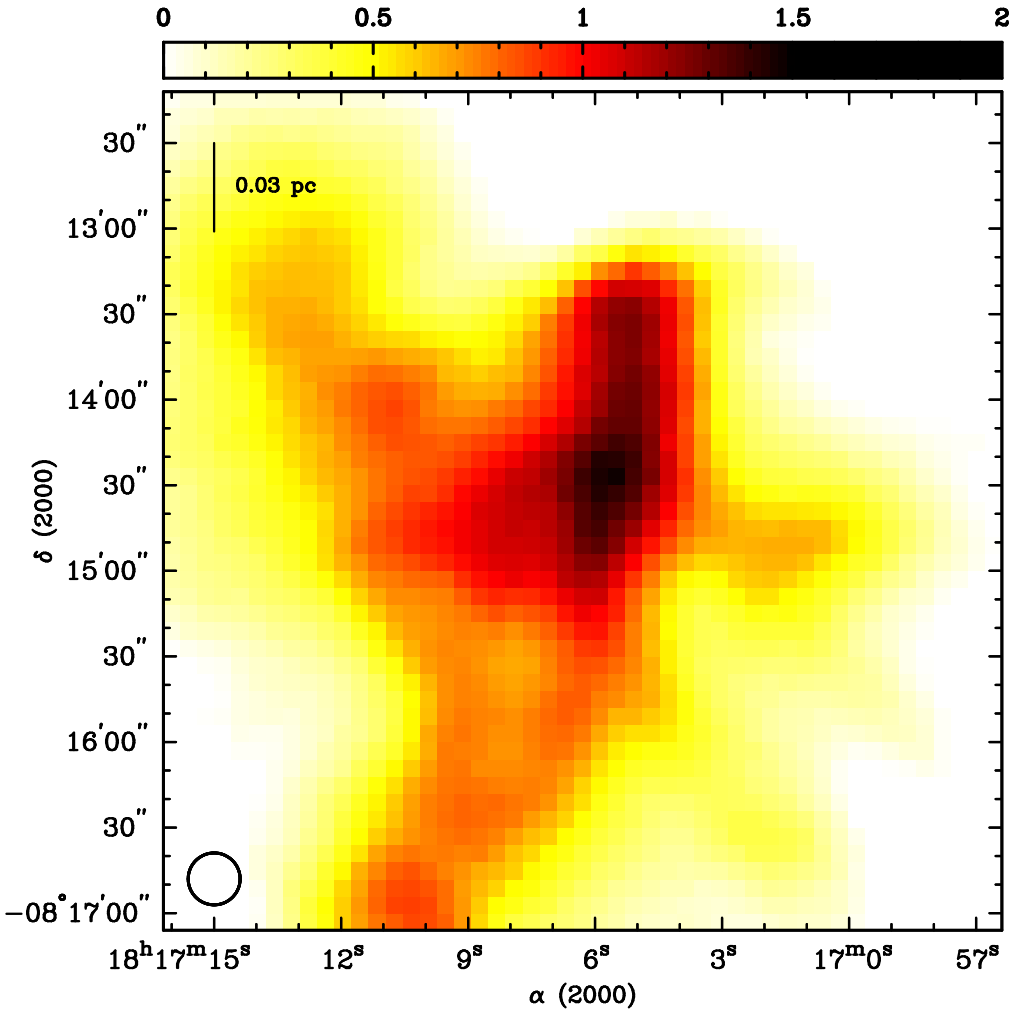

Figure 3.3: Continuum emission at 250 μm toward L429 obtained using Herschel-SPIRE. The data are in units of Jy beam^{-1}. The circle shows the size of the SPIRE beam with a geometric mean FWHM of $18\overset{''}{.}2$.

3.2.4 L1014

L1014 is a dense core in Cygnus at a distance of 258 ± 50 pc (Maheswar et al. 2011). Figure 3.4 shows continuum emission at 250 μm toward L1014 from Herschel-SPIRE. Due to lack of any associated outflow and not having been detected by IRAS, Visser et al. (2002) identified L1014 as a starless core. Later on, Young et al. (2004a), using Spitzer data of the core, detected the presence of a substellar object, L1014-IRS, with very low luminosity ($\sim$ 0.09 $L_\odot$) inside the dark cloud L1014. Young et al. (2004a) suggested that L1014-IRS is surrounded by an envelope of mass $\sim$ 1.7 $M_\odot$ and disk-like components and the central object is likely to grow to higher masses if the accretion continues.

To study further the molecular environment of L1014-IRS, the lowest luminosity isolated protostar known at the time, Crapsi et al. (2005b) observed emission spectra from various molecular species toward L1014. The data suggested that physical and chemical properties of L1014 resemble that of a "moderately evolved" dense core with central H_2 number density of 2.5×10^5 cm^{-3} and total mass $\sim$ 2 $M_\odot$. L1014 appears to be highly deuterated with $N(N_2D^+)/N(N_2H^+) \sim 10\%$ and shows a very compact N_2H^+ emission region (radius $\sim$ 0.03 pc). No signatures of infall or outflow were detected by Crapsi et al. (2005b), however. Bourke et al. (2005) discovered a compact ($\sim$ 500 AU), low-mass ($< 10^{-4}$ $M_\odot$), and low velocity ($<$ 4 km s^{-1}) bipolar outflow[3] associated with L1014-IRS by searching for emission spectra of CO (J = 2−1) using Submillimetre Array (SMA). Radio continuum emission observations toward L1014 suggest that L1014-IRS is not a very young protostar but an extremely low luminosity object that has been undergoing accretion for the past several thousand years and is currently in a low accretion mode (Shirley et al. 2007).

[3]A continuous or episodic discharge of gas from a protostar or stellar object.

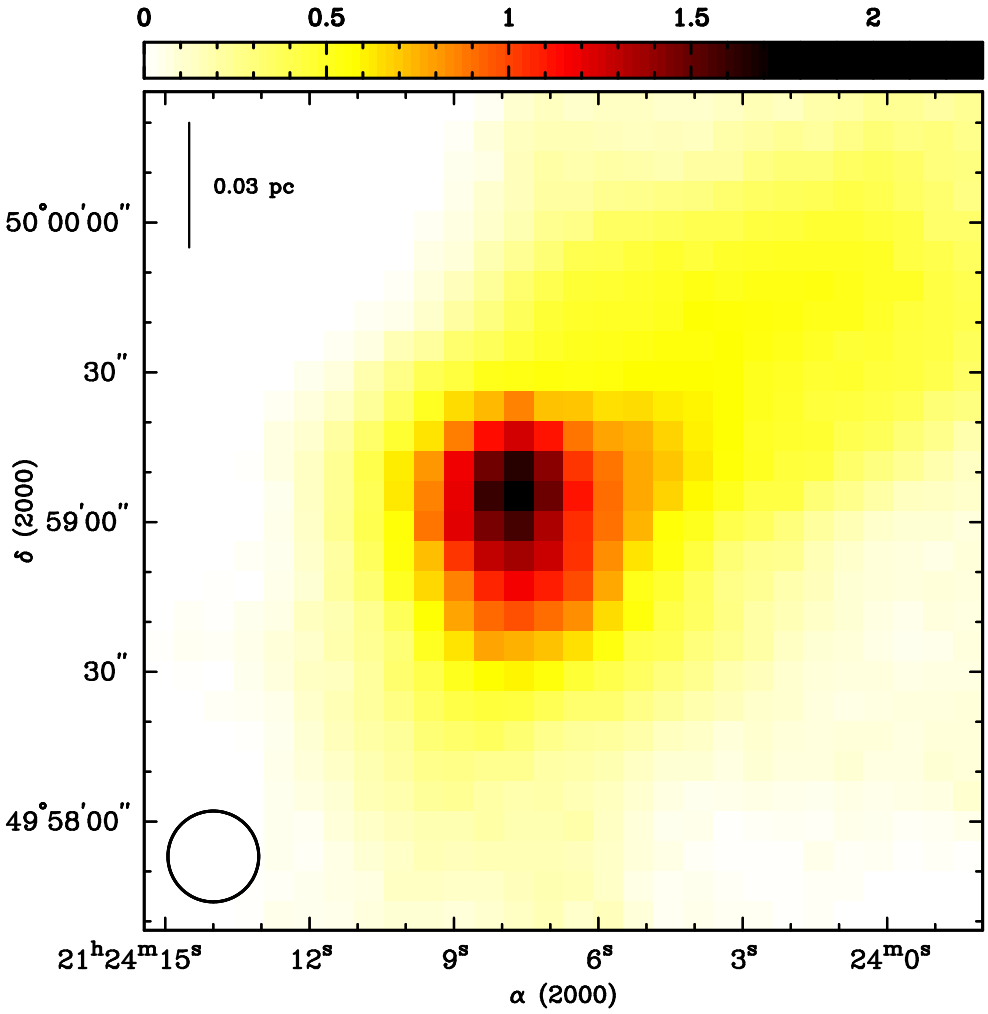

Figure 3.4: Continuum emission at 250 μm toward L1014 obtained using Herschel-SPIRE. The data are in units of Jy beam^{-1}. The circle shows the size of the SPIRE beam with a geometric mean FWHM of $18\overset{''}{.}2$.

3.2.5 L1521F

L1521F is a condensation in TMC. Figure 3.5 shows continuum emission at 250 μm toward L1521F from Herschel-SPIRE. It was first identified as "starless" using Palomar Observatory Sky Survey (POSS) maps and the NH_3 survey of TMC by Myers et al. (1979). The distance to L1521F has recently been estimated to be 136 $\pm$ 36 pc (Maheswar et al. 2011). The core was later discovered to host a VeLLO object, L1521F-IRS with $L < 0.07\ L_{\odot}$ (Bourke et al. 2006) using observations from the Spitzer Space Telescope at mid-infrared wavelengths ($> 5\ \mu$m). An outflow associated with L1521F-IRS was first identified by Takahashi et al. (2013) using interferometric observations of ^{12}CO (2−1) emission spectra and 1.3 mm continuum emission using the SMA. The outflow appears to be compact but poorly collimated. The outflow characteristics (i.e., mass, velocity, and momentum) are lower compared to the physical parameters of outflows associated with low mass or high mass star forming regions. Takahashi et al. (2013) suggest that the outflow is a remnant of the first hydrostatic core and an undeveloped outflow associated with the protostar. The low bolometric luminosity of L1521F-IRS (0.034 - 0.05 $L_{\odot}$; Bourke et al. 2006; Terebey et al. 2009) and the small size of its associated outflow lobes suggest that L1521F-IRS is at least an order of magnitude younger than Class 0 protostars (i.e., younger than 10^4 years) and has a substellar mass. It is suggested that L1521F is currently in the low activity mode of an episodic (i.e., non-steady) accretion (Takahashi et al. 2013).

L1521F shows indications of infall in various molecular emission lines such as HCO^+ (3−2) and (4−3) (Onishi et al. 1999) and CS (2−1) (Lee et al. 1999). Onishi et al. (1999) estimated the infall velocity in L1521F to be ~ 0.2 km s^{-1} - 0.3 km s^{-1}. Interferometric observations of N_2H^+, CCS, and continuum emission toward L1521F by Shinnaga et al. (2004) reveal the clumpy structure of the core and suggest that the outer envelope of the core (size ≤ 0.08 pc; traced by CCS emission) is rotating in the opposite sense of the core central compact region (size ≤ 0.03 pc; traced by N_2H^+ emission). The deuteration level of L1521F ($N(N_2D^+/N(N_2H^+)$) has been measured to be ~ 0.1 (Crapsi et al. 2004; Schnee et al. 2013). The central number density of L1521F is estimated to be $\sim 1.0 \times 10^6$ cm^{-3} (e.g., Onishi et al. 1999; Crapsi et al. 2004). Some of the estimations of L1521F total mass in the literature are: 3 $M_{\odot}$ (assuming a radius of 0.1 pc; Onishi et al. 1999), 1.51 $\pm$ 0.02 $M_{\odot}$ (using 850 μm continuum data; Shinnaga et al. 2004), 5.5 $\pm$ 0.5 $M_{\odot}$ (using 1.2 mm continuum data; Crapsi et al. 2004).

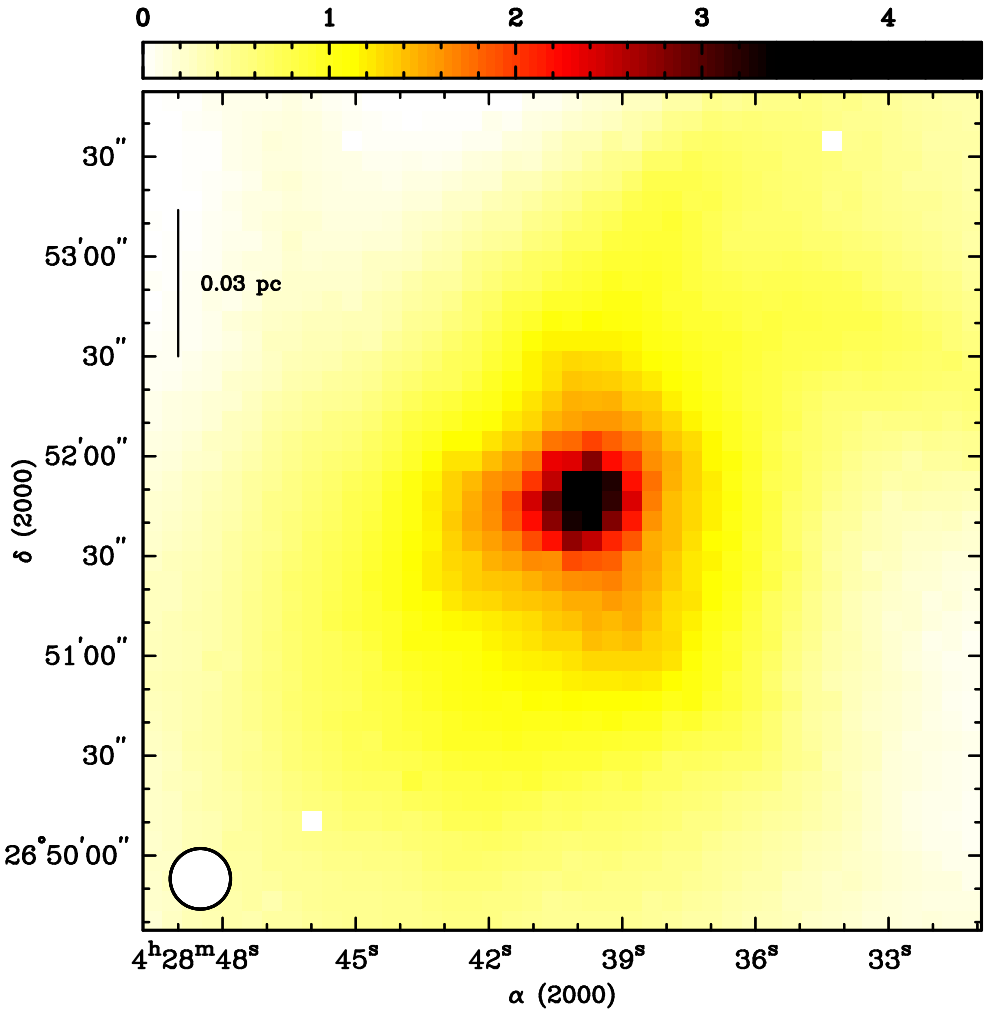

Figure 3.5: Continuum emission at 250 μm toward L1521f obtained using Herschel-SPIRE. The data are in units of Jy beam^{-1}. The circle shows the size of the SPIRE beam with a geometric mean FWHM of $18\overset{''}{.}2$.

3.3 Observations and Data Reduction

We mapped the five cores in our sample in molecular emission of NH_3 (1,1), NH_3 (2,2), and N_2H^+ (1−0). We also use continuum emission maps of these cores at 250 μm acquired with Herschel-SPIRE. We describe our observation strategy and data reduction method for each dataset below.

3.3.1 Green Bank Telescope

Single-dish observations of the NH_3 (J, K) = (1,1) and (2,2) emission lines at respective frequencies of 23.694495 GHz and 23.722633 GHz (Ho & Townes 1983) toward the cores in our sample were acquired using the 100-m diameter Robert C. Byrd GBT, located near Green Bank, WV, USA in March 2011. The observing strategy and data reduction process are similar to the methods described in §2.2.1. Table 3.1 lists the coordinates of off-positions, map sizes, and the final 1 σ rms sensitivities for each core. Peak positions and peak intensities of the main hyperfine component for NH_3 (1,1) and (2,2) emission lines are listed in Tables 3.2 and 3.2.

Table 3.1: Coordinates of off-positions for GBT and NRO observations

Core	R.A. J2000	Decl. J2000	map radius (arcmin)	rms[a] (K)
L1521F	04 28 39.1	27 06 35.7	$10'$	0.1
L1517B	04 55 18.3	30 52 47	$7'$	0.1
L429	18 17 05.8	−07 59 05.3	$6'$	0.3
L694-2	19 41 04.5	11 12 02.3	$6'$	0.1
L1014	21 24 07.5	50 13 59.5	$7'$	0.1

[a]The final 1 σ rms sensitivities of the central regions of the original maps where the targets are located are given on the main beam temperature (T_{mb}) scale per 0.04 km s^{-1} velocity channel.

Table 3.2: Peak positions and peak intensities of NH_3 (1,1) emission maps toward the cores in the sample.

Core	R.A. J2000	Decl. J2000	T_{mb} (K)
L1521F	04 28 39.3	26 51 42	6.67
L1517B	04 55 18.0	30 37 47	6.61
L429	18 17 05.6	−08 13 36	8.12
L429-E[a]	18 17 13.3	−08 13 30	5.29
L694-2	19 41 04.6	10 57 00	5.11
L1014	21 24 06.4	49 58 54	1.24

[a]L429-E is the emission region detected east of L429 (see Figure 3.8a).

Table 3.3: Peak positions and peak intensities of NH_3 (2,2) emission maps toward the cores in the sample.[a]

Core	R.A. J2000	Decl. J2000	T_{mb} (K)
L1521F	04 28 38.4	26 51 48	1.31
L1517B	04 55 17.5	30 37 47	1.62
L429	18 17 05.2	−08 13 42	1.64
L694-2	19 41 04.6	10 56 48	0.83

[a]The peak positions of NH_3 (2,2) emission toward L1014 and L429-E are not given due to the faintness of the emission toward these regions.

3.3.2 Nobeyama 45 m Radio Telescope

Single-dish observations of the N_2H^+ (J = 1−0) emission line toward four cores (L1517B, L429, L694-2, and L1014) were carried out using the NRO 45-m Telescope in Nobeyama, Japan in April 2011 (Note that L1521F was not observed using NRO). The observing strategy and data reduction process are similar to the methods described in §2.2.2. We used the same off-positions as used for the GBT observations (see Table 3.1). The final 1 σ rms sensitivities are listed in Table (3.4).

Table 3.4: Peak positions, peak intensities, original map size, and rms sensitivity of N_2H^+ (J = 1−0) emission maps toward the cores in the sample.

Core	R.A. J2000	Decl. J2000	T_{mb} (K)	map size	rms[a] (K)
L1517B	04 55 16.4	30 37 31	1.4	$4' \times 4'$	0.1
L429	18 17 05.5	−08 13 36	1.8	$2' \times 2'$	0.1
L429-E[b]	18 17 13.5	−08 13 28	1.0	...	...
L694-2	19 41 04.7	10 57 14	2.0	$2' \times 2'$	0.1
L1014	21 24 08.1	49 58 58	0.5	$3' \times 3'$	0.1

[a]The final 1 σ rms sensitivities are given on the T_{mb} scale per 0.05 km s^{-1} velocity channel.
[b]L429-E is the emission region detected east of L429 (see Figure 3.8c).

3.3.3 Herschel Space Observatory

In this analysis, we use 250 μm continuum emission data of the cores in our sample. The cores L1521F and L1517B, located in Taurus filaments and satellite regions, were observed using Spectrometer and Imaging Receiver Array (SPIRE) photometer on Herschel as part of Herschel GBS (André et al. 2010; Ladjelate et al. 2014, in prep). The data products for L1521F and L1517B were provided by the Herschel GBS archive[4]. For detailed information on the acquisition and reduction of these data, see Kirk et al. (2013).

GBS observations do not include L694-2, L429, and L1014. Therefore, we use 250 μm continuum emission data of these cores taken by Herschel-SPIRE as part of a Herschel Open Time (OT1) project led by S. Schnee (Project ID: OT1-sschnee-1). Photometer maps of the three cores were observed at the short (PSW), medium (PMW) and long (PLW) wavelengths corresponding to 250 μm, 350 μm, and 500 μm (Griffin et al. 2010). SPIRE provides three different observing modes for the photometer: large area maps, small area maps, and point source photometry. All three cores were observed in the small area mapping mode using two short cross-scans. All photometer maps were retrieved from Herschel archive.

The Herschel 250 μm beam is slightly elliptical ($18\overset{''}{.}7 \times 17\overset{''}{.}5$) with a geometric mean FWHM of $18\overset{''}{.}2$. To focus on the flux density corresponding to the core, we removed the Planck-derived offset that was added to Herschel GBS archive image. Also, to remove completely the background continuum emission from each core's immediate environment, we follow the method described in 2.2.4 to calculate and subtract the average continuum emission from the pixels outside of each core. Tables 3.5 and 3.6 list the location of the continuum emission peak and the corresponding 1 σ rms sensitivities for each core in $18\overset{''}{.}2$ FWHM and $32\overset{''}{}$ FWHM spatial resolutions, respectively. For each core, the Planck-derived offset at 250 μm is listed in Table 3.5.

[4]http://gouldbelt-herschel.cea.fr/archives

Table 3.5: Peak positions, rms sensitivities, and Planck-derived offsets for the 250 μm continuum data from Herschel/SPIRE for a 18$''$.2 FWHM beam.

Core	R.A.	Decl.	rms[a]	Planck offset
	J2000	J2000	K	MJy Sr^{-1}
L1521F	04 28 39.0	26 51 35	0.02	37.28
L1517B	04 55 17.5	30 37 58	0.01	35.94
L429	18 17 05.5	−08 14 27	0.02	109.77
L694-2	19 41 05.1	10 56 49	0.02	67.17
L1014	21 24 07.7	49 59 05	0.02	118.80

Table 3.6: Peak positions and rms sensitivities for the 250 μm continuum data from Herschel/SPIRE for a 32$''$ FWHM beam.

Core	R.A.	Decl.	rms
	J2000	J2000	Jy beam^{-1}
L1521F	04 28 39.3	26 51 36	0.04
L1517B	04 55 17.5	30 37 53	0.02
L429	18 17 06.0	−08 14 30	0.04
L694-2	19 41 04.6	10 56 54	0.05
L1014	21 24 07.7	49 59 00	0.04

3.4 Results

Figures 3.6 through 3.10 show the integrated intensity maps of the observed emission lines toward the cores in our sample. The integrated intensity maps were made by summing over the entire emission spectrum including all hyperfine components, but excluding channels with emission lower than twice the corresponding map rms noise level. The overlaid contours correspond to the background-subtracted continuum emission at 250 μm observed with Herschel-SPIRE. (Note again that the N_2H^+ data of L1521F were not acquired.) Also, the NH_3 (2,2) emission line was not detected toward L1014, therefore a corresponding integrated intensity map is not presented.

L1521F: The NH_3 emission toward L1521F is compact and the integrated intensity has a single maximum in both transitions, with the overall morphology matching

that of the continuum emission very closely (Figures 3.6a and 3.6b). The maximum of the NH_3 (1,1) integrated intensity coincides with the maximum of continuum emission, while the maximum of the NH_3 (2,2) emission is offset toward west by only 18″.

L1517B: The morphologies of the integrated intensity maps of NH_3 (1,1) and (2,2) emission closely follow that of the 250 μm continuum emission. Both integrated intensities are single peaked with maxima located within only 9″ from that of the continuum emission toward the south (Figures 3.7a and 3.7b). The integrated intensity of the N_2H^+ (1−0) transition also coincides with the continuum emission. It, however, appears to be double-peaked with one of the maxima close to that of the continuum emission and the second offset by 32″ toward the SW (Figure 3.7c).

L429: The structure of L429 is certainly the most complicated among the cores in our sample. The overall morphology of NH_3 (1,1) and NH_3 (2,2) integrated intensities toward L429 resemble that of the continuum emission. NH_3 (1,1) emission shows two peaks. The brighter and fainter peaks are offset from the peak of continuum emission by $\sim 1^{'}$ and $\sim 2^{'}$ toward the north and east, respectively (Figures 3.8a and 3.8b). We refer to the emission region on the east of L429, as L429-E. Similarly to NH_3 (1,1) emission, the integrated intensity of N_2H^+ emission also matches the morphology of continuum emission with two maxima $\sim 1^{'}$ and $\sim 2^{'}$ north and east of the continuum emission peak (Figure 3.8c).

L694-2: It is evident from the 250 μm continuum contours of L694-2 that the core is embedded in a larger filament of dust and gas. The morphologies of the integrated intensity maps of NH_3 (1,1) and (2,2) toward L694-2 closely match that of the 250 μm continuum emission with the integrated intensity maxima located very close to that of the continuum emission (Figures 3.9a and 3.9b). Although, the overall structure of the integrated intensity map of the N_2H^+ (1−0) emission toward L694-2 follows that of the continuum emission, the N_2H^+ emission peak is offset from that of the continuum by 25″ (Figures 3.9c).

L1014: Both NH_3 (1,1) and N_2H^+ (1−0) emission toward L1014 are much fainter compared to the rest of the sources in our sample. Also, the NH_3 (2,2) emission was not detected in our observations toward L1014. The overall morphologies of the integrated intensities of NH_3 (1,1) and N_2H^+ (1−0) emission lines are compact and single-peaked and follow the shape of the 250 μm continuum emission closely (Figures 3.10a and 3.10b). The NH_3 (1,1) integrated intensity peaks 14″ away from the continuum maximum toward the SW. The maximum of the N_2H^+ (1−0) integrated

intensity is located 9″ away from the continuum peak toward the SE.

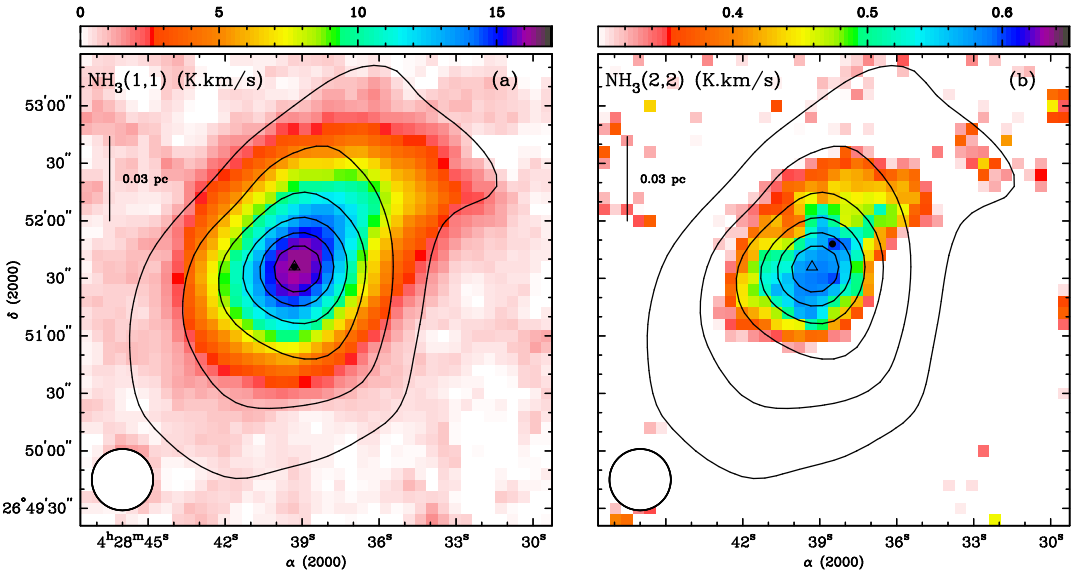

Figure 3.6: Integrated intensity maps of NH_3 (1,1) (*a*) and NH_3 (2,2) (*b*) emission toward L1521F. The colour scale is in K km s^{-1}. The contours correspond to dust continuum emission at 250 μm. In panels both panels, the resolution of the continuum data has been smoothed to that of the GBT data, $\sim 32''$ FWHM, and the contours start at 1.0 Jy $beam^{-1}$ and increase in steps of 1.0 Jy $beam^{-1}$. In both panels, the black dot shows the peak of the integrated intensity of the corresponding molecular emission and the triangles show the peaks of the continuum emission. The circle delineates the size of the corresponding beam. Note that the N_2H^+ data of L1521F have not been acquired.

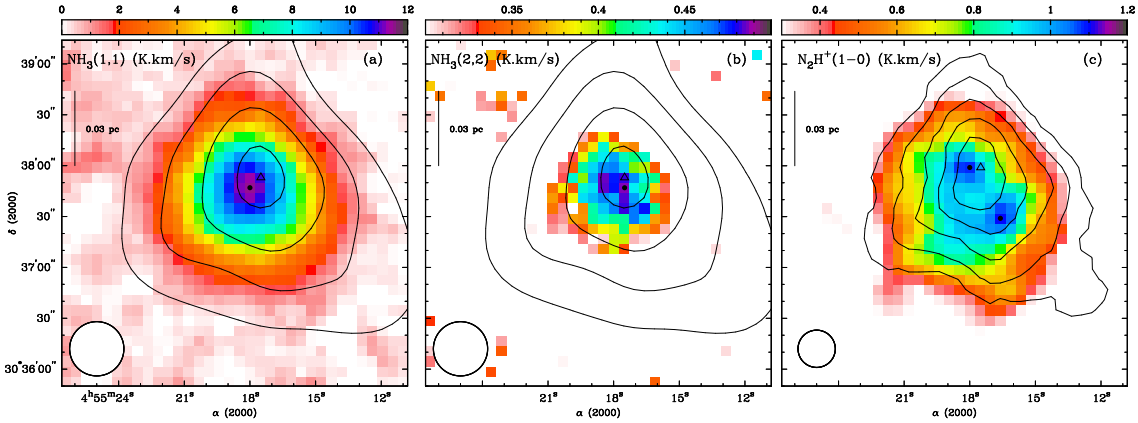

Figure 3.7: Integrated intensity maps of NH_3 (1,1) (a), NH_3 (2,2) (b), and N_2H^+ (1−0) (c) emission toward L1517B. The colour scale is in K km s^{-1}. The contours correspond to dust continuum emission at 250 μm. In panels (a) and (b), the resolution of the continuum data has been smoothed to that of the GBT data, $\sim 32''$ FWHM, and the contours start at 0.5 Jy beam^{-1} and increase in steps of 0.5 Jy beam^{-1}. In panel (c), the resolution of the continuum data has been smoothed to that of the NRO data, $\sim 22''.9$ FWHM, and the contours start at 0.5 Jy beam^{-1} and increase in steps of 0.1 Jy beam^{-1}. In all panels, the triangles show the peaks of the continuum emission and the black dots show the peak position of the corresponding continuum emission. The circle delineates the size of the corresponding beam. The positions of the continuum and molecular emission peaks are determined separately for each resolution.

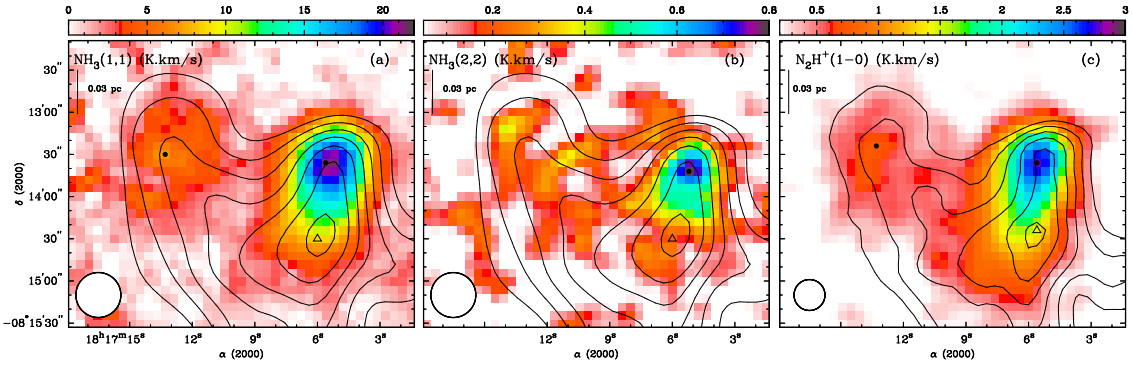

Figure 3.8: Integrated intensity maps of NH_3 (1,1) (a), NH_3 (2,2) (b), and N_2H^+ (1−0) (c) emission toward L429. The colour scale is in K km s^{-1}. The contours correspond to dust continuum emission at 250 μm. In panels (a) and (b), the resolution of the continuum data has been smoothed to that of the GBT data, $\sim 32''$ FWHM, and the contours start at 0.5 Jy beam^{-1} and increase in steps of 0.5 Jy beam^{-1}. In panel (c), the resolution of the continuum data has been smoothed to that of the NRO data, $\sim 22''.9$ FWHM, and the contours start at 0.4 Jy beam^{-1} and increase in steps of 0.2 Jy beam^{-1}. In all panels, the triangles show the peaks of the continuum emission and the black dots show the peak position of the corresponding continuum emission. The circle delineates the size of the corresponding beam. The positions of the continuum and molecular emission peaks are determined separately for each resolution.

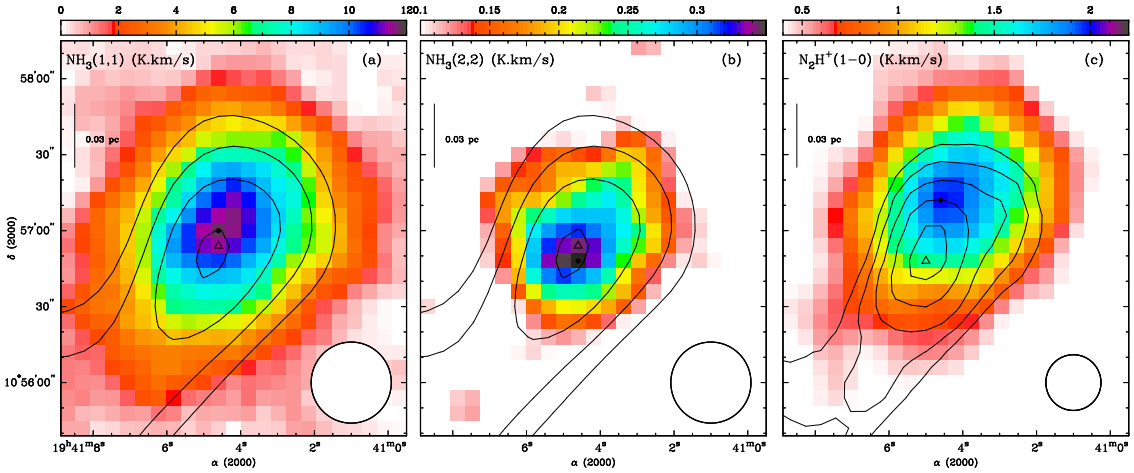

Figure 3.9: Integrated intensity maps of NH_3 (1,1) (a), NH_3 (2,2) (b), and N_2H^+ (1−0) (c) emission toward L694-2. The colour scale is in K km s^{-1}. The contours correspond to dust continuum emission at 250 μm. In panels (a) and (b), the resolution of the continuum data has been smoothed to that of the GBT data, $\sim 32''$ FWHM, and the contours start at 0.05 Jy $beam^{-1}$ and increase in steps of 0.5 Jy $beam^{-1}$. In panel (c), the resolution of the continuum data has been smoothed to that of the NRO data, $\sim 22''.9$ FWHM, and the contours start at 0.1 Jy $beam^{-1}$ and increase in steps of 0.1 Jy $beam^{-1}$. In all panels, the triangles show the peaks of the continuum emission and the black dots show the peak position of the corresponding continuum emission. The circle delineates the size of the corresponding beam. The positions of the continuum and molecular emission peaks are determined separately for each resolution.

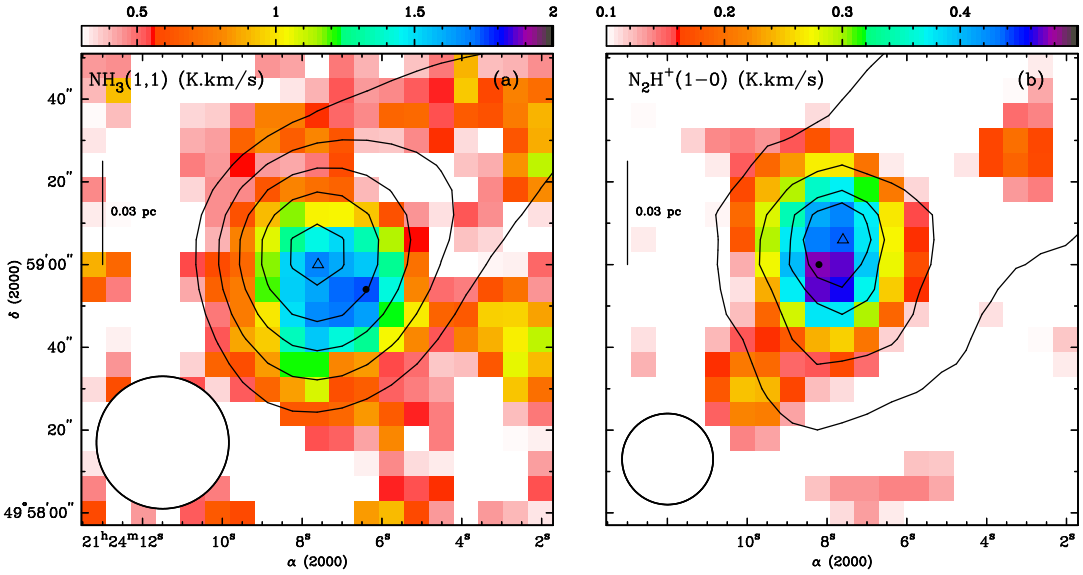

Figure 3.10: Integrated intensity maps of NH_3 (1,1) (a) and N_2H^+ (1−0) (b) emission toward L1014. The colour scale is in K km s^{-1}. The contours correspond to dust continuum emission at 250 μm. In panels (a) and (b), the resolution of the continuum data has been smoothed to that of the GBT data, $\sim 32''$ FWHM, and the contours start at 0.5 Jy $beam^{-1}$ and increase in steps of 0.5 Jy $beam^{-1}$. In panel (c), the resolution of the continuum data has been smoothed to that of the NRO data, $\sim 22''.9$ FWHM, and the contours start at 0.4 Jy $beam^{-1}$ and increase in steps of 0.4 Jy $beam^{-1}$. In all panels, the triangles show the peaks of the continuum emission and the black dots show the peak position of the corresponding continuum emission. The circle delineates the size of the corresponding beam. The positions of the continuum and molecular emission peaks are determined separately for each resolution. Note that NH_3 (2,2) emission line was not detected toward L1014.

3.5 Line Analysis

For each of the observed molecular transitions, the local standard of rest line centroid velocity (v_{LSR}), observed velocity dispersion (σ_v), and line intensity were determined by fitting ensembles of Gaussians appropriate for each line. A detailed description of our fitting procedure is included in §2.4. Although some of the cores in our sample show small asymmetries in the line profiles of NH_3 (1,1) and N_2H^+ (1−0), the line profiles do not significantly depart from Gaussians, and therefore we only fit the lines using Gaussian profiles. We describe the results of fitting the observed emission lines toward each core below.

3.5.1 NH_3

For the brighter cores in our sample, i.e., L1521F, L1517B, and L694-2, we restricted our analysis of the NH_3 (1,1) and (2,2) data to pixels where the main NH_3 (1,1) component has a SNR higher than 10. For L429, with relatively fainter NH_3 emission, we restricted the analysis to pixels where the main NH_3 (1,1) component has a SNR higher than 6. Since NH_3 (2,2) line emission was not detected toward L1014, we do not present any further analysis on that core. Weighted means and median errors of the returned parameters (v_{LSR}, Δv, τ, and T_{ex}) from the HFS fits are shown in Table 3.7 for all four cores. Note that the reported observed line widths (Δv) in Table 3.7 are corrected for the artificial broadening by the instrumental velocity resolution (see §2.4.1). For each core, we used the best fit parameters and the corresponding 250 μm continuum map to determine some of its physical characteristics, such as T_K, $N(H_2)$, σ_T, σ_{NT}, σ_{NT}/c_s, $N(NH_3)$, and $X(NH_3)$. The details of these calculations can be found in §2.4.1. The weighted means and median errors for each of the parameters are listed in Tables 3.8 and 3.9.

Table 3.7: The weighted mean values of the fitting parameters of NH_3 (1,1) spectral line emission toward four cores. The values inside the brackets are the median errors.

Core	v_{LSR} (km s^{-1})	Δv (km s^{-1})	τ	T_{ex} (K)
L1521F	6.373 (0.002)	0.251 (0.004)	10.4 (0.4)	7.8 (0.1)
L1517B	5.652 (0.002)	0.195 (0.004)	8.9 (0.4)	8.1 (0.2)
L429	6.561 (0.008)	0.41 (0.02)	6.4 (0.6)	8.0 (0.2)
L429-E	6.727 (0.009)	0.25 (0.02)	2.8 (0.9)	7 (1)
L694-2	9.335 (0.003)	0.288 (0.005)	10.0 (0.5)	6.3 (0.1)

Table 3.8: The weighted mean values of T_K and $N(H_2)$ of four cores determined using the fitting parameters of the observed NH_3 emission spectra. The values inside the brackets are the median errors.

Core	T_K (K)	$N(H_2)$ ($/10^{21}$ cm^{-2})
L1521F	9.3 (0.3)	16.8 (0.7)
L1517B	9.8 (0.4)	6.7 (0.6)
L429	9.2 (0.8)	9 (1)
L429-E	10 (1)	3.6 (0.8)
L694-2	9.0 (0.4)	6.6 (0.7)

Table 3.9: The weighted mean values of the physical properties of four cores determined using the fitting parameters of the observed NH_3 emission spectra. The values inside the brackets are the median errors.

Core	σ_T (km s^{-1})	σ_{NT} (km s^{-1})	σ_{NT}/c_s	$N(NH_3)$ ($/10^{15}$ cm^{-2})	$X(NH_3)$ ($/10^{-7}$)
L1521F	0.067 (0.001)	0.091 (0.003)	0.48 (0.02)	1.2 (0.8)	0.7 (0.2)
L1517B	0.069 (0.001)	0.046 (0.004)	0.25 (0.03)	0.8 (0.5)	1.0 (0.4)
L429	0.067 (0.003)	0.16 (0.01)	0.9 (0.1)	1.3 (0.9)	0.7 (0.4)
L429-E	0.071 (0.004)	0.09 (0.01)	0.5 (0.1)	0.4 (0.1)	0.6 (0.3)
L694-2	0.066 (0.001)	0.104 (0.004)	0.58 (0.03)	1.2 (0.6)	1.5 (0.5)

L1521F: The v_{LSR} map of L1521F (Figure 3.11a) shows a complex distribution. Indeed, the observations and modelling of N_2H^+ and and CCS emission lines toward L1521F by Shinnaga et al. (2004) suggest that the core has a clumpy structure with its central part rotating in the opposite direction of the core envelope. L1521F is a highly centrally concentrated core with relatively colder temperatures detected toward the central region (Figures 3.11b and 3.11c). The velocity dispersion in L1521F appears to be more turbulent toward the south-western part of the core and grows to be more quiescent toward the northern and eastern regions (Figure 3.11e). Figure 3.11f shows that the core is dominated by thermal velocity dispersion, however. Our measurement of σ_{NT}/c_s is less than unity over the entire region, implying that the core is entirely subsonic.

L1517B: The v_{LSR} map of NH_3 (1,1) emission line toward L1517B shows a clear gradient in the east-west direction (Figure 3.13a), which could indicate rotational motions in the core. The core shows relatively lower temperatures and a higher concentration of column density toward the centre (Figures 3.13b and 3.13c). L1517B is not as centrally compact as some of the other cores in our sample, however (e.g., see $N(H_2)$ map of L1521F, Figure 3.11c). L1517B appears to be a quiescent core with lower σ_{NT} toward the core centre and increasing non-thermal velocity dispersions toward the outer regions, especially toward the northern and western edges of the core (see Figure 3.13e). This interpretation is also bolstered by the low σ_{NT}/c_s toward the core centre (Figure 3.13f). The non-thermal velocity dispersion σ_{NT} appears to be lower than the thermal sound speed over the entire core, suggesting that the core is entirely subsonic.

L429 and L429-E: The v_{LSR} map of NH_3 (1,1) clearly shows that L429 is at a lower v_{LSR} compared to L429-E (Figure 3.15a). A decrease in T_K toward the centre of L429 is evident in Figure 3.15b and core appears to be more centrally concentrated with higher H_2 column density compared to the adjacent region L429-E (Figure 3.15c). L429 is more turbulent than L429-E (Figure 3.15e) and appears transonic (i.e., $\sigma_{NT}/c_s \sim 1$), while the adjacent region, L429-E, is dominated by subsonic motions (Figure 3.15f).

L694-2: The v_{LSR} map of NH_3 (1,1) emission line toward L694-2 shows C-shaped contours of constant velocity near the peak of the corresponding emission line. This feature is reproduced by radiative transfer modelling of collapsing rotating cores by Walker et al. (1994) and has been described as a signature of a dense core with uniform rotation and increasing infall speed toward the centre (Figure 3.17a). The

core is moderately centrally concentrated and shows colder temperatures toward the centre (Figures 3.17b and 3.17c). Although the core appears to be more turbulent toward the eastern regions (Figure 3.17e), our measurement of $\sigma_{NT}/c_s < 1$ over the entire core, suggesting that the core is entirely subsonic (Figure 3.17f).

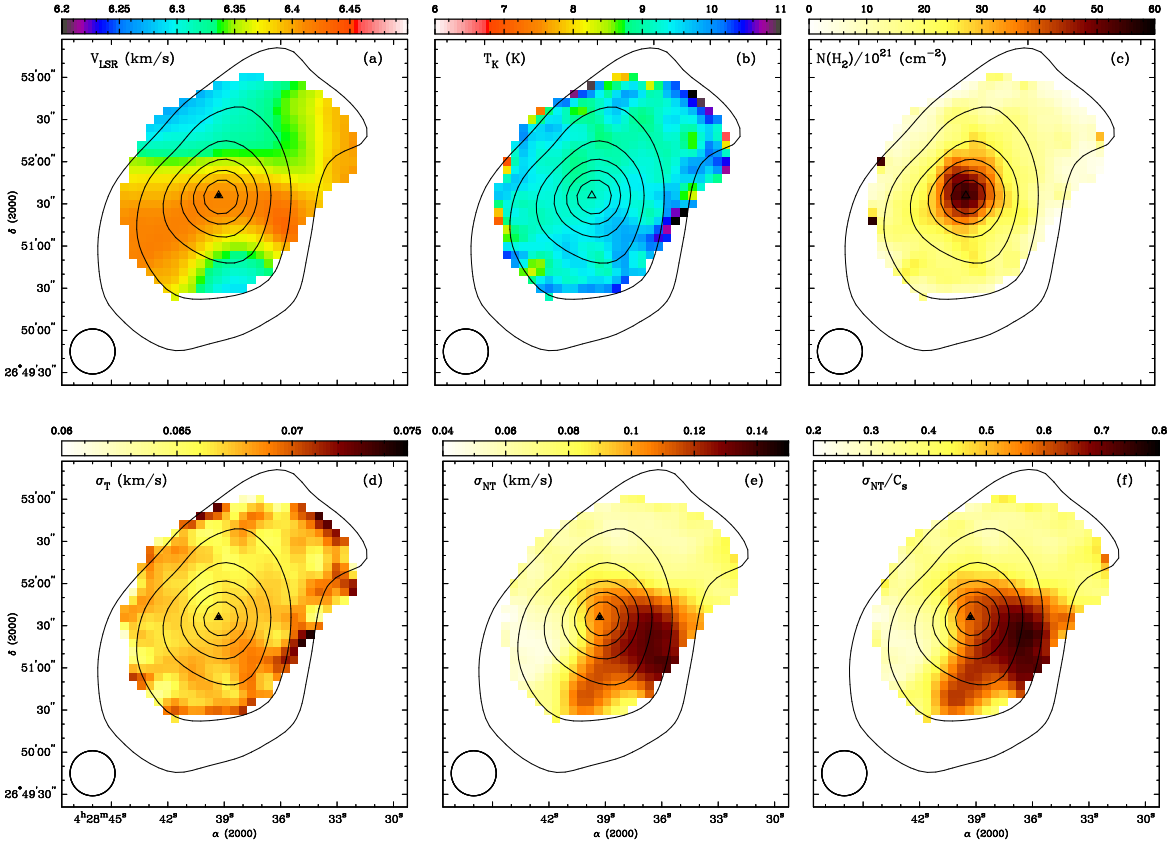

Figure 3.11: Maps of (a) v_{LSR}, (b) T_K, (c) $N(\mathrm{H_2})$, (d) σ_T, (e) σ_{NT}, and (f) σ_{NT}/c_s calculated using NH_3 (1,1) emission toward L1521F at 32″ FWHM. The contours correspond to continuum emission at 250 μm, starting at 1.0 Jy beam^{-1} and increase in steps of 1.0 Jy beam^{-1}. The black dot shows the peak of the NH_3 (1,1) emission and the triangle shows the dust continuum emission peaks. The resolution of the continuum data are smoothed to the resolution of the GBT data, $\sim$ 32″ FWHM. The 32″ FWHM beam of the GBT is delineated with the circle.

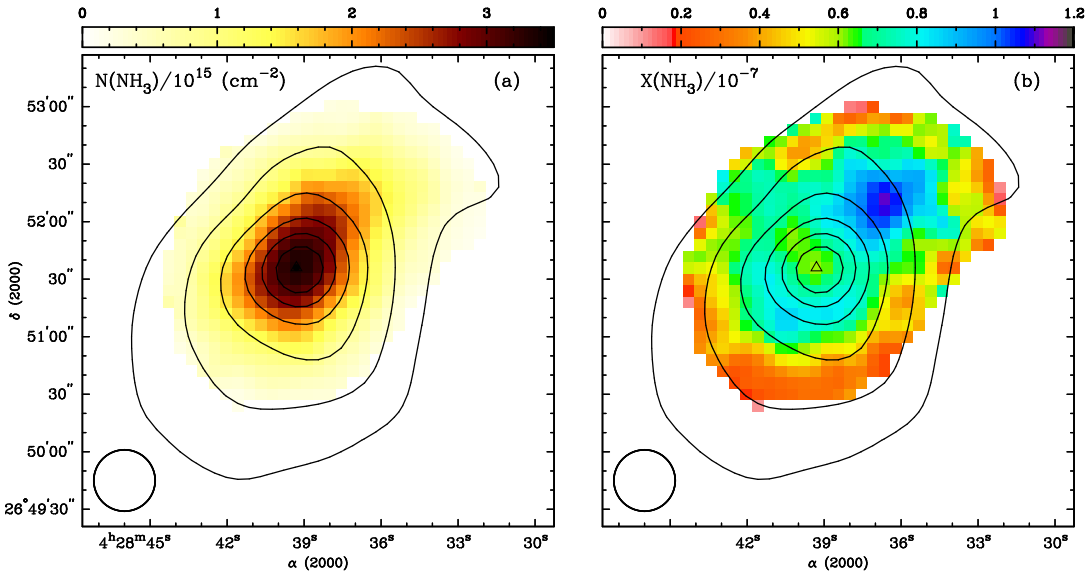

Figure 3.12: Maps of (a) $N(\mathrm{NH_3})$ and (b) $X(\mathrm{NH_3})$ toward L1521F. The contours correspond to continuum emission at 250 μm, starting at 1.0 Jy beam^{-1} and increase in steps of 1.0 Jy beam^{-1}. The black dot shows the peak of the $\mathrm{NH_3}$ (1,1) emission and the triangle shows the dust continuum emission peaks. The resolution of the continuum data are smoothed to the resolution of the GBT data, $\sim 32''$ FWHM. The $32''$ FWHM beam of the GBT is delineated with the circle.

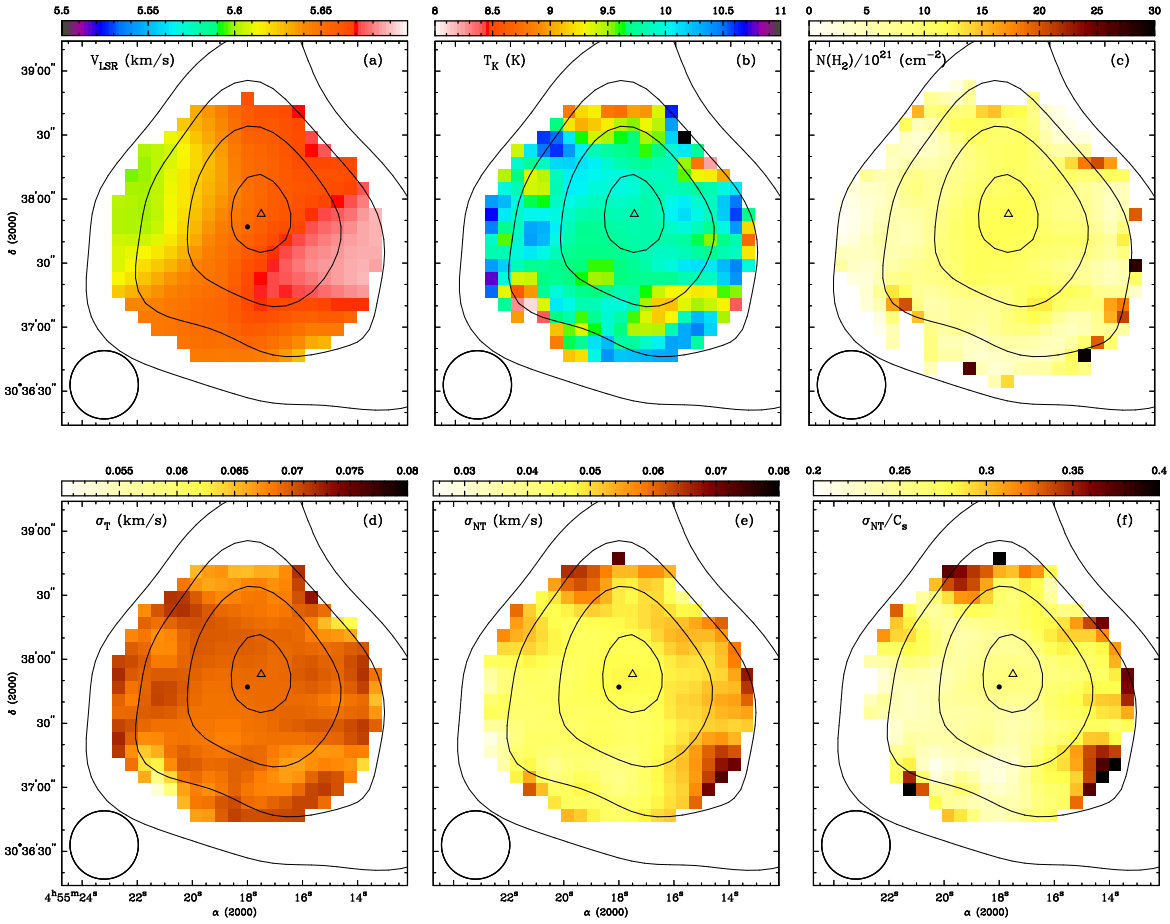

Figure 3.13: Maps of (a) v_{LSR}, (b) T_K, (c) $N(\mathrm{H_2})$, (d) σ_T, (e) σ_{NT}, and (f) σ_{NT}/c_s calculated using NH_3 (1,1) emission toward L1517B at 32″ FWHM. The contours correspond to continuum emission at 250 μm, starting at 0.5 Jy beam^{-1} and increase in steps of 0.5 Jy beam^{-1}. The black dot shows the peak of the NH_3 (1,1) emission and the triangle shows the dust continuum emission peaks. The resolution of the continuum data are smoothed to the resolution of the GBT data, $\sim$ 32″ FWHM. The 32″ FWHM beam of the GBT is delineated with the circle.

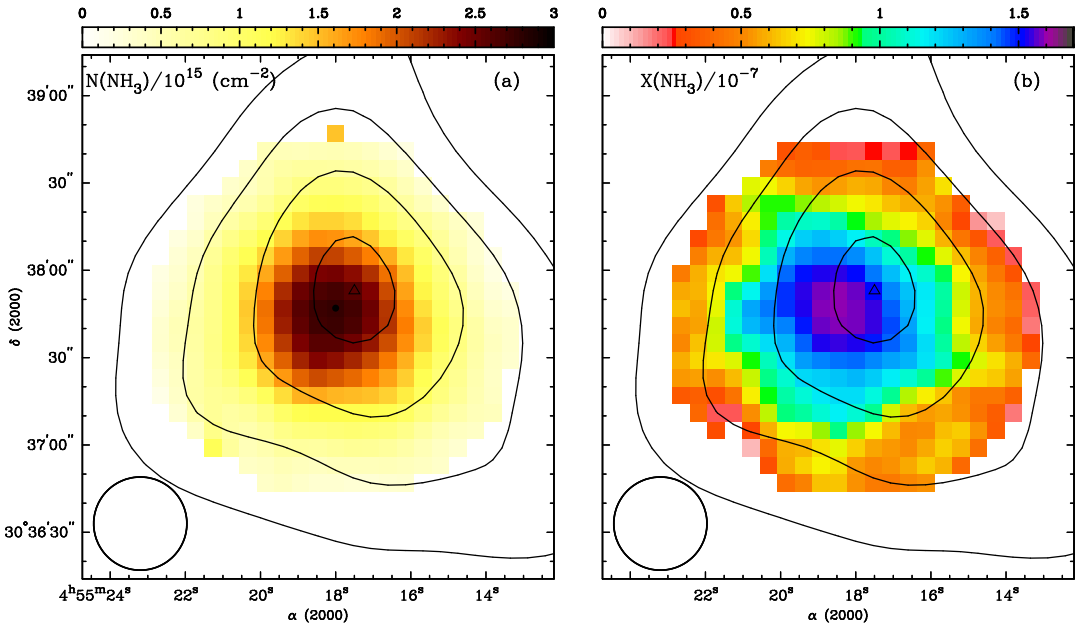

Figure 3.14: Maps of (a) $N(\mathrm{NH_3})$ and (b) $X(\mathrm{NH_3})$ toward L1517B. The contours correspond to continuum emission at 250 μm, starting at 0.5 Jy beam^{-1} and increase in steps of 0.5 Jy beam^{-1}. The black dot shows the peak of the $\mathrm{NH_3}$ (1,1) emission and the triangle shows the dust continuum emission peaks. The resolution of the continuum data are smoothed to the resolution of the GBT data, $\sim 32''$ FWHM. The $32''$ FWHM beam of the GBT is delineated with the circle.

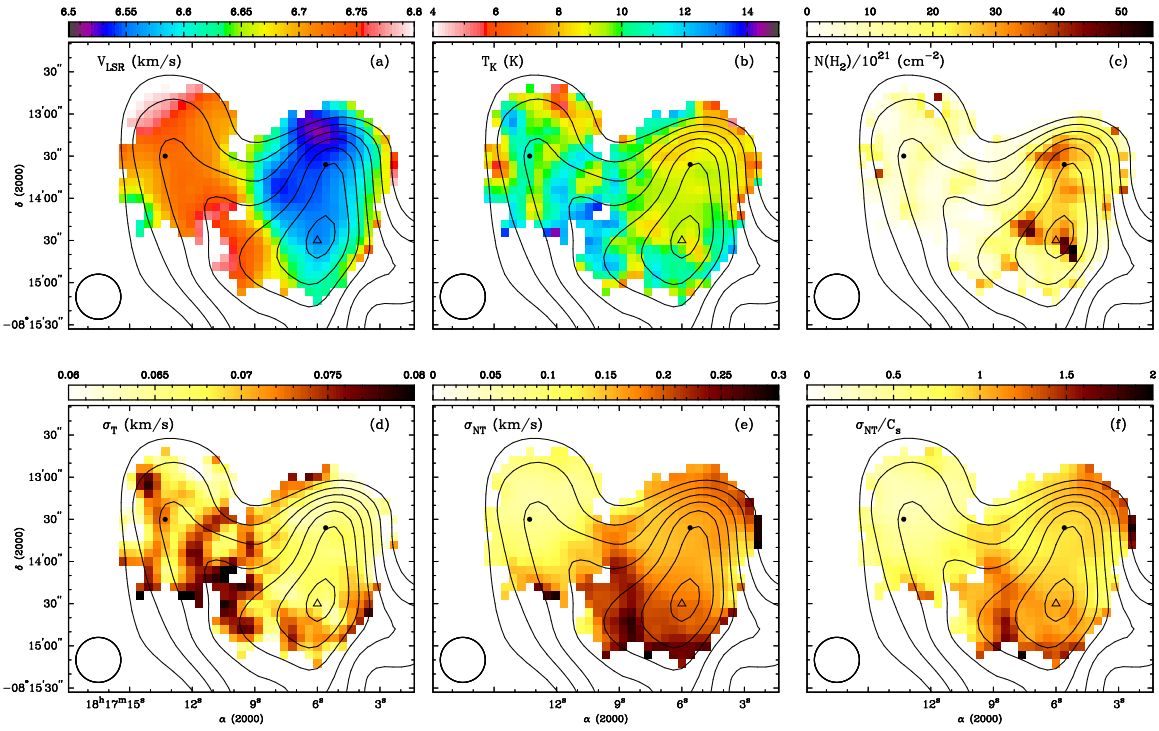

Figure 3.15: Maps of (a) v_{LSR}, (b) T_K, (c) $N(\mathrm{H_2})$, (d) σ_T, (e) σ_{NT}, and (f) σ_{NT}/c_s calculated using NH_3 (1,1) emission toward L429 at $32''$ FWHM. The contours correspond to continuum emission at 250 μm, starting at 0.5 Jy beam^{-1} and increase in steps of 0.5 Jy beam^{-1}. The black dots show the peaks of the NH_3 (1,1) emission and the triangle shows the dust continuum emission peaks. The resolution of the continuum data are smoothed to the resolution of the GBT data, $\sim 32''$ FWHM. The $32''$ FWHM beam of the GBT is delineated with the circle.

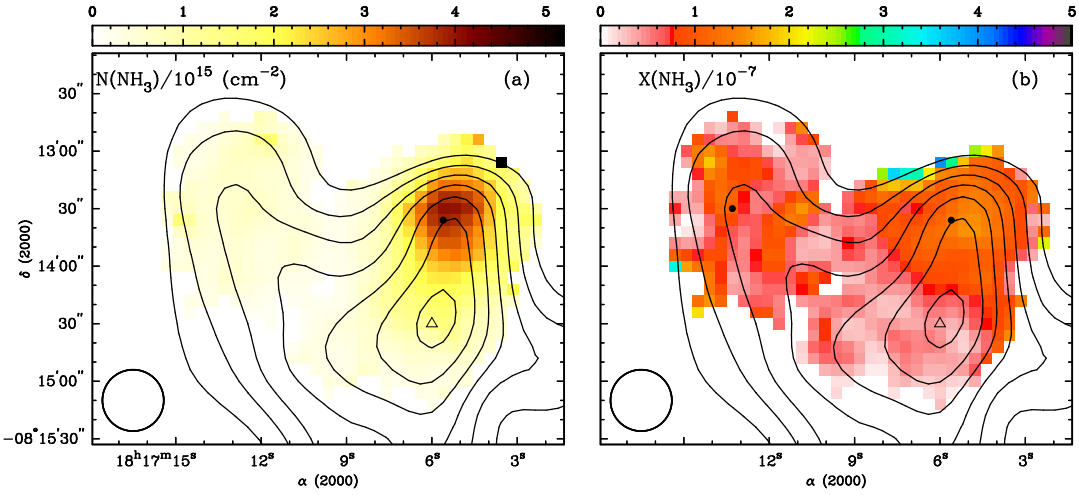

Figure 3.16: Maps of (*a*) $N(\mathrm{NH_3})$ and (*b*) $X(\mathrm{NH_3})$ toward L429. The contours correspond to continuum emission at 250 μm, starting at 0.5 Jy beam^{-1} and increase in steps of 0.5 Jy beam^{-1}. The black dot shows the peak of the $\mathrm{NH_3}$ (1,1) emission and the triangle shows the dust continuum emission peaks. The resolution of the continuum data are smoothed to the resolution of the GBT data, $\sim 32''$ FWHM. The $32''$ FWHM beam of the GBT is delineated with the circle.

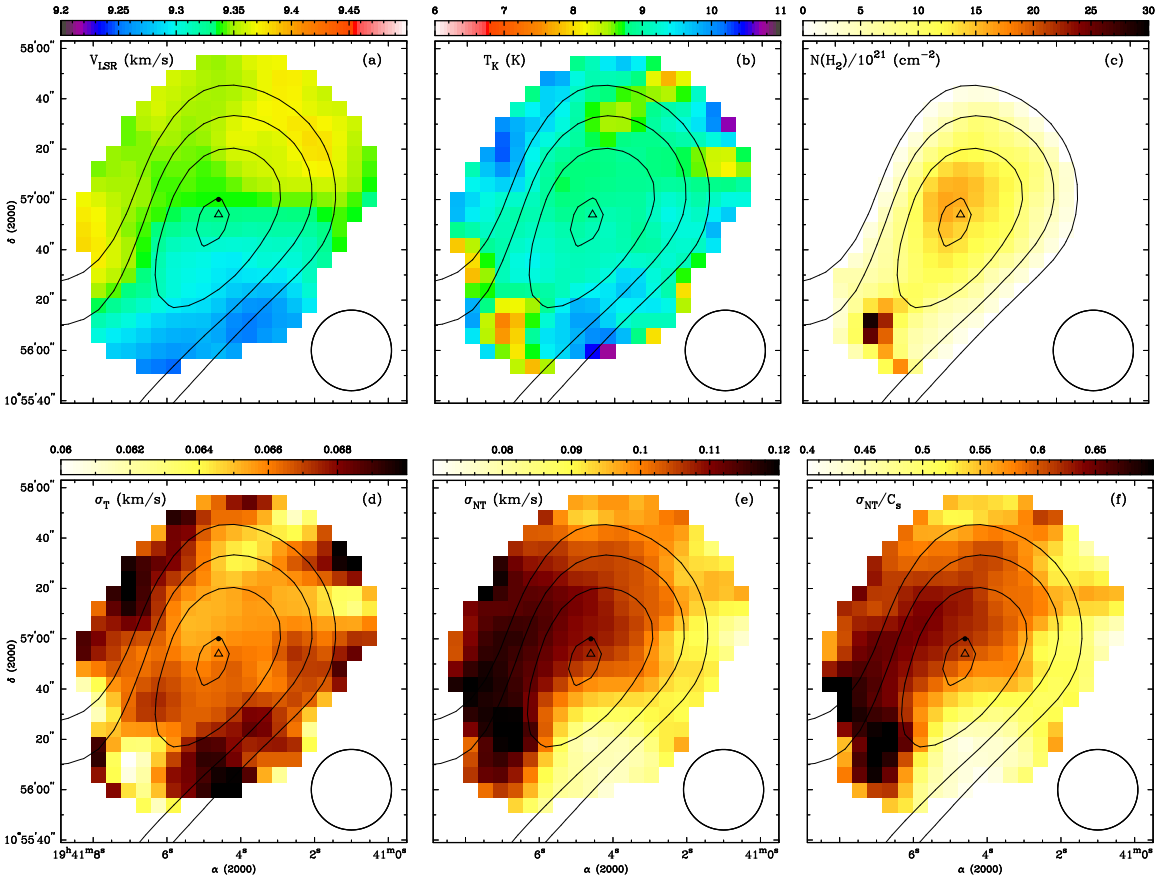

Figure 3.17: Maps of (a) v_{LSR}, (b) T_K, (c) $N(\mathrm{H_2})$, (d) σ_T, (e) σ_{NT}, and (f) σ_{NT}/c_s calculated using NH_3 (1,1) emission toward L694-2 at 32″ FWHM. The contours correspond to continuum emission at 250 μm, starting at 0.05 Jy beam^{-1} and increase in steps of 0.5 Jy beam^{-1}. The black dot shows the peak of the NH_3 (1,1) emission and the triangle shows the dust continuum emission peaks. The resolution of the continuum data are smoothed to the resolution of the GBT data, $\sim$ 32″ FWHM. The 32″ FWHM beam of the GBT is delineated with the circle.

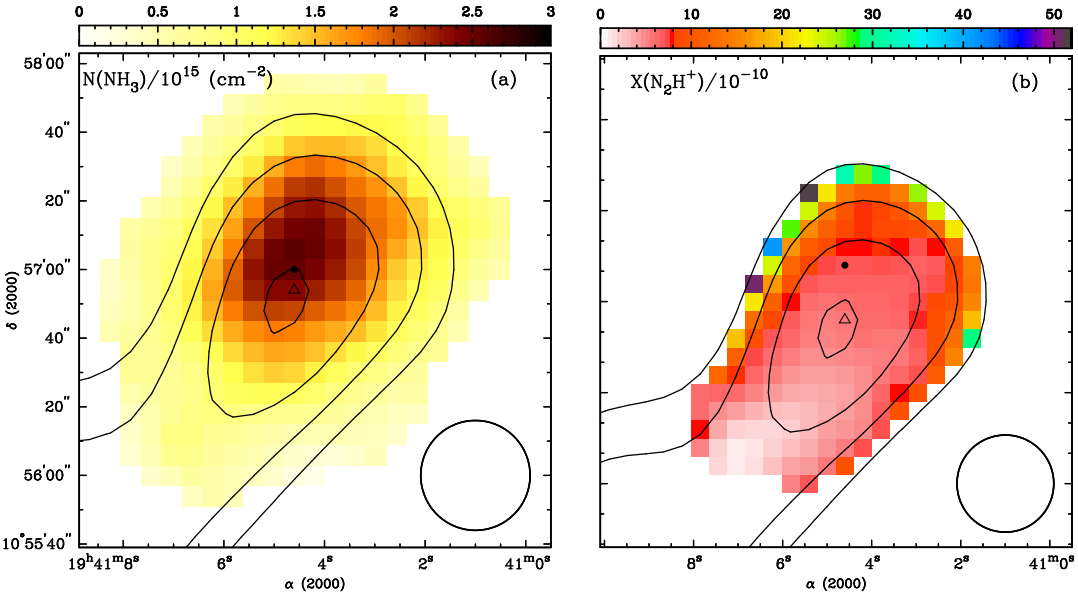

Figure 3.18: Maps of (*a*) $N(NH_3)$ and (*b*) $X(NH_3)$ toward L694-2. The contours correspond to continuum emission at 250 μm, starting at 0.05 Jy beam^{-1} and increase in steps of 0.5 Jy beam^{-1}. The black dot shows the peak of the NH_3 (1,1) emission and the triangle shows the dust continuum emission peaks. The resolution of the continuum data are smoothed to the resolution of the GBT data, $\sim 32''$ FWHM. The $32''$ FWHM beam of the GBT is delineated with the circle.

3.5.2 N_2H^+

For all cores observed in N_2H^+ (1−0) emission (i.e., L1517B, L429, L694-2, and L1014), we restricted our analysis of the N_2H^+ (1−0) data to pixels where the isolated N_2H^+ (1−0) component has a SNR higher than 5. Since N_2H^+ (1−0) emission toward L1014 is very faint and none of the pixels show emission with SNR higher than 5, we do not present any further analysis on the N_2H^+ (1−0) data of that core. Following the method described in §2.4, we fit N_2H^+ (1−0) spectra toward each core using ensembles of Gaussians. Table 3.10 lists the weighted means and median errors of the returned parameters (v_{LSR}, Δv, τ, and T_{ex}) for all three cores. As mentioned previously, the reported observed line widths (Δv) in Table 3.7 are corrected for the artificial broadening by the instrumental velocity resolution (see §2.4.1). For each core, we used the best fit parameters and the corresponding T_K map to determine the distribution of σ_T, σ_{NT}, and σ_{NT}/c_s across the core. The details of these calculations can be found in §2.4.1. The weighted means and median errors for σ_T, σ_{NT}, σ_{NT}/c_s, $N(N_2H^+)$, and $X(N_2H^+)$ for each core is listed in Table (3.11). Below we discuss the distributions of these parameters across each of the targets in our sample.

L1517B: The v_{LSR} map of N_2H^+ emission toward L1517B (Figure 3.19a) is in agreement with that of the NH_3 emission, showing a gradient in east-west direction and suggesting that the core is experiencing rotational motion. Similarly to the velocity dispersion maps of NH_3 emission, the core appears to be quiescent and subsonic in the velocity dispersion maps of N_2H^+ (Figures 3.19c and 3.19d).

L694-2: The N_2H^+ (1−0) emission toward L694-2 shows the C-shaped constant v_{LSR} contours near the peak of N_2H^+ emission (Figure 3.23a). This is in agreement with the v_{LSR} distribution of the core measured using NH_3 emission and could indicate that L694-2 is a rotating infalling core. Our measurements of velocity dispersions of N_2H^+ (1−0) spectra suggest that velocity dispersion in the core is dominated by thermal motions and the core is subsonic (Figures 3.23c and 3.23d).

L429: The v_{LSR} map of N_2H^+ emission toward L429 is in agreement with that of NH_3 (1,1) emission and shows that L429 is at a lower v_{LSR} compared to L429-E (Figure 3.21a). Again, L429 appears to be transonic and more turbulent than the adjacent region, L429-E (Figures 3.21c and 3.21d).

Table 3.10: The weighted mean values of the fitting parameters of N_2H^+ (1−0) spectral line emission toward four cores. The values inside the brackets are the median errors.

Core	v_{LSR} (km s^{-1})	Δv (km s^{-1})	τ	T_{ex} (K)
L1517B	5.835 (0.002)	0.200 (0.001)	6.9 (0.8)	4.19 (0.09)
L429	6.725 (0.003)	0.41 (0.01)	8.6 (0.6)	4.42 (0.05)
L429-E	6.902 (0.003)	0.22 (0.01)	9 (1)	3.79 (0.05)
L694-2	9.590 (0.002)	0.258 (0.001)	8.1 (0.6)	4.6 (0.1)

Table 3.11: The weighted mean values of the physical properties of three cores in our sample determined using the fitting parameters of the observed N_2H^+ (1−0) emission spectra. The values inside the brackets are the median errors.

Core	σ_T (km s^{-1})	σ_{NT} (km s^{-1})	σ_{NT}/c_s	$N(N_2H^+)$ ($/10^{12}$ cm^{-2})	$X(N_2H^+)$ ($/10^{-10}$)
L1517B	0.053 (0.001)	0.071 (0.002)	0.39 (0.02)	3.4 (0.9)	4 (1)
L429	0.051 (0.002)	0.172 (0.004)	0.96 (0.05)	8 (3)	4 (1)
L429-E	0.054 (0.003)	0.099 (0.004)	0.51 (0.05)	3.4 (0.7)	3 (2)
L694-2	0.051 (0.001)	0.099 (0.002)	0.56 (0.02)	5 (2)	5 (2)

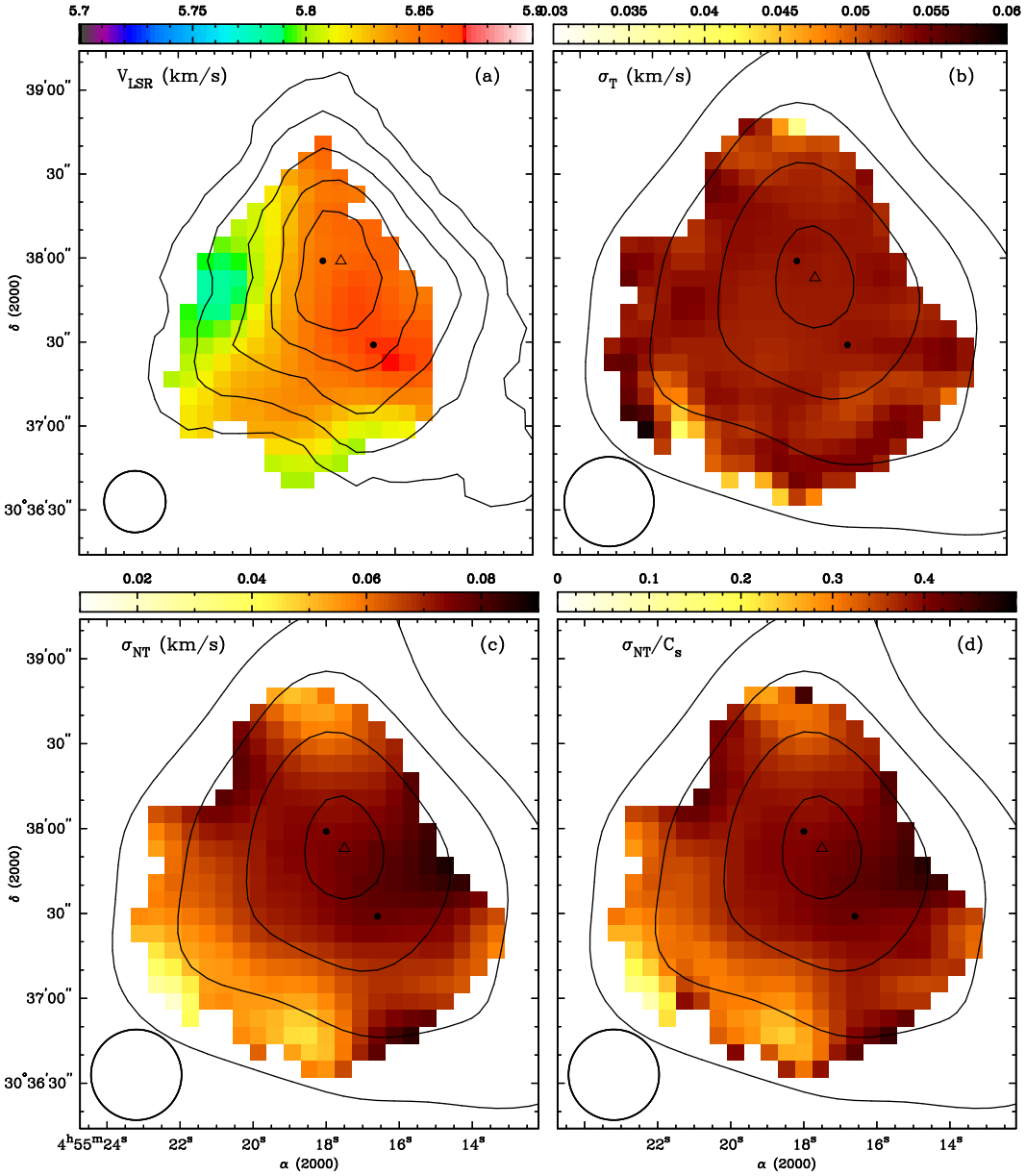

Figure 3.19: Maps of (a) v_{LSR}, (b) σ_T, (c) σ_{NT}, (d) σ_{NT}/c_s calculated using N_2H^+ (1−0) emission toward L1517B. The v_{LSR} map (a) is at the NRO original spatial resolution ($\sim$ 22″.9 FWHM). The contours correspond to continuum emission at 250 μm (smoothed to $\sim$ 22″.9 FWHM), starting at 0.5 Jy beam^{-1} and increasing in steps of 0.1 Jy beam^{-1}. The rest of the plots are made using the N_2H^+ (1−0) data smoothed to the resolution of the GBT, ($\sim$ 32″ FWHM). The contours in these plots correspond to continuum emission at 250 μm (smoothed to $\sim$ 32″ FWHM), starting at 0.5 Jy beam^{-1} and increasing in steps of 0.5 Jy beam^{-1}. The black dot shows the peak of the N_2H^+ (1−0) integrated intensity and the triangles show the peaks of the continuum emission. The circle shows the corresponding spatial resolution of each plot.

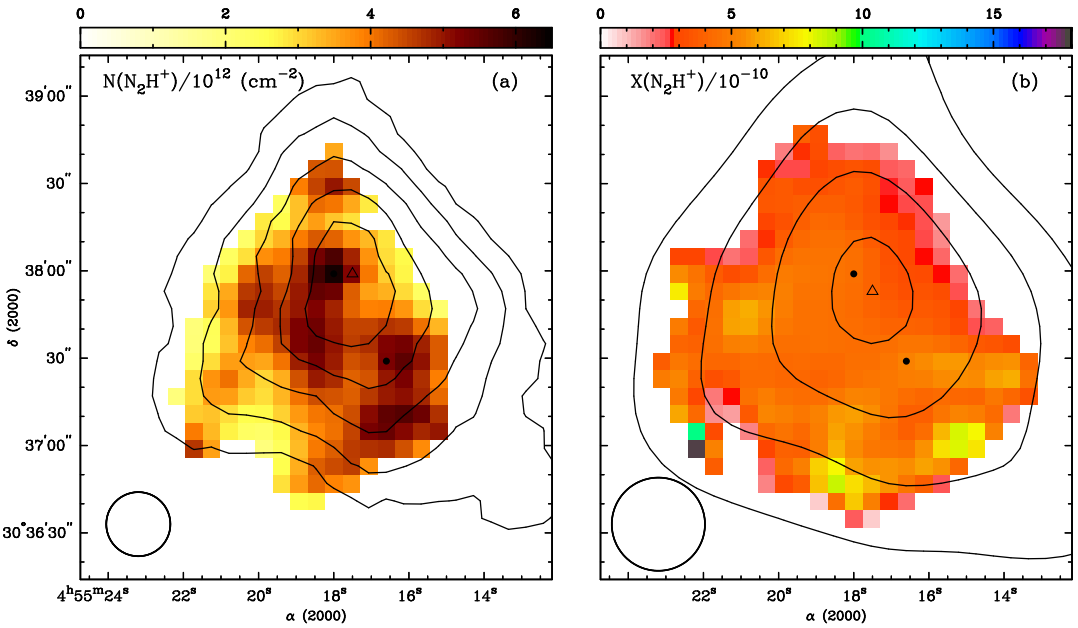

Figure 3.20: Maps of (a) $N(\mathrm{N_2H^+})$ and (b) $X(\mathrm{N_2H^+})$ toward L1517b. The v_{LSR} map (a) is at the NRO original spatial resolution ($\sim 22''.9$ FWHM). The contours in $N(\mathrm{N_2H^+})$ map correspond to continuum emission at 250 μm (smoothed to $\sim 22''.9$ FWHM), starting at 0.5 Jy beam^{-1} and increasing in steps of 0.1 Jy beam^{-1}. The $X(\mathrm{N_2H^+})$ plot is made using the $\mathrm{N_2H^+}$ (1$-$0) data smoothed to the resolution of the GBT, ($\sim 32''$ FWHM). The contours in this plot correspond to continuum emission at 250 μm (smoothed to $\sim 32''$ FWHM), starting at 0.5 Jy beam^{-1} and increasing in steps of 0.5 Jy beam^{-1}. The black dot shows the peak of the $\mathrm{N_2H^+}$ (1$-$0) integrated intensity and the triangles show the peaks of the continuum emission. The circle shows the corresponding spatial resolution of each plot.

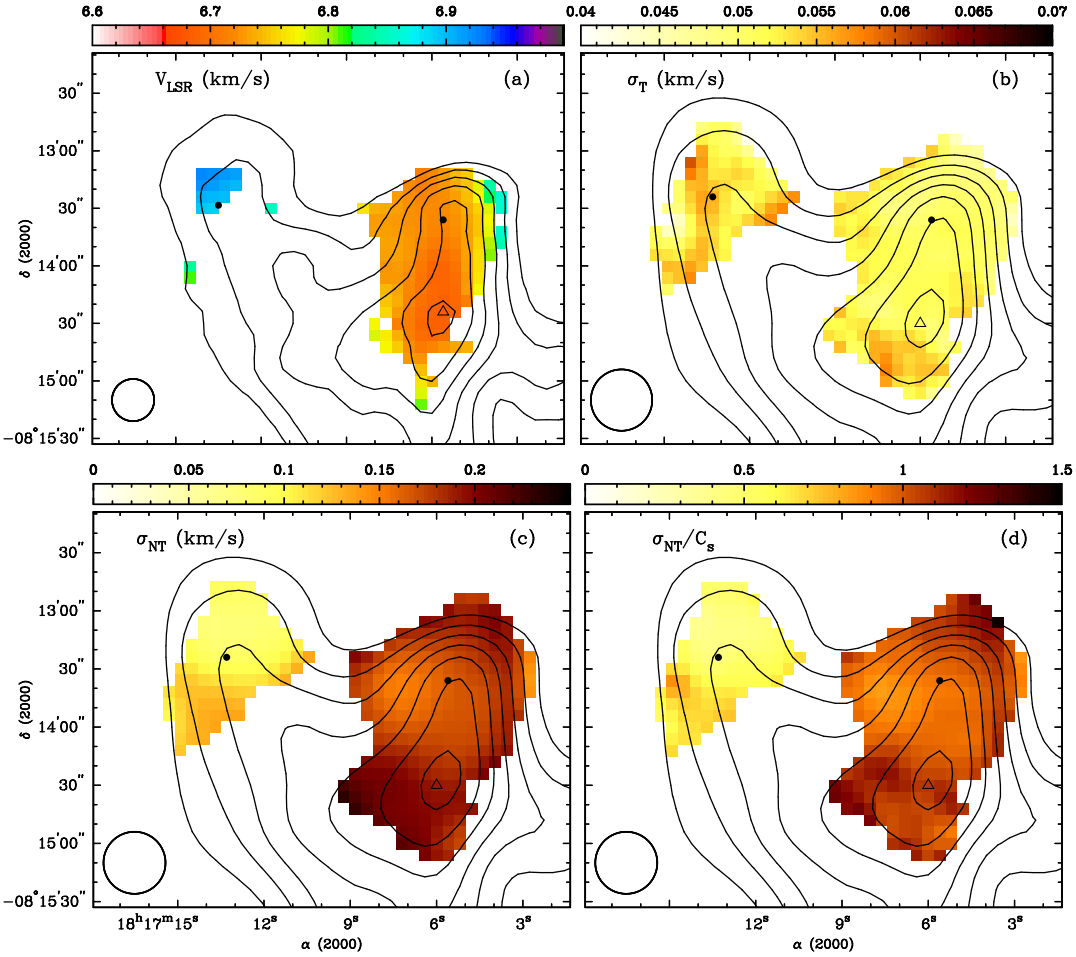

Figure 3.21: Maps of (a) v_{LSR}, (b) σ_T, (c) σ_{NT}, (d) σ_{NT}/c_s calculated using N_2H^+ (1−0) emission toward L429. The v_{LSR} map (a) is at the NRO original spatial resolution ($\sim 22''.9$ FWHM). The contours correspond to continuum emission at 250 μm (smoothed to $\sim 22''.9$ FWHM), starting at 0.4 Jy beam^{-1} and increasing in steps of 0.2 Jy beam^{-1}. The rest of the plots are made using the N_2H^+ (1−0) data smoothed to the resolution of the GBT, ($\sim 32''$ FWHM). The contours in these plots correspond to continuum emission at 250 μm (smoothed to $\sim 32''$ FWHM), starting at 0.5 Jy beam^{-1} and increasing in steps of 0.5 Jy beam^{-1}. The black dots show the peaks of the N_2H^+ (1−0) integrated intensity and the triangle shows the peak of the continuum emission. The circle shows the corresponding spatial resolution of each plot.

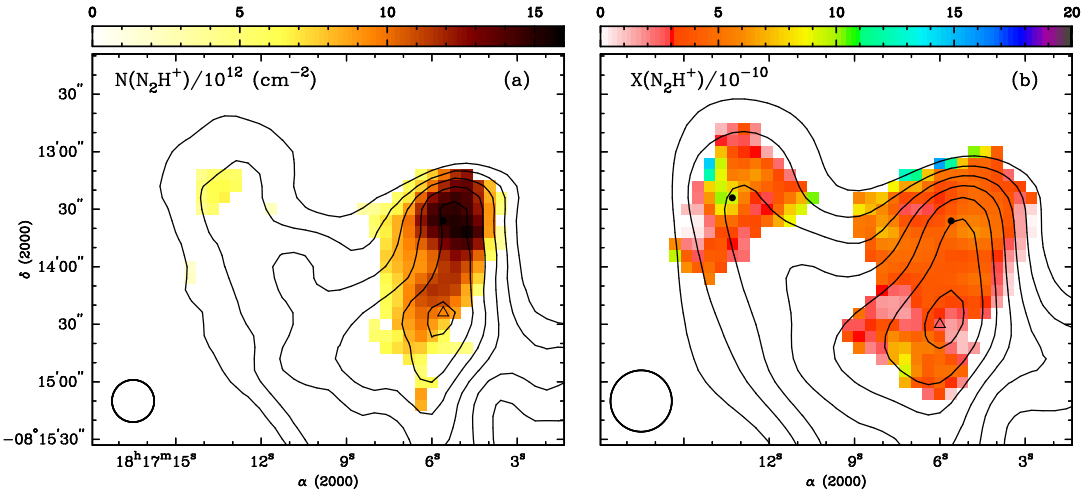

Figure 3.22: Maps of (a) $N(\mathrm{N_2H^+})$ and (b) $X(\mathrm{N_2H^+})$ toward L429. The v_{LSR} map (a) is at the NRO original spatial resolution ($\sim 22''.9$ FWHM). The contours in $N(\mathrm{N_2H^+})$ map correspond to continuum emission at 250 μm (smoothed to $\sim 22''.9$ FWHM), starting at 0.4 Jy beam^{-1} and increasing in steps of 0.2 Jy beam^{-1}. The $X(\mathrm{N_2H^+})$ plot is made using the $\mathrm{N_2H^+}$ (1−0) data smoothed to the resolution of the GBT, ($\sim 32''$ FWHM). The contours in this plot correspond to continuum emission at 250 μm (smoothed to $\sim 32''$ FWHM), starting at 0.5 Jy beam^{-1} and increasing in steps of 0.5 Jy beam^{-1}. The black dot shows the peak of the $\mathrm{N_2H^+}$ (1−0) integrated intensity and the triangles show the peaks of the continuum emission. The circle shows the corresponding spatial resolution of each plot.

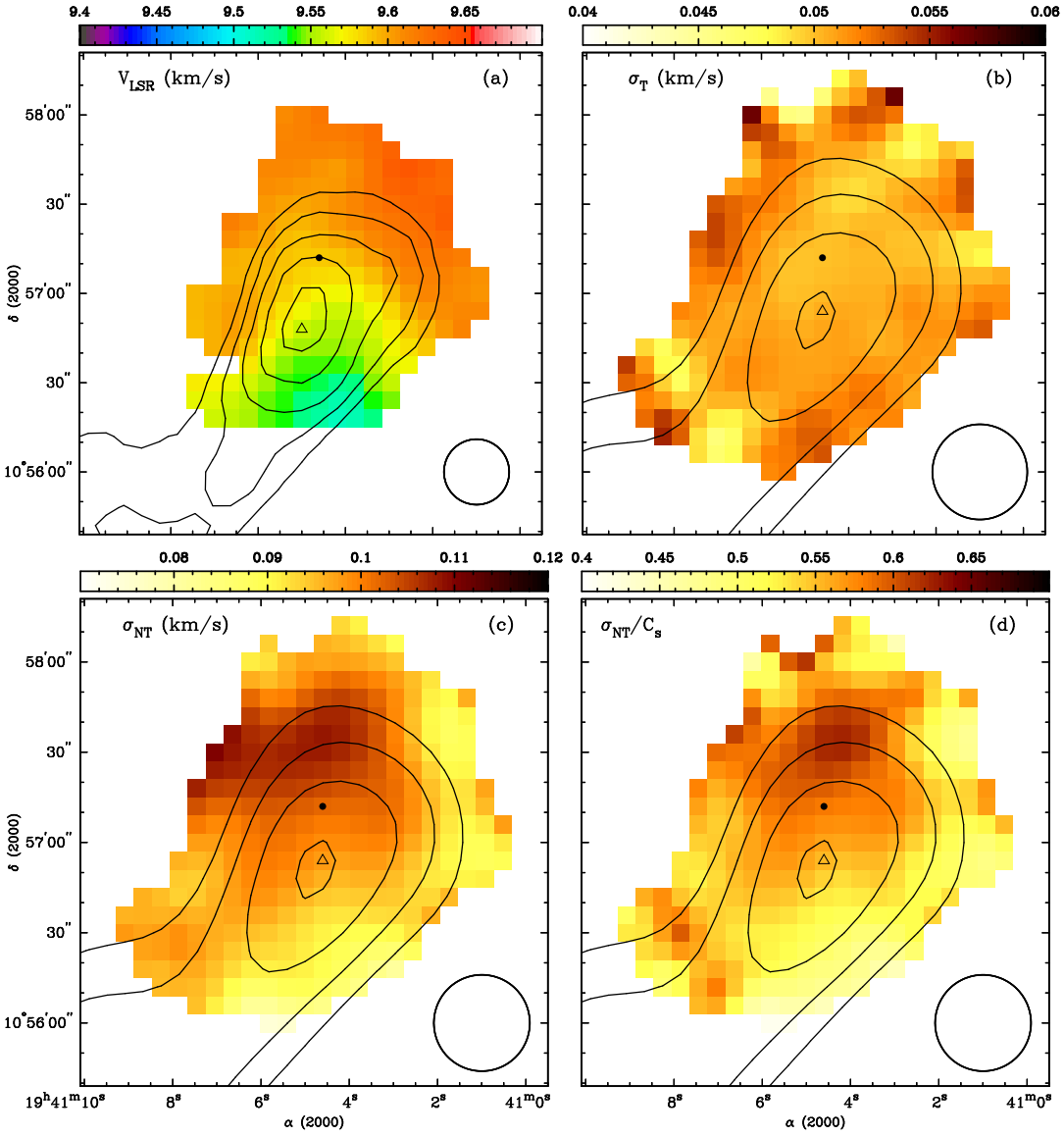

Figure 3.23: Maps of (a) v_{LSR}, (b) σ_T, (c) σ_{NT}, (d) σ_{NT}/c_s calculated using N_2H^+ (1−0) emission toward L694-2. The v_{LSR} map (a) is at the NRO original spatial resolution ($\sim$ 22″.9 FWHM). The contours correspond to continuum emission at 250 μm (smoothed to $\sim$ 22″.9 FWHM), starting at 0.1 Jy beam^{-1} and increasing in steps of 0.1 Jy beam^{-1}. The rest of the plots are made using the N_2H^+ (1−0) data smoothed to the resolution of the GBT, ($\sim$ 32″ FWHM). The contours in these plots correspond to continuum emission at 250 μm (smoothed to $\sim$ 32″ FWHM), starting at 0.05 Jy beam^{-1} and increasing in steps of 0.5 Jy beam^{-1}. The black dot shows the peak of the N_2H^+ (1−0) integrated intensity and the triangles show the peaks of the continuum emission. The circle shows the corresponding spatial resolution of each plot.

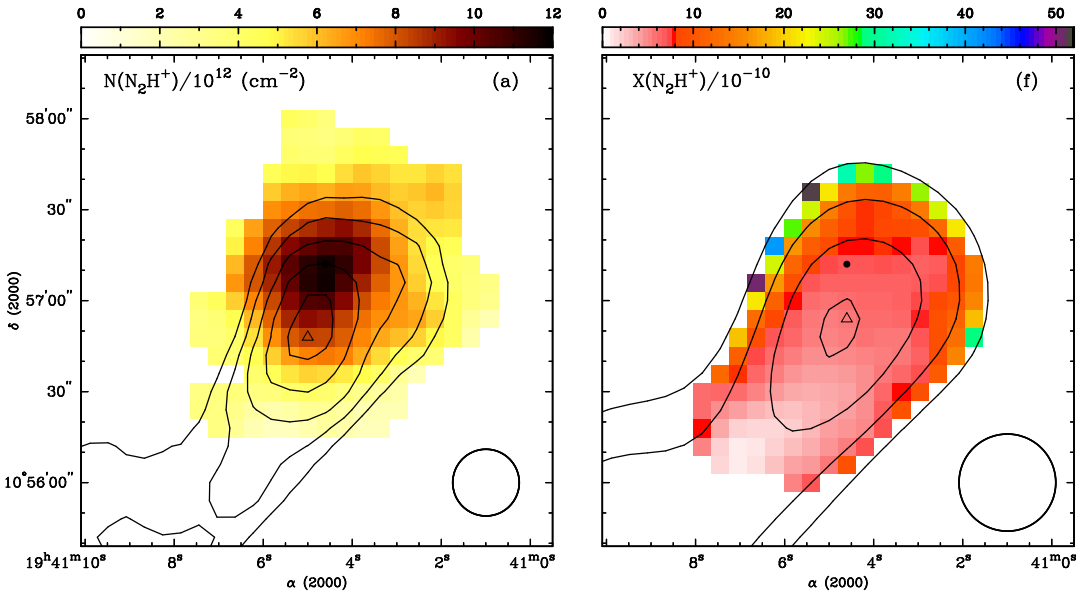

Figure 3.24: Maps of (a) $N(\mathrm{N_2H^+})$ and (b) $X(\mathrm{N_2H^+})$ toward L694-2. The v_{LSR} map (a) is at the NRO original spatial resolution ($\sim 22''.9$ FWHM). The contours in $N(\mathrm{N_2H^+})$ map correspond to continuum emission at 250 μm (smoothed to $\sim 22''.9$ FWHM), starting at 0.1 Jy beam^{-1} and increasing in steps of 0.1 Jy beam^{-1}. The $X(\mathrm{N_2H^+})$ plot is made using the $\mathrm{N_2H^+}$ (1$-$0) data smoothed to the resolution of the GBT, ($\sim 32''$ FWHM). The contours in this plot correspond to continuum emission at 250 μm (smoothed to $\sim 32''$ FWHM), starting at 0.05 Jy beam^{-1} and increasing in steps of 0.5 Jy beam^{-1}. The black dot shows the peak of the $\mathrm{N_2H^+}$ (1$-$0) integrated intensity and the triangles show the peaks of the continuum emission. The circle shows the corresponding spatial resolution of each plot.

3.6 Summary

In this chapter, we presented single-dish observations of NH_3 (1,1) and (2,2) and N_2H^+ (1−0) emission lines as well as continuum emission at 250 μm toward five cores in our sample, L694-2, L429, L1517B, L1521F, and L1014. These data reveal the kinematic structure and temperature distribution of these cores. (Note that L1014 is excluded from the results of our comparison below due to low SNR in our observations toward this core.)

1. L429 demonstrates the most complicated structure in both molecular emission and dust continuum emission among the cores in our sample. The morphologies of the integrated intensities of NH_3 and N_2H^+ toward L429 follow the general shape of the dust continuum emission. Their maxima, however, are significantly offset from that of the continuum emission.

   The molecular emission integrated intensities of the rest of the cores in our sample follow the morphology of their corresponding continuum emission well, and their maxima are located close (within the beam width) of the corresponding peak location of the continuum emission.

2. All cores appear to have similar weighted mean kinetic temperatures in the range $\sim$ 9 K − 10 K, with the line-of-sight averaged T_K distribution of each core slightly decreasing toward the corresponding centre.

3. All of the cores in our sample show roughly similar values of thermal velocity dispersions $\sim$ 0.6 km s^{-1}.

4. L429 is the most turbulent core in our sample. With a non-thermal velocity dispersion of $\sim$ 0.16 km s^{-1}, L429 is a relatively transonic core. The rest of the cores in our sample are all subsonic, with L1517B being the most quiescent core.

5. L1521F is the most centrally concentrated core in our sample, with its H_2 column density significantly higher than the other cores and is followed in decreasing order by L429, L1517B, and L694-2.

Chapter 4

Radiative Transfer Modelling of NH_3 (1,1) and (2,2) Emission toward L694-2 and L1521F

4.1 Introduction

Observed emission spectra are the results of integration along the line of sight. Therefore, characteristics of the observed emission spectra (e.g., intensity, line width, and velocity) are the averaged values of these quantities along the line-of-sight and across the telescope beam. It is, however, important to note that these characteristics depend on the three-dimensional structure of the physical parameters of the source (e.g., temperature, density, molecular abundance, and velocity), and therefore are not necessarily constant along the line-of-sight. Simple techniques of spectral line analysis are based on the assumption of uniform source structure to allow the radiative transfer equation to be solved analytically (see Chapter 2) and do not provide information on the three-dimensional structure of the source. One way to approach this problem is by constructing models of the physical characteristics of a region and testing them through radiative transfer techniques that simulate strengths and profiles of the observed spectra to find the model that best fits the observations. One should keep in mind that usually there are multiple possible solutions.

Over the years, several radiative transfer codes have been introduced, such as MOLLIE (in 3D; Keto 1990; Keto et al. 2004; Keto & Rybicki 2010), RATRAN (in 1D and 2D; Hogerheijde & van der Tak 2000), and Line Modelling Engine (LIME; in 3D;

Brinch & Hogerheijde 2010). Several authors have used these codes to model physical structures in various low-mass and high-mass star-forming regions. For example, Keto et al. (2004) investigated the density structures of three cores by radiative transfer modelling of N_2H^+ (1−0) observations using MOLLIE. Crapsi et al. (2007) used RATRAN in its one-dimensional mode to model the single-dish (Effelsberg) and the combined (single-dish and interferometric from Effelsberg and VLA) data of NH_3 (1,1) and (2,2) emission lines toward L1544. For that case, the single-dish data alone were best reproduced by a constant $T_K = 8.75$ K across the core. The combined dataset, however, was best reproduced by a T_K profile that decreased from 12 K to 5.5 K toward the core centre. This change in the radial profile of T_K across the core resulted in a 50% increase in the density of the core. Also, the NH_3 column density of L1544 increased by a factor of ~ 2, implying that, unlike CO molecule, NH_3 is not significantly depleted toward the centre of L1544.

Outer regions of cores are heated due to the presence of Interstellar Radiation Fields (ISRFs). We expect the innermost regions of starless cores to be relatively colder compared to their outer edges due to the shielding of the core centre. Also, IR continuum radiation provides an effective cooling mechanism due to the cores being optically thin to their own radiation in IR. Models and observations of thermal continuum emission from dust provide evidence for the decrease in dust temperature from $\sim$ 12 K at core surfaces to $\sim$ 7 K in the centres (e.g., see Evans et al. 2001, Stutz et al. 2010, and Marsh et al. 2014). Variations in molecular abundance have also been previously observed toward the cold interior of many dense cores. For instance, Tafalla et al. (2002) detected significant decreases in the molecular abundances of $C^{18}O$ and CS toward L1498, L1495, L1400K, L1517B, and L1544. The same sample of cores, however, show a constant radial profile in the abundance of N_2H^+ and a central enhancement in the abundance of NH_3.

Do all starless cores show T_K and T_d gradients on small scales? How are the temperatures and molecular abundances affected by the formation of a protostar in the core interior? Detailed radiative transfer modelling of a wider sample of cores is essential to answer these questions. The cores studied should span evolutionary stages before and after the point of protostar formation. The sample will then reveal the temperature structure and ultimately the physical and chemical evolution of cores on the brink of star formation. With this goal in mind, we selected two cores from our sample (described in Chapter 3), L694-2 and L1521F, observed their NH_3 emission at high resolution using JVLA, and investigated their physical structure by extensive

radiative transfer modelling of combinations of low resolution and high resolution NH_3 data using MOLLIE. Comparisons of the physical structure of a starless core like L694-2 with that of a more evolved core such as L1521F that contains a protostellar VeLLO can shed light on how physical parameters of the region are affected through the evolution of the core from being starless to forming a protostellar object.

MOLLIE uses the Accelerated Λ Iteration (ALI) technique[1] developed by Rybicki & Hummer (1991) to solve numerically the radiative transfer equation in three-dimensions . The rays are distributed in various angles and impact parameters, with each ray passing through the entire modelled volume. The intensity field at each location is calculated by integrating along each of the rays. The radiation quantities are determined by angle and frequency averaging over the rays that pass through each cell in the volume of the model (Keto et al. 2004). We use MOLLIE to reproduce NH_3 (1,1) and (2,2) spectra, in Local Thermodynamic Equilibrium (LTE) with the number of Λ iterations set to unity.

Assumption of LTE is appropriate for the modelling of NH_3 (1,1) and (2,2) emission, due to two circumstances. First, for NH_3, the rotational transition, $(J+1, K) \rightarrow (J, K)$, occur in the far infrared with Einstein A coefficients ~ 1 s^{-1} (Rohlfs & Wilson 2004). Therefore, these *nonmetastable* states are only populated in regions with extremely high H_2 densities ($\sim 10^8 - 10^9$ cm^{-3}) or in the vicinity of strong infrared radiation fields. Thus, in cold cores virtually all of the population is in the lowest level of each K-ladder (i.e., $J, K = 1, 1$ or $J, K = 2, 2$ or $J, K = 3, 3$, etc.). These energy states are referred to as *metastable* due to their very slow decay rate ($\sim 10^{-9}$ s^{-1}; Ho & Townes 1983 and Rohlfs & Wilson 2004). Second, for symmetric top molecules such as NH_3, pure rotational transitions are only allowed when $\Delta J = \pm 1$ and $\Delta K = 0$ (Bunker & Jensen 2006), and therefore dipole transitions between different K-ladders are forbidden. In typical molecular cloud conditions, the excitation of inversion doublets[2] in the metastable states are mainly due to collisions. Such conditions are equivalent to LTE. In this case, knowledge of the collision rates of the hyperfine transitions of NH_3 (1,1) and (2,2) is not required and we use the relative intensities of the hyperfine transitions from Kukolich (1967) and Rydbeck et al. (1977) to model the observed spectra of NH_3 (1,1) and (2,2). A similar approach was employed by Crapsi et al. (2007) and Juvela et al. (2012). A non-LTE version of

[1] Λ iteration is the process of iterating between level populations and the radiation field using Λ operators.

[2] The ability of the N atom to quantum tunnel through the hydrogen atom plane splits the J = K rotational states into inversion doublets.

MOLLIE, specifically designed for modelling in detail the hyperfine structure of NH_3, is currently under development and will provide an exciting opportunity to investigate further the physical structure of these cores in the future.

In this chapter, we present interferometric observations of NH_3 (1,1) and (2,2) emission lines toward L694-2 and L1521F obtained using JVLA. We also investigate the internal physical structure of L694-2 and L1521F by simulating their observed NH_3 emission using the radiative transfer code MOLLIE. We describe the details of our JVLA observations and data reduction methods in §4.2. §4.3 presents the integrated intensity maps of the observed molecular emission toward L694-2 and L1521F. §4.4 explains our method for determining the total column density profiles of L694-2 and L1521F. We discuss the details of how we configured MOLLIE and our findings regarding the internal structures of L694-2 and L1521F in §4.5. We compare our results of the radiative transfer modelling of the two cores in §4.6. Finally, §4.7 summarizes our results.

4.2 Observations and Data Reduction

4.2.1 Jansky Very Large Array (JVLA)

Interferometric observations of the NH_3 (J, K) = (1,1) and (2,2) emission lines toward the cores in our sample were acquired using the JVLA, located near Socorro, NM, USA from February through April, 2013. We observed the targets using the JVLA in D configuration using single pointings. The JVLA correlator was configured to use the 8-bit sampler and two basebands. Each baseband had one subband with 8 MHz bandwidth and 2048 channels in dual polarization mode. Each subband was used to observe either of the NH_3 (1,1) or (2,2) lines at 23.6945 GHz or 23.7226 GHz, respectively. We also observed with uniform sensitivity all of the satellite sets of hyperfine transitions over 3.5 MHz and 3 MHz frequency range for the NH_3 (1,1) and (2,2) line, respectively. We placed the NH_3 (1,1) and (2,2) lines in the middle of two adjacent 128 MHz boundaries of the 8-bit sampler to avoid suckouts[3]. This setting yielded a velocity resolution of 0.05 km s^{-1} (i.e., frequency resolution of 3.9 KHz) for each line, sufficient to resolve each. In the K-band, the primary beam (i.e., the field-of-view) of the JVLA is $\sim 2'$ FWHM. In D configuration, the synthesized beam (i.e., the resolution) of the JVLA is $\sim 3''.2 \times 3''.6$ FWHM with a geometrical mean

[3]Suckouts are small spectral gaps in the bandwidth with reduced sensitivity.

beam width of $\sim 3''.4$ FWHM.

At the beginning of each track, we observed the flux and bandpass calibrators for 10 minutes. We used the phase calibrators to check pointing accuracy on the target every 45 minutes. To monitor and calibrate phase variations, we cycled through observations of the target and the corresponding phase calibrator with 2 minutes of integration on the phase calibrator and 4.5 minutes of integration on the target, ensuring that each target observation was bracketed by phase measurements. We also used the phase calibrator to check pointing accuracy every 45 minutes. Table (4.1) lists the targets and their corresponding flux, bandpass, and phase calibrators.

The JVLA data were reduced using the CASA (4.2) data reduction package on the cluster master server at the New Mexico Array Science Center (NMASC). We carefully inspected and flagged the data with poor phase stability, unexpectedly high amplitude measurements, or target data not bracketed with phase measurements. Subsequently, we applied bandpass, flux, and phase calibrations. For each core, we imported the single-dish maps of NH_3 (1,1) and (2,2) (see Chapter 3) into CASA using the task IMPORTFITS and re-gridded the position and velocity axes of the single-dish data to those of the JVLA data using the task IMREGRID. We deconvolved and Fourier transformed the JVLA data from the spatial frequency (u, v) plane into the image plane using the task CLEAN with natural weighting and the GBT data of each core (see §3.3.1) as the model. The combination of JVLA and GBT data was carried out in the same step.

Table 4.1: List of flux, bandpass, and phase calibrators for each source as well as rms sensitivities of the combined NH_3 (1,1) emission maps.

Core	rms[a] (K)	Flux/Bandpass Calibrator	Phase Calibrator	Distance (pc)
L694-2	0.3	3C286	J1925+2106	230 ± 30[b]
L1521F	0.6	3C48	J0359+3220	136 ± 36[c]

[a]The final 1 σ rms sensitivities of the central regions of the maps (i.e., toward the most central regions of the cores) given on the T_{mb} scale per 0.05 km s^{-1} velocity channel.

[b]Kawamura et al. (2001)

[c]Maheswar et al. (2011)

4.3 Observational Results

Figures 4.1 and 4.2 show the integrated intensity maps of the NH_3 (1,1) and (2,2) emission lines toward L694-2 and L1521F, respectively, using the combined data from JVLA and GBT. The integrated intensity maps were made by summing over the entire emission spectrum including all hyperfine components, excluding any channels with emission lower than twice the corresponding map rms noise level.

The single-dish integrated intensity maps of NH_3 (1,1) and (2,2) emission lines toward L694-2 (Figures 3.9a and 3.9b) both show single peak locations at the centre. The integrated intensity map of NH_3 (1,1) from the combined data, however, shows a ring-shaped structure toward the centre of L694-2 with two peak locations on either sides of the ring (Figure 4.1a). The NH_3 (2,2) integrated intensity map from combined data shows multiple peak locations close to the central region of the core (Figure 4.1b). Both integrated intensity maps of NH_3 (1,1) and (2,2) emission lines toward L1521F using the combined data show single peaks toward the core centre (Figures 4.2a and 4.2b). This is in agreement with the NH_3 (1,1) and (2,2) single-dish integrated intensity maps toward L1521F (Figures 3.6a and 3.6b). Note that the typical values shown for the integrated intensity maps of NH_3 (1,1) are a factor of $\sim 10 - 20$ larger than the values shown for the integrated intensity maps of NH_3 (2,2). Hence, the latter is much more intrinsically noisy than the former.

Table 4.2: Peak positions and intensities of the combined NH_3 (1,1) emission maps.

Core	R.A.	Decl.	T_{mb}
	J2000	J2000	(K)
L694-2	19 41 04.97	10 57 00	6.46
L1521F	04 28 38.67	26 51 35	8.71

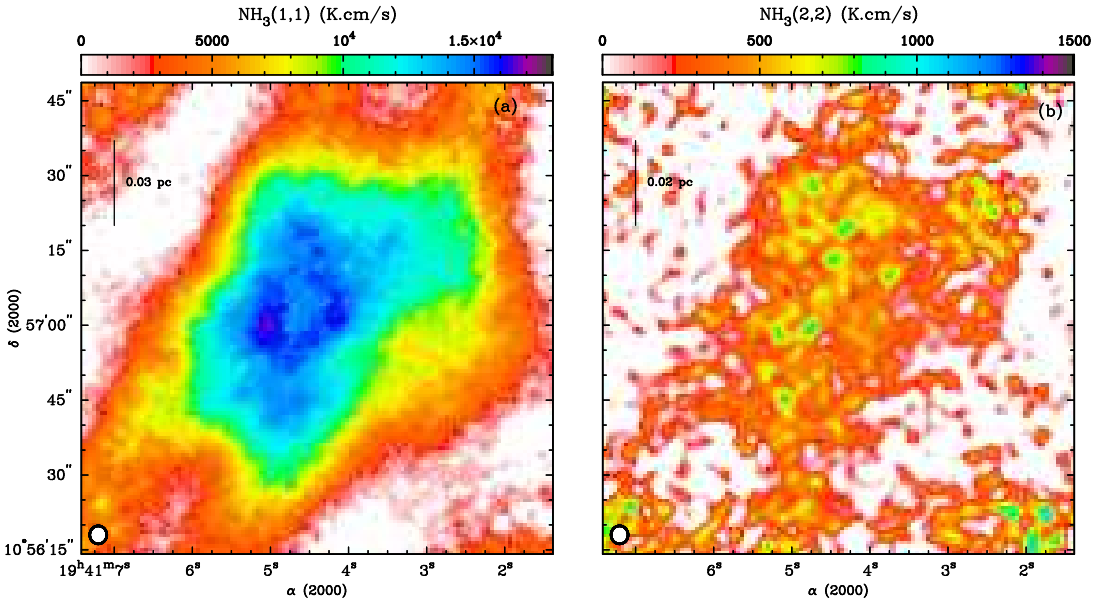

Figure 4.1: Integrated intensity maps of NH_3 (1,1) (*a*) and NH_3 (2,2) (*b*) emission toward L694-2 using combined data from JVLA and GBT. The colour scale is in K cm s^{-1}. The circle delineates the size of the JVLA beam ($\sim 3''.2 \times 3''.6$ FWHM).

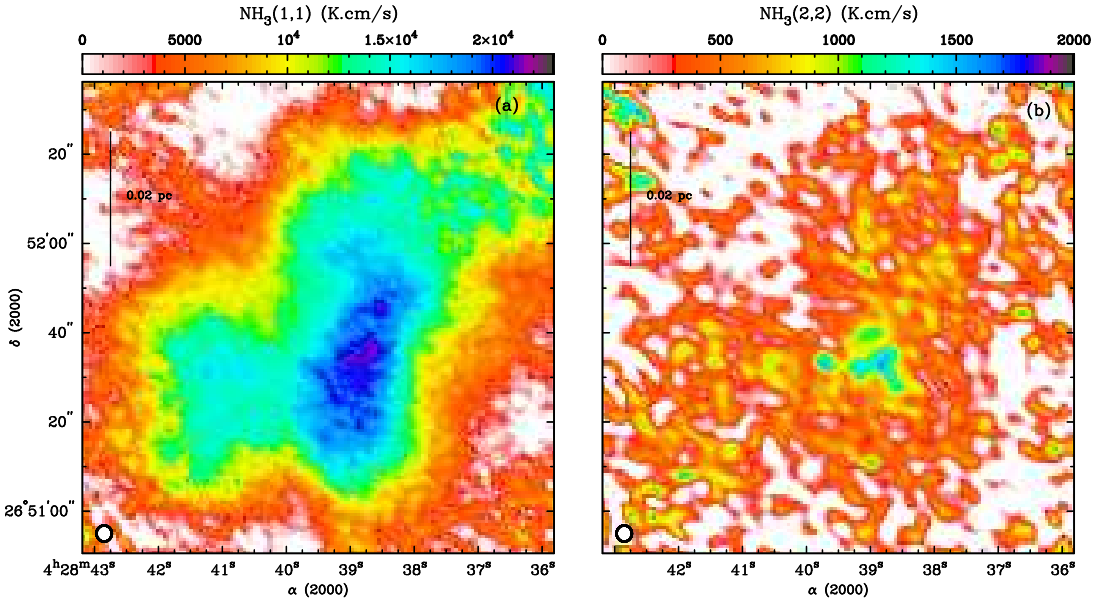

Figure 4.2: Integrated intensity maps of NH_3 (1,1) (*a*) and NH_3 (2,2) (*b*) emission toward L1521F using combined data from JVLA and GBT. The colour scale is in K cm s^{-1}. The circle delineates the size of the JVLA beam ($\sim 3''.2 \times 3''.6$ FWHM).

4.4 Density Profiles

Assuming spherical symmetry and using the azimuthally averaged Herschel 250 μm data, we used the same method described in §2.5.2.1 to determine the density profiles of the cores L694-2 and L1521F. Figures 4.3 and 4.4 show the azimuthal averages of total column densities, N_{total}, versus the projected distance from the continuum emission peak (diamonds) toward the cores L694-2 and L1521F, respectively. In each plot, the curve is the best fit of Equation (2.11), the analytical approximation to a BE sphere, to the data. The increased levels of N_{tot} for some of the data points (distance $>$ 10000 AU) in Figure 4.3 is due to the additional contribution of flux from the filament, where L694-2 is located. As mentioned in §3.3.3, we tried to remove the background emission from each cores surrounding environment as much as possible. Note that these data points are not included in the determining the best fit of Equation (2.11) to L694-2 data and do not affect the final results. The best fit parameters for each core are listed in Table 4.3. We used these values and the weighted mean of T_K for each core (see Table 3.8) to calculate the total mass, radius, central number density (n_c), and sound speed (c_s). The results for these quantities are listed in Table 4.4.

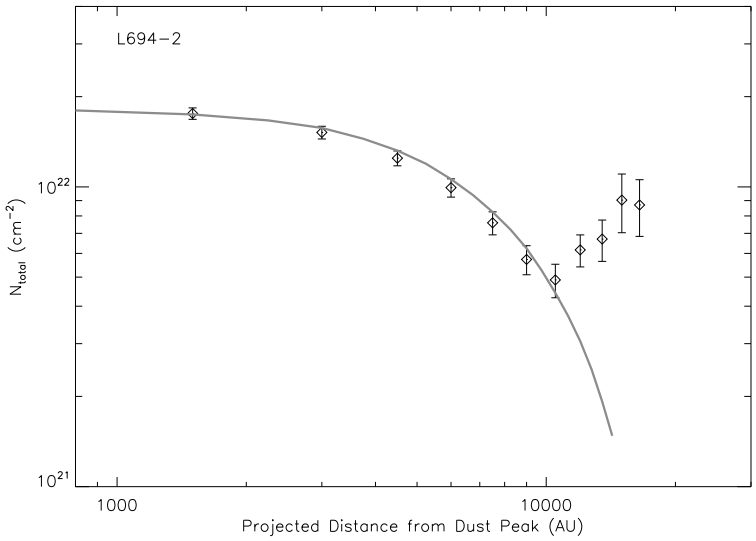

Figure 4.3: Azimuthal average of total column density, N_{total}, of L694-2 versus the projected distance from the continuum emission peak (diamonds). The curve is the best fit of Equation (2.11) to the data.

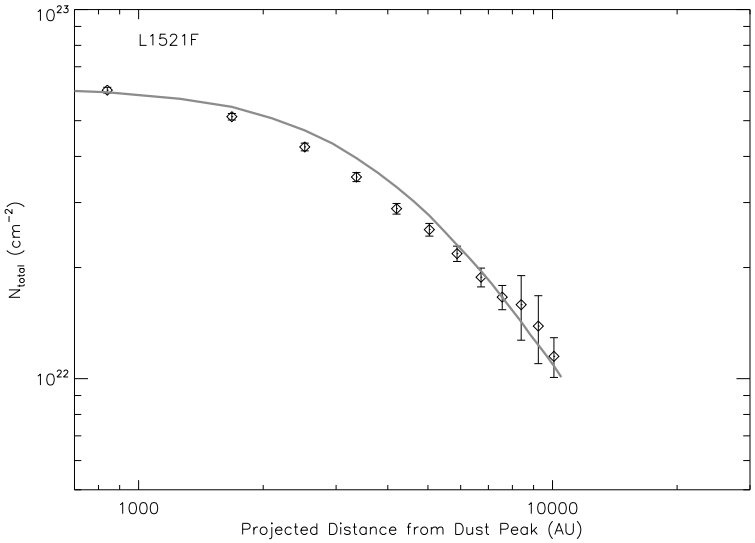

Figure 4.4: Azimuthal average of total column density, N_{total}, of L1521F versus the projected distance from the continuum emission peak (diamonds). The curve is the best fit of Equation (2.11) to the data.

Table 4.3: Best fit parameters to fit the total column density profile using Equation (2.11).

Core	Σ_c (cm^{-2})	a (pc)	c
L694-2	$(3.5 \pm 0.4)\times10^{22}$	0.013 ± 0.011	6.0 ± 0.8
L1521F	$(9.4 \pm 0.5)\times10^{22}$	0.009 ± 0.001	9 ± 1

Table 4.4: Physical characteristics calculated using the best fit parameters of Equation (2.11) listed in Table 4.3.

Core	M ($M_\odot$)	R (pc)	n_c (cm^{-3})	c_s (km s^{-1})
L694-2	2.3 ± 0.6	0.08 ± 0.01	$(3.2 \pm 0.4)\times10^5$	0.18
L1521F	4.7 ± 1.7	0.08 ± 0.01	$(1.2 \pm 0.1)\times10^6$	0.18

4.5 Radiative Transfer Modelling

To determine the radial profiles of the gas kinetic temperature, T_K, and ammonia fractional abundance, $X(\mathrm{NH_3})$, of the two cores, L694-2, and L1521F, we used the 3D molecular line transport radiative transfer code, MOLLIE (Keto 1990; Keto et al. 2004; Keto & Caselli 2008; Keto & Caselli 2010). MOLLIE considers a three-dimensional grid of physical parameters (e.g., density, temperature, velocity, turbulence, and molecular abundance) and simulates the molecular emission spectra, which can then be compared with observed line profiles.

For each core, the number density distribution is assumed to be $n(r) = n_c a^2/(r^2 + a^2)$ (Dapp & Basu 2009), where a is the radii of the inner flat region and n_c is the number density of the central region. The central number density, n_c, is related to the central density, ρ_c, such that, $n_c = \frac{\rho_c}{m_H \mu_p}$. Note that $\mu_p = 2.37$ is the mean molecular weight per free particle, and $\mu_{H_2} = 2.8$ is the mean molecular weight per hydrogen molecule (Cox 2000; Kauffmann et al. 2008). For modelling, we input a and n_c as fixed values into MOLLIE. The values of a and n_c for each core are listed in Tables 4.3 and 4.4.

Due to the high central density (i.e., $n_c > 10^5$ cm^{-3}; Di Francesco et al. 2007) observed in these cores (see Table 4.4), we assumed dust and gas to be coupled, i.e., $T_d = T_K$ and ignored the possible break-down of this assumption in the outer regions of the cores. We assume that $X(\mathrm{NH_3})$ and T can be parametrized as following (Tafalla et al. 2002; Crapsi et al. 2007):

$$X(\mathrm{NH_3}) = X_0 \, (n(r)/n_c)^{\beta}, \tag{4.1}$$

$$T = T_{\mathrm{out}} - \frac{T_{\mathrm{out}} - T_{\mathrm{in}}}{1 + (r/r_T)^{1.5}}. \tag{4.2}$$

In the above equations, X_0 is the fractional abundance of $\mathrm{NH_3}$ at the core centre and β is a power law index. The temperatures at the core centre and infinity (not the edge of the core) are given by T_{in} and T_{out}, respectively, and r_T is a length scale that determines the shape of the temperature profile. The structure of the velocity dispersion, σ_v in each core is parametrized as

$$\sigma_v = \sqrt{\sigma_T^2 + \sigma_{NT}^2}, \tag{4.3}$$

where σ_T and σ_{NT} are the thermal and non-thermal velocity dispersions. For each core, we used the weighted mean of σ_{NT} (listed in Table 3.8) as a fixed input to the model, and σ_T was determined by MOLLIE using Equation (2.7) and T at each position inside the modelled core.

For each core, we carried out the modelling in two steps: Firstly, we assumed constant profiles for temperature and fractional abundance of ammonia (i.e., $T = T_{\rm in}$ and $X(\rm NH_3) = X_0$) and ran MOLLIE using a wide, two-dimensional grid of values for $T_{\rm in}$ and X_0 to produce thousands of simulated data cubes. We compared these cubes to the observed data, and constrained the approximate range of temperature and abundance in the core. Secondly, we assumed that the abundance and temperature are parametrized as Equations (4.1) and (4.2). Therefore, we used a five-dimensional grid of values for X_0, β, $T_{\rm in}$, $T_{\rm out}$, and r_T to produce tens of thousands of simulated data cubes for comparison with the observed data and further explored the radial profiles of temperature and abundance. Note that to model each core we performed both of these steps at resolutions of $32''$ for comparison with the single-dish data from GBT and $3.4''$ FWHM for comparison with the combined JVLA and GBT data. For each core, the single-dish data capture the outer parts of the core but do not resolve the innermost region. On the other hand, the combined datasets, although not capturing the outer parts of the cores, resolve the structure at the centre of each one.

To quantify the uncertainties between the synthesized data cubes and the observed ones, we calculate the azimuthal averages of the emission intensity in each velocity channel for both synthesized and observed data cubes with the corresponding $\rm NH_3$ integrated intensity peak at the centre and radial bins of one pixel ($= 6''$ and $1.4''$ at low resolution and high resolution modes, respectively). We next calculated the χ^2 value for each radial bin in each velocity channel using

$$\chi^2 = \left(\frac{T_{\rm model} - T_{\rm obs}}{\Delta T_{\rm obs}} \right)^2, \tag{4.4}$$

where $T_{\rm obs}$ and $T_{\rm model}$ are the (azimuthally averaged) observed and synthesized emission intensities in a main beam temperature scale, and $\Delta T_{\rm obs}$ is the rms noise level of the observed data. Subsequently, we calculated the reduced χ^2 value for each radial bin given by

$$\chi^2_{\rm red} = \frac{1}{D} \sum \chi^2, \tag{4.5}$$

where D is the number of degrees of freedom defined as the number of velocity channels with emission minus the number of independent model inputs. Emission free channels are not included in the sum. Finally, we use the mean $\chi^2_{\rm red}$ of all radial bins to find the best reproductions of the observed data. Note that we obtain lower $\chi^2_{\rm red}$ modelling of high resolution data compared to that of low resolution data, due to the higher noise level of the high resolution data. For L694-2, the rms sensitivities are respectively 0.1 K and 0.3 K for the single-dish and the combined data. For L1521F, the rms sensitivities are 0.1 K and 0.6 K for the single-dish and the combined data, respectively.

The gradient in v_{LSR} across L1521F (see Figure 3.11) and L694-2 (see Figure 3.17) are $\sim$ 0.15 km s^{-1}, which is equivalent to only four velocity channels. Therefore, we argue that rotation will have a relatively small effect on our results, and we ignore the rotational motion in cores by azimuthally averaging the molecular line profiles.

We used the cluster Nestor of WestGrid located at the University of Victoria to run MOLLIE. Nestor is geared toward large parallel jobs. Based on the size of the parameter space, the spatial resolution of the products, and the availability of the computing resources, we used different numbers of processors (8, 16, or 32) with 16 GB of memory per processor. Nestor is able to produce a grid of 30,000 data products in $\sim$ 2 days depending on the model settings and the availability of the resources. The data products were then copied to a server at the National Science Infrastructure (NRC Herzberg) for imaging and analysis. The imaging stage was performed using IDL of Research Systems Incorporated. Imaging a grid of 30,000 data cubes takes $\sim$ 2 days.

4.5.1 L694-2

Infall velocities in L694-2 have been estimated to be in the range of 0.05 km s^{-1} to 0.09 km s^{-1} (Lee et al. 2004; Williams et al. 2006). We used a constant infall velocity of 0.075 km s^{-1} to model the NH_3 emission spectra of L694-2.

In the low spatial resolution mode, the synthesized data cubes had 32 pixels along each direction of R.A. and decl. with each pixel 6″ in width. The spectral resolution matched that of the GBT data of NH_3 (1,1) emission toward L694-2 (i.e., $\sim$ 0.04 km s^{-1}). The synthesized data were convolved with a Gaussian of 32″ FWHM to simulate the effect of the telescope beam. To capture the entire core, we used 14 radial bins in the $\chi^2_{\rm red}$ calculations. In the high spatial resolution mode, we configured MOLLIE to

produce data cubes with 64 pixels along each direction of R.A. and decl. with each pixel 1″.4 in width. The velocity resolution of the data cubes was ~ 0.05 km s^{-1} to match that of the interferometric data. To simulate the effect of the telescope beam, we convolved the data products with a Gaussian of 3″.4 FWHM. In this case, we used 30 radial bins for the $\chi^2_{\rm red}$ calculations.

4.5.1.1 Low Resolution

NH_3 (1,1) Spectra

2D Grid: We started by using constant profiles for temperature and fractional abundance of ammonia (i.e., $T = T_{\rm in}$ and $X(NH_3) = X_0$) and running MOLLIE using a wide two-dimensional grid of values for $T_{\rm in}$ and X_0 to produce 676 synthesized data cubes to constrain roughly the approximate range of temperature and NH_3 abundance in the core. Table 4.5 lists the specifications of the two-dimensional grid of values taken in by MOLLIE for modelling of the single-dish data of L694-2. Figure 4.5 shows the distribution of $\chi^2_{\rm red}$ for the data cubes produced by MOLLIE using this grid of parameters. The plot shows a clear minimum in the $\chi^2_{\rm red}$. In this case, the synthesized data cube that best fits the observed single-dish NH_3 (1,1) data toward L694-2 was produced using constant temperature and NH_3 abundance at $T = 7$ K and $X(NH_3)$ $= 2.0 \times 10^{-7}$ with a $\chi^2_{\rm red}$ of 5.96.

Table 4.5: The characteristics of the two-dimensional grid of values taken in by MOLLIE for modelling of the single-dish and combined (i.e., single-dish and interferometric) data of L694-2.

Parameter	Range	Step
X_0	$10^{-9} \leq X_0 \leq 10^{-4}$	Each decade divided in five increments
$T_{\rm in}$ (K)	$5 \leq T_{\rm in} \leq 30$	1 K

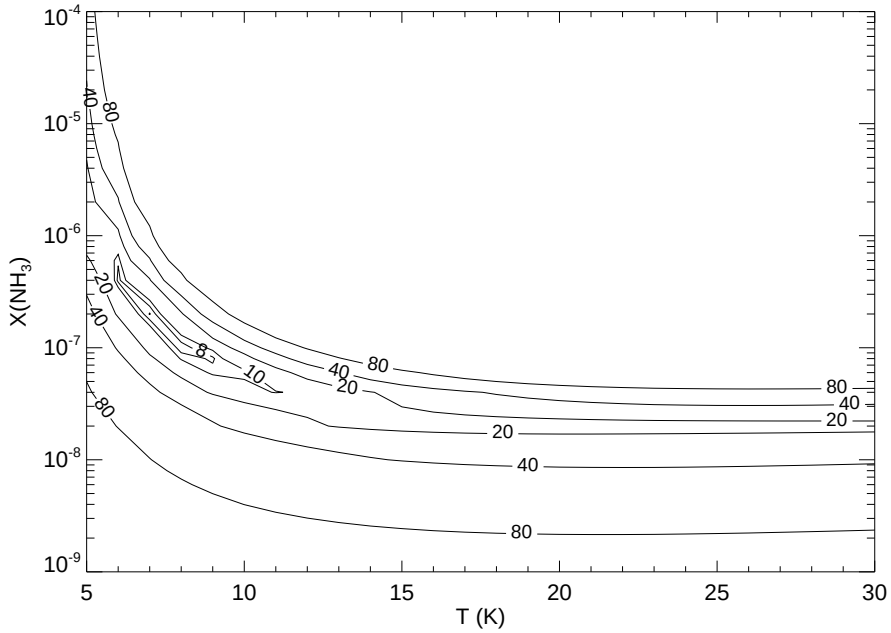

Figure 4.5: Plot of the distribution of $\chi^2_{\rm red}$ values of synthesized spectra of L694-2 at low resolution using a two-dimensional grid.

5D Grid: To determine the radial profile of NH_3 abundance and temperature inside the core, we assumed that these two quantities are parametrized as Equations (4.1) and (4.2), respectively. Table 4.6 shows the specifications of the five-dimensional grid of parameters considered by MOLLIE. In this case, we produced 55,440 synthesized data cubes. We reached a minimum $\chi^2_{\rm red}$ of 5.84, with the corresponding synthesized best fit cube produced by $X_0 = 4.0 \times 10^{-7}$, $\beta = 0.25$, $T_{\rm out} = 19$ K, $T_{\rm in} = 7$ K, and $r_T = 1$ pc.

Table 4.6: The characteristics of the five-dimensional grid of values taken in by MOLLIE for modelling of the single-dish data of L694-2.

Parameter	Range	Step
X_0	$10^{-8} \leq X_0 \leq 2 \times 10^{-6}$	Each decade divided in five increments
β	$-2 \leq \beta \leq 2$	-2, -1, -0.5, -0.25, 0, 0.25, 0.5, 1, 2
$T_{\rm out}$ (K)	$9 \leq T_{\rm out} \leq 21$	2 K
$T_{\rm in}$ (K)	$5 \leq T_{\rm in} \leq 20$	1 K
r_T (pc)	$0.001 \leq r_T \leq 10$	1 dex

Figure 4.6 shows the distributions of $\chi^2_{\rm red}$ for the model parameters (taken two

at a time). Note that the plots in Figure 4.6 focus on the region in the parameter space where the minimum $\chi^2_{\rm red}$ is located. Figures 4.6a, 4.6c, and 4.6f clearly show a region in the parameter space constrained by $10^{-7} \lesssim X_0 \lesssim 10^{-6}$, $0 \lesssim \beta \lesssim 0.5$, and 6 K $\lesssim T_{\rm in} \lesssim$ 8 K, where $\chi^2_{\rm red}$ is less than 8 and is approaching a minimum. Our calculations of the minimum $\chi^2_{\rm red}$ strongly favour larger r_T values (i.e., 1 pc and 10 pc; see Figures 4.6d, 4.6g, 4.6i, 4.6j). It is evident from Equation (4.2) that for r_T values much greater than the core radius ($R \sim 0.08$ pc for L694-2), the temperature is effectively constant inside the core and it is not possible to constrain $T_{\rm out}$ well (see Figures 4.6b, 4.6e, and 4.6h).

Figures 4.7 and 4.8 show normalized histograms of the model parameter values that produce the fifty ($\chi^2_{\rm red} \leq 6.8$) and twenty ($\chi^2_{\rm red} \leq 6.4$) synthesized data cubes that best match the single-dish observed data of NH_3 (1,1) emission toward L694-2, i.e., the lowest $\chi^2_{\rm red}$ values. The values $X_0 = 4 \times 10^{-7}$, $\beta = 0.25$, $T_{\rm in} = 7$ K, and $r_T \gg R$ are most likely to yield synthesized spectra that best match the observed data. (These values also produce the synthesized data cube corresponding to the globally minimum $\chi^2_{\rm red}$ in the five-dimensional parameter space.) Due to the large value of r_T favoured by the χ^2 test, $T_{\rm out}$ cannot be constrained. Note that $r_T = 0.1$ pc (i.e., $r_T \sim R$) can produce synthesized spectra with low $\chi^2_{\rm red}$ only when paired with low values of $T_{\rm out}$ (e.g. $T_{\rm out} = 9$ K; see Figure 4.6i). It is evident from Figure 4.7 that for each model parameter there is a range of values that can reproduce synthesized spectra with relatively low $\chi^2_{\rm red}$. Table 4.7 lists the range of acceptable values for each model parameter.

Figure 4.9 shows the observed and synthesized spectra of NH_3 (1,1) emission at the core centre (i.e., the location of maximum NH_3 (1,1) integrated intensity at $32''$ FWHM resolution, see Table 3.2), 0.03 pc ($\sim$ one third of core radius), and 0.06 pc ($\sim$ two third of core radius) toward west. At the core centre, the intensity of the main hyperfine component of the synthesized spectra is slightly lower than the observed intensity, while the brightness of the satellite components toward the same position are better matched by the synthesized data. On the other hand, the intensity of the main hyperfine component toward locations offset from the core centre is slightly over-produced by MOLLIE. Such differences in how well synthesized spectra can match one component versus the others could be due to a slight departure from LTE conditions in L694-2. (Note that we assume LTE conditions and use the relative intensities of the hyperfine components expected in LTE conditions to build the synthesized spectra.) Despite of such shortcomings, MOLLIE was able to reproduce well the

general characteristics such as, the line widths for all hyperfine components and the intensities for the satellite components of the single-dish data of NH_3 (1,1) emission toward different positions in L694-2.

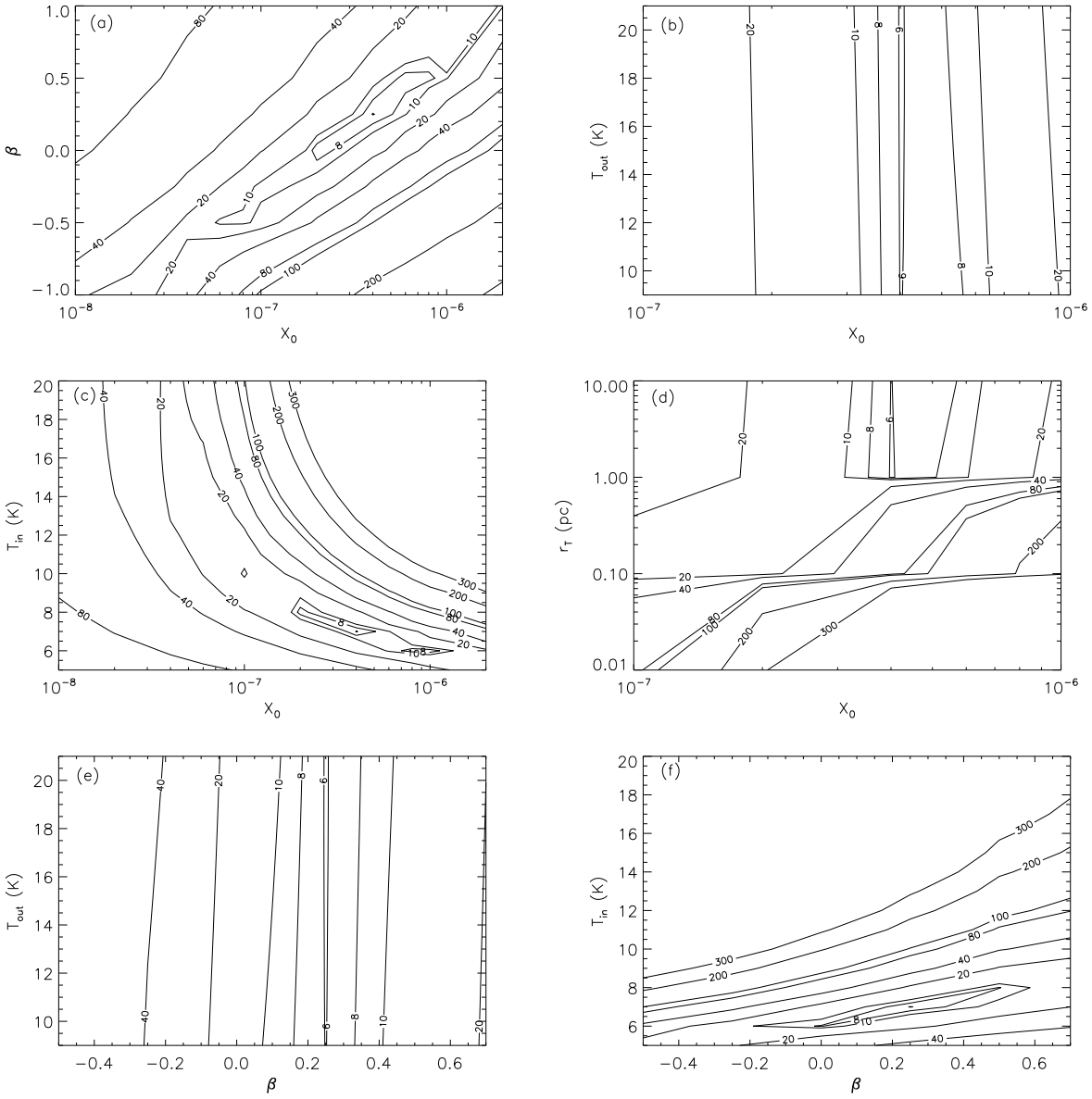

Figure 4.6: Plot of the distribution of $\chi^2_{\rm red}$ values of synthesized spectra of L694-2 produced by MOLLIE at low resolution using a five-dimensional grid.

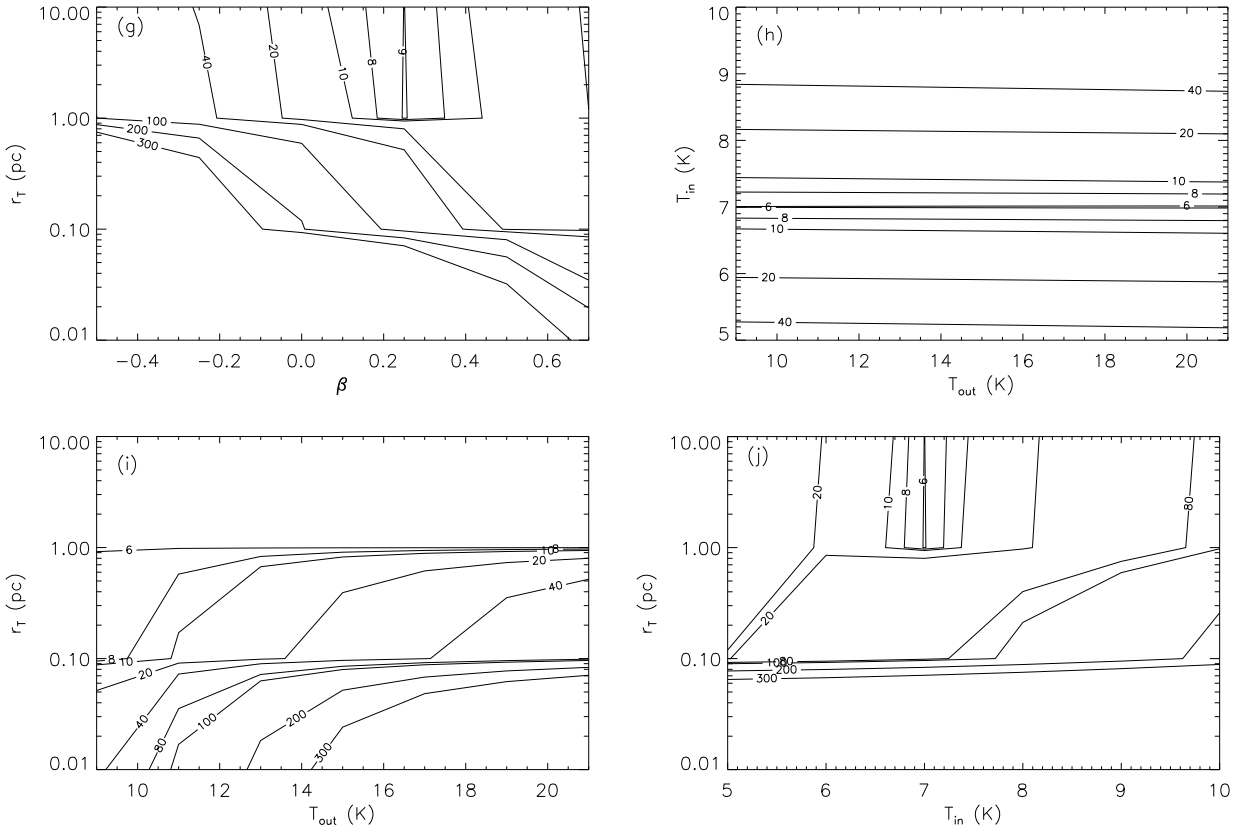

Figure 4.6: Continued.

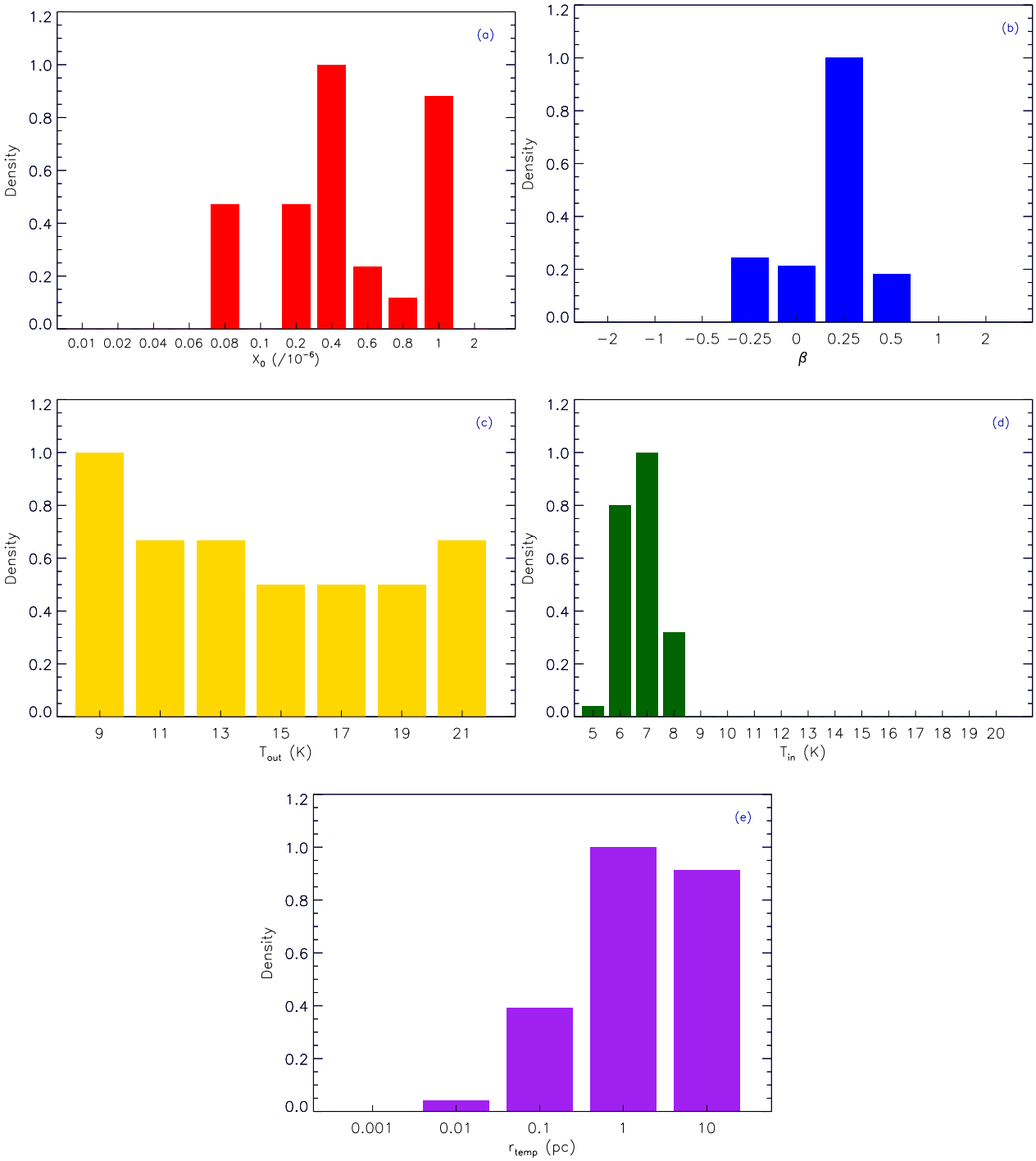

Figure 4.7: Normalized histograms of the model parameters that produce the best fifty synthesized data cubes ($\chi^2_{\rm red} \leq 6.8$) using a five-dimensional grid in the low-resolution mode for L694-2.

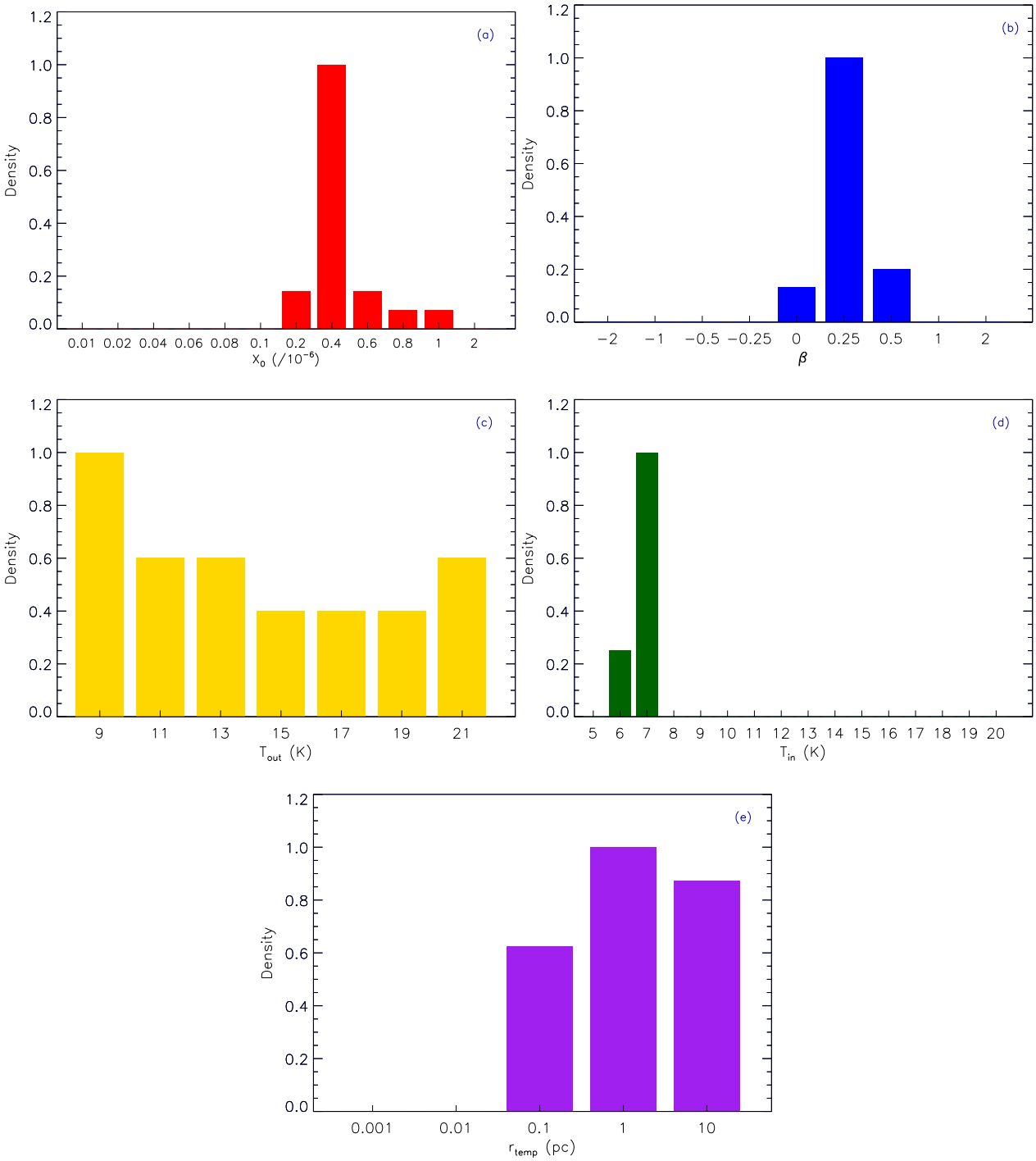

Figure 4.8: Normalized histograms of the model parameters that produce the best twenty synthesized data cubes ($\chi^2_{\rm red} \leq 6.4$) using a five-dimensional grid in the low-resolution mode for L694-2.

Table 4.7: Range of acceptable values for model parameters to reproduce NH_3 (1,1) spectra of L694-2 at low spatial resolution.

Parameter	Range	Best Fit
X_0	$10^{-7} \leq X_0 \leq 10^{-6}$	4.0×10^{-7}
β	$-0.25 \leq \beta \leq 0.5$	0.25
$T_{\rm out}$ (K)	unconstrained	...
$T_{\rm in}$ (K)	$6 \leq T_{\rm in} \leq 8$	7 K
r_T (pc)	$r_T \gg 0.1$	...

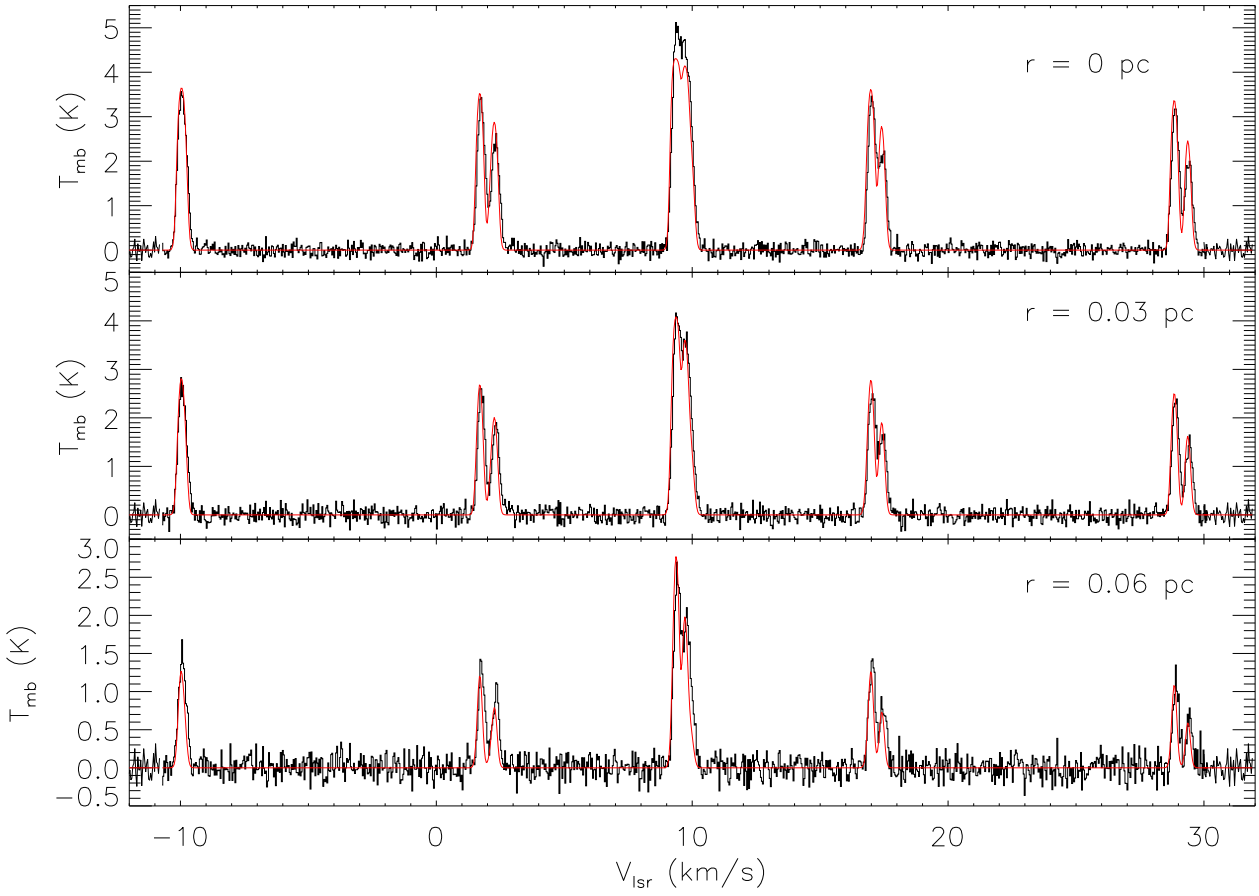

Figure 4.9: Observed (*black*) and synthesized (*red*) NH_3 (1,1) spectra of L694-2 at low spatial resolution. From top to bottom: The spectra at the core centre (*top*), 0.03 pc away from the centre toward west (*middle*), and 0.06 pc away from the centre toward west (*bottom*).

NH_3 (2,2) Spectra

We produced synthesized data cubes of NH_3 (2,2) emission at low spatial resolution using the same parameter space described in Table 4.6. Due to the low sensitivity of the observed data, however, modelling of weaker NH_3 (2,2) does not provide any further constraints on the model parameters. Therefore, we only present the synthesized spectra produced using the model parameters that yield the best match to the NH_3 (1,1) observed data (i.e., $X_0 = 4.0 \times 10^{-7}$, $\beta = 0.25$, $T_{\rm out} = 19$ K, $T_{\rm in} = 7$ K, and $r_T = 1$ pc). Figure 4.10 shows the observed and synthesized spectra of the main hyperfine component of NH_3 (2,2) emission toward L694-2. We only detect the main hyperfine component of NH_3 (2,2) in our observed spectra, therefore only this component is presented in the plots. Due to the smaller size of the NH_3 (2,2) emission region (compared to that of NH_3 (1,1)), we only present the spectra in two locations inside the core. It is evident that the model parameters that produce the best match to the NH_3 (1,1) spectra also yield synthesized NH_3 (2,2) spectra that well match the intensity and line width of the corresponding observed line profiles.

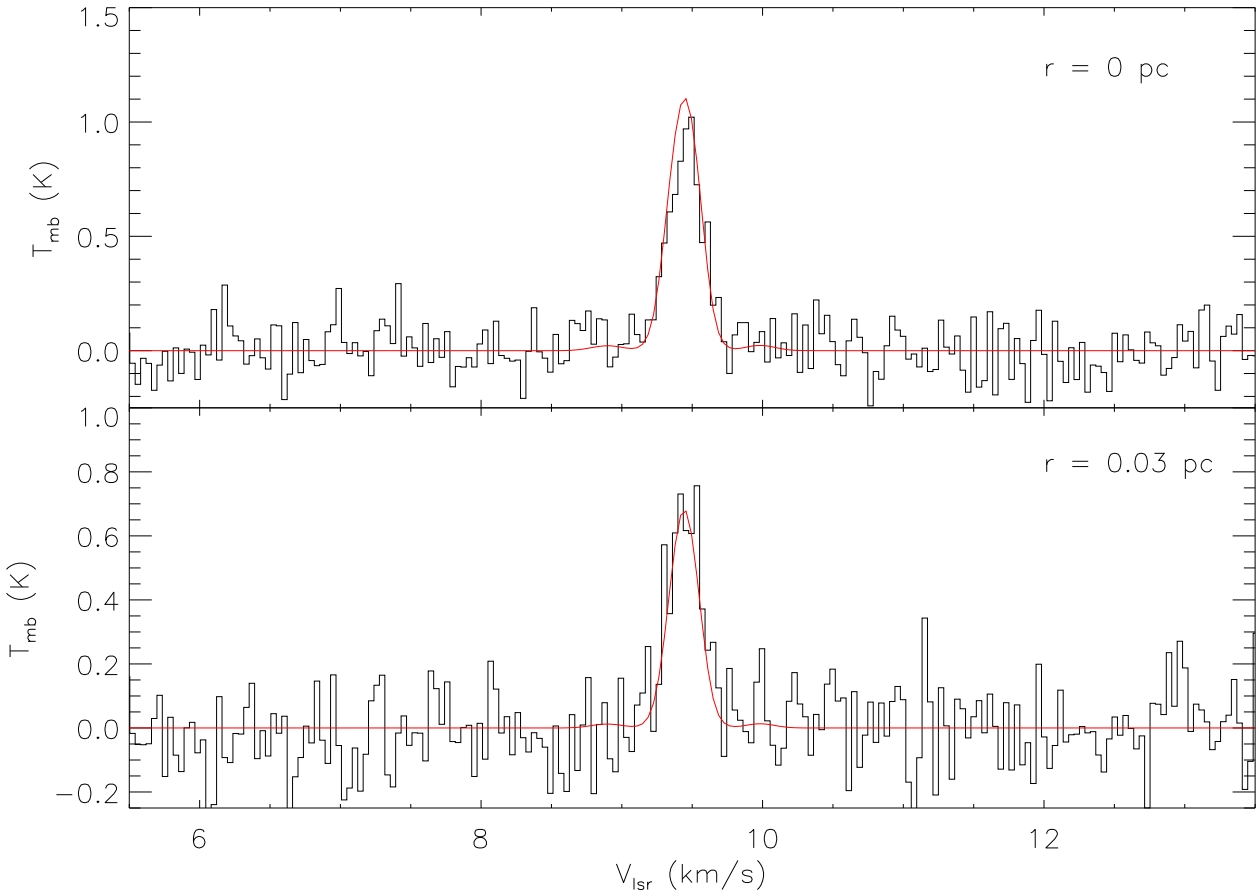

Figure 4.10: Observed (*black*) and synthesized (*red*) NH_3 (2,2) spectra of L694-2 at low spatial resolution. From top to bottom: The spectra at the core centre (*top*), 0.03 pc away from the centre toward west (*bottom*).

4.5.1.2 High Resolution

NH_3 (1,1) Spectra

2D Grid: Similar to our method in §4.5.1.1, we started by assuming constant profiles of T and $X(NH_3)$ across L694-2 and used MOLLIE to produce 676 synthesized data cubes to constrain roughly the approximate range of temperature and NH_3 abundance over a wide two-dimensional grid of values. In this case, we used the same two-dimensional grid described in Table 4.5. Figure 4.11 shows the resulting $\chi^2_{\rm red}$ surface for the data cubes produced by MOLLIE. The plot shows a clear minimum in the $\chi^2_{\rm red}$. In this case, the $\chi^2_{\rm red}$ reached a minimum of 1.94 that corresponded to a synthesized data cube produced by using constant temperature and NH_3 abundance at $T = 9$ K and $X(NH_3) = 1.0 \times 10^{-7}$. Note that the best fit two-dimensional model

parameters in the low resolution mode (i.e., $X(\mathrm{NH_3}) = 2.0 \times 10^{-7}$ and $T = 7$ K) do provide a good fit to the observed data at high resolution with relatively low $\chi^2_{\mathrm{red}} = 2.28$.

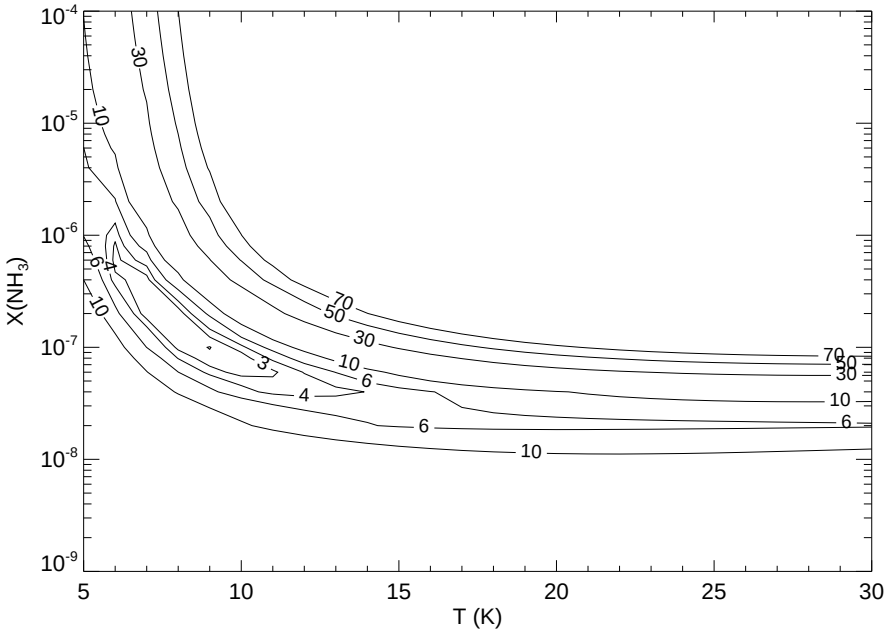

Figure 4.11: Plot of the distribution of χ^2_{red} values of synthesized spectra of L694-2 produced by MOLLIE at high spatial resolution using a two-dimensional grid.

5D Grid: Following the method described in §4.5.1.1, we assumed that two quantities are parametrized as Equations (4.1) and (4.2), respectively, and defined a five-dimensional parameter space to determine the radial profile of $\mathrm{NH_3}$ abundance and temperature inside the core. In this case, the grid is very similar to the five-dimensional grid we used in §4.5.1.1, with only a slight modification. Since our results of modelling the single-dish data of L694-2 show that the index β varies in the range $-0.25 \leq \beta \leq 0.5$, we focused on $-1 \leq \beta \leq 1$. Table 4.8 shows the specifications of the grid of values used to reproduce the combined data of $\mathrm{NH_3}$ (1,1) emission toward L694-2. In this case, we produced 43,120 synthesized data cubes. Six synthesized data cubes corresponded to the minimum χ^2_{red} of 1.48. These data cubes were produced by the following parameters $X_0 = 2.0 \times 10^{-7}$, $\beta = 0.0$, $T_{\mathrm{in}} = 8$ K, $r_T = 10$ pc, and $T_{\mathrm{out}} = 9$ K, 11 K, 13 K, 15 K, 17 K, and 19 K.

The panels in Figure 4.12 show the distributions of χ^2_{red} for the model parameters. Figures 4.12a, 4.12c, and 4.12f clearly show a region in parameter space constrained by $6 \times 10^{-8} \lesssim X_0 \lesssim 6 \times 10^{-7}$, $-0.5 \lesssim \beta \lesssim 0.5$, and 6 K $\lesssim T_{\mathrm{in}} \lesssim$ 10 K, where χ^2_{red} is less than 3 and is approaching a minimum. Similar to our results in §4.5.1.1, the χ^2_{red}

Table 4.8: The characteristics of the five-dimensional grid of values taken in by MOLLIE for modelling of the combined data of L694-2.

Parameter	Range	Step
X_0	$10^{-8} \leq X_0 \leq 2 \times 10^{-6}$	Each decade divided in five increments
β	$-1 \leq \beta \leq 1$	-1, -0.5, -0.25, 0, 0.25, 0.5, 1
$T_{\rm out}$ (K)	$9 \leq T_{\rm out} \leq 21$	2 K
$T_{\rm in}$ (K)	$5 \leq T_{\rm in} \leq 20$	1 K
r_T (pc)	$0.001 \leq r_T \leq 10$	1 dex

test strongly favours $r_T \gg R$ (i.e., 1 pc and 10 pc; see Figures 4.12d, 4.12g, 4.12i, 4.12j). Large values of r_T result in an approximately constant temperature profile throughout the core and do not provide any strong constraints on the value of $T_{\rm out}$ (see Figures 4.12b, 4.12e, and 4.12h).

To demonstrate which model parameters are more likely to reproduce the observed data we again show normalized histograms of model parameter values that produce fifty ($\chi^2_{\rm red} \leq 1.79$) and twenty ($\chi^2_{\rm red} \leq 1.7$) synthesized data cubes that best match the combined dataset of NH_3 (1,1) emission toward L694-2 in Figures 4.13 and 4.14, respectively. The values $X_0 = 2 \times 10^{-7}$, $\beta = 0.0$, $T_{\rm in} = 8$ K, and $r_T \gg R$ are most likely to yield synthesized spectra that best match the observed data. Similar to our results of the modelling of the single-dish data, $T_{\rm out}$ cannot be constrained due to the large value of r_T favoured by the χ^2 test. Table 4.9 lists the range of acceptable values for each model parameter. At the high resolution mode, $X_0 = 2.0 \times 10^{-7}$, $\beta = 0.0$, and $T_{\rm in} = 8$ K correspond to the synthesized data cube that provides the globally minimum $\chi^2_{\rm red}$ in the five-dimensional parameter space and are most likely to yield synthesized data cubes that well match the observed data.

To explore further the best value of β and investigate the possibilities of a slight enhancement in the central abundance of NH_3 versus a slight decrease in $X(NH_3)$ at the core centre, we ran MOLLIE using a finer grid of values for β (i.e., $-0.5 \leq \beta \leq 0.5$ in steps of 0.1). Here, the $\chi^2_{\rm red}$ test strongly favoured $0.0 \leq \beta \leq 0.5$, suggesting a possible slight enhance in $X(NH_3)$ at the centre.

Figure 4.15 shows the observed and synthesized spectra of NH_3 (1,1) emission at the core centre (i.e., location of maximum NH_3 (1,1) integrated intensity at $3''.4$ FWHM resolution, see Table 4.2), 0.017 pc ($\sim$ one third of the radius of the emission

region mapped by JVLA; see Figure 4.1), and 0.034 pc ($\sim$ two thirds of the radius of the emission region mapped by JVLA; see Figure 4.1) toward west. In all three locations, the intensities of most of the hyperfine components of the synthesized spectra appear slightly lower compared to their corresponding counterpart in the observed spectra. The line width of the hyperfine components, however, are well reproduced by MOLLIE and we identify the synthesized data cube as a good match to the observed data of NH_3 (1,1) emission toward L694-2 at high spatial resolution.

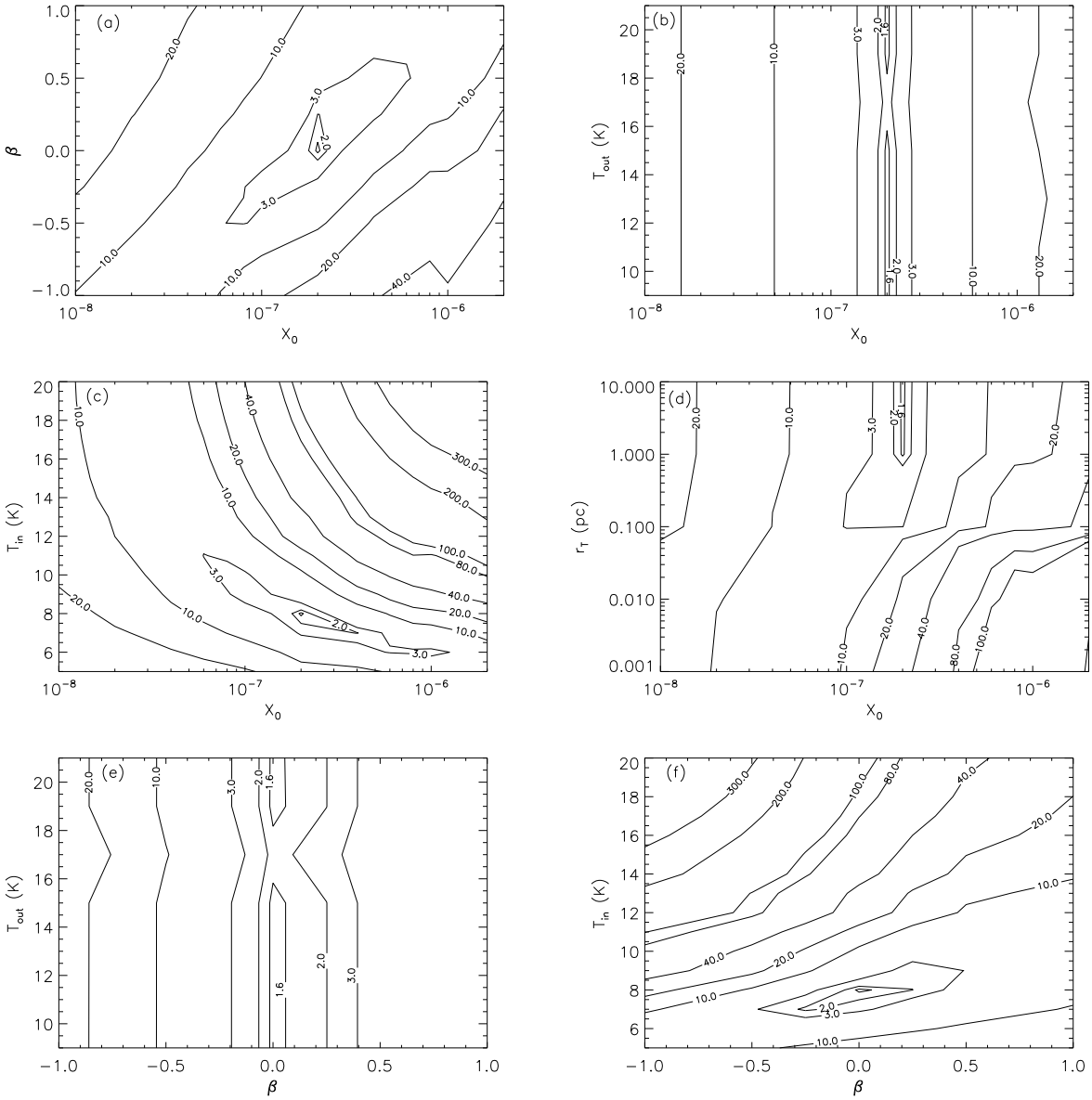

Figure 4.12: Plot of the distribution of $\chi^2_{\rm red}$ values of synthesized spectra of L694-2 produced by MOLLIE at high resolution using a five-dimensional grid.

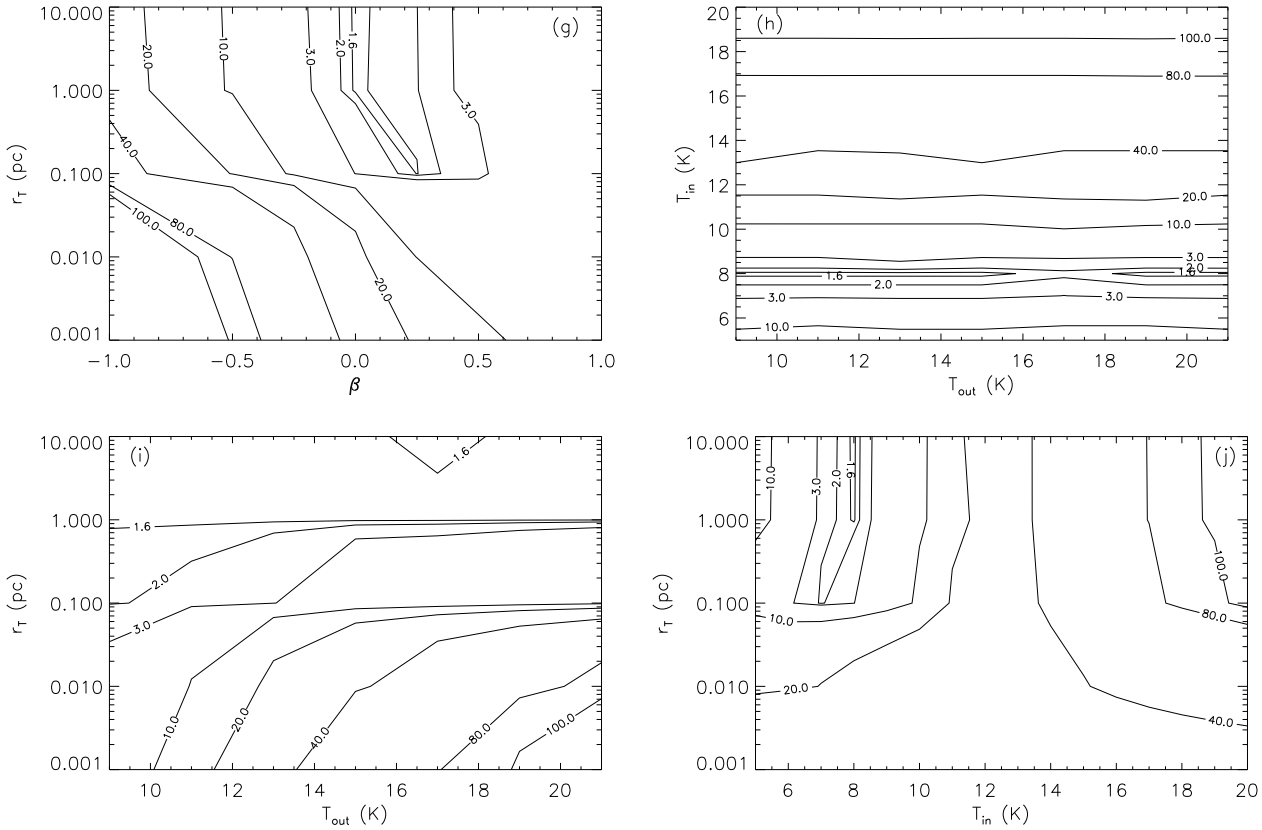

Figure 4.12: Continued.

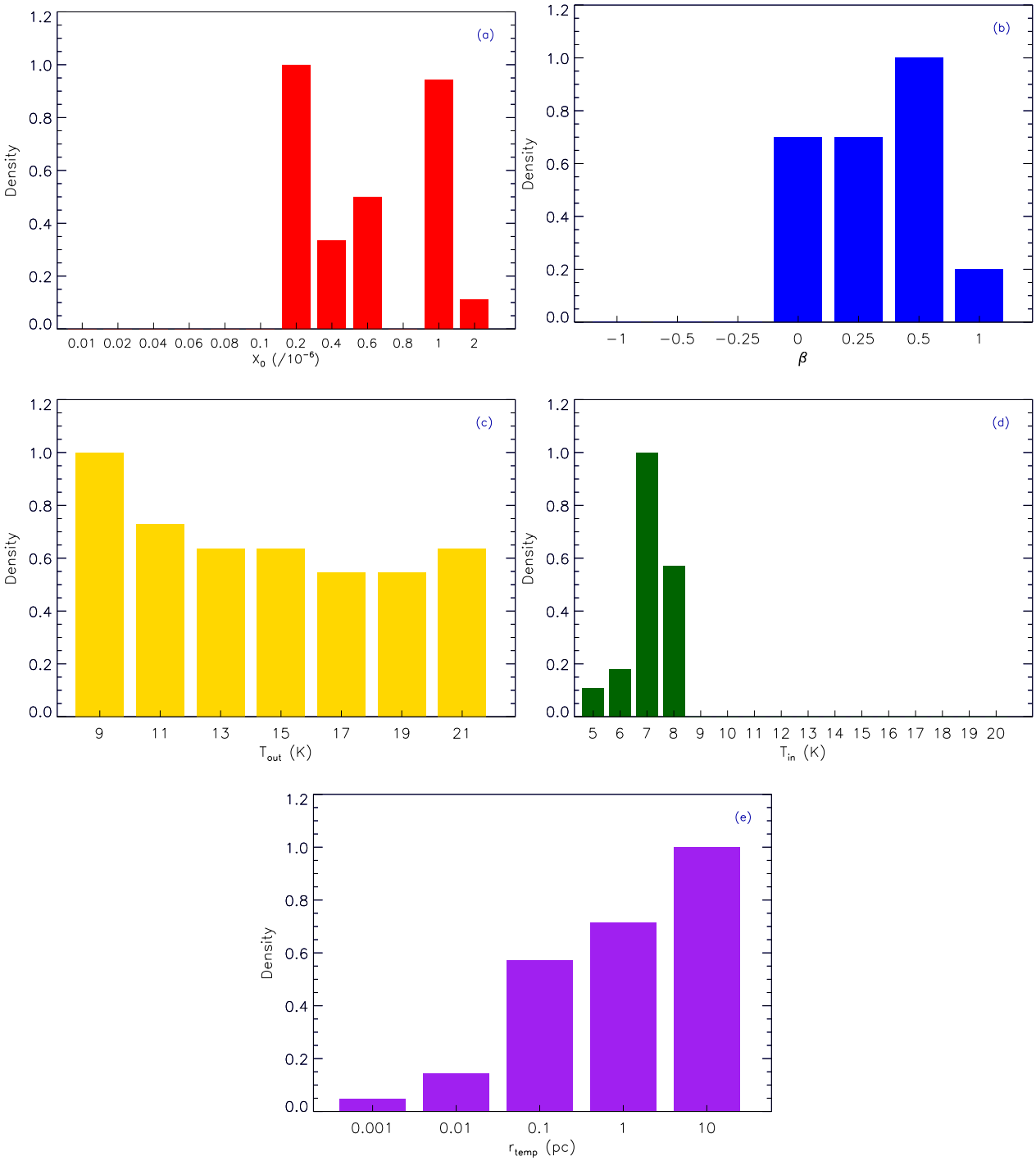

Figure 4.13: Normalized histograms of the model parameters that produce the best top fifty synthesized data cubes ($\chi^2_{\rm red} \leq 1.79$) using a five-dimensional grid at the high resolution mode for L694-2.

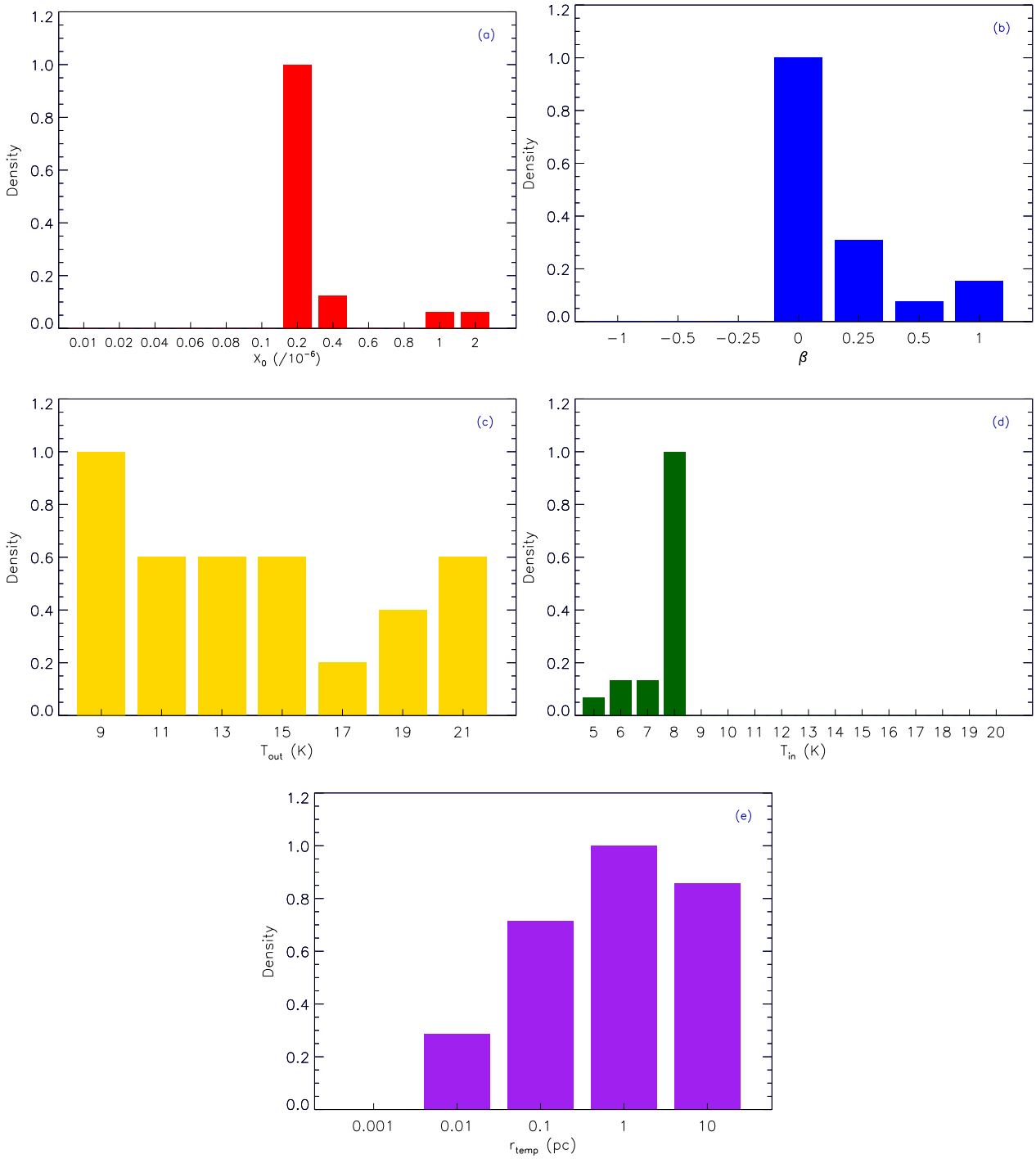

Figure 4.14: Normalized histograms of the model parameters that produce the best top twenty synthesized data cubes ($\chi^2_{\rm red} \leq 1.7$) using a five-dimensional grid at the high resolution mode for L694-2.

Table 4.9: Range of acceptable values for model parameters to reproduce NH_3 (1,1) spectra of L694-2 at high spatial resolution.

Parameter	Range	Best Fit
X_0	$2 \times 10^{-7} \leq X_0 \leq 2 \times 10^{-6}$	2.0×10^{-7}
β	$0.0 \leq \beta \leq 1.0$	0.0
$T_{\rm out}$ (K)	unconstrained	...
$T_{\rm in}$ (K)	$5 \leq T_{\rm in} \leq 8$	8 K
r_T (pc)	$r_T \gg 0.1$	10 pc

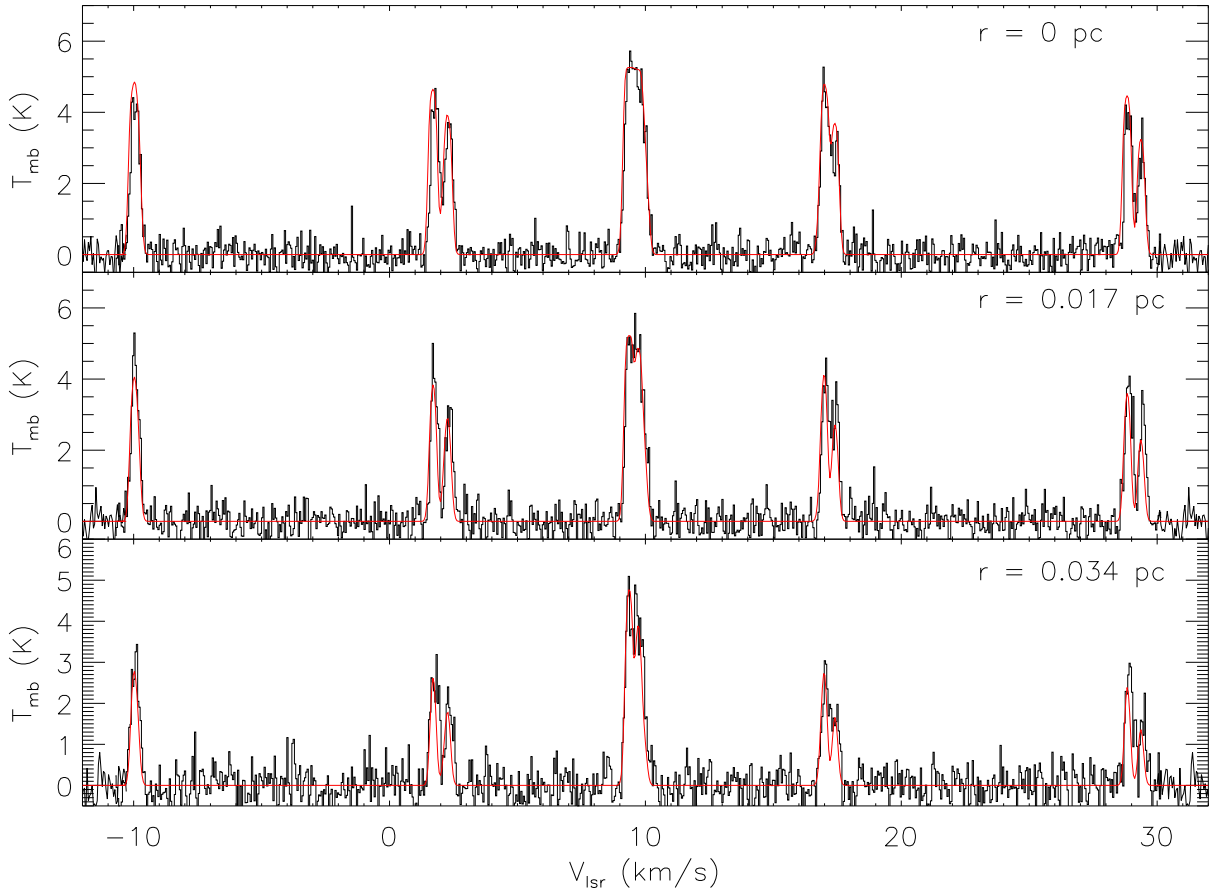

Figure 4.15: Observed (*black*) and synthesized (*red*) NH_3 (1,1) spectra of L694-2 at high spatial resolution. From top to bottom: The spectra at the core centre (*top*), 0.017 pc away from the centre toward west (*middle*), and 0.034 pc away from the centre toward west (*bottom*).

NH_3 (2,2) Spectra

Figure 4.16 shows the observed and synthesized spectra of the main hyperfine component of NH_3 (2,2) emission toward L694-2 at high spatial resolution. The synthesized spectra are produced using the model parameters that yield the best match to the NH_3 (1,1) observed data at high spatial resolution (i.e., $X_0 = 2.0 \times 10^{-7}$, $\beta = 0.0$, $T_{\rm out} = 9$ K, $T_{\rm in} = 8$ K, and $r_T = 10$ pc). Due to the smaller size of the NH_3 (2,2) emission region (compared to that of NH_3 (1,1)), we only present the spectra in two locations inside the core. It is evident that the line profiles of the synthesized NH_3 (2,2) spectra are higher in intensity and have slightly wider line widths compared to the line profiles of the observed spectra in both locations toward L694-2.

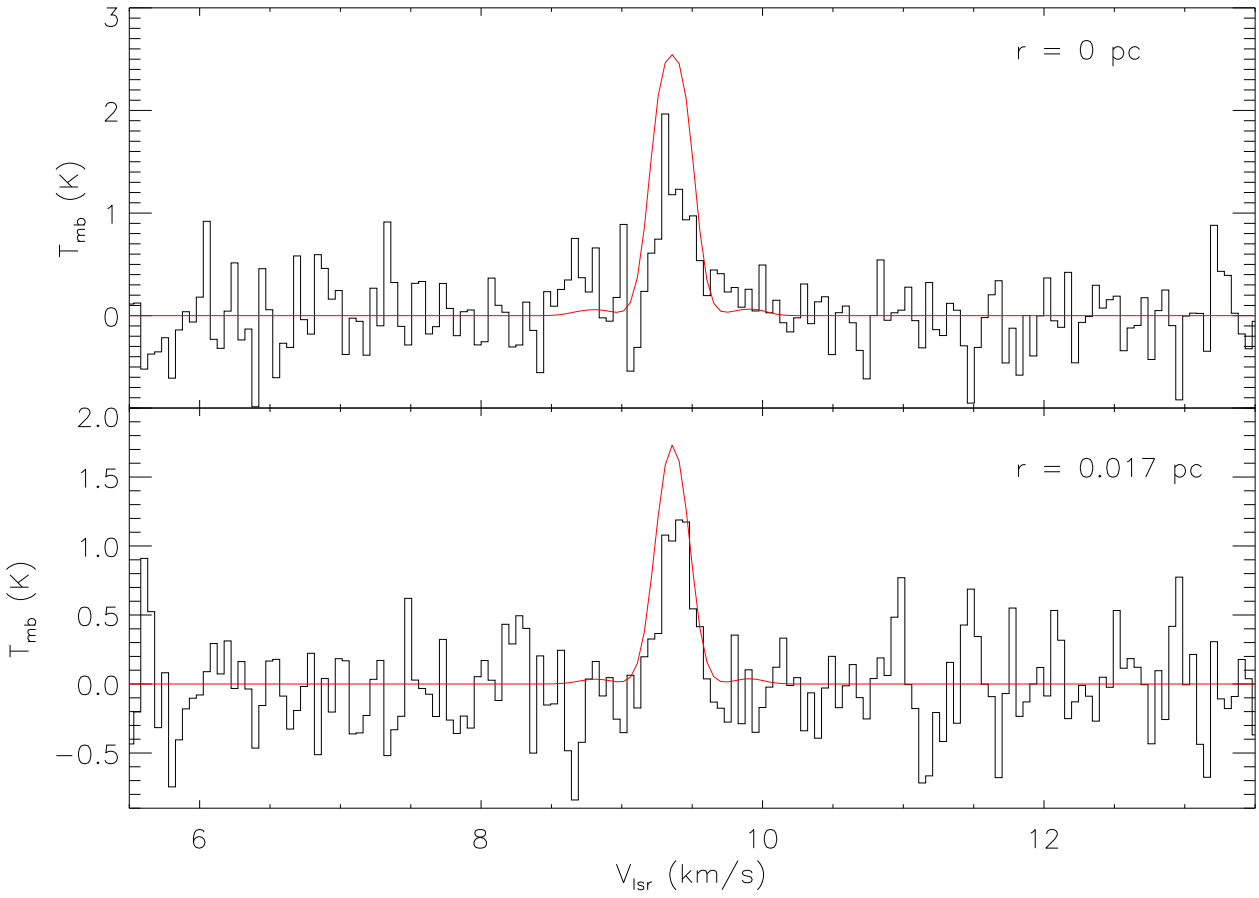

Figure 4.16: Observed (*black*) and synthesized (*red*) NH_3 (2,2) spectra of L694-2 at high spatial resolution. From top to bottom: The spectra at the core centre (*top*), 0.017 pc away from the centre toward west (*bottom*)

Our results from modelling of NH_3 (1,1) emission line toward L694-2 using the

single-dish (GBT) and combined (GBT and JVLA) datasets show that the variations in the radial profiles of temperature and NH_3 abundance are not significant. The temperature profile is effectively constant at 7 K and 8 K at low and high spatial resolutions, respectively. The radial profile of $X(NH_3)$ shows a slight enhancement toward the core centre at low spatial resolutions. At high spatial resolution, $X(NH_3)$ is consistent with a constant profile at 2×10^{-7} with the possibility of a small increase in central abundance. Figure 4.17 shows the radial profiles of T and $X(NH_3)$ at both low and high spatial resolutions using the model parameters that produced the data cubes with globally minimum $\chi^2_{\rm red}$ in the parameter space.

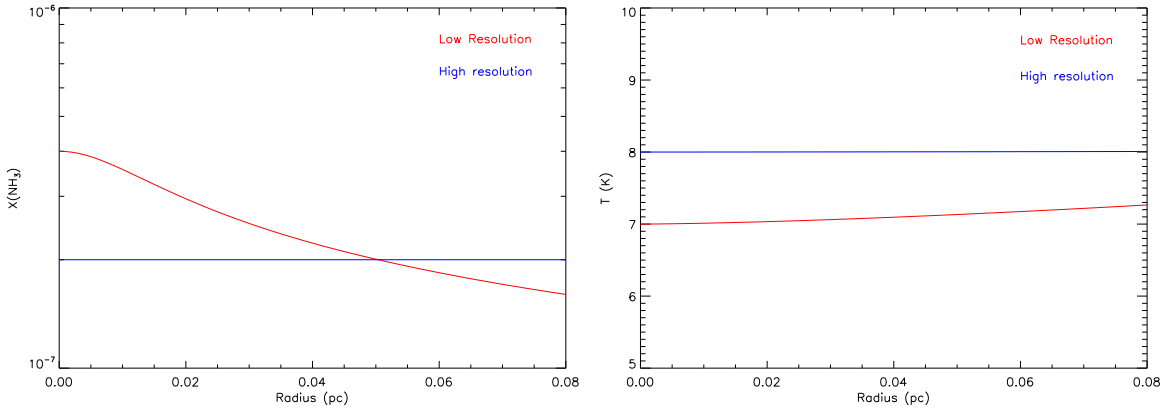

Figure 4.17: Radial profiles of $X(NH_3)$ and T of L694-2 at low (*red*) and high (*blue*) spatial resolutions using the model parameters that produced the data cubes with globally minimum $\chi^2_{\rm red}$ in the parameter space.

4.5.2 L1521F

L1521F has been identified as a strong infall candidate (see, e.g., Onishi et al. 1999, Crapsi et al. 2004, Crapsi et al. 2005a, Schnee et al. 2013). Onishi et al. (1999) estimated an infall velocity of ~ 0.2 km s^{-1} $-$ 0.3 km s^{-1} using Monte Carlo simulations of various emission lines of HCO^+ and $H^{13}CO^+$. Schnee et al. (2013) fit HCO^+ (3$-$2) emission line toward L1521F using the HILL5 model (De Vries & Myers 2005) and estimated an infall velocity of $\sim 0.42 \pm 0.01$ km s^{-1}. We do detect a slight asymmetry in the line profile of the main hyperfine component of NH_3 (1,1) toward L1521F. To try to reproduce the asymmetry, we first input a constant infall velocity of 0.25 km s^{-1} in MOLLIE. The resulting spectra showed much larger degree of asymmetry compared to that of the observed spectra, however. Therefore, we ignored the effect of infall and set the infall velocity to zero in the case of L1521F.

In the low spatial resolution mode, the synthesized data cubes had 64 pixels along each direction of R.A. and decl. with each pixel 6″ in width. To capture the entire core we used 23 radial bins in the $\chi^2_{\rm red}$ calculations. The rest of the specifications are similar to the configurations used for the modelling of L694-2. The details are described in §4.5.1.

4.5.2.1 Low Resolution

NH_3 (1,1) Spectra

2D Grid: Similar to our approach for the modelling of L694-2 (described in §4.5.2), we assumed constant profiles of T and $X(NH_3)$ across the core and used a wide two-dimensional parameter space to constrain roughly the range of possible temperature and abundance inside L1521F. The parameter space is described in Table 4.18 and produces 1,656 data cubes. Figure 4.18 shows the distribution of $\chi^2_{\rm red}$ for the data cubes produced by MOLLIE. Unlike the $\chi^2_{\rm red}$ distribution of the two-dimensional parameter space for L694-2 (i.e., Figures 4.5 and 4.11), where one clear global minimum was evident in the $\chi^2_{\rm red}$ distribution, Figure 4.18 shows four regions with $X(NH_3)$ in the range of $10^{-8} - 10^{-7}$ and temperatures between 5 K and 40 K with $\chi^2_{\rm red}$ less than 24. The global minimum $\chi^2_{\rm red}$ is equal to 19.88 and corresponds to the synthesized data cube produced by $X(NH_3) = 2.0 \times 10^{-8}$ and $T = 12$ K. It is also interesting to note that the minimum $\chi^2_{\rm red}$ achieved using the two-dimensional parameter space for L1521F (= 19.88) is significantly higher than its counterpart calculated for L694-2 (= 5.96; see §4.5.1.1). This could suggest that constant profiles of $X(NH_3)$ and T are not the best options to describe the physical structure of L1521F.

Table 4.10: The characteristics of the two-dimensional grid of values taken in by MOLLIE for modelling of the single-dish data of L1521F.

Parameter	Range	Step
X_0	$10^{-10} \leq X_0 \leq 10^{-3}$	Each decade divided in five increments
$T_{\rm in}$ (K)	$5 \leq T_{\rm in} \leq 50$	1 K

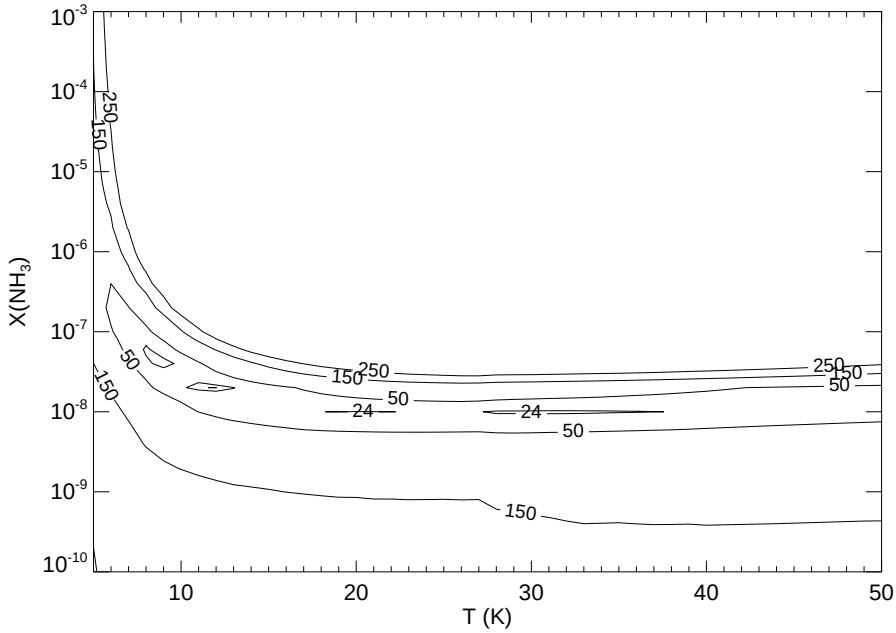

Figure 4.18: Plot of the distribution of $\chi^2_{\rm red}$ values of synthesized spectra of L1521F produced by MOLLIE at low resolution using a two-dimensional grid.

Wide 5D Grid: Due to the wide range of temperatures with relatively lower $\chi^2_{\rm red}$ values in the previous stage of modelling of L1521F data, we started our investigations of the five-dimensional parameter space with a wide and coarsely sampled grid of values to narrow the ranges of possible model parameters. This wide five dimensional grid is described in Table 4.11 and yields 31,752 synthesized data cubes. For each model parameter, Figure 4.19 shows the range of values favoured by low $\chi^2_{\rm red}$ from the fifty data cubes that best match the observations. Again, note that the purpose of this step is *only* to narrow the range of acceptable values for each model parameter. Due to the presence of a VeLLO inside L1521F, we sampled a wide range of temperatures for $T_{\rm in}$ and $T_{\rm out}$. We found out that $T_{\rm in}$ is primarily $\leq$ 11 K, whereas $T_{\rm out}$ showed a broad range of relatively well-fit temperature values. Since this core is not externally heated by other mechanisms, we would expect $T_{\rm out}$ to be less than $\sim$ 20 K. Such low values of T are also confirmed by the dust temperature maps of the surroundings of L1521F derived using Herschel data (J. Kirk, private communication), where T_{dust} of the surrounding of L1521F is $\sim$ 15 K. Although gas and dust temperatures are not necessarily equal at lower densities outside of cores, we do not expect them to be significantly different. Therefore, we exclude all $T_{\rm out} > 20$ K from future analysis.

Table 4.11: Specifications of the wide five-dimensional grid for modelling L1521F at low resolution.

Parameter	Range	Step
X_0	$5 \times 10^{-9} \leq X_0 \leq 5 \times 10^{-6}$	Each decade divided in two increments
β	$-2 \leq \beta \leq 2$	-2, -1, -0.5, -0.25, 0, 0.25, 0.5, 1, 2
$T_{\rm out}$ (K)	$10 \leq T_{\rm out} \leq 50$	5 K
$T_{\rm in}$ (K)	$5 \leq T_{\rm in} \leq 31$	2 K
r_T (pc)	$0.001 \leq r_T \leq 1$	1 dex

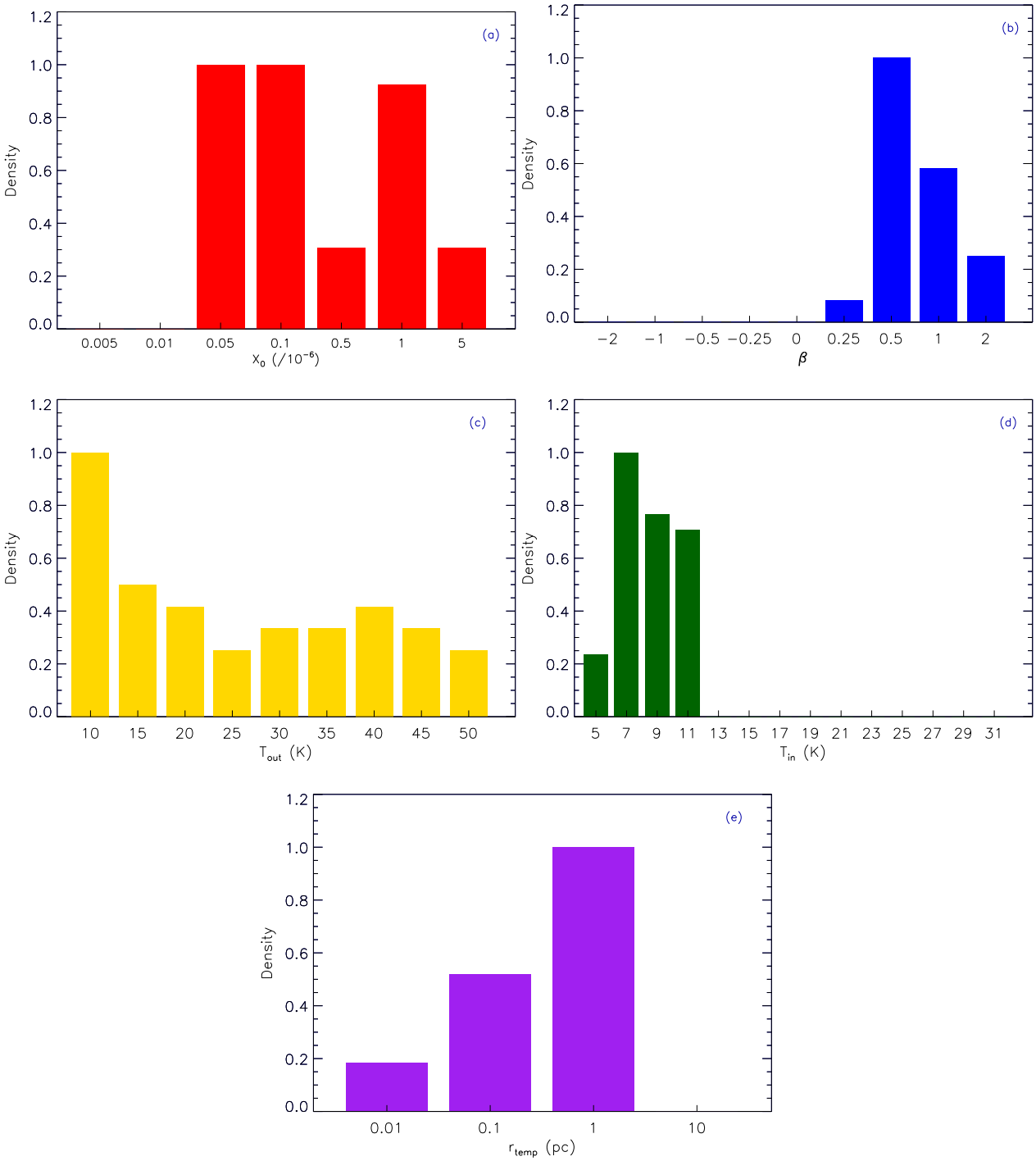

Figure 4.19: Normalized histograms of the values of model parameters from the wide five dimensional grid (described in Table 4.11) that produce the best fifty synthesized data cubes at the low-resolution mode for L1521F.

Narrow 5D Grid: Using the results of the wide five dimensional grid of values (described in Table 4.11), we ran MOLLIE using a fine five-dimensional grid of values to reproduce the NH_3 (1,1) spectra toward L1521F at low spatial resolution. The specifications of this new five-dimensional parameter space are given in Table 4.12. This grid of values produced 23,040 simulated data cubes. We reached a minimum $\chi^2_{\rm red}$ of 7.55, which corresponded to the simulated data cube produced by $X_0 = 4.0 \times 10^{-7}$, $\beta = 1.0$, $T_{\rm out} = 10$ K, $T_{\rm in} = 5$ K, and $r_T = 0.01$ pc.

Table 4.12: Specifications of the fine five-dimensional grid for modelling L1521F at low resolution.

Parameter	Range	Step
X_0	$6 \times 10^{-8} \leq X_0 \leq 4 \times 10^{-6}$	Each decade divided in five increments
β	$0.0 \leq \beta \leq 2.5$	0.5
$T_{\rm out}$ (K)	$9 \leq T_{\rm out} \leq 20$	1 K
$T_{\rm in}$ (K)	$3 \leq T_{\rm in} \leq 10$	1 K
r_T (pc)	$0.01 \leq r_T \leq 10$	1 dex

Figure 4.20 shows the $\chi^2_{\rm red}$ surfaces for the model parameters (taken two at a time). Figures 4.20a, 4.20b, 4.20c, and 4.20d show that data cubes with relatively low $\chi^2_{\rm red}$ are located in a region constrained by $10^{-7} \lesssim X_0 \lesssim 10^{-6}$ with $X_0 = 4.0 \times 10^{-7}$ producing the minimum $\chi^2_{\rm red}$. The model parameter β also is well constrained in the range $0.5 - 1.5$, with $\beta = 1.0$ producing the best results (see Figures 4.20a, 4.20e, 4.20f, and 4.20g). We are not able to place any strong constraints on $T_{\rm out}$, however, $\chi^2_{\rm red}$ certainly favours $T_{\rm out} \lesssim 16$ K (see Figures 4.20b, 4.20e, 4.20h, 4.20i). Unlike our results of modelling L694-2, for L1521F we are not able to constrain $T_{\rm in}$ relatively well. The range 3 K $\lesssim T_{\rm in} \lesssim$ 8 K produces data cubes with relatively low $\chi^2_{\rm red}$ and $T_{\rm in}$ = 5 K produces the best result (see Figures 4.20c, 4.20f, 4.20h, and 4.20j). Another difference between the modelling results of L694-2 and L1521F is apparent in the values of r_T favoured in each case. Figures 4.20d, 4.20g, 4.20i, and 4.20j suggest that lower values of r_T (i.e., 0.01 pc and 0.1 pc) produce the best match to the observed NH_3 (1,1) spectra of L1521F, whereas NH_3 (1,1) spectra of L694-2 were best matched by larger values of r_T.

We show normalized histograms of the model parameters that are more likely to reproduce the observed data in Figures 4.21 and 4.22. The two model parameters that

define the shape of NH_3 abundance are well constrained by $10^{-7} \lesssim X_0 \lesssim 10^{-6}$ and $0.5 \lesssim \beta \lesssim 1.5$ with $X_0 = 4.0 \times 10^{-7}$ and $\beta = 1.0$ being the most likely values. (Note that $X_0 = 4.0 \times 10^{-7}$ and $\beta = 1.0$ are also the values that produce the minimum $\chi^2_{\rm red}$.) On the other hand, the three parameters that define the radial temperature profile (i.e., $T_{\rm out}$, $T_{\rm in}$, and r_T) are not relatively well constrained. Figure 4.22e shows that lower values of r_T reproduce the observed spectra better compared to the larger values of r_T, indicating that the temperature profile of L1521F is likely not constant throughout the core.

Figure 4.23 shows the observed and best-fit synthesized spectra of NH_3 (1,1) emission at the centre of L1521F , 0.03 pc, and 0.06 pc toward north. Toward the core centre, the intensity of the main hyperfine component is slightly lower in the simulated spectra compared to that of the observed spectra, whereas some of the satellite hyperfine components are slightly overproduced. This could indicate a slight departure from LTE conditions inside L1521F. All hyperfine components shown in the middle panel of Figure 4.23 are underproduced in brightness. Close to the edge of L1521F (see Figure 4.23 bottom panel), MOLLIE overproduces the main hyperfine component, while producing relatively good matches to the satellite lines. The hyperfine components in all three panels appear slightly narrower compared to the observed profiles. This difference is possibly due to not including the effect of infall (or rotational) motions in the modelling of L1521F.

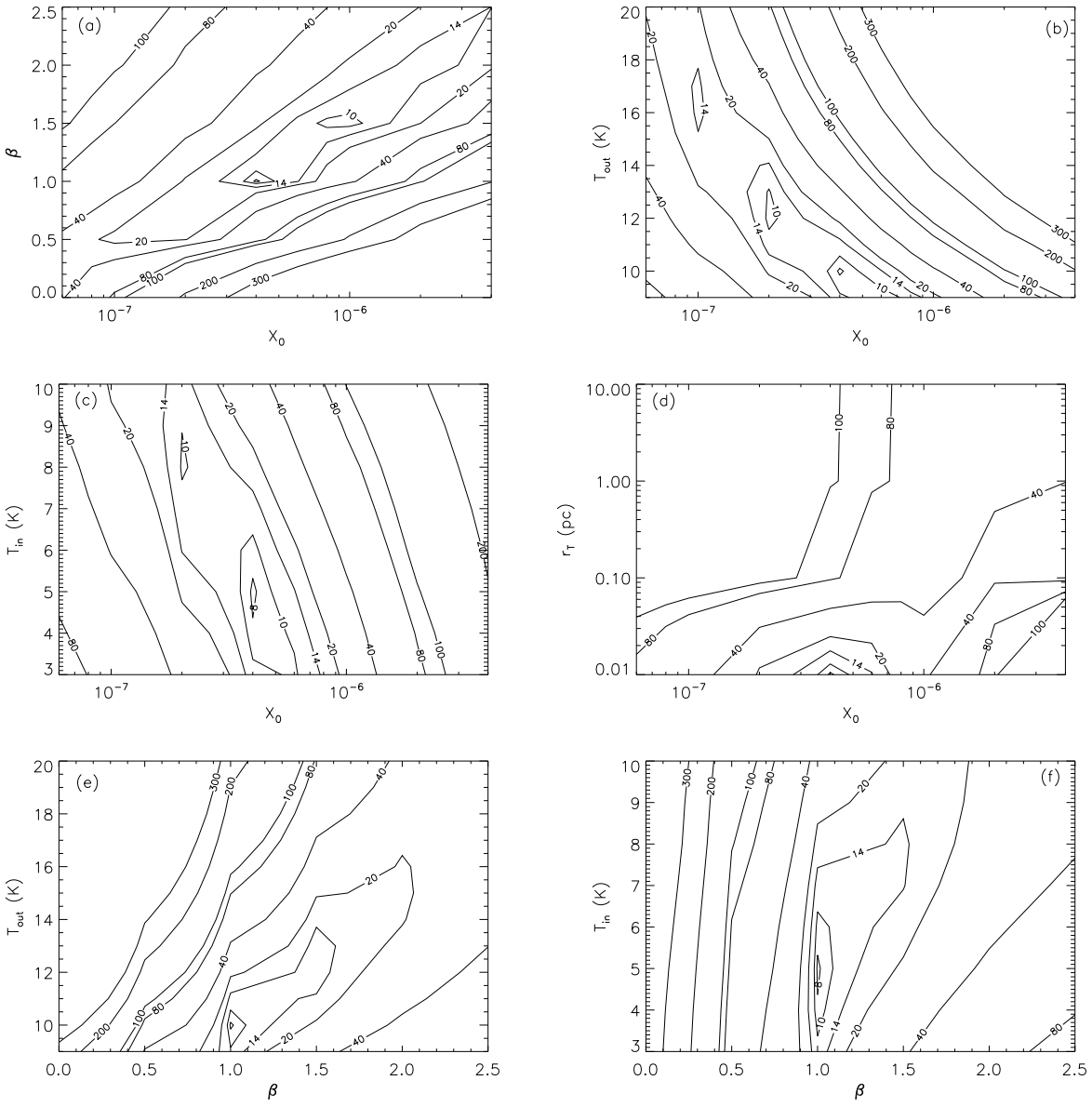

Figure 4.20: Plot of the distribution of $\chi^2_{\rm red}$ values of synthesized spectra of L1521F produced by MOLLIE at low resolution using a five-dimensional grid.

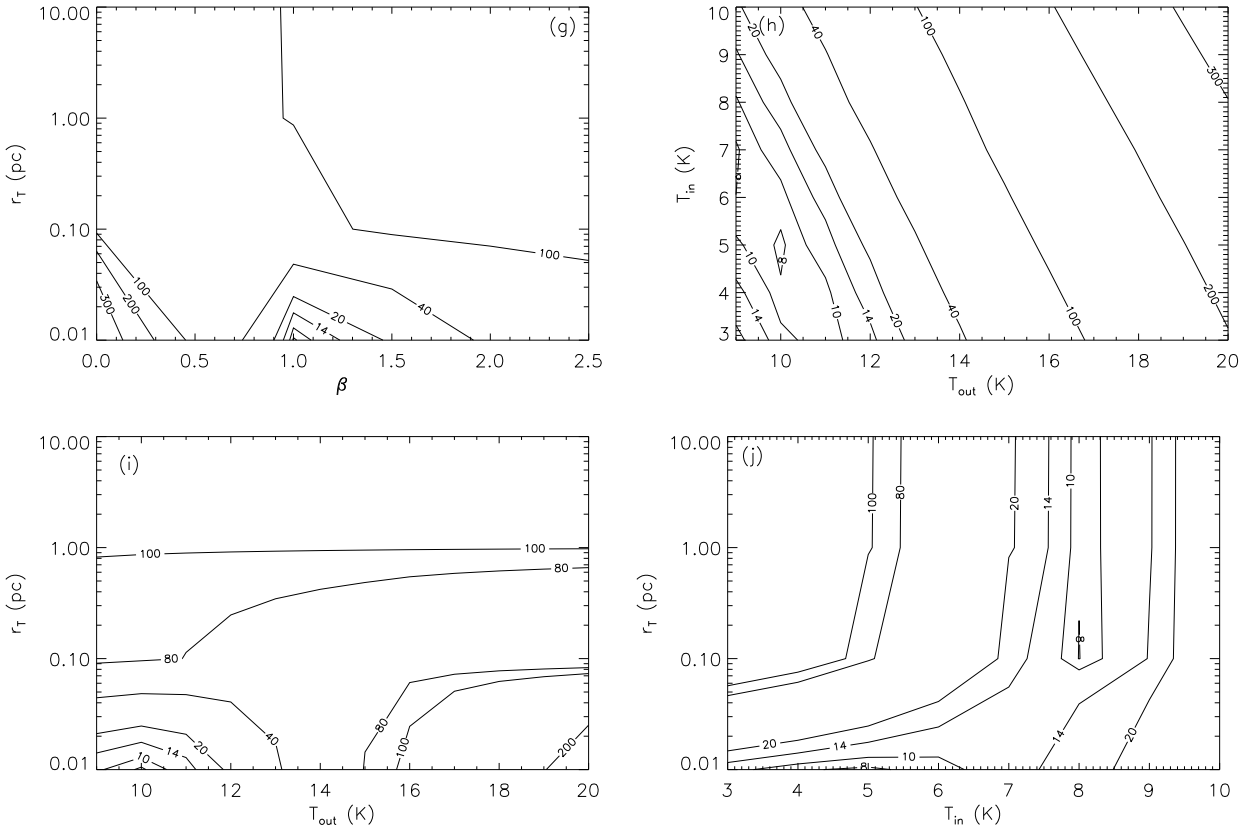

Figure 4.20: Continued.

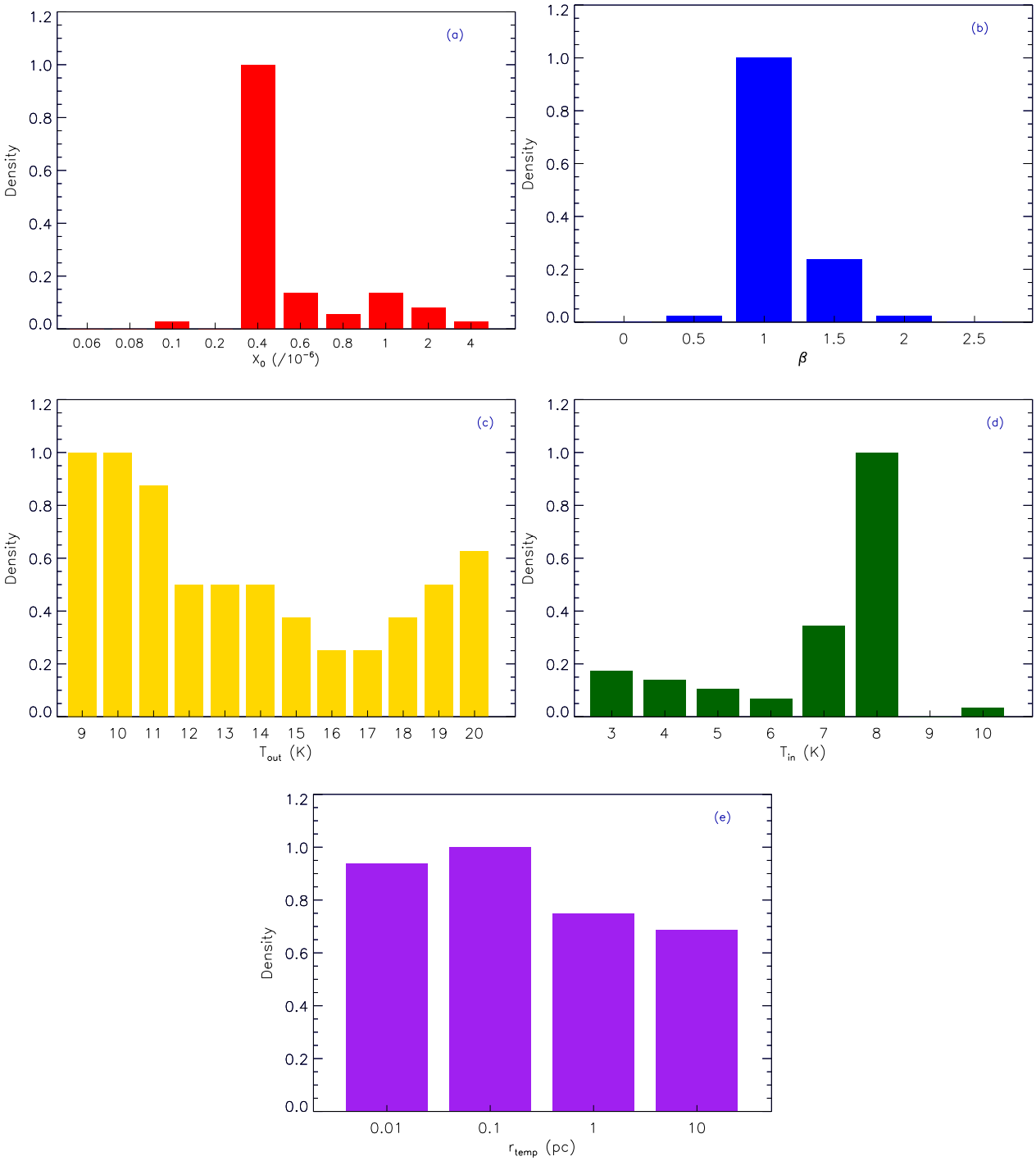

Figure 4.21: Normalized histograms of the model parameters in a five dimensional grid that produce the best fifty synthesized data cubes ($\chi^2_{\rm red} < 8.45$) using a five-dimensional grid in the low-resolution mode for L1521F.

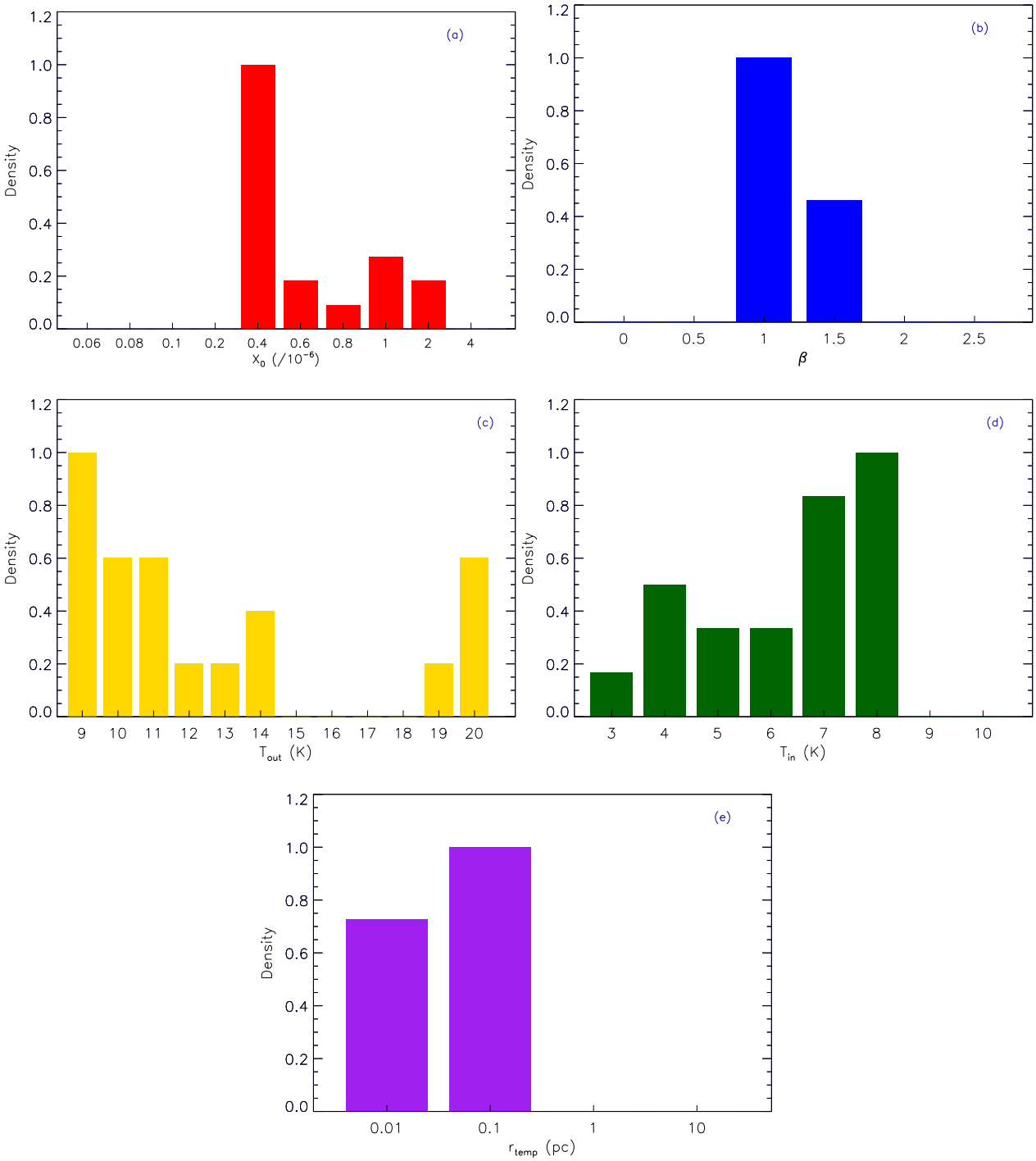

Figure 4.22: Normalized histograms of the model parameters in a five dimensional grid that produce the best twenty synthesized data cubes ($\chi^2_{\rm red} < 8.25$) using a five-dimensional grid in the low-resolution mode for L1521F.

Table 4.13: Range of acceptable values for model parameters to reproduce NH_3 (1,1) spectra of L1521F at low spatial resolution.

Parameter	Range	Best Fit
X_0	$10^{-7} \lesssim X_0 \lesssim 10^{-6}$	4.0×10^{-7}
β	$0.5 \lesssim \beta \lesssim 2.0$	1.0
$T_{\rm out}$ (K)	unconstrained	...
$T_{\rm in}$ (K)	$3 \lesssim T_{\rm in} \lesssim 8$	8
r_T (pc)	$r_T \lesssim 0.1$ pc	...

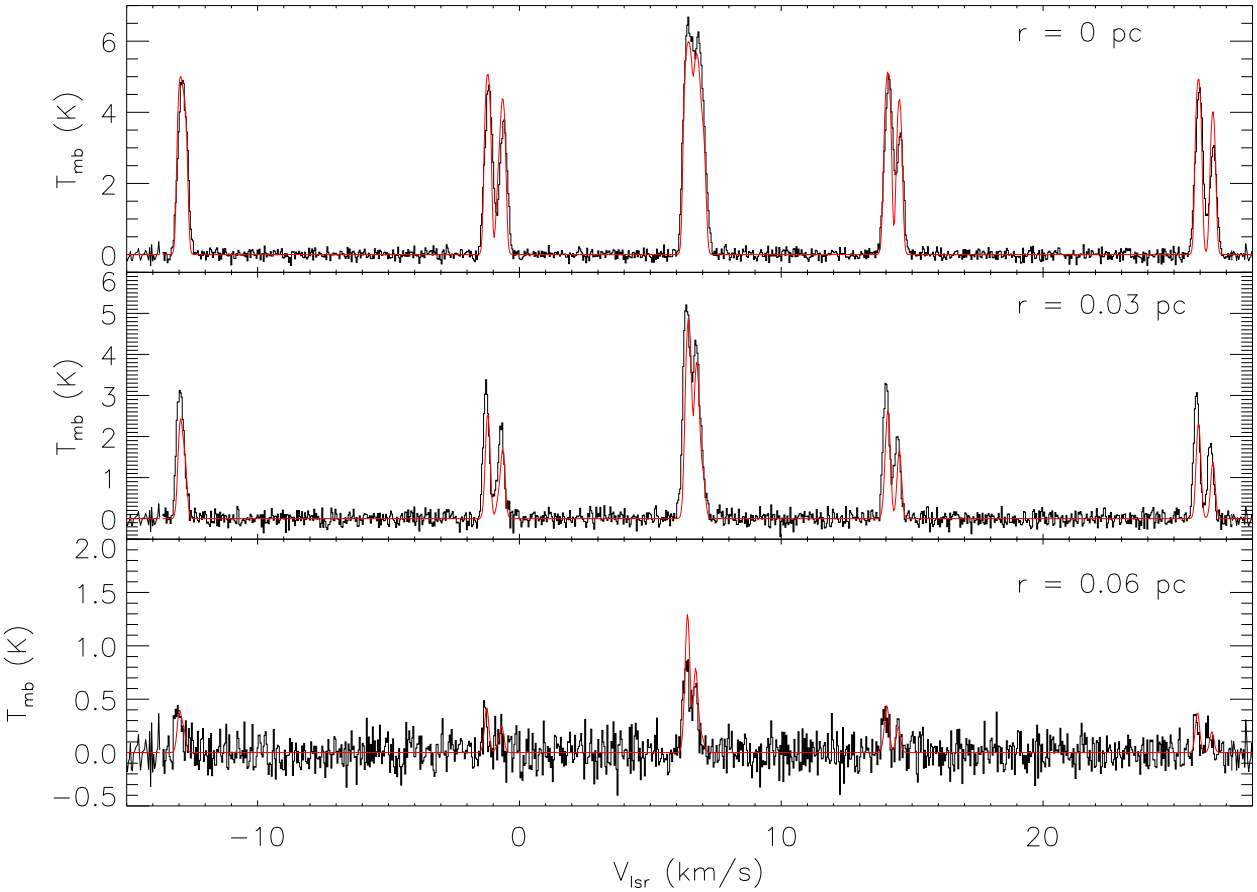

Figure 4.23: Observed (*black*) and synthesized (*red*) NH_3 (1,1) spectra of L1521F at low spatial resolution. From top to bottom: The spectra at the core centre (*top*), 0.03 pc away from the centre toward north (*middle*), and 0.06 pc away from the centre toward north (*bottom*).

NH_3 (2,2) Spectra

Figure 4.24 shows the observed and synthesized spectra of the main hyperfine component of NH_3 (2,2) emission toward L1521F. The synthesized spectra in this figure are produced using the model parameters that yield the best match to the observed NH_3 (1,1) spectra of L1521F. It is evident that the main hyperfine component of NH_3 (2,2) is overproduced by a factor of $\sim 2-3$, toward both positions in L1521F. Considering Codella et al. (1997) report very similar values for the main beam temperatures of the peaks of NH_3 (1,1) and (2,2) emission spectra toward L1521F observed with the GBT, it is highly unlikely that the discrepancy between simulated spectra produced by MOLLIE and the observed spectra is due to any data calibration issues. It is possible that a combination of model parameter values fit both NH_3 (1,1) and (2,2). This possibility will be investigated further in the future.

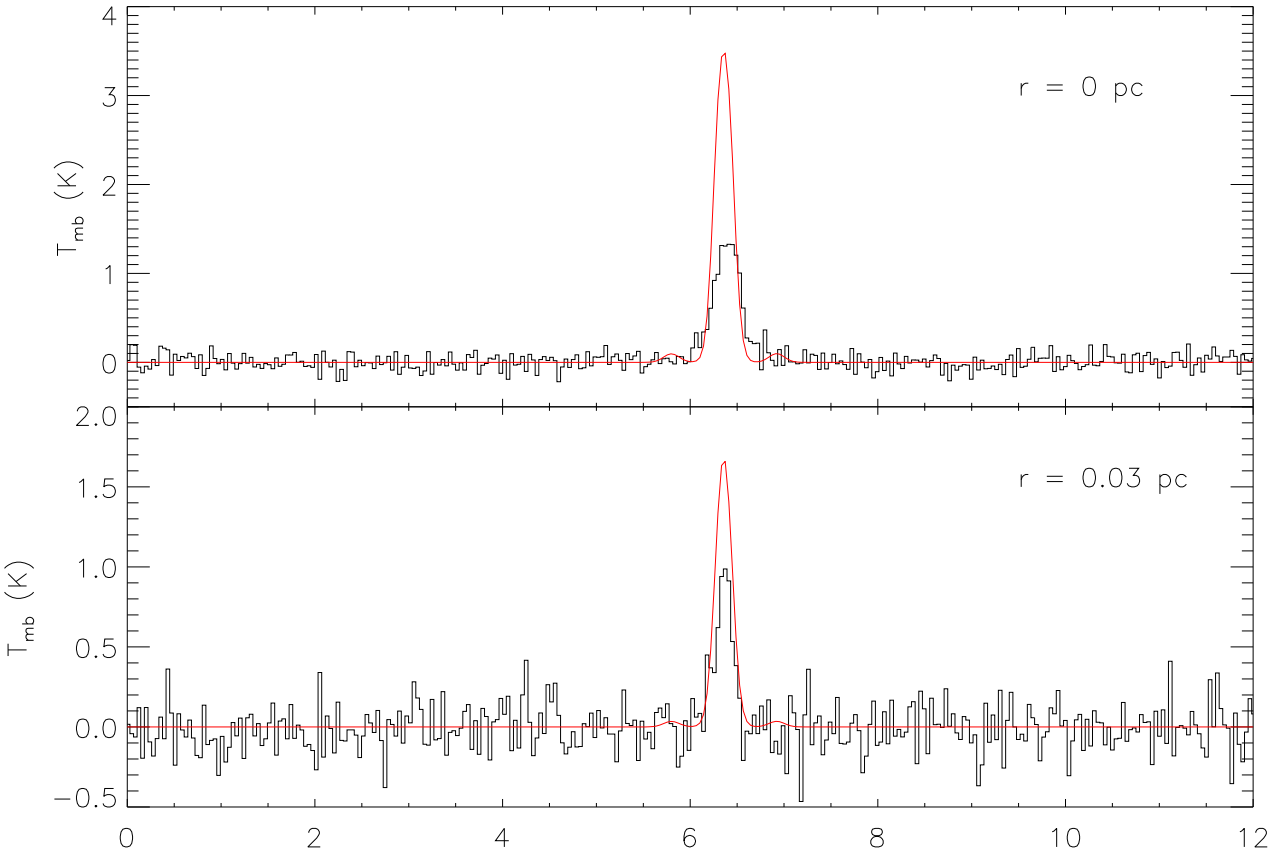

Figure 4.24: Observed (*black*) and synthesized (*red*) NH_3 (2,2) spectra of L1521F at low spatial resolution. From top to bottom: The spectra at the core centre (*top*), 0.03 pc away from the centre toward north (*bottom*).

4.5.2.2 High Resolution

NH_3 (1,1) Spectra

2D Grid: We produced 1,368 simulated data cubes of NH_3 (1,1) spectra toward L1521F in the high spatial resolution mode assuming constant radial profiles of $X(NH_3)$ and T. The two-dimensional parameter space is described in Table 4.14. A clear global minimum in χ^2_{red} can be seen in $5.0 \times 10^{-8} \lesssim X(NH_3) \lesssim 5.0 \times 10^{-6}$ and 5 K $\lesssim T \lesssim$ 17 K. The best reproduction of the observed spectra corresponds to $X(NH_3) = 8.0 \times 10^{-8}$ and $T = 9$ K with χ^2_{red} of 1.40.

Table 4.14: The characteristics of the two-dimensional grid of values taken in by MOLLIE for modelling of the combined (i.e., single-dish and interferometric) data of L1521F.

Parameter	Range	Step
X_0	$10^{-10} \leq X_0 \leq 10^{-3}$	Each decade divided in five increments
T_{in} (K)	$3 \leq T_{in} \leq 40$	1 K

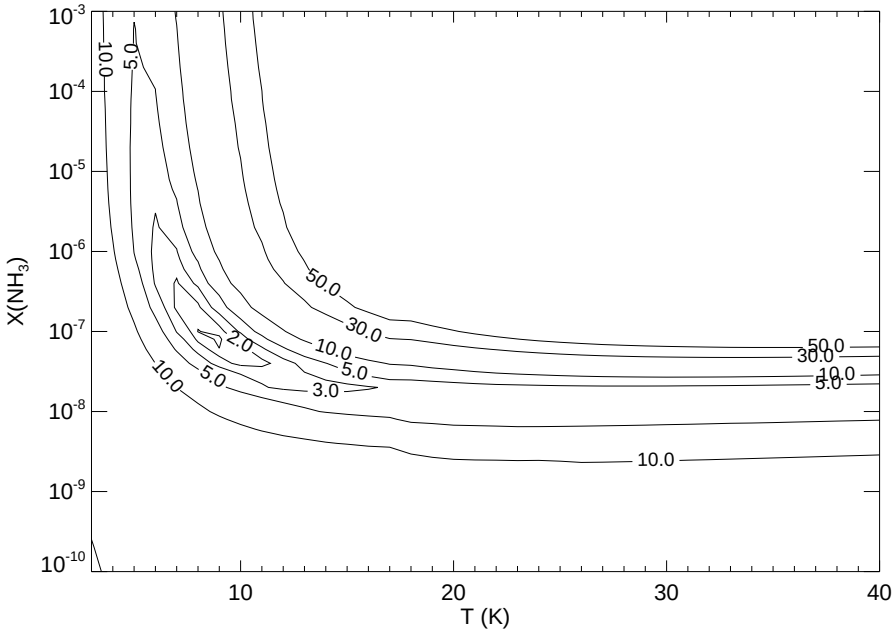

Figure 4.25: Plot of the distribution of χ^2_{red} values of synthesized spectra of L1521F produced by MOLLIE at high spatial resolution using a two-dimensional grid.

5D Grid: To define the five-dimensional grid for the modelling of NH_3 (1,1) emission line toward L1521F at high spatial resolution, we focused our attention

to the same region in the five-dimensional parameter space that was described in our relatively "fine" five-dimensional grid used for modelling of these data at low resolution (see §4.5.2.1). The specifications of the grid are described in Table 4.15. In this case, we produced 25,344 data cubes and reached a minimum $\chi^2_{\rm red}$ of 1.27, which corresponded to three simulated data cubes produced by $X_0 = 2.0 \times 10^{-7}$, $\beta = 0.5$, $T_{\rm out} = 14$ K, 15 K, and 16 K, $T_{\rm in} = 8$ K, and $r_T = 0.1$ pc.

Table 4.15: Specifications of the five-dimensional grid for modelling L1521F at high resolution.

Parameter	Range	Step
X_0	$6 \times 10^{-8} \leq X_0 \leq 6 \times 10^{-6}$	Each decade divided in five increments
β	$0.0 \leq \beta \leq 2.5$	0.5
$T_{\rm out}$ (K)	$9 \leq T_{\rm out} \leq 20$	1 K
$T_{\rm in}$ (K)	$3 \leq T_{\rm in} \leq 10$	1 K
r_T (pc)	$0.01 \leq r_T \leq 10$	1 dex

Figure 4.26 shows the $\chi^2_{\rm red}$ surfaces of the model parameters (taken two at a time). In this case, the global minimum $\chi^2_{\rm red}$ is located in a region constrained by $10^{-7} \lesssim X_0 \lesssim 10^{-6}$, $0.5 \lesssim \beta \lesssim 1.0$, and 6 K $\lesssim T_{\rm in} \lesssim$ 9 K (see Figures 4.26a, 4.26c, and 4.26f. The model parameters $T_{\rm out}$ and r_T appear to be less constrained, although 12 K $\lesssim T_{\rm out} \lesssim$ 18 K and $r_T = 0.1$ pc are strongly favoured by the $\chi^2_{\rm red}$ test and produce the best match to the observed data (see Figures 4.26b, 4.26d, 4.26e, 4.26g, 4.26h, 4.26i, 4.26j).

Figures 4.27 and 4.28 show normalized histograms of the values of the model parameters that are more likely to produce relatively good matches to the observed spectra. $X_0 = 2.0 \times 10^{-7}$, $\beta = 1.0$, $T_{\rm in} = 8$ K, and $r_T = 0.1$ pc are most likely to reproduce the observed NH_3 (1,1) spectra at high resolution. Note that these are the values that produce the simulated spectra corresponding to the minimum $\chi^2_{\rm red}$ as well. The most likely value of $T_{\rm out}$ is 9 K, although $T_{\rm out}$ is not as well constrained. We summarize the acceptable ranges and most likely values for each model parameter in Table 4.16.

Figure 4.29 shows the observed and simulated spectra of NH_3 (1,1) emission toward three locations inside L1521F. The intensity of most of the hyperfine components are under-produced in all three locations, especially toward the location most offset from

the centre (see Figure 4.29, bottom panel). The line widths are also lower in the simulated spectra compared to that of the observed spectra toward the positions offset from the centre (see Figure 4.29, bottom panel).

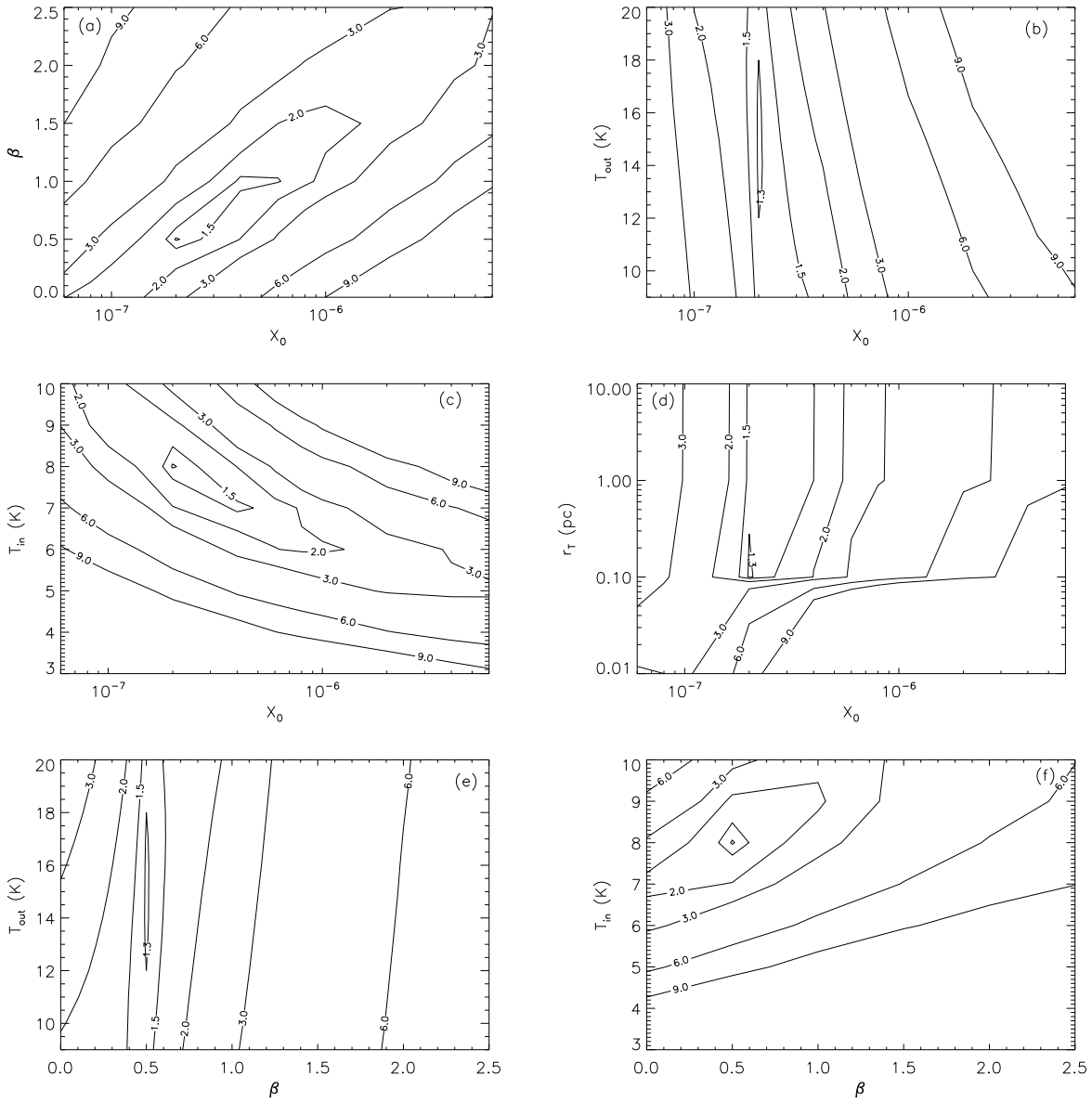

Figure 4.26: Plot of the distribution of $\chi^2_{\rm red}$ values of synthesized spectra of L1521F produced by MOLLIE at high resolution using a five-dimensional grid.

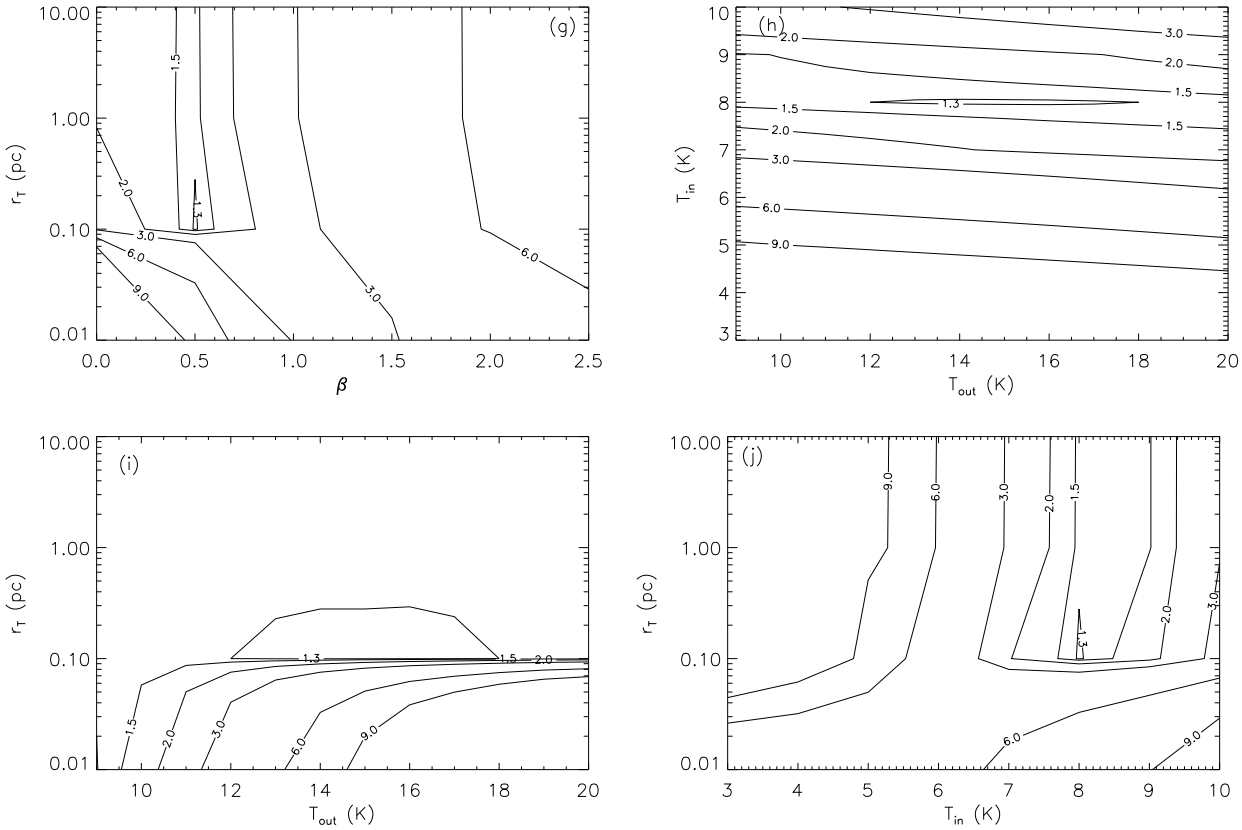

Figure 4.26: Continued.

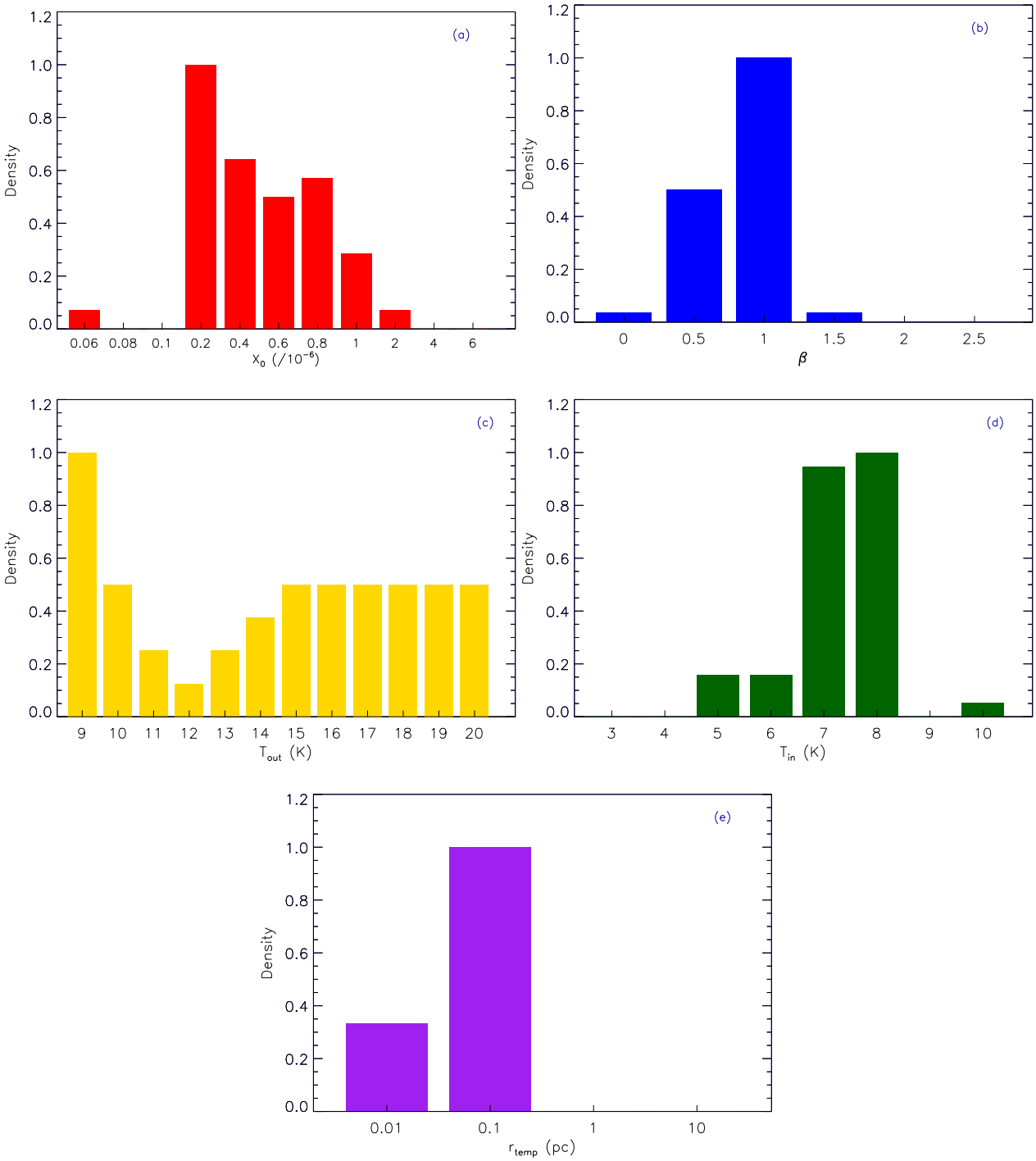

Figure 4.27: Normalized histograms of the model parameters in a five dimensional grid that produce the best fifty synthesized data cubes ($\chi^2_{\rm red} < 1.39$) using a five-dimensional grid in the high resolution mode for L1521F.

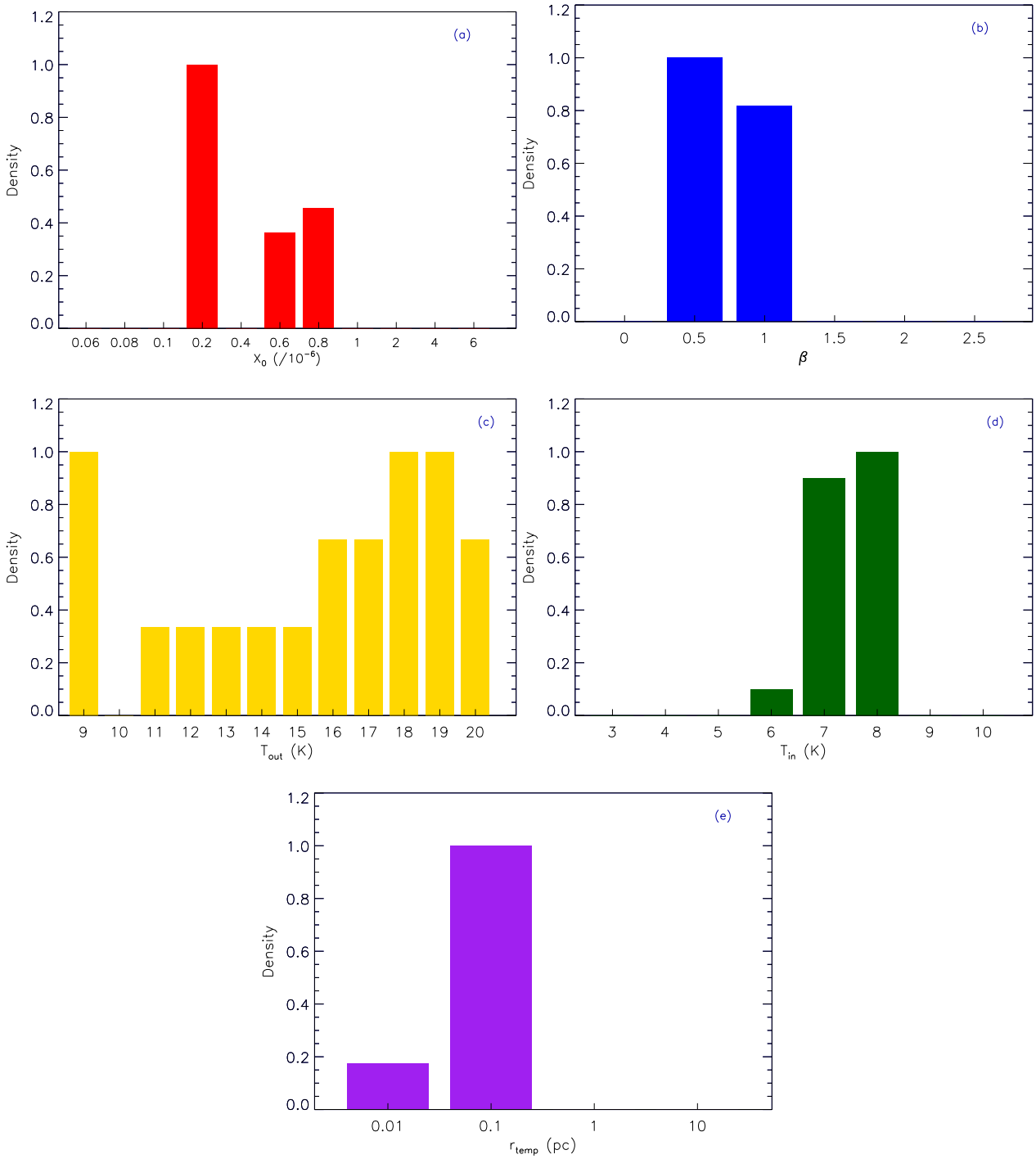

Figure 4.28: Normalized histograms of the model parameters in a five dimensional grid that produce the best twenty synthesized ($\chi^2_{\rm red} < 1.33$) data cubes using a five-dimensional grid in the high resolution mode for L1521F.

Table 4.16: Range of acceptable values for model parameters to reproduce NH_3 (1,1) spectra of L1521F at high spatial resolution.

Parameter	Range	Best Fit
X_0	$2.0 \times 10^{-7} \lesssim X_0 \lesssim 2.0 \times 10^{-6}$	2.0×10^{-7}
β	$0 \lesssim \beta \lesssim 1.5$	1.0
$T_{\rm out}$ (K)	unconstrained	9
$T_{\rm in}$ (K)	$5 \lesssim T_{\rm in} \lesssim 10$	8 K
r_T (pc)	$r_T \lesssim 0.1$ pc	0.1

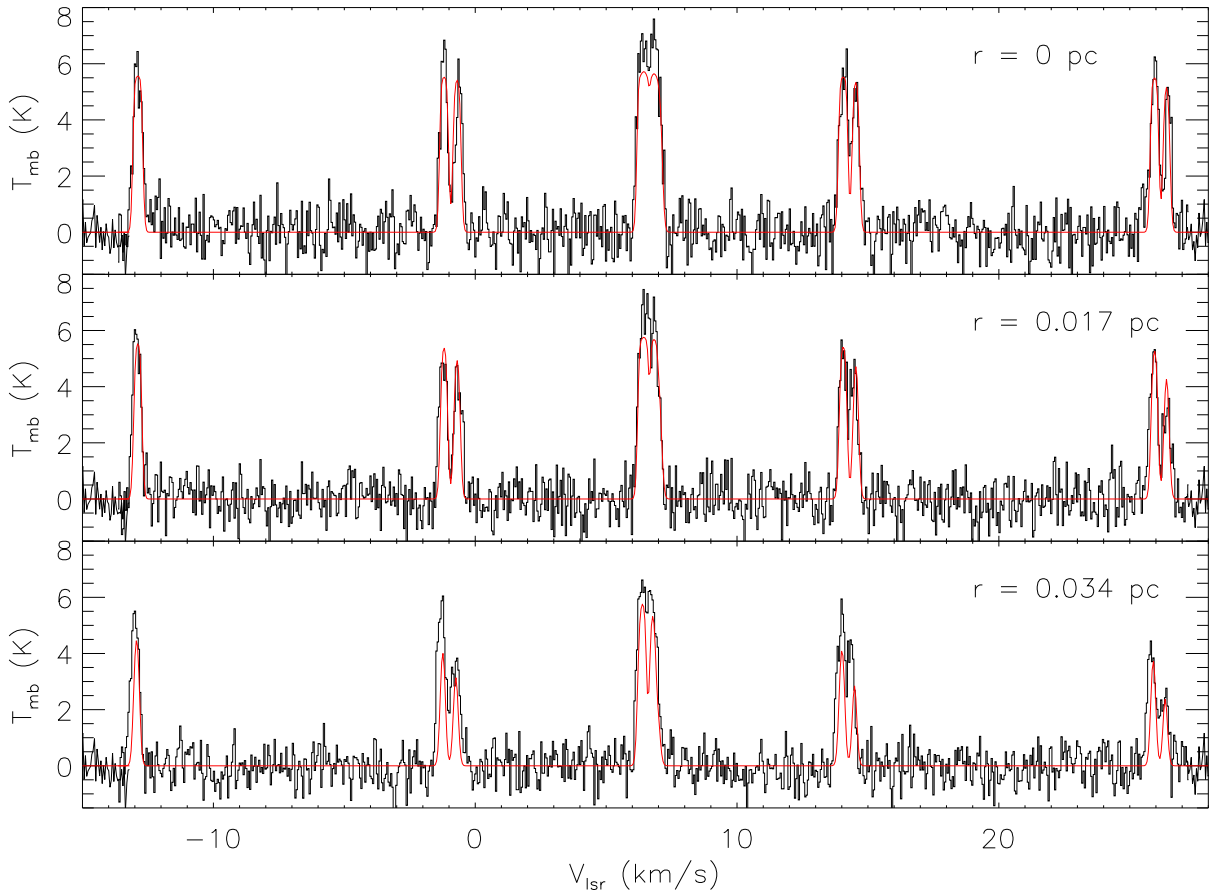

Figure 4.29: Observed (*black*) and synthesized (*red*) NH_3 (1,1) spectra of L1521F at high spatial resolution. From top to bottom: The spectra at the core centre (*top*), 0.017 pc away from the centre toward north (*middle*), and 0.034 pc away from the centre toward north (*bottom*).

NH_3 (2,2) Spectra

Figure 4.30 shows the observed and synthesized spectra of the main hyperfine component of NH_3 (2,2) emission toward L1521F at high spatial resolution. Again, the simulated spectra are produced using the model parameters that best reproduce the NH_3 (1,1) observed data at high spatial resolution toward L1521F (i.e., $X_0 = 2.0 \times 10^{-7}$, $\beta = 0.5$, $T_{\rm out} = 15$ K, $T_{\rm in} = 8$ K, and $r_T = 0.1$ pc). Although in both locations toward L1521F, the simulated spectra are brighter compared to the observed spectra, the difference between the two is not as sever as the discrepancy between the observed and simulated spectra of NH_3 (2,2) in low spatial resolution.

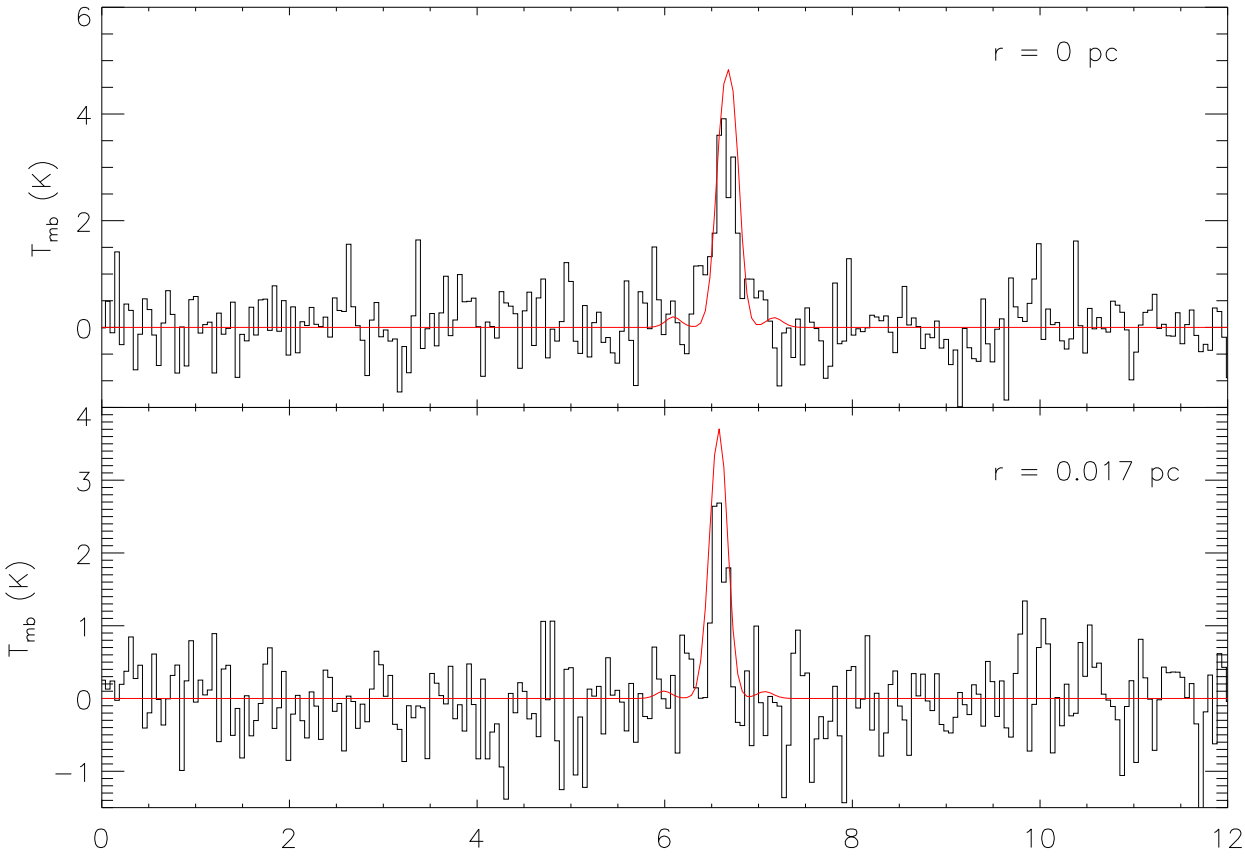

Figure 4.30: Observed (*black*) and synthesized (*red*) NH_3 (2,2) spectra of L1521F at high spatial resolution. From top to bottom: The spectra at the core centre (*top*), 0.017 pc away from the centre toward north (*bottom*)

Our results from modelling of NH_3 (1,1) emission line toward L1521F using the single-dish (GBT) and combined (GBT and JVLA) datasets strongly suggest that the radial profile of $X(NH_3)$ is not constant throughout the core and indeed shows a relatively strong enhancement toward the core centre. Although our analysis is

not able to constrain the parameters that define the radial profile of T as strongly, non-flat temperature profiles with increasing temperatures toward the core edge are certainly better at reproducing the observed NH_3 spectra toward L1521F.

Figure 4.31 shows the $X(NH_3)$ and T radial profiles at low and high spatial resolutions versus the core radius. Both profiles appear slightly more flat at high spatial resolution compared to that of the low spatial resolution. This is likely due to lower sensitivity of high resolution data compared to single-dish data. We note that the model parameter values that produce the global minimum $\chi^2_{\rm red}$ for NH_3 (1,1) spectra of L1521F at low resolution also reproduce the NH_3 (1,1) spectra at high resolution toward L1521F with relatively low $\chi^2_{\rm red}$ (= 1.34). Nonetheless, our analysis shows that $X(NH_3)$ and T are not constant throughout the core. NH_3 (1,1) spectra of L1521F are matched best by an $X(NH_3)$ profile with an enhancement toward the centre and temperature profile that increases toward the core edge.

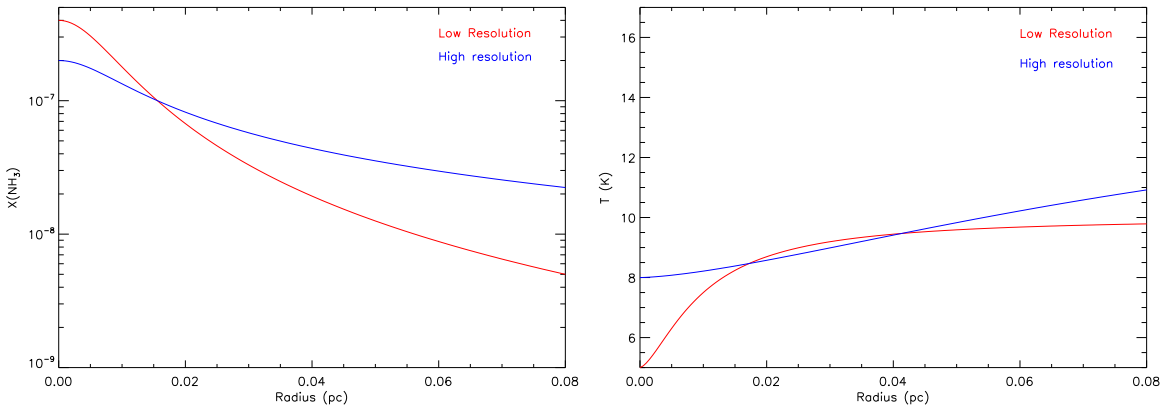

Figure 4.31: Radial profiles of $X(NH_3)$ and T of L1521F at low (*red*) and high (*blue*) spatial resolutions using the model parameters that produced the data cubes with globally minimum $\chi^2_{\rm red}$ in the parameter space.

4.6 Comparison of L694-2 and L1521F

We have simulated the observed single-dish and interferometric data of the hyperfine structure of the NH_3 (1,1) emission line toward two dense cores, L694-2 and L1521F, using the radiative transfer code MOLLIE. L694-2 is an isolated starless core, whereas L1521F contains a protostellar VeLLO at its centre. The total column density profile of L694-2 (Figures 4.3) shows a relatively wide inner flat region and central number density of $\sim 3.2 \times 10^5$ cm^{-3}. In comparison, L1521F shows a highly concentrated

total column density profile (Figure 4.4) with a smaller inner flat region and higher central number density ($\sim 1.2 \times 10^6$ cm^{-3}).

The observed spectra of NH_3 (1,1) emission line toward L694-2 at both low and high spatial resolutions are best reproduced by a relatively flat NH_3 abundance profile with a slight increase in the central abundance ($X_0 \sim 2.0 - 4.0 \times 10^{-7}$) and a constant temperature profile ($\sim$ 7 K $-$ 8 K). Figure 4.17 shows the radial profiles of T and $X(NH_3)$ that best reproduce the observed NH_3 (1,1) spectra at low and high spatial resolutions. Note that the physical models of a BE sphere and an isothermal cylinder can both reproduce the shape of the density structure of L694-2 (Harvey et al. 2003a; Harvey et al. 2003b). The BE model, however, fails to account for the amount of extinction observed toward L694-2. Therefore, Harvey et al. (2003a) suggest that a cylindrical model slightly tilted to the line of sight can reproduce the shape of the L694-2 density structure, explain the discrepancy in the normalization of the BE model, and describe the asymmetrical shape of L694-2 core. In this study, we use a spherically symmetric BE density structure as an input to MOLLIE for the radiative transfer modelling of L694-2. We note that inputing a cylindrical density structure into MOLLIE can alter the shape of the best-fit temperature and molecular abundance profiles. We will explore this option in a future study.

Observed NH_3 (1,1) spectra of L1521F are best reproduced by $X(NH_3)$ and T profiles that are *not* constant throughout the core. The preferred $X(NH_3)$ profile, at both spatial resolutions, show an enhancement toward the centre. The central NH_3 abundance of L1521F is $\sim (2.0 - 4.0) \times 10^{-7}$, similar to that of L694-2, but falls off to values $\sim 10^{-8}$ at the core edge. The temperature profiles that best reproduce the NH_3 (1,1) spectra at both low and high spatial resolution show colder temperatures (5 K $-$ 8 K) at the core centre and increase to warmer temperatures ($\sim$ 10 K $-$ 11 K) toward the core edges (see Figure 4.31).

Increases in the central abundance of NH_3 (with constant N_2H^+ abundance throughout the core), have been observed toward other dense cores such as L1517B, L1498, (Tafalla et al. 2002; Tafalla et al. 2004) and L1544 (Tafalla et al. 2002; Crapsi et al. 2007). This effect has also been reproduced in chemical models by Aikawa et al. (2005). In the more diffuse regions of molecular clouds, CO is the major source of N_2H^+ destruction due to proton transfer from N_2H^+ to CO. The product of this transfer, N_2, reacts with H_3^+ to replenish the N_2H^+ abundance. In the central regions of dense cores, however, CO is likely less abundant as a result of molecular freeze-out onto dust grains. In this case, N_2H^+ recombines with an electron to form NH,

which reacts with H_2 and H_3^+ to produce NH_3 (Aikawa et al. 2005). The increase in central $X(NH_3)$ is suggested to occur if the density ratio $n(CO)/n(e)$ falls below $\sim 10^3$ (Aikawa et al. 2005). Enhancement in central $X(NH_3)$ has been reproduced for cores with central densities of $\sim 3 \times 10^5$ (similar to that of L694-2 (present study), L1517B, and L1498; Tafalla et al. 2002; Tafalla et al. 2004) and $\sim 3 \times 10^6$ (similar to that of L1521F (present study) and L1544; Crapsi et al. 2007).

Radiative transfer modelling of the combined single-dish and interferometric observations of NH_3 (1,1) and (2,2) toward the evolved starless core L1544 suggests a sharp decrease from 12 K to 5.5 K in the temperature profile of the core toward the centre and an enhancement in the central NH_3 abundance with $X_0 \sim 8.0 \times 10^{-9}$. Figure 4.32 shows a comparison of the radial profiles of $X(NH_3)$ and T for L1544, L694-2, and L1521F. Although the suggested central $X(NH_3)$ of L1544 is lower than that of L1521F ($\sim 4.0 \times 10^{-7}$), the temperature profiles and general shape of the abundance profiles of the two cores are similar. L1521F is generally colder than L1544 except at the core edge and centre. Note that both L1521F and L1544 have high central densities ($\sim 10^6$ cm^{-3}) and high CO depletion factors[4] (11.0 ± 1.8 for L1521F and 14.0 ± 2.2 for L1544; Crapsi et al. 2005a).

Of the two targets selected for this study, L1521F is the more evolved core and is closer to L1544 in evolutionary stage than L694-2. Although previous studies by Williams et al. 1999, Ohashi et al. 1999, and Crapsi et al. 2005a present evidence for the presence of inward motions inside L1544, this core still appears to be starless in Spitzer observations (Bourke et al. 2006). The comparison of our results with that of Crapsi et al. (2007) suggest that internal structure of less evolved starless cores, such as L694-2, can be explained using relatively constant temperature and molecular abundance profiles. As the core evolves and becomes more centrally concentrated, however, the central regions of the core experience a decrease in temperature. The combination of higher densities and lower temperatures could prompt the depletion of CO molecules even further, leading to the enhancement of the NH_3 abundance at the centre. We emphasize that Crapsi et al. (2007) do not provide any information on the uncertainties or the acceptable ranges for the model parameters, and therefore it is difficult to compare our results with their findings any further.

Our findings regarding the low temperatures close to the centre of L1521F is in agreement with the lack of detection in the emission lines of organic molecules, such

[4]CO depletion factor is defined as the ratio of CO canonical abundance ($= 9.5 \times 10^{-5}$; Frerking et al. 1982) and the fractional CO abundance ($X(CO) = N(CO)/N(H_2)$) derived from observations.

as CH_3OH and CH_3CN, toward the protostellar object, L1521F-IRS, by Takakuwa et al. (2011). CH_3OH emission is generally detected toward Class 0 protostars (e.g., toward L1157 by Goldsmith et al. 1999 and toward NGC1333 IRAS 2A by Jørgensen et al. 2005). Hence, the lack of CH_3OH emission toward L1521F-IRS implies that the protostar is indeed young (less than 10^5 years) and its surrounding warm ($\sim$ 100 K) region is smaller than 100 AU in size (Takakuwa et al. 2011). The recent detection of a relatively small and poorly collimated outflow associated with L1521F-IRS by Takahashi et al. (2013) also suggest that L1521F is less than $\sim 10^4$ years old and is currently in a low accretion phase. Therefore, it is not surprising that L1521F-IRS has yet to disrupt its surroundings drastically and that the surrounding dense gas region is still experiencing a decreasing temperature profile toward the core centre.

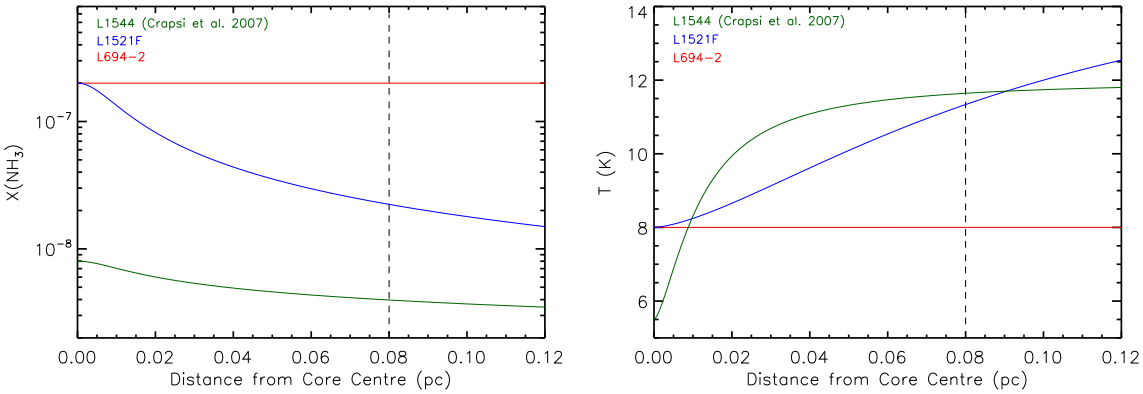

Figure 4.32: Comparison of the radial profiles of $X(NH_3)$ (*right*) and T (*left*) for L1544 (from Crapsi et al. 2007), L694-2, and L1521F at high spatial resolution using the model parameters that produced the data cubes with globally minimum χ^2_{red} in the parameter space. The dashed line shows the core radii for L1521F and L694-2 at 0.08 pc.

4.7 Summary

In this chapter, we presented radiative transfer modelling of NH_3 (1,1) emission toward two dense cores, L694-2 and L1521F, using the radiative transfer code MOLLIE. The results lead us to believe that relatively constant temperature ($\sim$ 7 K $-$ 8K) and NH_3 abundance ($\sim 2.0 - 4.0 \times 10^{-7}$) profiles can best describe the internal structure of L694-2. The NH_3 (1,1) spectra toward L1521F, the more chemically evolved core in our sample, however, are best matched by a temperature profile that shows colder temperatures ($\sim$ 5 K $-$ 8 K) at the centre and increases to warmer temperatures ($\sim$ 10 K $-$ 11 K) at the edge and an abundance profile that increases toward the centre

($X_0 \sim 2.0 - 4.0 \times 10^{-7}$). Comparisons of the temperature and abundance profiles of L1521F and L694-2 with those of L1544 (Crapsi et al. 2007) suggest that a sharp decrease in temperature at the core centre and an enhancement of the central NH_3 abundance are more prevalent toward evolved cores and are coincident with the high concentration of density in such environments.

Future radiative transfer modelling of emission lines from other molecular species (e.g., N_2H^+) toward L694-2 and L1521F will give us a more complete picture of the physical conditions of these cores. Our estimations of the model parameters can also improve significantly by using radiative transfer models that are capable of reproducing the lines in non-LTE conditions. Indeed, studying the molecular emission of a larger sample of dense cores with various evolutionary stages is necessary to improve our knowledge of the initial conditions of star formation.

Chapter 5

Summary and Conclusions

This dissertation presents an extensive study of molecular emission line observations of a sample of six isolated dense cores. Based on various molecular line and continuum diagnostics, we have selected several cores believed to be near the stage of gravitational collapse. These cores are either starless and on the brink of gravitational collapse (L694-2, L429, L1517B, and L1689-SMM16; Crapsi et al. 2005a, Sadavoy et al. 2010a), or contain a protostellar VeLLO and currently experiencing mass accretion (L1521F and L1014; Crapsi et al. 2005a; Kauffmann et al. 2008). Due to their isolation and proximity to the Sun, the internal physical conditions of these cores can be probed relatively easily. Observations and analysis of molecular emission toward this sample of cores provides an exciting opportunity to deepen our understanding of the initial conditions of star formation.

In Chapters 2 and 3, we assumed that gas and dust temperatures are equal inside each core and the hyperfine energy levels of the inversion doublets are populated according to LTE conditions. We also assumed that for all observed transitions, energy levels are populated uniformly along the line-of-sight (i.e., T_{ex} is constant along the line-of-sight). The latter allowed us to solve the radiative transfer equation analytically and determine the distributions of the (line-of-sight averaged) physical parameters of the targets on the plane-of-the-sky. In Chapter 4, however, we used a radiative transfer model to study the regions of interest in three dimensions and took into account the variation in the physical parameters of the region along the-line-of-sight. We summarize the results of this dissertation below.

5.1 Single-dish Observations of Highly Concentrated Dense Cores in NH_3 and N_2H^+ Line Emission

As nitrogen-based species, NH_3 and N_2H^+ are observed to remain abundant in environments where other molecular tracers are observed to be depleted (e.g., CO, CS, and HCO^+). They can also trace well the physical characteristics of dense cores because their transitions can be excited collisionally at the low temperatures ($T < 10$ K) and high densities ($n \sim 10^{4-6}$ cm^{-3}) of such cores (Di Francesco et al. 2007). Therefore, we observed dense cores L1521F, L1517B, L429, L694-2, and L1014 in NH_3 (1,1) and (2,2) emission using the GBT. In addition, we used NRO to observe all cores, except L1521F, in N_2H^+ (1−0) emission line. We outline the results of our analysis below:

1. The integrated intensities of all observed emission lines toward L1521F, L1517B, L694-2, and L1014 are roughly round-shaped and show single peaks (except for N_2H^+ emission toward L1517B, which shows two maxima). For each core, the morphologies of the integrated intensities match closely that of the corresponding 250 μm continuum emission. The offsets between the continuum emission maxima and the peaks of the integrated intensities are smaller than the beam widths used to carry out the molecular line observations. Both continuum and molecular line data of L429, however, show more complex structures compared to other cores. A second peak toward the east is visible in both NH_3 and N_2H^+ emission lines toward L429. The structure of molecular emission integrated intensities toward L429 also follow the morphology of the corresponding continuum emission. The offsets between the locations of the maxima of line and continuum emission, however, are larger than the corresponding beam widths and more significant compared to other cores in our sample.

2. We used NH_3 (1,1) and (2,2) emission lines to calculate the (line-of-sight averaged) gas kinetic temperature toward each core. The weighted mean of T_K is in the range ~ 9 K $- 10$ K toward all cores in our sample. For each core, the distribution of T_K on the plane-of-the-sky appears to decrease slightly toward the corresponding core center.

3. The thermal velocity dispersions of all cores are ~ 0.06 km s^{-1} $- 0.07$ km s^{-1}. For each core, the corresponding distribution is either roughly constant

throughout the core (L1521F and L1517B) or slightly decreases toward the center (L429, L429-E, and L694-2).

4. The distributions of the non-thermal velocity dispersions are non-uniform across the cores. L429 shows the highest value of σ_{NT} ($\sim$ 0.16 km s^{-1}) in our sample and appears to be transonic. All of the other cores in our sample are subsonic with L1517B showing the lowest value of σ_{NT} ($\sim$ 0.046 km s^{-1}).

5. The H_2 column density distributions of all of the cores in our sample show central concentrations. L1521F is the most centrally concentrated core in our sample with the highest amount of H_2 column density and is followed in decreasing order by L429, L1517B, and L694-2.

5.2 Physical and Chemical Characteristics of L1689-SMM16, an Oscillating Prestellar Core in Ophiuchus

Due to lack of previous studies on molecular emission toward SMM16 and our access to a significantly more extensive dataset of single-dish observations of molecular emission lines toward this particular core, we dedicated a separate analysis to SMM16. In addition to single-dish observations of SMM16 in NH_3 (1,1) and (2,2) and N_2H^+ (1$-$0) performed along other cores in our sample, we acquired Mopra data of NH_2D ($1^a_{1,1} - 1^s_{0,1}$), N_2H^+ (1$-$0) (again), HCN (1$-$0), HNC (1$-$0), $H^{13}CO^+$ (1$-$0), and HCO^+ (1$-$0) emission lines toward SMM16. We describe the results of our analysis on SMM16:

1. The morphologies of integrated intensity emission from nitrogen-based molecules, NH_3 and N_2H^+, trace the structure of the 250 μm continuum emission very closely. Due to the faintness of NH_2D emission toward SMM16, it is difficult to draw any conclusions regarding the correlation between the morphology of NH_2D emission and that of dust continuum. The integrated intensity of HCO^+ (1$-$0), however, shows a significant offset from the continuum emission, whereas the other carbon-bearing species, HCN (1$-$0), HNC (1$-$0), and $H^{13}CO^+$ (1$-$0), show more similarities in the structures of their integrated intensities with that of dust continuum emission.

2. The line-of-sight averaged distributions of fractional abundances of NH_3, N_2H^+, HCN, and HNC decrease toward the center of SMM16. We note, however, that this trend appears to be steeper for the carbon-bearing species compared to the nitrogen-based molecules. These observations leads us to believe that these two groups of molecular species are tracing different layers of the core, i.e., NH_3 and N_2H^+ are more effective in tracing the inner regions, whereas HCN and HNC can probe the outer parts more effectively.

3. Unlike the observed NH_3 and N_2H^+ toward SMM16 that do not show any signs of asymmetries in their line profiles, HCN (1−0) and HNC (1−0) emission clearly show red-skewed asymmetries in their line profiles. Furthermore, HCO^+ (1−0) is observed to have a red-skewed double peaked profile implying that the foreground layers of SMM16 are experiencing expanding (outward) motions. By fitting the observed HCN (1−0) and HNC (1−0) emission lines using the HILL5 model, we estimated the expansion speed to be ~ 0.2 km s^{-1} $-$ 0.3 km s^{-1}.

4. We estimate a relatively high level of deuteration and $X(NH_3)/X(N_2H^+)$ toward SMM16. These two findings both agree with values from other starless cores. This, and the absence of a protostellar object associated with SMM16 in the Spitzer and Herschel archival data, suggest that SMM16 is indeed starless.

5. We determine the mass (~ 4.7 M$_\odot$) and outer radius ($R \sim 0.065$ pc) of SMM16 using 250 μm continuum data from Herschel-SPIRE. Performing Jeans and virial analyses and comparing the physical structure of SMM16 to that of a BE sphere suggest that SMM16 is a gravitationally bound, super-Jeans core and appears to be unstable to collapse.

6. The observed expanding motions in the foreground layers of a gravitationally bound starless core, such as SMM16, might suggest that the core is undergoing the breathing mode of oscillation. Indeed, various layers of the core could be experiencing oscillatory motions in different modes.

5.3 Radiative Transfer Modelling of NH_3 Emission toward L694-2 and L1521F

We selected two targets, L694-2 and L1521F, from our sample of six dense cores and modelled their NH_3 emission using the three-dimensional radiative transfer code MOLLIE. In this analysis, we assumed that energy levels are populated according to LTE conditions and dust and gas temperatures are equal throughout the core. We outline the results of the radiative transfer modelling of the two cores and their comparison here:

1. The starless core L694-2 is less evolved compared to L1521F and shows a significantly less concentrated density profile. A combination of relatively constant $X(NH_3)$ profile with a slight increase toward the center ($X_0 \sim 2 - 4 \times 10^{-7}$ cm^{-3}) and relatively flat temperature profile (~ 7 K $- 8$ K) best reproduce the observed NH_3 spectra of L694-2 at both low and high spatial resolutions.

2. L1521F is the most highly concentrated core in our sample and contains a protostellar VeLLO. Non-flat abundance and temperature profiles are best at reproducing the observed NH_3 spectra toward L1521F, with the central abundance $\sim 2 - 4 \times 10^{-7}$ cm^{-3} and rolling off to $\sim 10^{-8}$ cm^{-3} at the core edge and the central temperature of ~ 5 K $- 8$ K increasing to 10 K $- 11$ K toward the outer regions. The small size of the poorly collimated bipolar outflow associated with L1521F-IRS (Takahashi et al. 2013) and the absence of emission from organic molecules toward the location of L1521F-IRS (Takakuwa et al. 2011) imply that L1521F-IRS is an extremely young protostellar object that has not yet disturbed the physical structure (i.e., molecular abundance and temperature) of its surrounding dense gas. This particular source provides a unique opportunity to study the physical and chemical conditions of sites of low mass star formation at the exact moment of gravitational collapse.

3. Previously, L1544 was the only highly concentrated core to have had its internal gas temperature modelled with a radiative transfer code (see Crapsi et al. 2007). Our work here has tripled the sample of such cores so modelled, allowing new insight into similarities and differences of their internal characteristics with evolution. The similarities between L1521F and L1544, an evolved starless core in Taurus, in terms of their material density, CO depletion factor, NH_3

abundance, and temperature profiles lead us to believe that during their evolution toward forming a protostellar object, cores become significantly centrally concentrated, which causes their internal gas temperatures to drop at their centers. These changes can induce CO molecules to experience an even higher level of depletion, which leads to an enhancement in the central abundance of NH_3 molecules.

5.4 Future Work

The analysis presented in this dissertation can be extended in many directions.

In Chapters 2 and 3 of this dissertation, we assumed the excitation temperatures of various layers of gas in each of the targets to be constant along the line-of-sight and determined the distributions of the (line-of-sight averaged) physical parameters of the targets on the plane-of-the-sky. This approach allow us to solve the radiative transfer equation analytically and determine the physical parameters of the region efficiently. This method has been used in the past to study regions with more complicated geometries (e.g., clusters) and affected by environmental effects, such as outflows and protostars. For isolated regions, one can use radiative transfer models to probe the internal physical conditions more accurately and in three dimensions. The analysis presented in Chapter 4 involves the study of the three-dimensional distributions of the temperature and molecular abundance profiles using a radiative transfer model. It is important to note that in this analysis we do not determine how the temperatures and abundances vary with projected distance. A detailed comparison between the results of these two methods is necessary to determine the advantages and disadvantages of each one. Indeed, radiative transfer modelling of candidate oscillating cores, such as SMM16, can be an effective way to study this short-lived and intriguing stage in the evolution of dense cores.

The results of the modelling analysis presented in Chapter 4, specifically the temperature profiles, can be refined further by simulating the continuum emission at various wavelengths and comparing them to the observed spectra. One can use this approach to improve the density profile, which is currently a fixed input to the model, and the temperature profile iteratively. Furthermore, reproductions of several observed lines from multiple molecular species is another method to refine the estimations of the physical parameters of dense cores.

In this dissertation, we modelled NH_3 spectra of L1521F and L694-2 assuming

Local Thermodynamic Equilibrium (LTE) condition. Using radiative transfer models that are capable of reproducing the molecular lines in non-LTE conditions can provide more accurate estimations of the internal conditions of dense cores.

Finally, observations and radiative modelling of a larger sample of dense cores spanning over a large range in the evolutionary track of dense cores and in multiple molecular transitions is necessary to achieve a more complete picture of the physical and chemical processes involved in the formation of a starless core and its progression to forming a star.

Appendix A

Additional Information

A.1 Calculation of Molecular Column Densities

The propagation of radiation with a specific intensity I_ν through a gaseous medium is governed by

$$\frac{dI_\nu}{ds} = -\alpha_\nu I_\nu + j_\nu \tag{A.1}$$

In the case of a uniform medium with constant absorption coefficient (α_ν) and emission coefficient (j_ν) over the path length Δs, the solution to the above equation is

$$I_\nu(\Delta s) = I_\nu(0)\exp\left(-\alpha_\nu \Delta s\right) + \frac{j_\nu}{\alpha_\nu}(1 - \exp\left(-\alpha_\nu \Delta s\right)). \tag{A.2}$$

We consider the special case where both emission and absorption are due to a transition between two discrete levels in an atom or molecule. Assuming the emission is isotropic, the emission coefficient per unit solid angle is given by

$$j_\nu = \frac{h\nu_{rest}}{4\pi} n_u A_{ul} \phi(\nu), \tag{A.3}$$

where $\phi(\nu)$ is the relative probability of emission into a photon frequency ν near the line centre frequency ν_{rest} and A_{ul} is the Einstein coefficient for spontaneous emission. In this case, the total absorption coefficient is

$$\alpha_\nu = \frac{h\nu_{rest}}{4\pi}(n_l B_{lu} - n_u B_{ul})\phi(\nu), \tag{A.4}$$

where the first term is the contribution from the true absorption and the second term is the correction for stimulated emission. In the above equation, B_{lu} and B_{ul} are the Einstein coefficients for absorption and stimulated emission, respectively. From Equations (A.3) and (A.4), we find

$$\begin{aligned} \frac{j_\nu}{\alpha_\nu} &= \frac{n_u A_{ul}}{n_l B_{lu} - n_u B_{ul}} \\ &= \frac{2h\nu_{rest}^3/c^2}{\exp(h\nu_{rest}/kT_{ex}) - 1}, \end{aligned} \tag{A.5}$$

i.e., the blackbody function. To derive the above equation, we used the relations between the Einstein coefficients

$$A_{ul} = \frac{2h\nu_0^3}{c^2} B_{ul} \tag{A.6}$$

and

$$g_l B_{lu} = g_u B_{ul}, \tag{A.7}$$

and the definition of excitation temperature (T_{ex})

$$\frac{n_u}{n_l} = \frac{g_u}{g_l} \exp\left(\frac{-\Delta E_{ul}}{kT_{ex}}\right). \tag{A.8}$$

The medium's optical thickness τ_ν is defined by $\alpha_\nu \Delta s$ and therefore is given by

$$\tau_\nu = \frac{h\nu_{rest}}{4\pi}(n_l B_{lu} - n_u B_{ul})\phi(\nu)\Delta s \tag{A.9}$$

$$= \frac{c^2}{8\pi\nu_{rest}^2}\phi(\nu)\Delta s\, n_u\, A_{ul}\, (\exp(h\nu_{rest}/kT_{ex}) - 1) \tag{A.10}$$

Integrating over the frequency range, we find

$$\int \tau_\nu d\nu = \frac{c^2}{8\pi\nu_{rest}^2}\Delta s\, n_u\, A_{ul}\, (\exp(h\nu_{rest}/kT_{ex}) - 1) \int \phi(\nu) d\nu \tag{A.11}$$

Noting that

$$\int \phi(\nu) d\nu = 1, \tag{A.12}$$

we find

$$\int \tau_\nu d\nu = \frac{c^2}{8\pi\nu_{rest}^2}\Delta s\, n_u\, A_{ul}\, (\exp(h\nu_{rest}/kT_{ex}) - 1) \tag{A.13}$$

Note that the column density of the species in the energy level of interest is given by

$$N_u = n_u \Delta s, \tag{A.14}$$

where n_u is the volume density of the species in the energy level of interest (in this case the upper level) and Δs is the cloud thickness. Therefore,

$$N_u = \frac{8\pi\nu_{rest}^2}{c^2}\frac{1}{A_{ul}}\frac{1}{(\exp(h\nu_{rest}/kT_{ex})-1)}\int \tau_\nu d\nu. \tag{A.15}$$

Here, we consider the further special case of two rotational states of a molecule. The fractional population of a given rotational state is given by

$$f_J = \frac{g_J \exp(-E_J/kT_{rot})}{Q_{rot}(T_{rot})}, \tag{A.16}$$

where $Q_{rot}(T_{rot}) = \sum_i g_i \exp(-E_i/kT_{rot})$ is the rotational partition function of the species and rotational temperature, T_{rot}, is the excitation temperature that describes the level populations of rotational energy levels. The total column density of the species is therefore given by

$$N_{tot} = \frac{N_u\, Q_{rot}(T_{rot}) \exp(E_u/kT_{rot})}{g_u}. \tag{A.17}$$

Assuming that all molecular levels are populated according to the same excitation temperature, T_{ex}, the total column density of the molecule is given by (see e.g., Rohlfs & Wilson 2004; Rosolowsky et al. 2008; Johnstone et al. 2010)

$$N_{tot} = \frac{8\pi\nu_{\rm rest}^2}{c^2}\frac{1}{A_{ul}}\frac{1}{g_u}\, Q_{rot}\,(T_{rot})\frac{\exp(E_u/T_{rot})}{\exp(h\nu_{\rm rest}/k_B\, T_{ex})-1}\int \tau_\nu\, d\nu. \tag{A.18}$$

In the above equation, h and k_B are respectively the Planck and Boltzmann constants in cgs units, $\nu_{\rm rest}$(Hz) is the rest frequency of the emission line, A_{ul} ($\rm s^{-1}$) is the Einstein A coefficient for the observed transition, g_u and E_u (K) are respectively the statistical weight and energy of the upper level for the rotational transition, and $Q(T_{ex})$ is the rotational partition function of the molecule. Assuming the observed emission lines have Gaussian profiles, we can use Equation (2.3), Equation (2.5) and $\Delta v = 2\sqrt{2\ln 2}\sigma_v$ to determine the integral in Equation (A.18) (see e.g., Rosolowsky et al. 2008; Johnstone et al. 2010)

$$\int \tau_\nu d\nu = \sqrt{2\pi}\,\tau\,\sigma_\nu = \sqrt{2\pi}\frac{\nu_{rest}}{c}\,\sigma_v\,\tau = \frac{\sqrt{\pi}}{2\sqrt{\ln 2}}\frac{\nu_{rest}}{c}\Delta v\,\tau \tag{A.19}$$

$$N_{tot} = \frac{8\pi\nu_{\rm rest}^3}{c^3}\frac{\sqrt{\pi}}{2\sqrt{\ln 2}}\frac{1}{A_{ul}}\frac{1}{g_u}\,Q_{rot}\,(T_{rot})\frac{\exp(E_u/T_{rot})}{\exp(h\nu_{\rm rest}/k_B\,T_{ex})-1}\,\Delta v\,\tau. \tag{A.20}$$

To calculate the column density of NH_3, we used Equation (A.20) (Devine et al. 2011), where again T_{rot} is the rotational temperature that relates the populations in the rotational levels NH_3 (1, 1) and (2, 2) to their energy difference ΔE. We calculated T_{rot} using the method described in Rosolowsky et al. (2008). For the other observed species, we used $T_{rot} = T_{ex}$, where T_{ex} is the excitation temperature of the observed rotational transition. Therefore, in such cases Equation (A.20) is modified to the following

$$N_{tot} = \frac{8\pi\nu_{\rm rest}^3}{c^3}\frac{\sqrt{\pi}}{2\sqrt{\ln 2}}\frac{1}{A_{ul}}\frac{1}{g_u}\,Q\,(T_{ex})\frac{\exp(E_u/T_{ex})}{\exp(h\nu_{\rm rest}/k_B\,T_{ex})-1}\,\Delta v\,\tau. \tag{A.21}$$

We used the partition function values for $T_{ex} \leq 50$ K from the JPL spectral line catalog for NH_3 (Pickett et al. 1998) and from the Cologne Database for Molecular Spectroscopy (CDMS; Müller et al. 2001) for the rest of the molecules in our sample. For the linear molecules (N_2H^+, HNC, HCN), we interpolated the partition function values using $\alpha+\beta T_{ex}$. NH_3 is a prolate symmetric top molecule and NH_2D is a slightly asymmetric top molecule. Therefore, in case of NH_3 and NH_2D, we interpolated the partition function data points using $\alpha+\beta T_{ex}^{1.5}$ to derive the functional form of $Q(T_{ex})$ (Busquet et al. 2010; Blake et al. 1987). The partition function values presented in the JPL catalog for NH_3 already include the para-to-ortho ratio. Also, the upper level degeneracy (g_u) given in the JPL catalog accounts for both of the parity states of the NH_3 (1,1) emission line (Shanshan Yu and Brian Drouin 2013, private communication). Similar methods of calculating NH_3 column density have been previously employed by other authors, e.g., Purcell et al. (2009) and Devine et al. (2011). For comparison, we also calculated $N(NH_3)$ toward SMM16 using the method described in Friesen et al. (2009) and derived similar values. Furthermore, the partition function values presented in the CDMS catalog for NH_2D already include the para-to-ortho ratio (Busquet et al. 2010; Holger S. P. Müller 2013, private communication). Table A1 lists best fit parameters for the partition function of each molecule along with

other parameters used in the calculation of the column densities.

Table A1: Parameters used in column density calculations.

Molecule	Transition	A_{ul} (s^{-1})	g_u	E_u (K)	$Q(T)$
NH_2D [1]	$J_{K_a,K_c} = 1^a_{1,1} - 1^s_{0,1}$	7.82×10^{-6}	27	20.68	$4.47 + 0.77T_{ex}^{1.5}$
HCN [1]	J = 1 − 0	2.41×10^{-5}	9	4.25	$1.13 + 1.41T_{ex}$
HNC [1]	J = 1 − 0	2.69×10^{-5}	3	4.35	$0.38 + 0.46T_{ex}$
N_2H^+ [1]	J = 1 − 0	3.89×10^{-5}	27	4.47	$3.41 + 4.01T_{ex}$
NH_3 [2]	J,K = 1,1	1.68×10^{-7}	6	23.26	$2.57 + 0.11T_{rot}^{1.5}$

Note. — References: (1) The data for A_{ul}, g_u, and $Q(T_{ex})$ are taken directly from CDMS (Müller et al. 2001; Müller et al. 2005). The data for E_u are from Splatalogue entries from CDMS. (2) In case of NH_3 (1,1), the data for g_u and $Q(T_{rot})$ are directly from JPL molecular spectroscopy catalog (Pickett et al. 1998), and the data for A_{ul} and E_u are from Splatalogue entries from JPL molecular spectroscopy catalog.

Bibliography

Aguti, E. D., Lada, C. J., Bergin, E. A., Alves, J. F., & Birkinshaw, M. 2007, ApJ, 665, 457

Aikawa, Y., Herbst, E., Roberts, H., & Caselli, P. 2005, ApJ, 620, 330

Alves, J. F., Lada, C. J., & Lada, E. A. 2001, Nature, 409, 159

Anathpindika, S., & Di Francesco, J. D. 2013, MNRAS, 430, 1854

André, P., Men'shchikov, A., Bontemps, S., Könyves, V., Motte, F., Schneider, N., Didelon, P., Minier, V., Saraceno, P., Ward-Thompson, D., di Francesco, J., White, G., Molinari, S., Testi, L., Abergel, A., Griffin, M., Henning, T., Royer, P., Merín, B., Vavrek, R., Attard, M., Arzoumanian, D., Wilson, C. D., Ade, P., Aussel, H., Baluteau, J.-P., Benedettini, M., Bernard, J.-P., Blommaert, J. A. D. L., Cambrésy, L., Cox, P., di Giorgio, A., Hargrave, P., Hennemann, M., Huang, M., Kirk, J., Krause, O., Launhardt, R., Leeks, S., Le Pennec, J., Li, J. Z., Martin, P. G., Maury, A., Olofsson, G., Omont, A., Peretto, N., Pezzuto, S., Prusti, T., Roussel, H., Russeil, D., Sauvage, M., Sibthorpe, B., Sicilia-Aguilar, A., Spinoglio, L., Waelkens, C., Woodcraft, A., & Zavagno, A. 2010, A&A, 518, L102

André, P., Ward-Thompson, D., & Barsony, M. 2000, Protostars and Planets IV, 59

André, P., Ward-Thompson, D., & Motte, F. 1996, A&A, 314, 625

Bacmann, A., Lefloch, B., Ceccarelli, C., Castets, A., Steinacker, J., & Loinard, L. 2002, A&A, 389, L6

Bacmann, A., Lefloch, B., Ceccarelli, C., Steinacker, J., Castets, A., & Loinard, L. 2003, ApJ, 585, L55

Barranco, J. A., & Goodman, A. A. 1998, ApJ, 504, 207

Basu, S., & Jones, C. E. 2004, MNRAS, 347, L47

Benson, P. J., Caselli, P., & Myers, P. C. 1998, ApJ, 506, 743

Benson, P. J., & Myers, P. C. 1989, ApJS, 71, 89

Bergin, E. A., Alves, J., Huard, T., & Lada, C. J. 2002, ApJ, 570, L101

Bergin, E. A., Ciardi, D. R., Lada, C. J., Alves, J., & Lada, E. A. 2001, ApJ, 557, 209

Bergin, E. A., Neufeld, D. A., & Melnick, G. J. 1998, ApJ, 499, 777

Bertoldi, F., & McKee, C. F. 1992, ApJ, 395, 140

Blake, G. A., Sutton, E. C., Masson, C. R., & Phillips, T. G. 1987, ApJ, 315, 621

Bonnor, W. B. 1956, MNRAS, 116, 351

Bourke, T. L., Crapsi, A., Myers, P. C., Evans, II, N. J., Wilner, D. J., Huard, T. L., Jørgensen, J. K., & Young, C. H. 2005, ApJ, 633, L129

Bourke, T. L., Myers, P. C., Evans, II, N. J., Dunham, M. M., Kauffmann, J., Shirley, Y. L., Crapsi, A., Young, C. H., Huard, T. L., Brooke, T. Y., Chapman, N., Cieza, L., Lee, C. W., Teuben, P., & Wahhaj, Z. 2006, ApJ, 649, L37

Brinch, C., & Hogerheijde, M. R. 2010, A&A, 523, A25

Broderick, A. E., Keto, E., Lada, C. J., & Narayan, R. 2007, ApJ, 671, 1832

Bunker, P. R., & Jensen, P. 2006, Molecular symmetry and spectroscopy

Busquet, G., Palau, A., Estalella, R., Girart, J. M., Sánchez-Monge, Á., Viti, S., Ho, P. T. P., & Zhang, Q. 2010, A&A, 517, L6

Caselli, P., Benson, P. J., Myers, P. C., & Tafalla, M. 2002, ApJ, 572, 238

Caselli, P., Myers, P. C., & Thaddeus, P. 1995, ApJ, 455, L77

Caselli, P., Walmsley, C. M., Tafalla, M., Dore, L., & Myers, P. C. 1999, ApJ, 523, L165

Cernicharo, J., Castets, A., Duvert, G., & Guilloteau, S. 1984, A&A, 139, L13

Chandrasekhar, S. 1957, An introduction to the study of stellar structure.

—. 1967, An introduction to the study of stellar structure

Codella, C., Welser, R., Henkel, C., Benson, P. J., & Myers, P. C. 1997, A&A, 324, 203

Cox, A. N. 2000, Allen's astrophysical quantities

Crapsi, A., Caselli, P., Walmsley, C. M., Myers, P. C., Tafalla, M., Lee, C. W., & Bourke, T. L. 2005a, ApJ, 619, 379

Crapsi, A., Caselli, P., Walmsley, C. M., Tafalla, M., Lee, C. W., Bourke, T. L., & Myers, P. C. 2004, A&A, 420, 957

Crapsi, A., Caselli, P., Walmsley, M. C., & Tafalla, M. 2007, A&A, 470, 221

Crapsi, A., Devries, C. H., Huard, T. L., Lee, J.-E., Myers, P. C., Ridge, N. A., Bourke, T. L., Evans, II, N. J., Jørgensen, J. K., Kauffmann, J., Lee, C. W., Shirley, Y. L., & Young, C. H. 2005b, A&A, 439, 1023

Dapp, W. B., & Basu, S. 2009, MNRAS, 395, 1092

De Vries, C. H., & Myers, P. C. 2005, ApJ, 620, 800

Devine, K. E., Chandler, C. J., Brogan, C., Churchwell, E., Indebetouw, R., Shirley, Y., & Borg, K. J. 2011, ApJ, 733, 44

Di Francesco, J., André, P., & Myers, P. C. 2004, ApJ, 617, 425

Di Francesco, J., Evans, II, N. J., Caselli, P., Myers, P. C., Shirley, Y., Aikawa, Y., & Tafalla, M. 2007, Protostars and Planets V, 17

Di Francesco, J., Johnstone, D., Kirk, H., MacKenzie, T., & Ledwosinska, E. 2008, ApJS, 175, 277

Ebert, R. 1955, ZAp, 37, 217

Elias, J. H. 1978, ApJ, 224, 857

Emerson, D. T., & Graeve, R. 1988, A&A, 190, 353

Emprechtinger, M., Caselli, P., Volgenau, N. H., Stutzki, J., & Wiedner, M. C. 2009, A&A, 493, 89

Evans, II, N. J. 1999, ARA&A, 37, 311

Evans, II, N. J., Rawlings, J. M. C., Shirley, Y. L., & Mundy, L. G. 2001, ApJ, 557, 193

Frerking, M. A., Langer, W. D., & Wilson, R. W. 1982, ApJ, 262, 590

Friesen, R. K., Di Francesco, J., Myers, P. C., Belloche, A., Shirley, Y. L., Bourke, T. L., & André, P. 2010a, ApJ, 718, 666

Friesen, R. K., Di Francesco, J., Shimajiri, Y., & Takakuwa, S. 2010b, ApJ, 708, 1002

Friesen, R. K., Di Francesco, J., Shirley, Y. L., & Myers, P. C. 2009, ApJ, 697, 1457

Friesen, R. K., Medeiros, L., Schnee, S., Bourke, T. L., Di Francesco, J., Gutermuth, R., & Myers, P. C. 2013, ArXiv e-prints

Fu, T.-M., Gao, Y., & Lou, Y.-Q. 2011, ApJ, 741, 113

Fuller, G. A., Myers, P. C., Welch, W. J., Goldsmith, P. F., Langer, W. D., Campbell, B. G., Guilloteau, S., & Wilson, R. W. 1991, ApJ, 376, 135

Galli, D., Walmsley, M., & Gonçalves, J. 2002, A&A, 394, 275

Gao, Y., & Lou, Y.-Q. 2010, MNRAS, 403, 1919

Goldsmith, P. F. 2001, ApJ, 557, 736

Goldsmith, P. F., Langer, W. D., & Velusamy, T. 1999, ApJ, 519, L173

Goodman, A. A., Barranco, J. A., Wilner, D. J., & Heyer, M. H. 1998, ApJ, 504, 223

Gottlieb, C. A., Lada, C. J., Gottlieb, E. W., Lilley, A. E., & Litvak, M. M. 1975, ApJ, 202, 655

Griffin, M. J., Abergel, A., Abreu, A., Ade, P. A. R., André, P., Augueres, J.-L., Babbedge, T., Bae, Y., Baillie, T., Baluteau, J.-P., Barlow, M. J., Bendo, G., Benielli, D., Bock, J. J., Bonhomme, P., Brisbin, D., Brockley-Blatt, C., Caldwell, M., Cara, C., Castro-Rodriguez, N., Cerulli, R., Chanial, P., Chen, S., Clark, E.,

Clements, D. L., Clerc, L., Coker, J., Communal, D., Conversi, L., Cox, P., Crumb, D., Cunningham, C., Daly, F., Davis, G. R., de Antoni, P., Delderfield, J., Devin, N., di Giorgio, A., Didschuns, I., Dohlen, K., Donati, M., Dowell, A., Dowell, C. D., Duband, L., Dumaye, L., Emery, R. J., Ferlet, M., Ferrand, D., Fontignie, J., Fox, M., Franceschini, A., Frerking, M., Fulton, T., Garcia, J., Gastaud, R., Gear, W. K., Glenn, J., Goizel, A., Griffin, D. K., Grundy, T., Guest, S., Guillemet, L., Hargrave, P. C., Harwit, M., Hastings, P., Hatziminaoglou, E., Herman, M., Hinde, B., Hristov, V., Huang, M., Imhof, P., Isaak, K. J., Israelsson, U., Ivison, R. J., Jennings, D., Kiernan, B., King, K. J., Lange, A. E., Latter, W., Laurent, G., Laurent, P., Leeks, S. J., Lellouch, E., Levenson, L., Li, B., Li, J., Lilienthal, J., Lim, T., Liu, S. J., Lu, N., Madden, S., Mainetti, G., Marliani, P., McKay, D., Mercier, K., Molinari, S., Morris, H., Moseley, H., Mulder, J., Mur, M., Naylor, D. A., Nguyen, H., O'Halloran, B., Oliver, S., Olofsson, G., Olofsson, H.-G., Orfei, R., Page, M. J., Pain, I., Panuzzo, P., Papageorgiou, A., Parks, G., Parr-Burman, P., Pearce, A., Pearson, C., Pérez-Fournon, I., Pinsard, F., Pisano, G., Podosek, J., Pohlen, M., Polehampton, E. T., Pouliquen, D., Rigopoulou, D., Rizzo, D., Roseboom, I. G., Roussel, H., Rowan-Robinson, M., Rownd, B., Saraceno, P., Sauvage, M., Savage, R., Savini, G., Sawyer, E., Scharmberg, C., Schmitt, D., Schneider, N., Schulz, B., Schwartz, A., Shafer, R., Shupe, D. L., Sibthorpe, B., Sidher, S., Smith, A., Smith, A. J., Smith, D., Spencer, L., Stobie, B., Sudiwala, R., Sukhatme, K., Surace, C., Stevens, J. A., Swinyard, B. M., Trichas, M., Tourette, T., Triou, H., Tseng, S., Tucker, C., Turner, A., Vaccari, M., Valtchanov, I., Vigroux, L., Virique, E., Voellmer, G., Walker, H., Ward, R., Waskett, T., Weilert, M., Wesson, R., White, G. J., Whitehouse, N., Wilson, C. D., Winter, B., Woodcraft, A. L., Wright, G. S., Xu, C. K., Zavagno, A., Zemcov, M., Zhang, L., & Zonca, E. 2010, A&A, 518, L3

Harvey, D. W. A., Wilner, D. J., Lada, C. J., Myers, P. C., & Alves, J. F. 2003a, ApJ, 598, 1112

Harvey, D. W. A., Wilner, D. J., Myers, P. C., & Tafalla, M. 2003b, ApJ, 597, 424

Herbst, E., Terzieva, R., & Talbi, D. 2000, MNRAS, 311, 869

Hily-Blant, P., Walmsley, M., Pineau Des Forêts, G., & Flower, D. 2010, A&A, 513, A41

Hirota, T., Yamamoto, S., Mikami, H., & Ohishi, M. 1998, ApJ, 503, 717

Ho, P. T. P., & Townes, C. H. 1983, ARA&A, 21, 239

Hogerheijde, M. R., & van der Tak, F. F. S. 2000, A&A, 362, 697

Hotzel, S., Harju, J., & Walmsley, C. M. 2004, A&A, 415, 1065

Johnstone, D., Rosolowsky, E., Tafalla, M., & Kirk, H. 2010, ApJ, 711, 655

Jørgensen, J. K., Bourke, T. L., Myers, P. C., Schöier, F. L., van Dishoeck, E. F., & Wilner, D. J. 2005, ApJ, 632, 973

Juvela, M., Harju, J., Ysard, N., & Lunttila, T. 2012, A&A, 538, A133

Kandori, R., Nakajima, Y., Tamura, M., Tatematsu, K., Aikawa, Y., Naoi, T., Sugitani, K., Nakaya, H., Nagayama, T., Nagata, T., Kurita, M., Kato, D., Nagashima, C., & Sato, S. 2005, AJ, 130, 2166

Kauffmann, J., Bertoldi, F., Bourke, T. L., Evans, II, N. J., & Lee, C. W. 2008, A&A, 487, 993

Kawamura, A., Kun, M., Onishi, T., Vavrek, R., Domsa, I., Mizuno, A., & Fukui, Y. 2001, PASJ, 53, 1097

Keto, E., Broderick, A. E., Lada, C. J., & Narayan, R. 2006, ApJ, 652, 1366

Keto, E., & Caselli, P. 2008, ApJ, 683, 238

—. 2010, MNRAS, 402, 1625

Keto, E., & Field, G. 2005, ApJ, 635, 1151

Keto, E., & Rybicki, G. 2010, ApJ, 716, 1315

Keto, E., Rybicki, G. B., Bergin, E. A., & Plume, R. 2004, ApJ, 613, 355

Keto, E. R. 1990, ApJ, 355, 190

King, I. 1962, AJ, 67, 471

Kirk, J. M., Ward-Thompson, D., & André, P. 2005, MNRAS, 360, 1506

Kirk, J. M., Ward-Thompson, D., Palmeirim, P., André, P., Griffin, M. J., Hargrave, P. J., Könyves, V., Bernard, J.-P., Nutter, D. J., Sibthorpe, B., Di Francesco, J., Abergel, A., Arzoumanian, D., Benedettini, M., Bontemps, S., Elia, D., Hennemann, M., Hill, T., Men'shchikov, A., Motte, F., Nguyen-Luong, Q., Peretto, N., Pezzuto, S., Rygl, K. L. J., Sadavoy, S. I., Schisano, E., Schneider, N., Testi, L., & White, G. 2013, MNRAS, 432, 1424

Kukolich, S. G. 1967, Phys. Rev., 156, 83

Kutner, M. L., & Ulich, B. L. 1981, ApJ, 250, 341

Lada, C. J., Bergin, E. A., Alves, J. F., & Huard, T. L. 2003, ApJ, 586, 286

Lada, C. J., & Lada, E. A. 2003, ARA&A, 41, 57

Ladd, N., Purcell, C., Wong, T., & Robertson, S. 2005, Publications of the Astronomical Society of Australia, 22, 62

Lai, S.-P., Velusamy, T., Langer, W. D., & Kuiper, T. B. H. 2003, AJ, 126, 311

Lee, C. W., & Myers, P. C. 1999, ApJS, 123, 233

—. 2011, ApJ, 734, 60

Lee, C. W., Myers, P. C., & Plume, R. 2004, ApJS, 153, 523

Lee, C. W., Myers, P. C., & Tafalla, M. 1999, ApJ, 526, 788

—. 2001, ApJS, 136, 703

Levshakov, S. A., Henkel, C., Reimers, D., Wang, M., Mao, R., Wang, H., & Xu, Y. 2013, A&A, 553, A58

Loinard, L., Torres, R. M., Mioduszewski, A. J., & Rodríguez, L. F. 2008, ApJ, 675, L29

Lou, Y.-Q., & Gao, Y. 2011, MNRAS, 412, 1755

Lou, Y.-Q., & Shen, Y. 2004, MNRAS, 348, 717

Loughnane, R. M., Redman, M. P., Thompson, M. A., Lo, N., O'Dwyer, B., & Cunningham, M. R. 2012, MNRAS, 420, 1367

Lovas, F. J., & Dragoset, R. A. 2004, J. Phys. Chem. Data 33: 177-355

Maheswar, G., Lee, C. W., & Dib, S. 2011, A&A, 536, A99

Mardones, D., Myers, P. C., Tafalla, M., Wilner, D. J., Bachiller, R., & Garay, G. 1997, ApJ, 489, 719

Markwardt, C. B. 2009, in Astronomical Society of the Pacific Conference Series, Vol. 411, Astronomical Data Analysis Software and Systems XVIII, ed. D. A. Bohlender, D. Durand, & P. Dowler, 251

Marsh, K. A., Griffin, M. J., Palmeirim, P., André, P., Kirk, J., Stamatellos, D., Ward-Thompson, D., Roy, A., Bontemps, S., Francesco, J. D., Elia, D., Hill, T., Könyves, V., Motte, F., Nguyen-Luong, Q., Peretto, N., Pezzuto, S., Rivera-Ingraham, A., Schneider, N., Spinoglio, L., & White, G. 2014, MNRAS, 439, 3683

Masters, J., Garwood, B., Langston, G., & Shelton, A. 2011, in Astronomical Society of the Pacific Conference Series, Vol. 442, Astronomical Data Analysis Software and Systems XX, ed. I. N. Evans, A. Accomazzi, D. J. Mink, & A. H. Rots, 127

McKee, C. F. 1999, in NATO ASIC Proc. 540: The Origin of Stars and Planetary Systems, ed. C. J. Lada & N. D. Kylafis, 29

Morales Ortiz, J. L., Olmi, L., Burton, M., De Luca, M., Elia, D., Giannini, T., Lorenzetti, D., Massi, F., & Strafella, F. 2012, A&A, 543, A65

Müller, H. S. P., Schlöder, F., Stutzki, J., & Winnewisser, G. 2005, Journal of Molecular Structure, 742, 215

Müller, H. S. P., Thorwirth, S., Roth, D. A., & Winnewisser, G. 2001, A&A, 370, L49

Myers, P. C., & Benson, P. J. 1983, ApJ, 266, 309

Myers, P. C., Benson, P. J., & Ho, P. T. P. 1979, ApJ, 233, L141

Myers, P. C., Mardones, D., Tafalla, M., Williams, J. P., & Wilner, D. J. 1996, ApJ, 465, L133

Narayanan, G., Moriarty-Schieven, G., Walker, C. K., & Butner, H. M. 2002, ApJ, 565, 319

Narayanan, G., Walker, C. K., & Buckley, H. D. 1998, ApJ, 496, 292

Nutter, D., Ward-Thompson, D., & André, P. 2006, MNRAS, 368, 1833

Ohashi, N., Lee, S. W., Wilner, D. J., & Hayashi, M. 1999, ApJ, 518, L41

Onishi, T., Mizuno, A., & Fukui, Y. 1999, PASJ, 51, 257

Ossenkopf, V., & Henning, T. 1994, A&A, 291, 943

Pagani, L., Bacmann, A., Cabrit, S., & Vastel, C. 2007, A&A, 467, 179

Palau, A., Estalella, R., Girart, J. M., Ho, P. T. P., Zhang, Q., & Beuther, H. 2007, A&A, 465, 219

Pavlyuchenkov, Y., Henning, T., & Wiebe, D. 2007, ApJ, 669, L101

Pickett, H. M., Poynter, R. L., Cohen, E. A., Delitsky, M. L., Pearson, J. C., & Müller, H. S. P. 1998, J. Quant. Spec. Radiat. Transf., 60, 883

Pillai, T., Kauffmann, J., Wyrowski, F., Hatchell, J., Gibb, A. G., & Thompson, M. A. 2011, A&A, 530, A118

Pineda, J. E., Goodman, A. A., Arce, H. G., Caselli, P., Foster, J. B., Myers, P. C., & Rosolowsky, E. W. 2010, ApJ, 712, L116

Purcell, C. R., Minier, V., Longmore, S. N., André, P., Walsh, A. J., Jones, P., Herpin, F., Hill, T., Cunningham, M. R., & Burton, M. G. 2009, A&A, 504, 139

Redman, M. P., Keto, E., Rawlings, J. M. C., & Williams, D. A. 2004, MNRAS, 352, 1365

Roberts, H., & Millar, T. J. 2000, A&A, 361, 388

Rohlfs, K., & Wilson, T. L. 2004, Tools of radio astronomy

Rosolowsky, E. W., Pineda, J. E., Foster, J. B., Borkin, M. A., Kauffmann, J., Caselli, P., Myers, P. C., & Goodman, A. A. 2008, ApJS, 175, 509

Roy, A., André, P., Palmeirim, P., Attard, M., Könyves, V., Schneider, N., Peretto, N., Men'shchikov, A., Ward-Thompson, D., Kirk, J., Griffin, M., Marsh, K., Abergel, A., Arzoumanian, D., Benedettini, M., Hill, T., Motte, F., Nguyen Luong,

Q., Pezzuto, S., Rivera-Ingraham, A., Roussel, H., Rygl, K. L. J., Spinoglio, L., Stamatellos, D., & White, G. 2014, A&A, 562, A138

Rybicki, G. B., & Hummer, D. G. 1991, A&A, 245, 171

Rydbeck, O. E. H., Sume, A., Hjalmarson, A., Ellder, J., Ronnang, B. O., & Kollberg, E. 1977, ApJ, 215, L35

Sadavoy, S. I., di Francesco, J., André, P., Pezzuto, S., Bernard, J.-P., Bontemps, S., Bressert, E., Chitsazzadeh, S., Fallscheer, C., Hennemann, M., Hill, T., Martin, P., Motte, F., Nguyen Luong, Q., Peretto, N., Reid, M., Schneider, N., Testi, L., White, G. J., & Wilson, C. 2012, A&A, 540, A10

Sadavoy, S. I., Di Francesco, J., Bontemps, S., Megeath, S. T., Rebull, L. M., Allgaier, E., Carey, S., Gutermuth, R., Hora, J., Huard, T., McCabe, C.-E., Muzerolle, J., Noriega-Crespo, A., Padgett, D., & Terebey, S. 2010a, ApJ, 710, 1247

Sadavoy, S. I., Di Francesco, J., & Johnstone, D. 2010b, ApJ, 718, L32

Sawada, T., Ikeda, N., Sunada, K., Kuno, N., Kamazaki, T., Morita, K.-I., Kurono, Y., Koura, N., Abe, K., Kawase, S., Maekawa, J., Horigome, O., & Yanagisawa, K. 2008, PASJ, 60, 445

Schmid-Burgk, J., Muders, D., Müller, H. S. P., & Brupbacher-Gatehouse, B. 2004, A&A, 419, 949

Schnee, S., Brunetti, N., Di Francesco, J., Caselli, P., Friesen, R., Johnstone, D., & Pon, A. 2013, ApJ, 777, 121

Shah, R. Y., & Wootten, A. 2001, ApJ, 554, 933

Shinnaga, H., Ohashi, N., Lee, S.-W., & Moriarty-Schieven, G. H. 2004, ApJ, 601, 962

Shirley, Y. L., Claussen, M. J., Bourke, T. L., Young, C. H., & Blake, G. A. 2007, ApJ, 667, 329

Shirley, Y. L., Nordhaus, M. K., Grcevich, J. M., Evans, II, N. J., Rawlings, J. M. C., & Tatematsu, K. 2005, ApJ, 632, 982

Shu, F. H. 1977, ApJ, 214, 488

Shu, F. H., Adams, F. C., & Lizano, S. 1987, ARA&A, 25, 23

Snyder, L. E., Hollis, J. M., & Buhl, D. 1977, ApJ, 215, L87

Sohn, J., Lee, C. W., Park, Y.-S., Lee, H. M., Myers, P. C., & Lee, Y. 2007, ApJ, 664, 928

Sorai, K., Sunada, K., Okumura, S. K., Tetsuro, I., Tanaka, A., Natori, K., & Onuki, H. 2000, in Society of Photo-Optical Instrumentation Engineers (SPIE) Conference Series, Vol. 4015, Society of Photo-Optical Instrumentation Engineers (SPIE) Conference Series, ed. H. R. Butcher, 86–95

Stahler, S. W., & Palla, F. 2005, The Formation of Stars

Stahler, S. W., & Yen, J. J. 2010, MNRAS, 407, 2434

Stutz, A., Launhardt, R., Linz, H., Krause, O., Henning, T., Kainulainen, J., Nielbock, M., Steinacker, J., & André, P. 2010, A&A, 518, L87+

Stutz, A. M., Bourke, T. L., Rieke, G. H., Bieging, J. H., Misselt, K. A., Myers, P. C., & Shirley, Y. L. 2009, ApJ, 690, L35

Sunada, K., Yamaguchi, C., Nakai, N., Sorai, K., Okumura, S. K., & Ukita, N. 2000, in Society of Photo-Optical Instrumentation Engineers (SPIE) Conference Series, Vol. 4015, Society of Photo-Optical Instrumentation Engineers (SPIE) Conference Series, ed. H. R. Butcher, 237–246

Swift, J. J., Welch, W. J., & Di Francesco, J. 2005, ApJ, 620, 823

Tafalla, M., Myers, P. C., Caselli, P., & Walmsley, C. M. 2004, A&A, 416, 191

Tafalla, M., Myers, P. C., Caselli, P., Walmsley, C. M., & Comito, C. 2002, ApJ, 569, 815

Tafalla, M., Santiago-García, J., Myers, P. C., Caselli, P., Walmsley, C. M., & Crapsi, A. 2006, A&A, 455, 577

Takahashi, S., Ohashi, N., & Bourke, T. L. 2013, ApJ, 774, 20

Takakuwa, S., Ohashi, N., & Aikawa, Y. 2011, ApJ, 728, 101

Tatematsu, K., Kandori, R., Umemoto, T., & Sekimoto, Y. 2008, PASJ, 60, 407

Tatematsu, K., Umemoto, T., Kandori, R., & Sekimoto, Y. 2004, ApJ, 606, 333

Tennekes, P. P., Harju, J., Juvela, M., & Tóth, L. V. 2006, A&A, 456, 1037

Terebey, S., Fich, M., Noriega-Crespo, A., Padgett, D. L., Fukagawa, M., Audard, M., Brooke, T., Carey, S., Evans, II, N. J., Guedel, M., Hines, D., Huard, T., Knapp, G. R., McCabe, C.-E., Menard, F., Monin, J.-L., & Rebull, L. 2009, ApJ, 696, 1918

Thompson, M. A., & White, G. J. 2004, A&A, 419, 599

Tsitali, A. E., Belloche, A., Commerçon, B., & Menten, K. M. 2013, A&A, 557, A98

Visser, A. E., Richer, J. S., & Chandler, C. J. 2002, AJ, 124, 2756

Walker, C. K., Narayanan, G., & Boss, A. P. 1994, ApJ, 431, 767

Walmsley, C. M., Churchwell, E., Nash, A., & Fitzpatrick, E. 1982, ApJ, 258, L75

Walsh, A. J., Myers, P. C., & Burton, M. G. 2004, ApJ, 614, 194

Walsh, A. J., Myers, P. C., Di Francesco, J., Mohanty, S., Bourke, T. L., Gutermuth, R., & Wilner, D. 2007, ApJ, 655, 958

Ward-Thompson, D., André, P., & Kirk, J. M. 2002, MNRAS, 329, 257

Ward-Thompson, D., Scott, P. F., Hills, R. E., & Andre, P. 1994, MNRAS, 268, 276

Williams, J. P., Lee, C. W., & Myers, P. C. 2006, ApJ, 636, 952

Williams, J. P., Myers, P. C., Wilner, D. J., & Di Francesco, J. 1999, ApJ, 513, L61

Yamaguchi, C., Sunada, K., Iizuka, Y., Iwashita, H., & Noguchi, T. 2000, in Society of Photo-Optical Instrumentation Engineers (SPIE) Conference Series, Vol. 4015, Society of Photo-Optical Instrumentation Engineers (SPIE) Conference Series, ed. H. R. Butcher, 614–623

Young, C. H., Jørgensen, J. K., Shirley, Y. L., Kauffmann, J., Huard, T., Lai, S.-P., Lee, C. W., Crapsi, A., Bourke, T. L., Dullemond, C. P., Brooke, T. Y., Porras, A., Spiesman, W., Allen, L. E., Blake, G. A., Evans, II, N. J., Harvey, P. M., Koerner, D. W., Mundy, L. G., Myers, P. C., Padgett, D. L., Sargent, A. I., Stapelfeldt, K. R., van Dishoeck, E. F., Bertoldi, F., Chapman, N., Cieza, L., DeVries, C. H., Ridge, N. A., & Wahhaj, Z. 2004a, ApJS, 154, 396

Young, K. E., Lee, J., Evans, II, N. J., Goldsmith, P. F., & Doty, S. D. 2004b, ApJ, 614, 252